Title
Improvements in Energy Decomposition Analysis for Single Determinant Methods

Author
Horn, Paul Richard

Publication Date
2015

Peer reviewed|Thesis/dissertation

IMPROVEMENTS IN ENERGY DECOMPOSITION ANALYSIS FOR SINGLE DETERMINANT METHODS

by

PAUL RICHARD HORN

A dissertation submitted in partial satisfaction of the
requirements for the degree of
Doctor of Philosophy

in

Chemistry

in the

Graduate Division

of the

University of California, Berkeley

Committee in charge:

Professor Martin Head-Gordon, Chair
Professor Stephen R. Leone
Professor Alexis T. Bell

Summer 2015

IMPROVEMENTS IN ENERGY DECOMPOSITION ANALYSIS FOR SINGLE DETERMINANT METHODS

Abstract

IMPROVEMENTS IN ENERGY DECOMPOSITION ANALYSIS FOR SINGLE DETERMINANT METHODS

by

PAUL RICHARD HORN

Doctor of Philosophy in Chemistry

University of California, Berkeley

Professor Martin Head-Gordon, Chair

This thesis is concerned with the decomposition of intermolecular interaction energies computed by Hartree-Fock theory or Kohn-Sham density functional theory into physically meaningful contributions. While there is no unique way to perform this energy decomposition analysis (EDA), such methods can be judged based on formal properties, physical content, and descriptive power. Throughout this work we assess and address the weaknesses of the Absolutely Localized Molecular Orbital (ALMO) energy decomposition scheme to develop a new scheme with terms describing five distinct physical contributions: permanent electrostatics, Pauli repulsion, exchange-correlation, polarization, and charge transfer. This scheme moreover has many desirable formal properties, satisfying all of the criteria for a good EDA method that we outline in the introduction.

To my parents,
Mary Jo and Richard,
for their love and encouragement.

Contents

List of Figures

List of Tables

Acknowledgments

This work would not have been possible without the help of my advisor, Professor Martin Head-Gordon, to whom I am particularly thankful for giving me the freedom and encouragement to pursure my own ideas. I have benefited greatly from the collective knowledge of the entire Head-Gordon group, and I hope that I have done my part to propagate and to contribute to this knowledge for the students who will come after me. I would like to thank in particular Dr. R. Julian Azar, Dr. Franziska Bell, Professor Andreas W. Hauser, Samuel Manzer, Yuezhi Mao, Narbe Mardirossian, Professor Nicholas J. Mayhall, and Dr. Eric Jon Sundstrom who all collaborated with me on various projects during my time at Berkeley and who, through these interactions, taught me a great deal. The Head-Gordon group is not only a group of excellent researchers but also of good friends, who, along with Alex Shearer and Chiara Heide, made my graduate school experience more enjoyable and productive.

Chapter 1

Introduction

1.1 Chemical Significance of Intermolecular Interactions

Intermolecular interactions refer to the attractions and repulsions that occur between molecular species that determine many of the properties of matter. These forces are vital (describing the enthalpic contributions) to understanding basic experiences: objects are hard, at a given temperature some compounds are solid while others are liquids or gasses, certain combinations of liquids are immiscible, some compounds dissolve in a given liquid and others do not, etc. Because these forces are so relevant to the way in which matter behaves, it is a goal of chemistry both to understand and to manipulate these forces, most notably by chemical modification of the compounds involved.

The above examples are certainly relevant to everyday life; however, there are also many other arguably more interesting applications of the study of intermolecular interactions that are relevant to research in chemistry and related fields. Knowledge of interactions is particularly relevant in reactive scattering experiments where the intermolecular forces determine the potential on which the reactants move. Other examples are experiments on molecular clusters where the excitation of a molecule within the cluster is modified by the presence of the other species, and these species in turn relax in response to the excitation. Additionally, some experiments result in the fragmentation of a molecule into a cluster of molecular units that would not otherwise form, and it is often of interest to know which of these clusters are stable and why.

Intermolecular interactions are also important in the study of catalysts. Catalysts increase the rates of reactions or alternatively decrease the severity of the conditions under which the reactions occur with sufficient yield by decreasing the energetic barrier between the reacting and product species. Catalysts are clearly important in improving the efficiency of chemical transformations in industry, but they are also important in a biological context where the regulation of finely tuned biological catalysts, enzymes, is critical to life-sustaining

processes. The configuration of the distorted reactants and the catalyst at the top of this barrier is called the transition structure, and its energy can be lowered if the species interact more strongly. These additional stabilizing interactions between the catalyst and reacting species are particularly important in enzymes where the active site performing that catalysis is embedded within a much larger molecular structure that interacts considerably with the reacting species. An additional important design consideration is that a simply stronger interaction in the transition state will not necessarily lower the barrier for the reaction. One must also consider the corresponding effects on the energies of the initial reactants and final products with the catalyst. Furthermore, the most relevant quantity is not the purely enthalpic energy but rather the free energy, which accounts for entropic effects. The details of interactions are also of considerable concern in transition structures because they can alter the selectivity of the catalyst, changing the relative energies of several possible transition structures which each lead to different products. The process of designing an optimal catalyst that balances these delicate effects for a given reaction can be assisted greatly by an understanding of the intermolecular interactions involved.

Knowledge of the total strength of interaction between some number of molecular species alone will not in general be sufficient to explain why certain clusters form or respond as they do or which sorts of chemical modifications are most appropriate to produce a desired outcome such as an increase in the rate of reaction. The experimental recourse to increase intuition and understanding is often to explore the consequences of a logical sequence of chemical modifications and then reason about what such a modification must mean in terms of physical contributions such as permanent electrostatics, induced electrostatics, polarization, dispersion, and charge transfer or donor-acceptor orbital interactions. These concepts have been historically very useful in chemistry as components of models for explaining observations, and they are discussed in more detail in Section 1.3 and throughout this thesis. Such descriptions require slightly more abstraction than what one might usually consider in the model for a physical system because, as useful and intuitive as these physical contributions may be, they do not usually correspond to observables. Calculations that can accurately describe the total intermolecular interaction as well as compute the contributions of these physical concepts, based again on some model but with well-formulated definitions of terms, are thus in a unique position to quickly build chemical intuition about the importance of certain modes of interaction in a system of interest by associating numerical values with these qualitative ideas. We now consider how one might perform such calculations.

1.2 Calculation of Interaction Energies

1.2.1 The Supermolecular Approach

In this work, we compute interaction (INT) energies (E_{INT}) using the supermolecular approach where the interaction energy is defined as the difference in energy between that of

the supersystem (E_{Super}) and the sum of the energies of the constituent atomic or molecular fragments in their complex geometries ($\{E_A\}$):

$$E_{\mathrm{INT}} = E_{\mathrm{Super}} - \sum_{A}^{frag} E_{\mathrm{A}} \tag{1.1}$$

This is slightly different from a binding energy (E_{BIND}), which in addition considers geometric distortions (GD), the energetic cost (E_{GD}) to distort fragments from their optimal geometries in isolation ($\{\tilde{A}\}$) to those that they adopt in the supermolecular complex ($\{A\}$).

$$E_{\mathrm{BIND}} = E_{\mathrm{INT}} + E_{\mathrm{GD}} \tag{1.2}$$

$$E_{\mathrm{GD}} = \sum_{A}^{frag} E_{\mathrm{A}} - E_{\tilde{\mathrm{A}}} \tag{1.3}$$

The calculation of interaction energies and binding energies is thus straightforward if we know in general how to compute the energies of molecular systems.

1.2.2 The Electronic Hamiltonian

We are interested in computing the lowest energy state of a system of particles, which can be determined by solving the time-independent Schrödinger equation:

$$\hat{H}|\Psi\rangle = E|\Psi\rangle \tag{1.4}$$

E is the energy of the state defined by the wavefunction, Ψ, which is a function of all particle coordinates, and $\hat{H}$ is the Hamiltonian describing the ways in which the particles in the system interact.

Equation 1.4 is too difficult to solve in general, and so we make approximations that are specific to our purpose, namely the description of systems of electrons and nuclei. In the Born-Oppenheimer approximation, the nuclear coordinates ($\{\mathbf{R}_X\}$) are fixed, and only the degrees of freedom of the electrons ($\{\mathbf{r}_i\}$) are considered, yielding an electronic energy for a given configuration of nuclei. This approximation is reasonable because the motions of the much more massive nuclei are considerably slower than those of the electrons, which see the nuclei as effectively stationary. The electronic energy combined with the nuclear-nuclear repulsion energy then defines the potential energy surface on which the nuclei move. The Hamiltonian for the electronic problem within the Born-Oppenheimer approximation in atomic units is as follows:

$$\hat{H}_{elec} = -\sum_{i} \frac{1}{2}\nabla_i^2 - \sum_{i}\sum_{X} \frac{Z_X}{r_{iX}} + \sum_{i}\sum_{j>i} \frac{1}{r_{ij}} \tag{1.5}$$

The first term with differential operators acting on the spatial coordinates of electrons describes the kinetic energy of these particles. The second term describes the attractive Coulombic interaction between the nuclei with positive charges $\{Z_X\}$ and the negatively charged electrons that are separated by a distance r_{iX}. The third term describes the repulsive interaction between electrons that are a distance r_{ij} apart. This simplified Hamiltonian alone is not in general sufficient to make the solution of the ground state energy and wavefunction computationally tractable. We thus further restrict the form of the electronic wavefunction to be a single Slater determinant, the antisymmetric product of one-electron functions. Electrons are fermions, and so wavefunctions describing electrons must be antisymmetric with respect to the interchange of the space and spin (α or β) coordinates of all pairs of electrons. Slater determinants are the simplest functions that guarantee this property.

1.2.3 Hartree-Fock Theory

Direct solution of the electronic structure problem with the restriction to a single Slater determinant electronic wavefunction yields Hartree-Fock theory. The energy in (spin unrestricted) Hartree-Fock theory can be written as:

$$\begin{aligned} E_{HF} = \quad & \mathrm{Tr}\left[(\mathbf{P}_\alpha + \mathbf{P}_\beta)\mathbf{T}\right] + \mathrm{Tr}\left[(\mathbf{P}_\alpha + \mathbf{P}_\beta)\mathbf{V}_{EN}\right] + E_{NN} && (1.6)\\ & + \tfrac{1}{2}\mathrm{Tr}\left[(\mathbf{P}_\alpha + \mathbf{P}_\beta)\mathbf{J}[\mathbf{P}_\alpha + \mathbf{P}_\beta]\right] && (1.7)\\ & - \tfrac{1}{2}\mathrm{Tr}\left[\mathbf{P}_\alpha\mathbf{K}[\mathbf{P}_\alpha]\right] - \tfrac{1}{2}\mathrm{Tr}\left[\mathbf{P}_\beta\mathbf{K}[\mathbf{P}_\beta]\right] && (1.8) \end{aligned}$$

$$(J[\mathbf{P}])_{\mu\nu} = \sum_{\lambda\sigma} (\mu\nu|\lambda\sigma)\, P^{\lambda\sigma} \tag{1.9}$$

$$(K[\mathbf{P}])_{\mu\nu} = \sum_{\lambda\sigma} (\mu\lambda|\nu\sigma)\, P^{\lambda\sigma} \tag{1.10}$$

$$(\mu\nu|\lambda\sigma) = \iint \omega_\mu(1)\omega_\nu(1) r_{12}^{-1} \omega_\lambda(2)\omega_\sigma(2) d\mathbf{r}_1 d\mathbf{r}_2 \tag{1.11}$$

where $\mathbf{P}_\sigma$ is the density matrix for spin $\sigma = \alpha$ or β, the projector into the span of the one-electron functions of the given spin that define the Slater determinant. The terms in the first line (1.6) correspond to the electron kinetic energy, the electron-nuclear attraction, and the nuclear-nuclear repulsion respectively. The second line (1.7) describes the average Coulombic repulsion between all electrons in the system. The third line (1.8) describes the contribution of exchange effects between electrons of the same spin and is a result of the antisymmetry of the electronic wavefunction. This exchange term also cancels out the contributions in the second line corresponding to the repulsion of an electron by itself, so called self-interaction. In practice, the functions defining $\mathbf{P}_\sigma$ are expanded in a larger basis set ($\{\omega_\mu\}$) of one-particle functions, and the lowest energy single Slater determinant wavefunction, corresponding to the ground state of the system, is determined by selecting the energetically optimal subspace from this larger span. While Hartree-Fock theory does include some amount of same-spin

correlation through the exchange term, the theory otherwise presents a mean-field description of electron-electron interactions where each electron feels only the average repulsion of all others. True electron correlation is absent from the theory by definition, resulting in a theory that often gives a quantitatively and sometimes a qualitatively incorrect description of intermolecular interactions.

1.2.4 Density Functional Theory

There are many approaches in electronic structure theory that reintroduce some of the electron-electron correlation effects that are absent in Hartree-Fock such as Configuration Interaction (CI), Møller-Plesset perturbation theory (MP), and Coupled Cluster theory (CC); however, the least computationally expensive and also most widely used method for including correlation is Density Functional Theory (DFT), which has its origin in the Hohenberg-Kohn theorems.[1] The first Hohenberg-Kohn theorem shows that the mapping of the ground state 3-space electron density, $\rho(\mathbf{r})$, to the electron-nuclear potential is unique and thereby that the mapping of the ground state density to the ground state energy is unique.

$$\rho(\mathbf{r}) = \rho_\alpha(\mathbf{r}) + \rho_\beta(\mathbf{r}) \tag{1.12}$$

$$\rho_\sigma(\mathbf{r}) = \sum_{\mu\nu} \omega_\mu(\mathbf{r}) P_\sigma^{\mu\nu} \omega_\nu(\mathbf{r}) \tag{1.13}$$

This establishes the density, $\rho(\mathbf{r})$, as the fundamental variable but requires that a universal energy functional of $\rho(\mathbf{r})$ be constructed that describes the electron kinetic energy and all (correlated) electron-electron repulsions. The second theorem provides a variational principal for solving for $\rho(\mathbf{r})$ given such a functional though with the additional constraint that all densities considered correspond to valid antisymmetric ground state wavefunctions of some system, the v-representability condition. Further work showed that this constraint could be relaxed, requiring instead that the density correspond to an antisymmetric N-electron wavefunction, the N-representability condition.[1] Kohn-Sham theory bypasses some of the practical computational difficulties of Hohenberg-Kohn DFT by restricting itself to single Slater determinant wavefunctions, which can in principle describe all N-representable densities, and by defining the following formally exact energy expression:

$$\begin{aligned} E_{KS} = \; & \mathrm{Tr}\left[(\mathbf{P}_\alpha + \mathbf{P}_\beta)\mathbf{T}\right] + \mathrm{Tr}\left[(\mathbf{P}_\alpha + \mathbf{P}_\beta)\mathbf{V}_{EN}\right] + E_{NN} \\ & + \tfrac{1}{2}\mathrm{Tr}\left[(\mathbf{P}_\alpha + \mathbf{P}_\beta)\mathbf{J}[\mathbf{P}_\alpha + \mathbf{P}_\beta]\right] \\ & + E_{XC}[\mathbf{P}_\alpha, \mathbf{P}_\beta] \end{aligned} \tag{1.14}$$

The Kohn-Sham energy expression is very similar to that for Hartree-Fock (Equation 1.6) with the contributions from the exact exchange matrix, $\mathbf{K}$, replaced with the exchange-correlation functional, $\mathrm{E}_{XC}[\mathbf{P}]$. We note that formally this is a functional of $\rho(\mathbf{r})$; however, in practice, it is often instead a functional of the density matrix, $\mathbf{P}$. The primary benefit of Kohn-Sham DFT over Hohenberg-Kohn DFT besides the simplicity of using single

Slater determinants to resolve N-representability is the use of the non-interacting kinetic energy, Tr [**PT**], which depends on the density matrix and not just $\rho(\mathbf{r})$. This circumvents the need to construct an approximate functional explicitly for the kinetic energy, which is generally much larger in magnitude than the correlation energy itself. Indeed this task has yet to be satisfactorily accomplished for molecular systems. The difference between the non-interacting kinetic energy and the exact kinetic energy of the correlated electrons in the system is described along with all other correlation effects by $\mathrm{E}_{XC}[\mathbf{P}]$.

Just as the universal functional of Hohenberg-Kohn theory is not known, the exact exchange-correlation functional of Kohn-Sham theory is not known either; however, there is a fairly well-defined hierarchy[2] of approximate functionals that in general offer increasingly more accurate descriptions of electron correlation. The first class of functionals are those based on the Local Density Approximation (LDA), and they depend on $\rho(\mathbf{r})$ alone. The next class of functionals employ the Generalized Gradient Approximation (GGA) and make use of both the density and the gradient of the density. Functionals based on the Meta-Generalized Gradient Approximation (Meta-GGA) additionally use the gradients of the orbitals defining the density matrix and thus have density matrix dependence. Hybrids are another exchange-correlation functional type that includes density matrix dependence, though in this case it is because some portion of exact Hartree-Fock exchange (Equation 1.8) is added. Functionals with a constant fraction of exact exchange are called global hybrids (GH), and those that interpolate between two distinct fractions of exact exchange in the short- and long-range are called range-separated hybrids (RSH). The latter are quite useful for mitigating self-interaction error, which can be particularly problematic for charged systems. A weakness of many density functionals lies in their inability to describe dispersion interactions (Section 1.3.4). This shortcoming is frequently ameliorated by the inclusion of density-independent empirical corrections such as Grimme's -D[3, 4] or a non-local density dependent functional such as VV10[5]. The classifications along these lines for the functionals used in this thesis appear in Table 1.1. We mention that there is another class of functionals called double hybrids, which additionally depend on the orthogonal complement of **P** through Møller-Plesset-like expressions. We do not make use of double hybrid functionals in this work.

1.3 Physical Contributions to Interactions

In Section 1.1, we mentioned that the total interaction energy alone is often not sufficient to satisfactorily answer chemically important questions and named several important physical concepts that are commonly used to explain the interactions between molecular fragments in chemical systems. We now describe these concepts in detail.

Functional	Class	Dispersion Correction
B3LYP[6–8]	GH GGA	None
ωB97[9]	RSH GGA	None
ωB97X[9]	RSH GGA	None
ωB97X-D[10]	RSH GGA	-D[3]
ωB97X-V[11]	RSH GGA	VV10[5]
M06-2X[12]	GH Meta-GGA	None
M06[12]	GH Meta-GGA	None

Table 1.1: Summary of functionals used in this work based on the functional hierarchy[2] and types of dispersion corrections described in the text.

1.3.1 Permanent Electrostatics

Permanent electrostatics refers to the interactions of the permanent moments, monopole, dipole, quadrupole, etc., of some number of molecular fragments. When the fragments are well-separated, the association of electrons and nuclei with each fragment in real space is unambiguous, and the term corresponds to the classical electrostatic interaction of the fragment charge distributions. The distance dependence of these interactions is well-known from the multipole expansions of classical charge distributions, R^{-1} for monopole-monopole, R^{-2} for monopole-dipole, R^{-3} for dipole-dipole, R^{-4} for dipole-quadrupole, etc., where R is the distance between the two charge distributions. Because interactions involving higher-order multipole terms decay more quickly, the long-range asymptotic behavior of the electrostatic interaction is determined by the lowest multipole moments on each fragment, and if there are low-order moments on both species, then this is often the dominant contribution to the entire interaction at long range. This interaction can be attractive or repulsive depending on whether the permanent moments of the fragments considered are aligned favorably or unfavorably. If the molecular fragments are in close proximity, these permanent moments still exist and contribute to the interaction, but ascribing electrons to the charge distributions of specific fragments becomes ambiguous.

1.3.2 Pauli Repulsion

The term Pauli repulsion or steric repulsion is often used to refer to volume-exclusion effects. Atoms certainly are not hard spheres; however, when they are brought into close contact, there is a rapid increase in energy that tends to force them apart. This increase in energy is primarily a consequence of higher electron kinetic energy, the "kinetic energy pressure"[13] exerted by electrons. The effect of electron antisymmetry, expressed in the Pauli principle as the fact that electrons cannot have the same space and spin coordinates, is that each electron effectively occupies a volume, and when electrons from different molecular fragments are brought into close contact, the average volume available to each electron

decreases, increasing the kinetic energy of the electrons as in the simple case of a particle in a box. As the name suggests, this is a purely repulsive contribution to the interaction energy, and it is expected to decay exponentially with distance as hydrogenic orbital overlap decays. Pauli repulsion becomes relevant at much greater fragment separations than those at which the nuclear-nuclear repulsion becomes singular, and it is thus the primary intermolecular force that balances all of the other attractive forces to determine the energetically optimal separation between molecular fragments.

1.3.3 Induced Electrostatics

Induced electrostatic or polarization contributions describe the on-fragment relaxation of each species to the presence of the nuclei and electrons of all other fragments. For large separations, other fragments can simply be considered classical charge distributions that, if permanent moments exist, produce an electric field, and the relaxation of a given species comes in the form of density rearrangements that create induced multipole moments favorably aligned to interact with this field. The ability to create these induced moments is determined by a property of the species itself, its polarizability. The distance dependence of the interaction of permanent moments and induced moments is well known from classical electrostatics. For instance, monopole induced-dipole interactions decay as R^{-4} and dipole induced-dipole interactions decay as R^{-6}. At short fragment separations, the relaxation is also influenced by the kinetic energy pressure exerted by the electrons of other fragments. Density rearrangements both act to relieve this pressure and are made with the kinetic energy consequences of relaxation in mind. In close contact, the tagging of electrons to fragments is again ambiguous, and similar difficulties arise in the definition of on-fragment relaxations. Because induced electrostatic interactions correspond to the effects of fragment relaxations, they always make attractive contributions to the interaction energy.

1.3.4 Dispersion and Other Correlation Effects

The above electrostatic terms describe a large portion of the electron-electron interaction between fragments especially when there are species with permanent multipole moments; however, these terms do not capture the effects of the correlated motions of electrons on one fragment due to the motions of the electrons on other fragments. These correlation effects are necessary for a quantitative description of the total interaction, and their inclusion is essential for the qualitative description of many relatively weakly bound systems, particularly those with no permanent moments. These inter-fragment correlations are the source of the well known dispersion contribution, which corresponds to the interaction of favorably aligned instantaneous dipoles. This interaction is manifestly attractive with an asymptotic distance dependence of R^{-6}, just as in the dipole induced-dipole interaction. At shorter fragment separations, the distinction between dispersion and other correlation effects, including exchange, which describes a degree of same-spin correlation, is less clear. Certainly not all

correlation is dispersion because the net contribution of electron correlation to binding can in fact be repulsive.[14] Exchange-correlation contributions to binding are expected to decay roughly exponentially in the short range just as Hartree-Fock exchange decays and transition to polynomial R^{-6} decay in the long range, describing dispersion.

1.3.5 Charge Transfer

Charge transfer contributions account for donor-acceptor inter-fragment orbital interactions, which serve both to delocalize electrons over the supermolecular complex and to allow net charge flow between species. These inter-fragment relaxations usually occur together and primarily lower the kinetic energy and the potential energy of the system respectively. Charge transfer contributions are uniformly attractive as they again correspond to a relaxation effect which is in this case inter-fragment in character. Like Pauli repulsion, the expected decay is approximately exponential due to the connection to orbital overlap, which makes this a predominantly short-range term. Also due to its dependence on orbital interactions, this term is quite sensitive to the relative orientation in addition to the separation of the molecular fragments in question and plays an important role in determining the details of minimum energy supermolecular structures.

1.3.6 Comments

We mention that chemists are particularly inclined to name interactions based on an observed structural motif. Such names include hydrogen bonds, ionic hydrogen bonds, halogen bonds, π stacking interactions, cation-π interactions, anion-π interactions, etc. These identifications are useful in the sense that one can relate back to another system that has a similar motif and for which one already has some intuition. This is the concept of transferability that is ubiquitous in chemistry. However, these categories can also be seen as clusterings of systems with similar distributions of the above physical contributions. In this thesis, we will analyze many systems that fall into such structural motif categories in terms of the physical contributions to their interactions.

One can also imagine extending the same reasoning about the attractions and repulsions between molecular units to truly intramolecular interactions such as the attraction of one part of a large organic molecule such as a protein to another part of the same molecule; however, the usual methods for computing intermolecular interaction energies are not immediately applicable, requiring system-specific modifications of otherwise black-box methodology to achieve something resembling a proper treatment. Intramolecular interactions are thus largely beyond the scope of this work as we are interested in well-defined methods.

1.4 Energy Decomposition Analysis

The goal of an Energy Decomposition Analysis (EDA) method is to divide an interaction energy as defined by some model chemistry such as Hartree-Fock (Section 1.2.3) or Kohn-Sham DFT (Section 1.2.4) into contributions from the physical concepts of Section 1.3. The primary issue with such a task is that, because the concepts do not correspond to observables, their definitions are not uniquely defined when fragments are close and their orbitals overlap. Virtually all chemically interesting systems fall into this overlapping regime where there are ambiguities in the meaning of intra-fragment and inter-fragment relaxation, creating difficulties in delineating polarization from charge transfer. Furthermore, we will see that when the occupied orbitals of fragments overlap, the density of the supersystem must distort relative to the simple sum of fragment densities in order to guarantee an antisymmetric wavefunction. The division of this distorted density among fragments is likewise not unique, and the combination of these two facts complicates the evaluation of the contributions from electron correlation and permanent electrostatics. There is of course some guidance from the less interesting, non-overlapping regime where Pauli repulsion and charge transfer are both zero and permanent electrostatic interactions are described entirely by classical electrostatics. Polarization and correlation contributions are well-defined in the long range as well, providing useful information about limiting behavior that a good EDA should match. While there is no a priori best EDA, there are several desirable qualities that we feel an EDA method should possess:

1. An EDA should partition the total interaction energy as computed by a well-defined electronic structure method into contributions from physically meaningful terms.

2. It should be maximally descriptive, assigning an energy to as many useful concepts as possible and avoiding the grouping of several effects into one term.

3. The EDA method should not put undue restrictions on the model chemistry such as the requirement of a specific type of basis expansion or a density functional with a specific form.

4. All terms should converge to a physically meaningful basis set limit. Together with the last requirement, this means that an EDA for the decomposition of Kohn-Sham DFT interaction energies should work for the exact functional and a complete basis set.

5. All terms with known asymptotic behavior should match this behavior within the limits of the given model chemistry.

6. The EDA should compute energies using only valid antisymmetric electronic wavefunctions. Classical calculations are only valid in uninteresting limits and should thus be avoided.

7. The energy terms that sum to the total interaction energy should be continuous if the total is likewise continuous.

8. An EDA should define its terms variationally, allowing for the application of the method to both weakly and strongly interacting system.

9. The decomposition of the interaction energy should not be significantly more computationally expensive than the evaluation of the interaction energy itself.

1.5 Outline

In this work, we describe the construction of an EDA method based on the Absolutely Localized Molecular Orbital EDA (ALMO-EDA)[15–17] developed at Berkeley and modified in order to satisfy the above desirable criteria for an EDA method. It should be clear at this point that such schemes require many choices in constructing meaningful definitions of terms, and we expend considerable effort explaining, justifying, and demonstrating the consequences of each of our choices throughout the text. A summary of our trajectory from the base method through our improvements and into applications of the final scheme is as follows.

1.5.1 Chapter 2

Radical-closed shell and radical-radical intermolecular interactions are less well-understood than those between closed shell species. With the objective of gaining additional insight, this work reports a generalization of the absolutely localized molecular orbital (ALMO) energy decomposition analysis (EDA) to open shell fragments, described by self-consistent field methods, such as standard density functional theory. The ALMO-EDA variationally partitions an intermolecular interaction energy into three separate contributions; frozen orbital interactions, polarization and charge transfer. The first examples involve comparison of the interactions of alkanes and alkyl radicals (methyl radical, methane, tertiary butyl radical, and isobutane) with sodium, potassium, hydronium and ammonium cations. A second series of examples involve benzene cation interacting with a series of nucleophiles in both on-top and side-on geometries. The ALMO-EDA yields a variety of interesting insights into the relative roles of its component contributions as the interacting partners and their geometries are changed. This work has been published in *J. Chem. Phys.*[18].

1.5.2 Chapter 3

The polarization energy in intermolecular interactions treated by self-consistent field (SCF) electronic structure theory is often evaluated using a constraint that the atomic orbital (AO) to molecular orbital transformation is blocked by fragments (the ALMO model

of Chapter 2). This approach is tied to AO basis sets, overestimates polarization energies in the overlapping regime, particularly in large AO basis sets, and lacks a useful complete basis set limit. In Chapter 3, these problems are addressed by the construction of polarization subspaces based on the responses of isolated fragments to weak electric fields. These subspaces are spanned by fragment electric-field response functions (FERFs), which can capture effects up to the dipole (D), or quadrupole (DQ) level, or beyond. Schemes are presented for the creation of both non-orthogonal and orthogonal fragment subspaces, and the basis set convergence of the polarization energies computed using these spaces is assessed. Numerical calculations for the water dimer, water-Na^+, water-Mg^{2+}, water-F^- and water-Cl^- show that the non-orthogonal DQ model is very satisfactory, with small differences relative to the orthogonalized model. Additionally, we prove a fundamental difference between the polarization degrees of freedom in the fragment-blocked approaches and in constrained density schemes. Only the former are capable of properly prohibiting charge delocalization during polarization. This work is currently under review in *J. Chem. Phys.*.

1.5.3 Chapter 4

An important intermediate in energy decomposition analysis (EDA) is the "first" wavefunction in which all electrons in the system are treated collectively, the initial supersystem wavefunction. It defines the so-called "frozen energy" that includes contributions such as permanent electrostatics and steric repulsions. This work explores the merits of two existing and two new but related initial supersystem wavefunctions, all of which are based on some mix of geometric and energetic optimality criteria. In order to generate numerical results we introduce a new algorithm for minimizing single determinant energies with a penalty function to approximately enforce constant 3-space density constraints, as required for three of the definitions considered. Numerical results for Ne_2, $(H_2O)_2$, BH_3-NH_3, ethane, Be^+-H_2O and CO^+-HF show that there is a large energy lowering associated with constant density orbital relaxation, relative to use of frozen fragment orbitals. By far the most important contribution is constant density inter-fragment relaxation, corresponding to charge transfer. This is unwanted in an EDA that attempts to separate CT effects, but may be useful in other contexts. The smaller constant density intramolecular relaxation is numerically most significant for strongly overlapping fragments, but does not appear to qualitatively change the results associated with the unrelaxed initial supersystem wavefunction formed from frozen fragment orbitals. The choice of target initial density (frozen orbital density vs sum of isolated fragments) has a relatively small effect in the examples considered. This work has just been submitted to *J. Chem. Phys.*

1.5.4 Chapter 5

In energy decomposition analysis (EDA) of Kohn-Sham density functional theory calculations, the so-called frozen (or pre-polarization) interaction energy contains contributions

from permanent electrostatics, dispersion, and Pauli repulsion. The standard classical approach to separating them suffers from several well-known limitations. As an alternative, we offer a definition of permanent electrostatics, Pauli repulsion, and exchange-correlation (subsuming dispersion) contributions to intermolecular interactions that employs valid antisymmetric electronic wavefunctions throughout. This method is based on the identification of individual fragment contributions to the initial supersystem wavefunction as determined by an energetic optimality criterion, and we compare the new scheme to the widely used approach based on the translation of classical charge distributions. The density deformations identified with individual fragments upon formation of the initial supersystem wavefunction are analyzed along with the distance dependence of the new and classical terms. Example applications include ammonia borane, water-Na^+, water-Cl^-, ethane dissociation, and the naphthalene dimer. This work has just been submitted to *J. Chem. Phys.*

1.5.5 Chapter 6

We present an improved Energy Decomposition Analysis (EDA) scheme that, unlike many other schemes with similar aims, employs only valid antisymmetric electronic wavefunctions, produces physically meaningful terms for all single determinant Kohn-Sham model chemistries, is variational, allowing for the treatment of both weak and strong interactions, and is furthermore maximally descriptive, separating out as many distinct physical contributions to the interaction energy as possible. We apply this new method, which notably incorporates a non-classical term describing permanent electrostatics, to one of the recently identified and controversial anti-electrostatic hydrogen bonding complexes, which we show to be not nearly as counterintuitive or surprising as it might first seem. We investigate the biologically relevant binding of adenine and thymine in stacked and planar configurations, and our scheme is able to distinguish the different origins of binding in the two while other less descriptive schemes fall short. We also examine the binding of a carbonyl ligand in $Cr(CO)_6$ and the many-body expansion of the interaction energy of a radical cationic complex that is an important intermediate in the dissociative photoionization of glycerol.

Chapter 2

Unrestricted ALMO-EDA

2.1 Introduction

The idea that one can take a molecule or, more generally, a fragment consisting of one or more atoms, which is understood in one chemical environment (such as a dilute gas) and make arguments about the effect of placing that fragment in another chemical environment by performing a sort of qualitative perturbation theory is central to chemistry. To facilitate this process, chemists have developed several ways to describe and categorize the interactions that are most important to the perturbation such as permanent electrostatics, polarization, charge transfer, and dispersion; however, when the interacting systems become complex, it can become difficult to understand intuitively which are the most relevant modes of interaction. Energy decomposition analysis (EDA) provides a way of quantifying the significance of the different modes of interaction by dividing the total binding energy into energy contributions from each. However, since there are no clearly defined operators corresponding to, for instance, the energy lowering due to the polarization of a molecule, the criteria by which EDA schemes should be judged are that the components be physically meaningful, efficiently calculable, and, to a lesser extent, theoretically satisfying.

To this end, many energy decomposition schemes have been proposed in the literature with varying levels of success. The popular Symmetry Adapted Perturbation Theory (SAPT) provides a means of calculating the total intermolecular interaction and also, by binning different terms in the expansion, can attribute all portions of the computed interaction energy to different physical contributions [19–29] . The SAPT calculated interaction energy can agree quite well with higher levels of theory, and the SAPT methods are computationally less expensive than the higher level of theory that they attempt to reproduce. However, SAPT calculations are generally also more expensive than standard SCF calculations. Another method that aims to calculate intermolecular interactions by taking advantage of a fragment scheme but with considerably lower cost is the well established effective fragment potential (EFP) method [30–33]. Another approach based on a different type of perturbation

theory is the Natural Energy Decomposition Analysis (NEDA) method [34–36], which draws considerably from both the framework and the interpretation of Natural Bonding Orbitals (NBOs) [37]. NBO and NEDA methods have proved tremendously valuable for elucidating *trends* across intermolecular interactions in diverse systems. However, caution is required in interpreting NBO/NEDA energy contributions quantitatively. Like NBO, the NEDA scheme is based on perturbation theory and yields an unlikely result, that charge transfer contributions are larger than the total interaction energy, for even weakly interacting systems such as water [36].

Alternatively, many methods calculate variationally optimized intermediate wave functions, beginning with the Kitaura and Morokuma (KM) EDA [38] for Hartree-Fock theory, and the Ziegler-Rauk approach for the Xα method [39–41]. There have been many subsequent implementations and improvements to these methods[42–45]. One noteworthy evolution of the KM-EDA is the variational evaluation of a polarization by using a fragment-blocked molecular orbital coefficient matrix [15, 46] to define an intermediate energy associated with polarization. This approach is employed in the block-localized wave function (BLW)-EDA [46–49] , and the Absolutely Localized MO (ALMO)-EDA (discussed in more detail below). It should be noted that this way of calculating polarization contributions is similar to the method employed by Sadlej[50] for the calculation of induction interactions for non-overlapping subsystems.

Another method is the density based scheme of Wu [51], which variationally optimizes the energy given a grid-based charge constraint. Wu et al. construct an initial total system density that is a sum of fragment densities by searching for the corresponding minimum energy antisymmetric wavefunction; however, during this procedure, the orbitals are permitted to delocalize over the entire system to minimize the kinetic energy contribution. Yet another density based method is Partition Theory[52, 53] , which obtains the total system density by the iterative solution of fragment problems and is thereby able to analyze the movement of charge among those fragments.

In this work, the ALMO-EDA[16] is extended to include spin unrestricted localized molecular orbitals, allowing for application to systems involving open shell species. The ALMO-EDA employs the same fragment blocking of the MO coefficients as the BLW-EDA, solving an efficient implementation [15] of the constrained variational equations for closed shell systems to yield the energy lowering due to polarization. Any self-consistent field (SCF) treatment of electronic structure can be handled, allowing for mean field Hartree-Fock (HF) theory, and most types of density-functional theory (DFT). A new treatment of charge transfer allows separation of forward and back-donation, following the intra-molecular polarization, as well as quantifying the amount of charge transferred in each direction.[17] Subsequently the closed shell ALMO-EDA has been successfully applied to a growing variety of problems, including neutral water clusters [54], the hydronium ion[55], organic reaction mechanisms[56, 57], ligand binding to metal centers[17], sulfate-water clusters[58], charge-transfer effects on complex spectra[59, 60], etc.

In the Absolutely Localized Molecular Orbital (ALMO) EDA scheme of Khaliullin et al.,

the total interaction energy of a system of fragments is partitioned into contributions from frozen orbital interactions, polarization, and charge transfer.

$$\Delta E_{\text{interaction}} = \Delta E_{\text{GD}} + \Delta E_{\text{FRZ}} + \Delta E_{\text{POL}} + \Delta E_{\text{CT}} \tag{2.1}$$

The first term, ΔE_{GD}, is the energy penalty associated with distorting isolated fragments from their optimal geometries to attain their respective geometries in the interacting complex. The second term, ΔE_{FRZ}, is the energy change associated with bringing infinitely separated, distorted fragments together into the interacting supermolecular geometry without allowing the orbitals, calculated at infinite separation, to relax (frozen). Physically, ΔE_{FRZ} includes both electrostatic interactions and Pauli repulsion effects. Electrostatics are favorable when multipole moments on the fragments align properly, but the interaction of overlapping filled orbitals can be quite unfavorable when inter-fragment distances are very short and exclusion requires considerable distortion of the density. The polarization contribution, ΔE_{POL}, is the energy lowering brought about by allowing the frozen orbitals to relax subject to the constraint that they remain absolutely localized (fragment-blocked MO coefficients). This constraint allows for the efficient calculation of a variational polarization energy, which precludes the formation of orbitals that span more than one fragment, which is an intuitive picture of the result of charge transfer interactions. The remaining interaction energy, ΔE_{CT}, recovered when the orbitals are allowed to fully relax and delocalize, is thus charge transfer.

The outline of this paper is as follows. The specific equations that are solved for each of the non-trivial components of the interaction energy, Eq. (2.1), in the case of open shell fragments are summarized in the Theory section. Some computational details are summarized before we turn to a series of pilot examples involving intermolecular interactions of open shell species in the Application section. The first class of examples are comparative interactions of methyl radical, methane, tertiary butyl radical, and isobutane with sodium, potassium, hydronium and ammonium cations. These interactions have been previous examined[61] with NBO methods, and an important role for hydrogen-bonding was elucidated. The second class of examples is relevant to nucleophilic aromatic substitution reactions[62] and involves the benzene radical cation interacting with a series of nucleophiles in both on-top and side-on geometries. The ability of the open shell ALMO-EDA to obtain results that are reasonable and insightful can be assessed from these pilot applications.

2.2 Theory

The notation adhered to in this work is as follows: Spatial MO: ψ; Spatial AO: ω; Fragment Indices: Capital Roman $X, Y...$; AO Indices: lower case Greek μ, $\nu...$; Virtual MO indices: $a, b...$; Occupied MO indices: $i, j...$; Generic MO indices: $r, s....$ This work incorporates wavefunction representations involving non-orthogonal orbitals and thus makes considerable use of tensors with both covariant (subscript) and contravariant (superscript)

indices.[63] Dots are used as placeholders for clear index ordering in quantities that have both covariant and contravariant indices. For instance, the matrix $\mathbf{C}_\alpha$ with matrix elements $(C_\alpha)^{X\mu}_{\bullet\ Yr}$ has rows corresponding to contravariant atomic orbitals and columns corresponding to covariant molecular orbitals. Equations are generally consistent with the covariant integral representation and employ the Einstein summation convention for covariant and contravariant indices with the exception of fragment indices, for which all summations are written explicitly.

2.2.1 Frozen Energy

The alpha and beta frozen orbitals are absolutely localized, and their MO coefficient matrices, for instance $(C_{\alpha,\mathrm{FRZ}})^{X\mu}_{\bullet\ Xr}$, are obtained as the block diagonal concatenation of fragment blocks of MO coefficient matrices from single point calculations on each fragment in isolation. These calculations are performed at the geometry each fragment adopts within the complex (hitherto referred to as the fragment's complex geometry), rather than the optimal isolated fragment geometry. The AO basis representation of the projector into the subspace spanned by the union of the frozen, occupied subset of MOs, $(T_{\alpha,\mathrm{FRZ}})^{X\mu}_{\bullet\ Xi}$, of these non-interacting fragments is the "frozen" density matrix, P_{FRZ}:

$$(P_{\alpha,\mathrm{FRZ}})^{X\mu Y\nu} = (T_{\alpha,\mathrm{FRZ}})^{X\mu}_{\bullet\ Xi}(\sigma_\alpha)^{XiYj}(T^T_{\alpha,\mathrm{FRZ}})^{\bullet\ Y\nu}_{Yj\ \bullet} \tag{2.2}$$

The inclusion of the contravariant alpha occupied MO metric, $(\sigma_\alpha)^{XiYj}$, is necessary to form a valid projector and thus accounts for Pauli repulsion. It also means the frozen density is not a sum of the non-interacting fragment densities for the general case of non-orthogonal fragment occupied subspaces. The contravariant alpha occupied MO metric is calculated as the inverse of the occupied, occupied block of the covariant alpha MO metric, $(\sigma_\alpha)_{XiYj}$:

$$(\sigma_\alpha)_{XiYj} = (T^T_\alpha)^{\bullet\ X\mu}_{Xi\ \bullet} S_{X\mu Y\nu}(T_\alpha)^{Y\nu\ \bullet}_{\bullet\ Yj} \tag{2.3}$$

$S_{X\mu Y\nu}$ is the covariant atomic orbital overlap metric. The frozen contribution to the interaction energy is simply the difference between the sum of the single point energies for each isolated fragment in its complex geometry and the trace of the frozen density with the full complex's core Hamiltonian, $\mathbf{H}_{\mathrm{core}}$, and Fock matrices,$\mathbf{F}_\alpha$ and $\mathbf{F}_\beta$, formed using the same frozen density:

$$\begin{aligned}\Delta E_{\mathrm{FRZ}} = \frac{1}{2}\mathrm{Tr}\,[&\mathbf{P}_{\alpha,\mathrm{FRZ}}(\mathbf{H}_{\mathrm{core}} + \mathbf{F}_\alpha\,[\mathbf{P}_{\alpha,\mathrm{FRZ}}, \mathbf{P}_{\beta,\mathrm{FRZ}}]) \\ &+ \mathbf{P}_{\beta,\mathrm{FRZ}}(\mathbf{H}_{\mathrm{core}} + \mathbf{F}_\beta\,[\mathbf{P}_{\alpha,\mathrm{FRZ}}, \mathbf{P}_{\beta,\mathrm{FRZ}}])] \\ &- \sum_Z^{\mathrm{Frgm}} E_{Z,\mathrm{Complex}}\end{aligned} \tag{2.4}$$

2.2.2 Polarization

The unrestricted ALMO wavefunction is the usual single Slater determinant of occupied spin molecular orbitals but with the constraint: the MO coefficient matrix must be block-diagonal in the fragments comprising the complex. This constraint is placed on the AO expansions of covariant spatial MO's for each spin:

$$|\psi_{Xr}\rangle_\alpha = |\omega_{X\mu}\rangle (C_\alpha)^{X\mu\bullet}_{\bullet Xr} \tag{2.5}$$

The frozen wavefunction is itself an ALMO wavefunction by construction, which is an appropriate initial guess for the ALMO SCF. The ALMO SCF is the variational energy lowering resulting from the relaxation of the frozen orbitals within this constraint of absolute locality that defines the polarization contribution in the ALMO EDA scheme. The block diagonal expansion of MOs inherently leads to non-orthogonal molecular orbitals between fragments for non-orthogonal AO basis sets because there are not in general a sufficient number of degrees of freedom in the non-zero blocks to achieve orthogonality [64].

With the ALMO constraint defined, the remaining portions of this section are thus devoted to a collection and recapitulation of the derivations of: the Hartree-Fock-like equations of Gianinetti[65, 66] and Stoll[64] which use the same AO expansion and make no assumption of orthogonality, the corresponding DIIS error vector equation[15], and the expressions used in charge transfer analysis[17]. The equations are presented assuming spin unrestricted spatial orbitals.

2.2.2.1 Unrestricted Gianinetti and Stoll Equations

The energy for a single Slater determinant with unrestricted spatial orbitals and its derivative with respect to a change in alpha occupied orbital coefficients are:

$$E = \frac{1}{2}\mathrm{Tr}\left[\mathbf{P}_\alpha(\mathbf{H}_{\mathrm{core}} + \mathbf{F}_\alpha) + \mathbf{P}_\beta(\mathbf{H}_{\mathrm{core}} + \mathbf{F}_\beta)\right] \tag{2.6}$$

$$\begin{aligned}\frac{\partial E}{\partial (T_\alpha)^{X\gamma\bullet}_{\bullet Xi}} &= \sum_{YZ}^{\mathrm{Frgm}} \frac{\partial E}{\partial (P_\alpha)^{Z\lambda,Y\sigma}} \frac{\partial (P_\alpha)^{Z\lambda,Y\sigma}}{\partial (T_\alpha)^{X\gamma\bullet}_{\bullet Xi}} \\ &= \sum_{YZ}^{\mathrm{Frgm}} (F_\alpha)_{Y\sigma,Z\lambda} \frac{\partial (P_\alpha)^{Z\lambda,Y\sigma}}{\partial (T_\alpha)^{X\gamma\bullet}_{\bullet Xi}}\end{aligned} \tag{2.7}$$

The required partial derivatives are:

$$\frac{\partial (P_\alpha)^{Z\lambda,Y\sigma}}{\partial (T_\alpha)^{X\gamma}_{\bullet\, Xi}} = \delta^{Z\lambda}_{X\gamma} (\sigma_\alpha)^{Xi,Yj} (T^T_\alpha)^{\bullet\, Y\sigma}_{Yj\,\bullet}$$
$$+ (T_\alpha)^{Z\lambda}_{\bullet\, Zk} \left(\frac{\partial (\sigma_\alpha)^{Zk,Yj}}{\partial (T_\alpha)^{X\gamma}_{\bullet\, Xi}} \right) (T^T_\alpha)^{\bullet\, Y\sigma}_{Yj\,\bullet}$$
$$+ (T_\alpha)^{Z\lambda}_{\bullet\, Zk} (\sigma_\alpha)^{Zk,Xi} \delta^{Y\sigma}_{X\gamma} \tag{2.8}$$

$$\frac{\partial (\sigma_\alpha)^{Zk,Yj}}{\partial (T_\alpha)^{X\gamma}_{\bullet\, Xi}} = -\sum_{AB}^{\text{Frgm}} (\sigma_\alpha)^{Zk,Al} \left(\frac{\partial (\sigma_\alpha)_{Al,Bm}}{\partial (T_\alpha)^{X\gamma}_{\bullet\, Xi}} \right) (\sigma_\alpha)^{Bm,Yj} \tag{2.9}$$

$$= -\sum_{A}^{\text{Frgm}} \left((\sigma_\alpha)^{Zk,Al} (T^T_\alpha)^{\bullet\, A\mu}_{Al\,\bullet} S_{A\mu,X\gamma} (\sigma_\alpha)^{Xi,Yj} + (\sigma_\alpha)^{Zk,Xi} S_{X\gamma,A\mu} (T_\alpha)^{A\mu\,\bullet}_{\bullet\, Al} (\sigma_\alpha)^{Al,Yj} \right)$$

After making the requisite substitutions, one obtains:

$$\frac{\partial E}{\partial (T_\alpha)^{X\gamma}_{\bullet\, Xi}} = 2 \sum_{YZ}^{\text{Frgm}} \left[\left(\delta^{Z\lambda}_{X\gamma} - \sum_{A}^{\text{Frgm}} S_{X\gamma,A\mu} (P_\alpha)^{A\mu,Z\lambda} \right) (F_\alpha)_{Z\lambda,Y\sigma} (T_\alpha)^{Y\sigma}_{\bullet\, Yj} (\sigma_\alpha)^{Yj,Xi} \right] \tag{2.10}$$

From the above equation, we obtain the following matrix equation for stationarity for each fragment, X, and each spin:

$$\mathbf{0} = \left[(\mathbf{1} - \mathbf{S}\mathbf{P}_\alpha) \mathbf{F}_\alpha \mathbf{T}_\alpha \boldsymbol{\sigma}_\alpha^{-1} \right]_{XX} \tag{2.11}$$

$\mathbf{T}_\alpha$ is again defined as the occupied block of $\mathbf{C}_\alpha$. Eq. (2.11) represents the usual requirement that the occupied-virtual block of the Fock matrix should be zero at convergence, while taking into account the reduced flexibility in the ALMO expansion. Occupied-occupied mixings do not alter the energy, and on-fragment rotations do not violate the constraint of the ALMO expansion. Thus, one is free to select the fragment diagonal blocks of the occupied-occupied contravariant- contravariant MO Fock matrix as diagonal without loss of generality.

$$[\boldsymbol{\sigma}_\alpha^{-1} \mathbf{T}_\alpha^T \mathbf{F}_\alpha \mathbf{T}_\alpha \boldsymbol{\sigma}_\alpha^{-1} - \epsilon_\alpha]_{XX} = 0 \tag{2.12}$$

There is a more amenable form of the above eigenvalue problem which can be solved for the covariant MOs on each fragment. It can be obtained by applying the following fragment-specific substitution:

$$(T_\alpha)^{Z\nu\,\bullet}_{\bullet\, Zl} (\sigma_\alpha)^{Zl,Xi} = \sum_{Y}^{\text{Frgm}} \sum_{j} (T_\alpha)^{Z\nu\,\bullet}_{\bullet\, Zl} (\sigma_\alpha)^{Zl,Xj} (\sigma_\alpha)^{Xj,Yk} (\sigma_\alpha)_{YkXi}$$
$$= \sum_{Y}^{\text{Frgm}} \sum_{j} \left((T_\alpha)^{Z\nu\,\bullet}_{\bullet\, Zl} (\sigma_\alpha)^{Zl,Xj} (\sigma_\alpha)^{Xj,Yk} (T^T_\alpha)^{\bullet\, Y\mu}_{Yk\,\bullet} \right) S_{Y\mu,X\lambda} (T_\alpha)^{X\lambda\,\bullet}_{\bullet\, Xi}$$
$$= \sum_{Y}^{\text{Frgm}} (P^X_{\alpha,G})^{Z\nu,Y\mu} S_{Y\mu,X\lambda} (T_\alpha)^{X\lambda\,\bullet}_{\bullet\, Xi} \tag{2.13}$$

With the following definition for the quantitiy $(P^X_{\alpha,G})^{Z\nu,Y\mu}$, which appears in the equations of Gianinetti:

$$(P^X_{\alpha,G})^{Z\nu,Y\mu} = \sum_j (T_\alpha)^{Z\nu}_{\bullet\, Zl} (\sigma_\alpha)^{Zl,Xj} (\sigma_\alpha)^{Xj,Yk} (T^T_\alpha)^{\bullet\, Y\mu}_{Yk\, \bullet}$$

The contraction over mismatched Xj indices above is valid becuase it corresponds to multiplication by the identity:

$$[\boldsymbol{\sigma}^{-1}_\alpha \boldsymbol{\sigma}_\alpha]_{XX} = \mathbf{I}_{XX} \tag{2.14}$$

Together with Eq. (2.11) and Eq. (2.12) this substitution yields the eigenvalue equations of Gianinetti for each fragment and spin:

$$\begin{aligned} \left[(\mathbf{1} - \mathbf{SP}_\alpha + \mathbf{SP}^X_{\alpha,G})\mathbf{F}_\alpha(\mathbf{1} - \mathbf{P}_\alpha\mathbf{S} + \mathbf{P}^X_{\alpha,G}\mathbf{S})\right]_{XX} [\mathbf{C}_\alpha]_{XX} \\ = \left[(\mathbf{S} - \mathbf{SP}_\alpha\mathbf{S} + \mathbf{SP}^X_{\alpha,G}\mathbf{S})\right]_{XX} [\mathbf{C}_\alpha]_{XX} [\epsilon_\alpha]_{XX} \end{aligned} \tag{2.15}$$

The additional projector into the orthogonal complement of the occupied space, $(\mathbf{S} - \mathbf{SP}_\alpha\mathbf{S}) \equiv \mathbf{SQ}_\alpha\mathbf{S}$, in the effective overlap of the generalized eigenvalue problem is necessary to avoid singularities. Alternatively, using the following substitution involving the quantity $(P^X_{\alpha,S})^{Z\nu,X\mu}$ found in Stoll's equations:

$$\begin{aligned} (T_\alpha)^{Z\nu}_{\bullet\, Zl} (\sigma_\alpha)^{Zl,Xi} = (T_\alpha)^{Z\nu}_{\bullet\, Zl} (\sigma_\alpha)^{Zl,Xj} (T^T_\alpha)^{\bullet\, X\mu}_{Xj\, \bullet} S_{X\mu,X\lambda} (T_\alpha)^{X\lambda\, \bullet}_{\bullet\, Xi} \\ = (P^X_{\alpha,S})^{Z\nu,X\mu} S_{X\mu,X\lambda} (T_\alpha)^{X\lambda\, \bullet}_{\bullet\, Xi} \\ (P^X_{\alpha,S})^{Z\nu,X\mu} = (T_\alpha)^{Z\nu}_{\bullet\, Zl} (\sigma_\alpha)^{Zl,Xj} (T^T_\alpha)^{\bullet\, X\mu}_{Xj\, \bullet} \end{aligned} \tag{2.16}$$

with Eq. (2.11) and Eq. (2.12) yields the fragment-by-fragment and spin-by-spin eigenvalue equations of Stoll:

$$\begin{aligned} \left[(\mathbf{1} - \mathbf{SP}_\alpha + \mathbf{SP}^X_{\alpha,S})\mathbf{F}_\alpha(\mathbf{1} - \mathbf{P}_\alpha\mathbf{S} + \mathbf{P}^X_{\alpha,S}\mathbf{S})\right]_{XX} [\mathbf{C}_\alpha]_{XX} \\ = [\mathbf{S}]_{XX} [\mathbf{C}_\alpha]_{XX} [\epsilon_\alpha]_{XX} \end{aligned} \tag{2.17}$$

In both Eq. (2.15) and Eq. (2.17), the problem of obtaining the polarized ALMO wavefunction of the supermolecular system is reduced to iterative fragment-by-fragment eigenvalue problems for each spin, coupled through the density and Fock builds. These equations arise from the minimization of the energy given the constraint of absolute locality in the MOs and do not involve any deletion of Fock matrix elements. Indeed, the full AO basis Fock matrix is involved. Additionally, only the contravariant metric for the occupied subspace is required, eliminating the need for the inversion of the full MO metric. Indeed the effort necessary to solve these equations iteratively is significantly less than required for conventional full diagonalization, as has previously been demonstrated in the closed shell case[15]

2.2.2.2 Unrestricted DIIS Error Vector

The DIIS algorithm[67] can be used to accelerate the convergence of the above equations with a small modification of the error vector that accounts for the reduction in degrees of freedom associated with the constrained AO expansion. The DIIS error vector is derived by considering an infinitesimal orthogonal update to the alpha density matrix correct to first order in the block diagonal anti-symmetric matrix, Δ_α, parametrizing the update:

$$\begin{aligned}(\tilde{P}_\alpha)^{K\kappa,L\lambda} \approx (T_\alpha)^{K\kappa\,\bullet}_{\bullet\,Kk}(\tilde{\sigma}_\alpha)^{Kk,Ll}(T_\alpha^T)^{\bullet\,L\lambda}_{Ll\,\bullet} \\ + (T_\alpha)^{K\kappa\,\bullet}_{\bullet\,Kk}\sigma_\alpha^{Kk,Ll}(T_\alpha^T)^{\bullet\,L\rho}_{Ll\,\bullet}S_{L\rho,L\pi}(\Delta_\alpha)^{L\pi,L\lambda} - (\Delta_\alpha)^{K\kappa,K\gamma}S_{K\gamma,K\mu}(T_\alpha)^{K\mu\,\bullet}_{\bullet\,Kk}\sigma_\alpha^{Kk,Ll}(T_\alpha^T)^{\bullet\,L\lambda}_{Ll\,\bullet}\end{aligned} \tag{2.18}$$

Here $(\tilde{P})^{K\kappa,L\lambda}_\alpha$ is the updated density and $(\tilde{\sigma})^{KkLl}_\alpha$ is the inverse of the metric of updated occupied MOs correct through first order in Δ_α:

$$\begin{aligned}(\tilde{\sigma}_\alpha)_{Mm,Nn} \approx (T_\alpha^T)^{\bullet\,M\mu}_{Mm\,\bullet}S_{M\mu,N\nu}(T_\alpha)^{N\nu\,\bullet}_{\bullet\,Nn} \\ + (T_\alpha^T)^{\bullet\,M\xi}_{Mm\,\bullet}S_{M\xi,M\gamma}(\Delta_\alpha)^{M\gamma,M\mu}S_{M\mu,N\nu}(T_\alpha)^{N\nu\,\bullet}_{\bullet\,Nn} \\ - (T_\alpha^T)^{\bullet\,M\mu}_{Mm\,\bullet}S_{M\mu,N\nu}(\Delta_\alpha)^{N\nu,N\rho}S_{N\rho,N\pi}(T_\alpha)^{N\pi\,\bullet}_{\bullet\,Nn}\end{aligned} \tag{2.19}$$

This transformation thus preserves MO overlap through first order on a fragment but allows inter-fragment overlaps to change, as desired. The error vector is then the derivative of the energy with respect to this update evaluated at $\Delta_\alpha = 0$:

$$\begin{aligned}\frac{\partial E}{\partial(\Delta_\alpha)^{X\xi,X\tau}} &= \sum_{KL}^{\text{Frgm}}\frac{\partial E}{\partial(\tilde{P}_\alpha)^{K\kappa,L\lambda}}\frac{\partial(\tilde{P}_\alpha)^{K\kappa,L\lambda}}{\partial(\Delta_\alpha)^{X\xi,X\tau}} \\ &= \sum_{KL}^{\text{Frgm}}(F_\alpha)_{L\lambda,K\kappa}\frac{\partial(\tilde{P}_\alpha)^{K\kappa,L\lambda}}{\partial(\Delta_\alpha)^{X\xi,X\tau}}\end{aligned} \tag{2.20}$$

The additional derivatives needed are:

$$\begin{aligned}\frac{\partial(\tilde{P}_\alpha)^{K\kappa,L\lambda}}{\partial(\Delta_\alpha)^{X\xi,X\tau}} = (T_\alpha)^{K\kappa\,\bullet}_{\bullet\,Kk}\frac{\partial(\tilde{\sigma}_\alpha)^{Kk,Ll}}{\partial(\Delta_\alpha)^{X\xi,X\tau}}(T_\alpha^T)^{\bullet\,L\lambda}_{Ll\,\bullet} \\ - \delta^{K\kappa}_{X\xi}\delta^{K\phi}_{X\tau}S_{K\phi K\eta}(T_\alpha)^{K\eta\,\bullet}_{\bullet\,Kk}(\sigma_\alpha)^{Kk,Ll}(T_\alpha^T)^{\bullet\,L\lambda}_{Ll\,\bullet} + (T_\alpha)^{K\kappa\,\bullet}_{\bullet\,Kk}(\sigma_\alpha)^{Kk,Ll}(T_\alpha^T)^{\bullet\,L\gamma}_{Ll\,\bullet}S_{L\gamma L\epsilon}\delta^{L\epsilon}_{X\xi}\delta^{L\lambda}_{X\tau}\end{aligned} \tag{2.21}$$

$$\begin{aligned}\frac{\partial(\tilde{\sigma}_\alpha)^{Kk,Ll}}{\partial(\Delta_\alpha)^{X\xi,X\tau}} = \sum_{M}^{\text{Frgm}}(\sigma_\alpha)^{Kk,Mm}(T_\alpha^T)^{\bullet\,M\mu}_{Mm\,\bullet}S_{M\mu,X\xi}S_{X\tau,X\rho}(T_\alpha)^{X\rho\,\bullet}_{\bullet\,Xn}(\sigma_\alpha)^{Xn,Ll} \\ - \sum_{N}^{\text{Frgm}}(\sigma_\alpha)^{Kk,Xm}(T_\alpha^T)^{\bullet\,X\lambda}_{Xm\,\bullet}S_{X\lambda,X\xi}S_{X\tau,N\nu}(T_\alpha)^{N\nu\,\bullet}_{\bullet\,Nn}(\sigma_\alpha)^{Nn,Ll}\end{aligned} \tag{2.22}$$

The DIIS error vector for the convergence of the Gianinetti and Stoll equations is thus:

$$\begin{aligned}[\mathbf{R}_\alpha]_{XX} &= \mathbf{S}_{XX}\left[\mathbf{P}_\alpha\mathbf{F}_\alpha(\mathbf{P}_\alpha\mathbf{S}-\mathbf{1})\right]_{XX} \\ &\quad - \left[(\mathbf{S}\mathbf{P}_\alpha-\mathbf{1})\mathbf{F}_\alpha\mathbf{P}_\alpha\right]_{XX}\mathbf{S}_{XX}\end{aligned} \tag{2.23}$$

which resembles the error vector equation of Pulay[67] but, like the equations to be solved, is both fragment-by-fragment and spin-by-spin.

2.2.3 Charge Transfer

As mentioned previously, the construction of the polarized wavefunction is such that it prevents the interfragment orbital mixings intuitively associated with charge transfer. An energy lowering from charge transfer interactions can thus be calculated as the difference between the energy of the unconstrained full SCF solution and the energy of the polarized solution. This is termed the variational charge transfer contribution to the energy, V-CT. Moreover, the ALMO wavefunction strictly precludes any movement of charge population between fragments by the Mulliken definition, forcing all such charge rearrangements to occur during the charge transfer phase of the calculation; the only time that the constraint of absolute locality is not enforced. It is thus possible to evaluate net movement of charge between fragments during charge transfer by Mulliken population analysis of the full SCF density.

It is often helpful to think about charge transfer interactions in terms of forward and back donation of electrons through specific orbital interactions. A textbook example is forward and back-donation in the bonding of ligands such as CO to a transition metal center.[17] Such directional, orbital specific information can be obtained by exploiting the stationarity of the variational, polarized ALMO wavefunction Eq. (2.11), specifically that the polarized Fock matrix elements between covariant virtual orbitals projected into the orthogonal complement of the occupied subspace, $\mathbf{Q}$, and contravariant occupied orbitals on the same fragment are zero. The projected virtuals, $\tilde{\mathbf{V}}$, used in the analysis of charge transfer are defined in terms of the unprojected, fragment blocked virtuals, $\mathbf{V}$, obtained from converging the Gianinetti or Stoll equations as:

$$\begin{aligned}\tilde{\mathbf{V}}_\alpha &= \mathbf{Q}_\alpha\mathbf{S}\mathbf{V}_\alpha = (\mathbf{I}-\mathbf{P}_\alpha\mathbf{S})\mathbf{V}_\alpha \\ (\tilde{V}_\alpha)^{Z\mu\bullet}_{\bullet X\tilde{a}} &= [\delta^{Z\mu}_{X\nu} - \sum_{Y}^{\text{Frgm}}(P_\alpha)^{Z\mu,Y\lambda}S_{Y\lambda,X\nu}](V_\alpha)^{X\nu\bullet}_{\bullet Xa}\end{aligned} \tag{2.24}$$

where the index $X\tilde{a}$ denotes the projected counterpart of virtual orbital a on fragment X. These virtual orbitals are in general not absolutely localized, but still carry a fragment label, and are still quite well localized.

The infinite-order singles perturbation theory (Roothaan step) energy lowering associated with the relaxation of the ALMO constraint must also be necessarily charge transfer in

character, and is given by [17, 68]

$$E_{\alpha,\text{P-CT}} = \text{Tr}\left[\mathbf{P}_\alpha \mathbf{F}_\alpha \mathbf{Q}_\alpha \mathbf{X}_\alpha\right]$$
$$= \sum_{WXYZ}^{\text{Frgm}} (\sigma_\alpha)^{Xi,Zk} (T_\alpha^T)_{Zk\bullet}^{\bullet Z\mu} (F_\alpha)_{Z\mu,W\nu} (\tilde{V}_\alpha)_{\bullet Y\tilde{a}}^{W\nu\bullet} (X_\alpha)_{\bullet Xi}^{Y\tilde{a}\bullet}$$
$$= \sum_{X\neq Y}^{\text{Frgm}} (F_\alpha)_{\bullet Y\tilde{a}}^{Xi\bullet} (X_\alpha)_{\bullet Xi}^{Y\tilde{a}\bullet} \tag{2.25}$$

The matrix of mixing parameters, $(X_\alpha)_{\bullet Xi}^{Y\tilde{a}\bullet}$, is determined by iteratively solving:

$$(F_\alpha)_{\bullet Xi}^{Y\tilde{a}\bullet} + \sum_{Z}^{\text{Frgm}} (F_\alpha)_{\bullet Z\tilde{b}}^{Y\tilde{a}\bullet} (X_\alpha)_{\bullet Xi}^{Z\tilde{b}\bullet}$$
$$- \sum_{W}^{\text{Frgm}} (X_\alpha)_{\bullet Wj}^{Y\tilde{a}\bullet} (F_\alpha)_{\bullet Xi}^{Wj\bullet}$$
$$- \sum_{WZ}^{\text{Frgm}} (X_\alpha)_{\bullet Wj}^{Y\tilde{a}\bullet} (F_\alpha)_{\bullet Z\tilde{b}}^{Wj\bullet} (X_\alpha)_{\bullet Xi}^{Z\tilde{b}\bullet} = 0 \tag{2.26}$$

This matrix of parameters in general has non-zero values describing rotations of all occupied orbitals on each fragment into all virtual orbitals on all fragments. However, because of the stationarity of the constrained solution, only amplitudes corresponding to inter-fragment orbital mixings give non-zero contributions to the Roothaan step energy correction Eq. (2.25).

In the case of supermolecular systems composed of only two fragments, X and Y, transformation of fragment X's occupied orbitals by the right eigenvectors, $(R_\alpha)_{Xi\bullet}^{\bullet X\bar{j}}$, and fragment Y's projected virtual orbitals by the left eigenvectors, $(L_\alpha)_{\bullet Y\bar{b}}^{Y\tilde{a}\bullet}$, from the SVD of $(X_\alpha)_{\bullet Xi}^{Y\tilde{a}\bullet}$ provides a basis, $\bar{r}$, in which each occupied orbital on X mixes with exactly one virtual orbital on Y because of the diagonal structure of $\mathbf{X}_\alpha$ in the SVD basis, $(x_\alpha)_{\bullet X\bar{j}}^{Y\bar{b}\bullet}$. In the ALMO EDA, these orbitals that allow for the description of charge transfer in terms of pairwise orbital interactions with corresponding energy lowering (cf. Eq. (2.28)) are termed complementary occupied-virtual orbital pairs (COVPs).

$$(X_\alpha)_{\bullet Xi}^{Y\tilde{a}\bullet} = (L_\alpha)_{\bullet Y\bar{b}}^{Y\tilde{a}\bullet} (x_\alpha)_{\bullet X\bar{j}}^{Y\bar{b}\bullet} (R_\alpha^T)_{\bullet Xi}^{X\bar{j}\bullet} \tag{2.27}$$

$$E_{\alpha,\text{P-CT}}^{X\to Y} = (R_\alpha^T)_{\bullet Xi}^{X\bar{j}\bullet} (F_\alpha)_{\bullet Y\tilde{a}}^{Xi\bullet} (L_\alpha)_{\bullet Y\bar{b}}^{Y\tilde{a}\bullet} (x_\alpha)_{\bullet X\bar{j}}^{Y\bar{b}\bullet} \tag{2.28}$$

A similar scheme can be used to ascribe a portion of the charge transferred to each orbital pair interaction

$$Q_{\alpha,\text{P-CT}}^{X\to Y} = (R_\alpha^T)_{\bullet Xi}^{X\bar{j}\bullet} (P'_\alpha)_{\bullet Y\tilde{a}}^{Xi\bullet} (L_\alpha)_{\bullet Y\bar{b}}^{Y\tilde{a}\bullet} (x_\alpha)_{\bullet X\bar{j}}^{Y\bar{b}\bullet} \tag{2.29}$$

where $\mathbf{P}'_\alpha$ is the updated density matrix after the Roothaan step. Furthermore, because one can perform the same procedure for the matrix $(X_\alpha)_{\bullet Yi}^{X\tilde{a}\bullet}$, it is possible to decompose charge

flow (and energy lowering) into contributions from forward and back-donation rather than the simple description of net charge flow afforded by traditional population analysis. This procedure can be conducted separately in the alpha and beta spaces, sometimes revealing interesting asymmetry (and sometimes intriguing lack of asymmetry) in the charge transfer components for the two spins in open shell systems.

While charge transfer analysis and, in the case of two fragment systems, COVP analysis can provide very insightful ways of looking at interactions between fragments, both depend on perturbation theory, a single matrix, $\mathbf{X}$, parametrizing the orbital mixings away from the polarized solution to obtain fragment-to-fragment and orbital-to-orbital derscriptions respectively. The use of perturbation theory means that some of the interaction energy is missing. The difference between the variational and perturbative charge transfer energy lowerings is termed the higher order charge transfer contribution, E_{HO}, as it necessarily involves orbital rotations corresponding to both intrafragment repolarization and further interfragment charge transfer occurring in response to the initial, pairwise decomposable charge transfer.

$$E_{\text{V-CT}} = E_{\text{P-CT}} + E_{\mathrm{HO}} \tag{2.30}$$

The energy lowering associated with higher order orbital relaxations is minimal for weakly interacting systems where a perturbative treatment of dative interactions is valid. In this work, the higher order correction constitutes only a small fraction of the variational charge transfer interaction, and so variational charge transfer energies are used predominantly for simplicity (recovering the full binding energy in fewer terms) while perturbative charge transfer energies are used as needed in the discussion of COVP analysis results. It should be noted that, by construction, basis set superposition error (BSSE) does not enter into the frozen or polarized terms; however, the charge transfer term does contain energy lowering attributable to BSSE effects and can be corrected if desired.

To conclude, it is worthwhile to note that the variational approach to defining the polarization contribution is a greedy one. All energy lowering associated with the molecule-blocked form of the ALMO constraint is associated with polarization. This contribution will implicitly include any part of charge transfer that can be described by the intersection of the one-particle Hilbert spaces associated with interacting molecules. Thus the values of polarization may include a contaminating component from charge transfer, while CT itself may be underestimated. However, we shall see from the results that the separation appears to be well-defined with the reasonably large Pople basis (6-311++G(3df,3pd)) employed in this study. For closed shell systems, even larger basis sets have been successfully used in applications such as the water dimer [15, 54]. Nonetheless, as we demonstrate elsewhere, [69] the values of polarization and charge transfer do not have well-defined complete basis set limits, but in fact are metastable in standard sequences of basis sets. The interested reader is invited to look at results in Appendix A for the 6-31+G(d,p) basis, considerably smaller than that employed in the remainder of this work, to assess the qualitative significance of the different energy partitionings between polarization and charge transfer. The

larger 6-311++G(3df,3pd) basis is chosen to better represent the total interaction between fragments. It should also be noted that the ALMO EDA at the SCF level does not separate out a contribution from dispersion as the construction of some density functionals might suggest is possible. Indeed, the interaction energy from pairwise potentials in -D methods [3] appears in the frozen term as it is unaltered as the density relaxes; however, this would not be the behavior of dispersion interactions in the exact density functional, which would incorporate some contribution from dispersion at each stage of the density relaxation. Thus, in order that the ALMO EDA maintain the correct behavior for the exact functional and in order that it also not be wed to specific density functional forms, a dispersion term is not defined at the SCF level in the ALMO EDA.

2.3 Computational Details

A development version of Q-Chem 3.2[70] was used for all calculations. Geometries for each system discussed in this work were calculated at the B3LYP/6-311++G(3df,3pd) level and verified to be valid minima by frequency calculations at the same level of theory (Appendix A). ALMO EDA with single Roothaan step and subsequent exact SCF CT correction as well as COVP analysis calculations were performed on each system at the B3LYP[6–8]/6-311++G(3df,3pd) level. Radical fragments in this work were chosen to be doublets with unpaired electrons of spin alpha. In the interest of completeness, ALMO EDA calculations were also performed on the same B3LYP/6-311++G(3df,3pd) system geometries using the 6-31+G(d,p) basis set and with the functionals: ωB97[9], ωB97X[9], ωB97x-D[10], M06[12], and M06-2X[12]. The results for a subset of the systems considered appear in Appendix A, and because they do not give a qualitatively different interpretation of the interactions, only the B3LYP/6-311++G(3df,3pd) EDA results will be discussed in the remainder of this work. Geometric distortions in all cases were determined using B3LYP/6-311++G(3df,3pd) isolated fragment geometries. Where applicable results were counterpoise corrected in order to account for spurious Basis Set Superposition Error. Orbital plots were generated using the Chimera[71] visualization program.

2.4 Applications

2.4.1 Alkyl Radicals

Intermolecular complexes involving alkyl radicals such as $CH_3^\bullet$ and $(CH_3)_3C^\bullet$ interacting with cations are interesting model systems for understanding the stabilization of transition structures associated with bond making and breaking reactions in proteins when OH and NH groups are present [61, 72]. Additionally, closed shell analogs can be easily constructed to compare the inter-fragment interactions. The cation pairs H_3O^+/Na^+ and NH_4^+/K^+ are of comparable size and have the same charge, suggesting that each member of the pair

should be able to achieve comparable electrostatic interactions because the monopoles will be at similar intermolecular distances. However, the alkali metal cations have only negligible orbital interactions (CT) with the alkyl species [61]. After recognizing the shortcomings of NBO/NEDA methods for analyzing the strong interactions in such systems, Hammerum[61] identified the differences in the binding energies of the molecular/alkali cation pairs as arising from hydrogen bonding interactions, noting that binding energies for the members of each cation pair with closed shell alkyl species were comparable.

Tab. (2.1) shows the partitioning of the total interaction energy according the ALMO EDA, and a graphical version of the data is presented in Fig. (2.1).

From both of these presentations, it is apparent that charge transfer orbital interactions are of negligible importance for systems containing alkali cations, as chemical intuition would suggest. Conversely, the hydronium and ammonium systems show considerable charge transfer interaction even with the closed shell alkyl species. The difference in CT between alkali and molecular cation pairs is however considerably greater than the difference in binding energy. The closer contacts in the molecular cation systems that are necessary to achieve optimal orbital overlap also incur large penalties to binding in the GD and FRZ terms, which are only partially canceled by the increased CT and polarization brought about by the closer (stronger) interaction.

The inter-fragment orbital gap (the energy difference between the donor HOMO and the acceptor LUMO) was calculated as the difference between the experimental ionization potential of the alkyl species less the experimental ionization potential of D_3O or NH_4 [73]. A plot of charge transfer energy lowering versus the inverse of the inter-fragment gap for systems containing a molecular cation, H_3O^+ or $NH_4{}^+$, appears in Fig. (2.2). This plot shows a rapidly increasing charge transfer contribution for the hydronium systems as the gap decreases. The charge transfer term likewise becomes more pronounced for the ammonium systems as the gap decreases; however, it does so not nearly as rapidly as in the hydronium case, which one might expect given the greater proton affinity of ammonia. The fact that classic perturbation theory arguments based on species in isolation are born out in the ALMO-EDA method for these simple systems highlights its physicality and potential for application to more complicated systems where chemical intuition becomes strained.

A graphical representation of the data from COVP analysis of these systems appears in Fig. (2.3). The fact that most of the energy lowering is captured by one or two pairs for each spin indicates that the SVD of charge transfer amplitudes was successful in condensing the information about all occupieds mixing with all virtuals into a small, conceptually tractable, number of pairwise interactions. It should be noted that the ordering of COVPs is based on the magnitude of the singular value and not the energy lowering, the two differing by the Fock matrix element in the COVP basis (cf. Eq. (2.28)). Fig. (2.3) shows that most of the charge transfer energy lowering comes from orbital mixings where the occupied orbital is on the alkyl species and the virtual orbital is on one of the molecular cations while CT interactions with alkali cations are almost non-existent. Donation by the alkyl species is chiefly in the alpha space when it is open shell (the alpha HOMO is higher in energy than

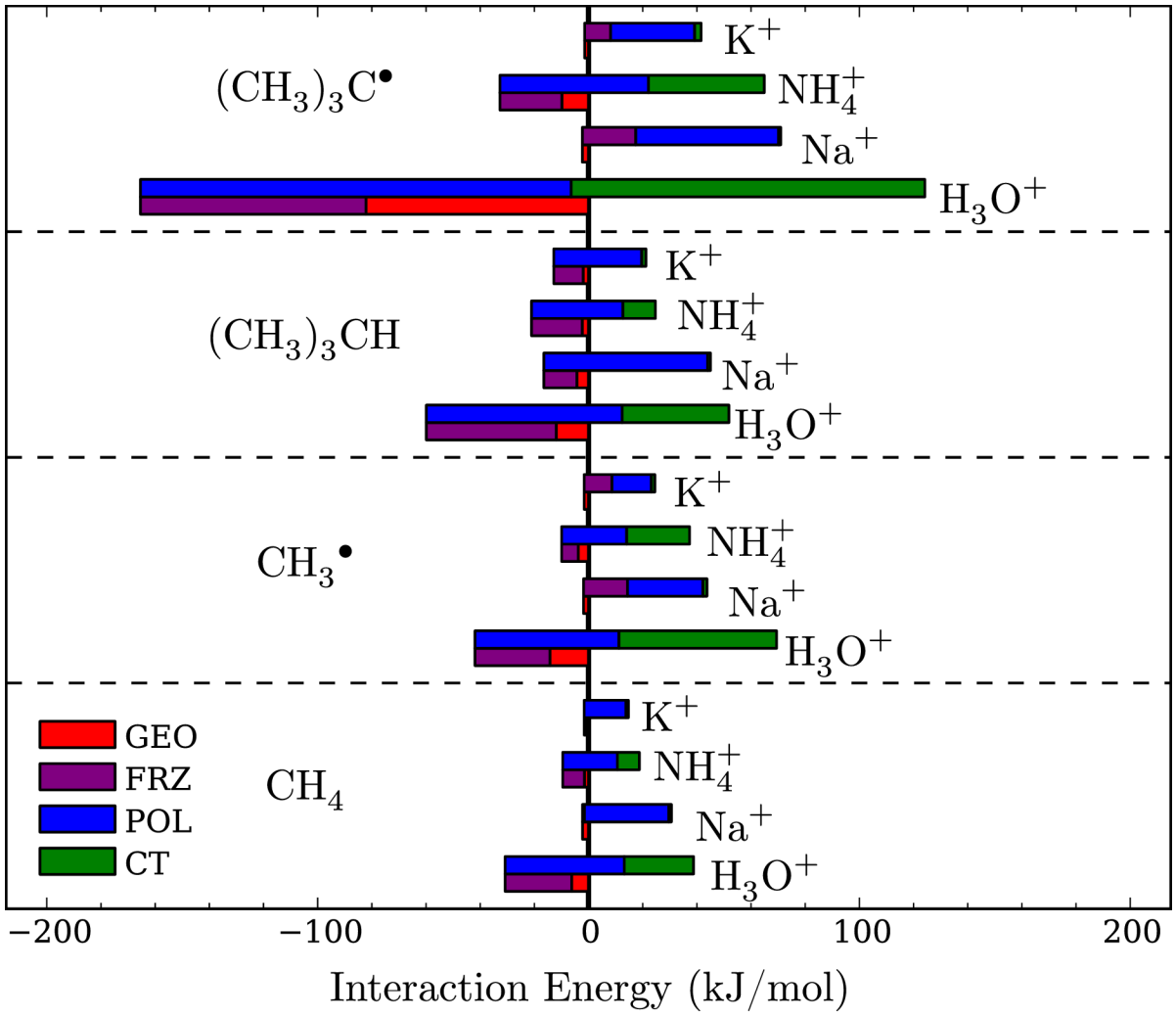

Figure 2.1: Alkyl Radical ALMO EDA Results: Unfavorable terms, such as geometric distortion are placed on the bottom of a double bar and grow to the left (negative). On the top bar, favorable terms such as polarization grow to the right (positive). By construction, the binding energy can then be read as the length of the bar to the right. Charge transfer is of much greater importance in systems involving molecular cations and, among those, for systems including a radical.

Table 2.1: Alkyl Radical ALMO EDA Results: EDA terms (kJ/mol) for systems containing an alkane or alkyl radical and a cation, either alkali or molecular. Note that the pairs H_3O^+/Na^+ and $NH_4{}^+/K^+$ are of comparable size, so one should expect comparable electrostatic interactions; however, FRZ and POL terms are noticeably larger in magnitude for the systems with molecular cations due to the closer interaction brought about by the charge transfer interactions exclusive to the molecular systems.

Alkyl Species	Cation	GD	FRZ	POL	V-CT	Bind
$(CH_3)_3C^\bullet$	K^+	1.4	-9.6	-31.0	-2.4	-41.6
	$NH_4{}^+$	9.9	22.8	-54.8	-42.7	-64.9
	Na^+	2.3	-19.7	-52.8	-0.7	-71.0
	H_3O^+	82.1	83.3	-159.0	-130.6	-124.2
$(CH_3)_3CH$	K^+	2.0	10.8	-32.5	-1.5	-21.2
	$NH_4{}^+$	2.3	18.7	-33.8	-12.0	-24.7
	Na^+	4.3	12.2	-60.5	-1.1	-45.0
	H_3O^+	11.9	48.0	-72.3	-39.4	-51.8
$CH_3^\bullet$	K^+	1.6	-10.3	-14.5	-1.3	-24.5
	$NH_4{}^+$	3.8	6.1	-24.0	-23.2	-37.3
	Na^+	1.8	-16.2	-27.9	-1.5	-43.7
	H_3O^+	14.3	27.7	-53.2	-58.2	-69.4
CH_4	K^+	1.0	0.6	-15.5	-0.9	-14.7
	$NH_4{}^+$	1.5	8.0	-20.2	-8.1	-18.7
	Na^+	2.2	-0.7	-31.1	-1.0	-30.6
	H_3O^+	6.2	24.6	-44.0	-25.6	-38.8

the beta HOMO) and necessarily distributed equally among the alpha and beta spaces when the alkyl species is closed shell. Back bonding to the alkyl unit is minimal but becomes more pronounced in the more strongly binding systems and occurs primarily in the beta space (the beta LUMO is lower in energy).

Depictions of the most important complementary occupied virtual orbital pairs for the interaction of hydronium with radical $(CH_3)_3C^\bullet$ and closed shell $(CH_3)_3CH$ in both the alpha and beta spaces, appear in Fig. (2.4) along with their corresponding energy lowerings. In all cases, the orbitals are well aligned for overlap, and donation is to a σ^* like virtual orbital (mesh) on the hydronium. The interaction resembles traditional hydrogen bonding interactions in the closed shell case, but begins to resemble chemical bonding in the radical. In the case of hydronium interacting with $(CH_3)_3C^\bullet$, the occupied orbital (transparent) of the alpha COVP is considerably different from that of the beta COVP, which has one fewer node. This observation is consistent with the interpretation that, in the radical case, the primary donation to the molecular cation is from the higher energy alpha HOMO and that, because it is lower lying, the beta occupied orbital participates as a donor orbital to a lesser

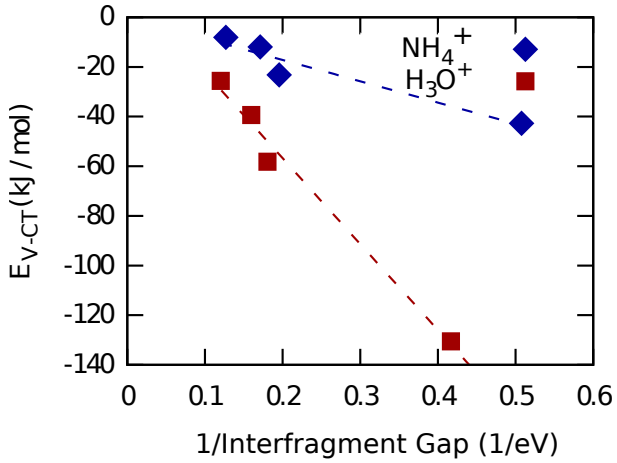

Figure 2.2: Variational Charge Transfer ($E_{\text{V-CT}}$; kJ/mol) Plotted Against the Inverse of the Interfragment Orbital Energy Gap (eV; Ionization potential of alkyl species less the electron affinity of the cation): Data is for alkyl systems containing molecular cations. The proportionality of energy denominators to energy lowerings shown by the linear relationships echoes the physicality of traditional perturbative treatments of orbital interactions. Groupings are motivated by steric considerations, and the relative slopes can be explained by the greater proton affinity of ammonia.

degree. Additionally, the nodal structure of the alpha occupied orbital for the radical species is similar to that of the closed shell species in both the alpha and beta spaces, as one might expect.

Polarization arises from the mixing of all occupied orbitals on a given fragment with all virtual orbitals on that same fragment. The strength of such mixings will generally be related to the HOMO LUMO gap within a fragment. The calculated intra-fragment gaps (beta) for the isolated, undistorted geometries are 4.5, 8.6, 6.4, and 10.6 eV for $(CH_3)_3C^{\bullet}$, $(CH_3)_3CH$, $CH_3^{\bullet}$, and CH_4, respectively. The gaps for the (quite unpolarizable) isolated cations are noticeably higher: 20.6, 16.0, 32.1, and 12.7 eV for K^+, NH_4^+, Na^+, and H_3O^+, respectively. The degree of polarization additionally depends on the proximity of the other, perturbing species to the more polarizable unit. The degree of proximity (optimized complex geometry) in turn depends on all modes of interaction. Moreover, the geometry is complicated by the constraints imposed by steric interactions. Fortunately, steric considerations are fairly uniform across the complexes for a given alkyl fragment since the concern is primarily the accessibility of the central carbon (or its CH bond).

A plot of the polarization contribution versus the binding energy, the term that encapsulates all forms of interaction and thus the motivation for close interfragment distances, appears in Fig. (2.5). Also in the figure are linear fits showing a strong relationship between POL and E_{Bind} within alkyl fragment groupings. The accessibility of the central carbon is comparable between the two radical species; however, the slope for $(CH_3)_3C^{\bullet}$ is considerably

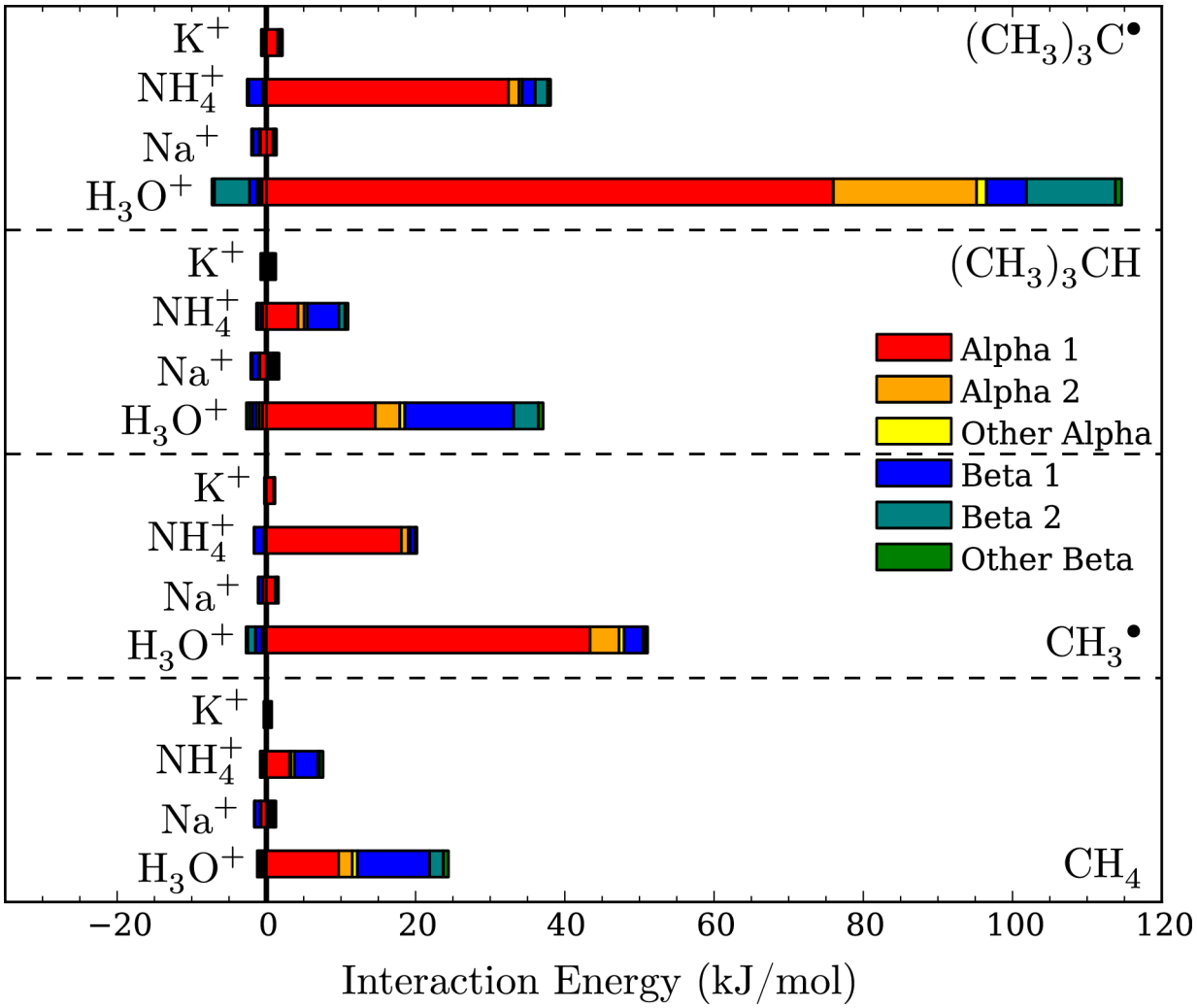

Figure 2.3: Alkyl COVP Results: All interactions are favorable, and the direction of growth from the zero line indicates the directionality of the charge transfer. Energy contributions to the left of zero involve COVPs with the acceptor orbital on the alkyl species while those on the right correspond to charge donation to the cation. Contributions from orbital interactions in the alpha space are denoted with warm colors and those in the beta space with cool colors to facilitate the recognition of symmetry or asymmetry with respect to spin. Each color indicates a different occupied-virtual orbital pair's energy contribution. Additionally, the total length of the bar indicates the magnitude of the charge transfer energy lowering calculated by perturbation theory. Notice that, in the alkali cation cases, donation is negligible while, for systems containing H_3O^+ and $NH_4{}^+$, charge transfer is primarily to the cation, symmetric with respect to spin for closed shell cases and primarily from the higher energy alpha HOMO of the alkyl species for the open shell cases.

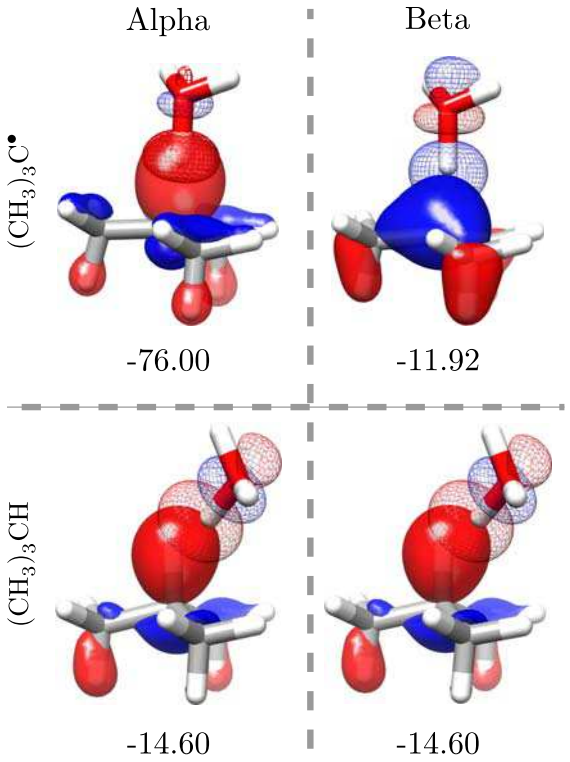

Figure 2.4: Representative COVP Images for Alkyl Systems: The most important COVPs in the alpha and beta spaces for the interaction of hydronium with the t-butyl radical ($(CH_3)_3C^\bullet$) and its closed shell analog ($(CH_3)_3CH$). The charge transfer energy lowering (kJ/mol) associated with each orbital pair is also shown. The virtual (acceptor) orbital of the pair is depicted as a mesh isosurface while that for the occupied (donor) orbital is represented with a translucent isosurface. The charge transfer interaction with the radical is reminiscent of chemical bonding with the alpha space charge transfer occurring from a higher energy orbital on the t-butyl radical than the beta space charge transfer.

greater than that for $CH_3^\bullet$, reflecting greater polarization per unit strength of interaction for the smaller gap $(CH_3)_3C^\bullet$. In the closed shell case, the hydrogen atom absent in the open shell case is most proximal to the perturbing species and thus critical to polarization; however, among the closed shell species, the ordering of slopes in Fig. (2.5) still matches the intra-fragment orbital gap ordering. It should be noted that the electronic structure of the isolated, undistorted fragments does not directly enter the ALMO calculation outside of the geometric distortion calculation. The ALMO EDA thus gives physically meaningful results commensurate with chemical intuition of isolated functional units (provided, as is true in this case, the identification of functional units is appropriate) and thus invites application to more complex interactions.

Geometric distortion is quite large for the more strongly bonding hydronium systems

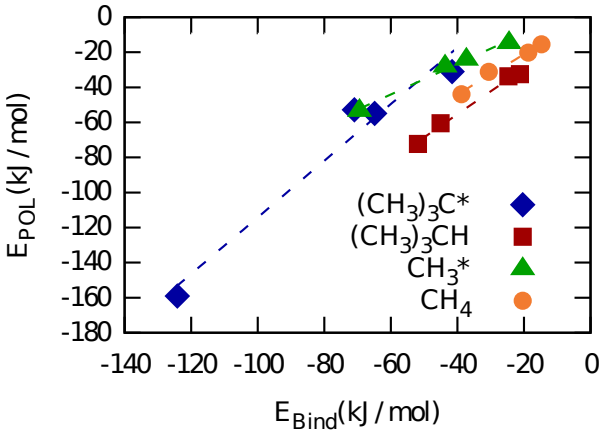

Figure 2.5: E_{POL}(kJ/mol) Plotted Against E_{Bind}(kJ/mol) for Alkyl Systems: Grouping is by alkyl species for steric reasons. There is a strong linear relationship between polarization and E_{Bind}, which encapsulates the overall degree of interaction, within steric groupings. Additionally, within radical/closed shell categories, there is an inverse relationship between the slopes and the respective alkyl intrafragment orbital gaps (cf. text).

particularly when a radical is involved and CT into the σ^* orbital, is substantial, causing the lengthening of the H-X bond. Most of the frozen orbital interactions in this set of systems are unfavorable, stemming in large part from strongly overlapping frozen occupied spaces that are highly repulsive and necessitate considerable density reorganization. Moreover, unfavorable frozen interactions are particularly prominent in structures with large charge transfer contributions as bringing atoms into close contact for better orbital overlap is often accompanied by increased core-core repulsions. It is interesting to note that the difference in interaction energy for the alkali cation species interacting with open shell as opposed to closed shell alkyl species is primarily due to the sign change of the frozen energy, which becomes favorable in the open shell case due to the lack of repulsion with the removed hydrogen.

2.4.2 Benzene Radical Cation Complexes

The strongly bound intermolecular systems involving benzene radical cations and nucleophiles are reminiscent of transition structures for nucleophilic aromatic substitution reactions [62]. Additionally, the benzene radical cation is sufficiently large to offer two binding sites that lead to noticeable differences in the character of the interaction even when the same species are involved (see below). For these reasons, we expand on the systems investigated both experimentally and theoretically by Mizuse et al.[62] to include not only different nucleophiles but also different orientations (local minima). The nucleophiles were chosen such that they spanned a large range of experimental[73] ionization potentials as these quantities

Table 2.2: Aryl Radical ALMO EDA Results: EDA terms (kJ/mol) and nucleophile Ionization Potentials (IP) [73] for systems containing the benzene radical cation and a nucleophile in the given orientation, on-top or side-on. Note, for on-top orientations, the erratic dependence of the total binding energy on nucleophile IP but nearly monotonic dependence of V-CT on the same quantity. The IP of benzene and thus the Electron Affinity (EA) of the aryl radical cation acceptor is 9.24 eV. [73]

Orientation	Nucleophile	GD	FRZ	POL	V-CT	Bind	IP(eV)
Top	PH_3	22.1	69.4	-22.3	-140.5	-71.4	9.87
	NH_3	10.3	46.4	-29.2	-107.0	-79.5	10.07
	CH_3COOH	27.2	-18.1	-20.3	-46.7	-57.9	10.65
	CH_3OH	3.8	7.7	-15.1	-45.4	-49.0	10.84
	CH_3Cl	2.2	8.8	-11.6	-38.1	-38.7	11.26
	HBr	2.1	26.2	-5.1	-46.2	-23.0	11.68
	CH_3CN	1.4	-19.9	-17.3	-22.8	-58.6	12.20
	H_2O	0.7	-11.1	-7.9	-17.0	-35.3	12.62
Side	CH_3COOH	2.4	-30.4	-11.7	-4.4	-44.1	10.65
	CH_3OH	0.6	-22.6	-9.0	-9.3	-40.4	10.84
	CH_3CN	0.3	-33.8	-12.9	-6.8	-53.1	12.20
	H_2O	0.3	-25.3	-6.9	-4.7	-36.6	12.62

were identified as important to explaining the geometric trends in terms of charge transfer in the original work.[62]

Tab. (2.2) contains the ALMO EDA data for these systems together with the experimental IP of the nucleophile. A graphical version of the EDA data for systems containing the aryl radical cation and a nucleophile appears in Fig. (2.6), and the corresponding COVP data appears in Fig. (2.7).

It is immediately apparent that a large range of binding energies is present; however, these binding energies only correlate roughly with ionization potential. The electron affinity of the benzene radical cation can be taken as equivalent to the ionization potential of benzene, 9.24 eV [73], and the difference between the nucleophile IP and the benzene IP can then be considered the inter-fragment orbital energy gap. A plot of the charge transfer contribution to the binding energy versus one over the inter-fragment gap for systems with an on-top orientation appears in Fig. (2.8). The linear fit indicates a strong correlation and reaffirms the connection between the ALMO charge transfer term and the long standing perturbation arguments made to explain orbital interactions. Again it should be noted that this connection arises naturally rather than explicitly by construction. Indeed, while the ALMO CT contribution can be calculated perturbatively, the perturbative correction is carried out using the orbitals and Fock matrix resulting from the self consistent polarization of the fragments, which, in the case of strongly interacting species such as these, are consider-

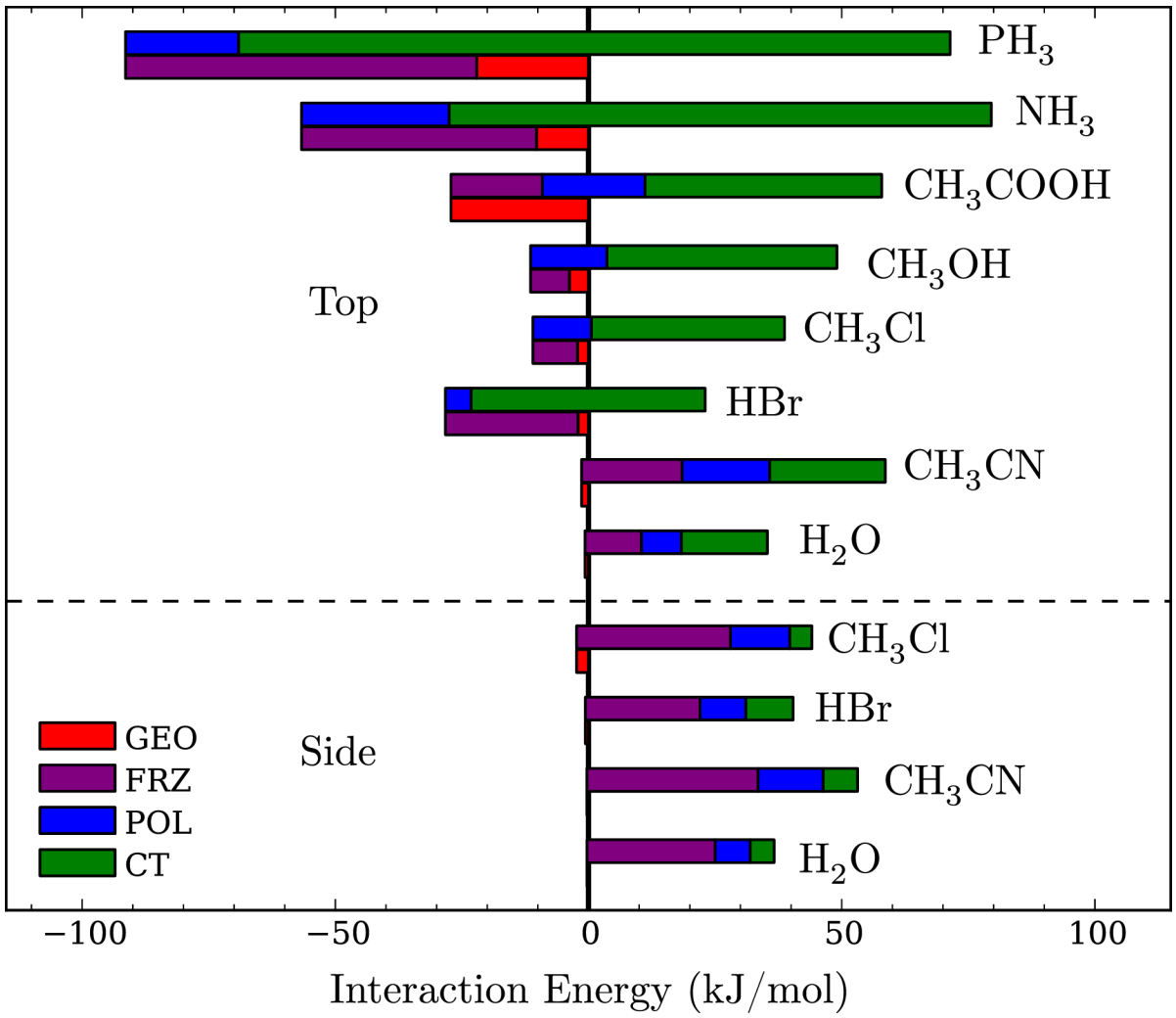

Figure 2.6: Aryl Radical EDA Results: Unfavorable terms, such as geometric distortion are placed on the bottom of a double bar and grow to the left (negative). On the top bar, favorable terms such as polarization grow to the right (positive). By construction, the binding energy can then be read as the length of the bar to the right. Notice the considerable shift toward dependence on frozen interactions rather than charge transfer when a species is oriented on the side rather than on top and also the very similar binding energy for water in the two orientations despite the considerably different character of interaction.

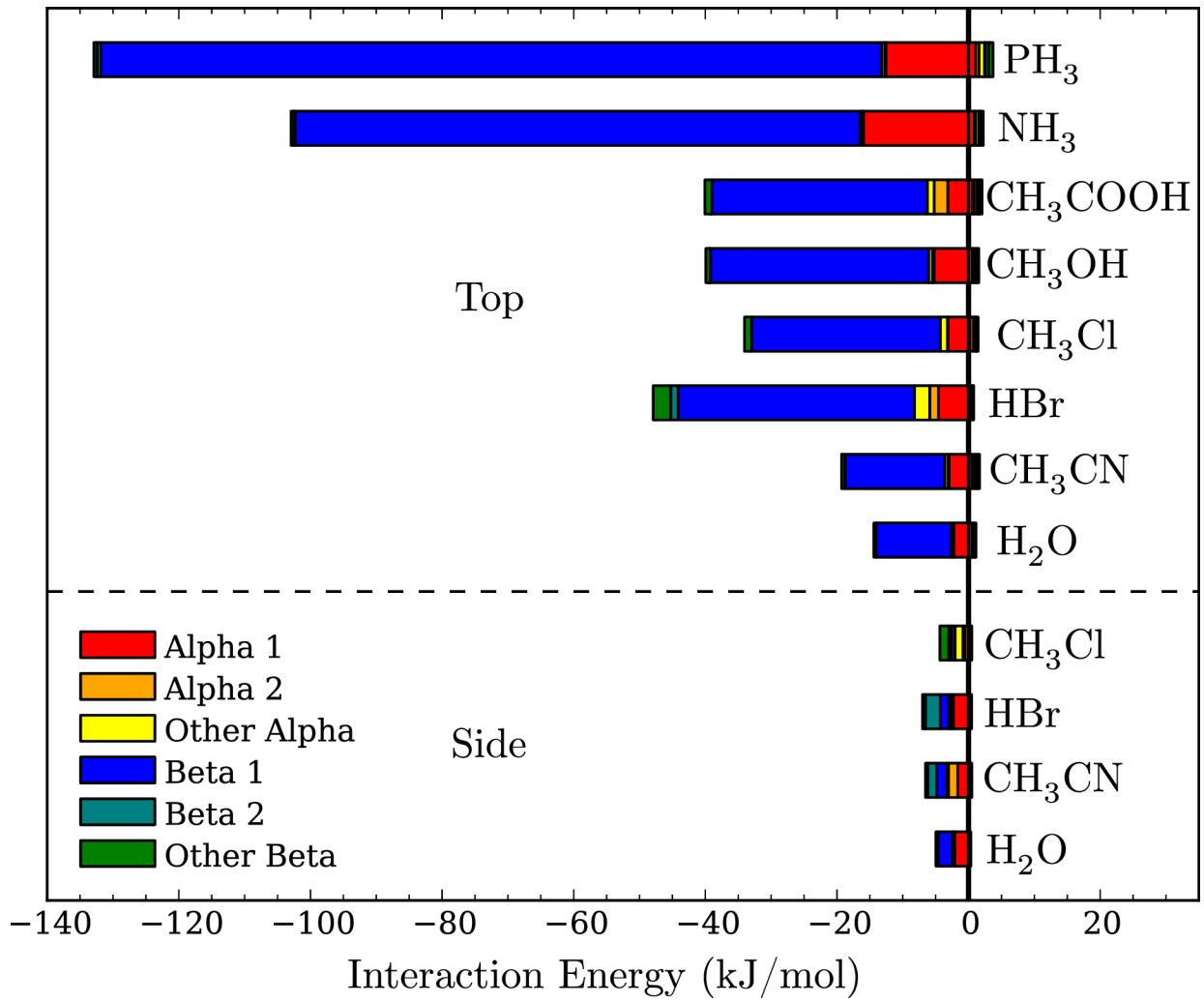

Figure 2.7: Aryl Radical COVP Results: All interactions are favorable, and the direction of growth from zero indicates the directionality of the charge transfer. Energy contributions to the left of zero involve COVPs with the acceptor orbital on the aryl radical cation species while those on the right correspond to charge donation to the nucleophile. Contributions from orbital interactions in the alpha space are denoted with warm colors and those in the beta space with cool colors to facilitate the recognition of symmetry or asymmetry with respect to spin. Each color indicates a different occupied-virtual orbital pair's energy contribution. Additionally, the total length of the bar indicates the magnitude of the charge transfer energy lowering calculated by perturbation theory. Charge transfer is primarily from the nucleophile to the electron deficient aryl radical cation and, for on-top systems, in the beta space as the radical has a lower-lying beta LUMO accessible in that orientation. Charge transfer is diminished for side-on systems but largely symmetric with respect to spin due to poor overlap with the low-lying beta orbital.

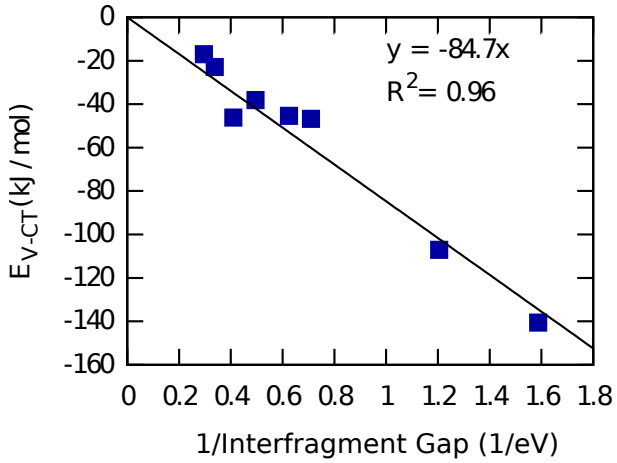

Figure 2.8: $E_{\text{V-CT}}$(kJ/mol) Plotted Against the Inverse of the Interfragment Orbital Energy Gap (eV; IP of nucleophile less IP of benzene): Data is for systems containing the aryl radical cation and on-top oriented nucleophile. The equation is of the form $E_{\text{V-CT}} = a/\text{Gap}$; a = -84.7 kJ $\cdot$ eV/mol, the accurate fit demonstrates the consistency of the ALMO V-CT term with a perturbation theory understanding of orbital interactions based on isolated species. Minimal error in the fit was incurred by forcing the physically meaningful zero intercept.

ably different from their "frozen" counterparts determined completely by the calculation of the species in isolation. This observation thus argues again for the physicality of the charge transfer term in the ALMO EDA.

It should be no surprise that the smallest intra-fragment gap is that of the benzene radical cation in the beta space (2.04 eV; undistorted). Steric limitations to orientation are uniformly minimal across the systems considered in this section. Thus, by the same arguments made above, the polarization should largely depend on how strongly the nucleophile is able to interact with the aryl cation because this determines how closely the nucleophile is able to approach. This degree of interaction is once more taken to be encapsulated in the total binding energy of the system, and the plot of polarization energy versus total binding energy. Fig. (2.9) again shows a relatively strong linear relationship between the two quantities despite the diversity of nucleophiles and orientations.

Because there are few other atoms hindering the approach of the two species, the most significant core-core repulsions should arise as a consequence of maximizing overlap for donor acceptor orbital interactions. Additionally, systems that do not have strong core-core repulsions should have fairly favorable frozen orbital energy contributions as the interaction is, after all, between a cation and one of several neutral molecules with considerable dipole moments. Indeed, the plot of V-CT versus FRZ, Fig. (2.10), for all super-molecular complexes containing the aryl radical cation, irrespective of nucleophile orientation, shows a fairly strong linear correlation despite the variety of systems.

It has been shown that smaller inter-fragment gaps generally lead to more charge transfer;

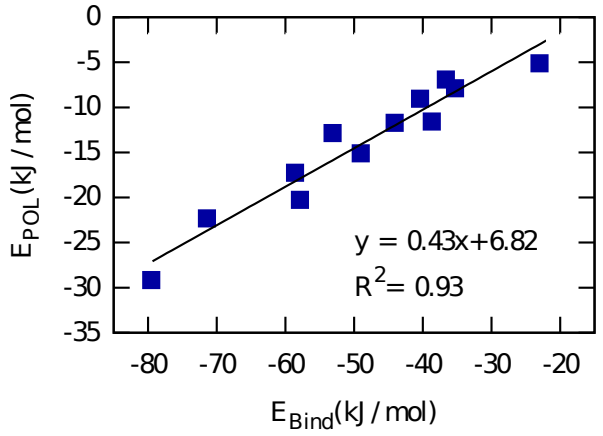

Figure 2.9: E_{POL}(kJ/mol) Plotted Against E_{Bind}(kJ/mol) for All Aryl Radical Cation Systems. All nucleophiles and orientations considered in this work are included. All systems are included in a single fit because the species with the smallest intrafragment orbital energy gap is in all cases the aryl radical cation and because steric concerns are fairly uniform. The fairly accurate fit despite the diversity of systems reaffirms the interpretation and strong physical content of the ALMO polarization term.

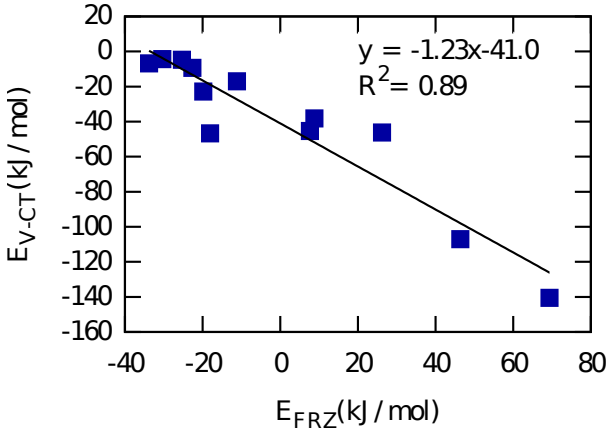

Figure 2.10: $E_{\text{V-CT}}$(kJ/mol) Plotted Against E_{FRZ}(kJ/mol) for all Aryl Radical Cation Systems. All nucleophiles and orientations considered in this work are included. The linear correlation demonstrates the origin of the unfavorable Frozen interaction terms for these systems: core-core and exchange interactions resulting from close proximity needed for improved orbital overlap.

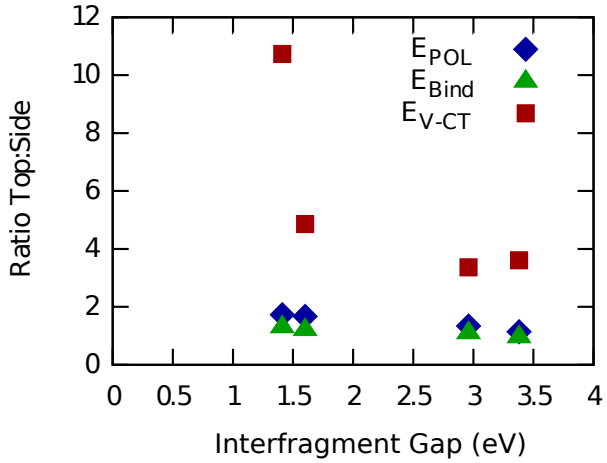

Figure 2.11: The Ratio (Top:Side) of the $E_{\text{V-CT}}$, E_{POL}, and E_{Bind} Contributions Plotted Against IP(eV): Systems shown are those with both an on-top and a side-on structure. This plot shows the considerable shift toward dependence on charge transfer interactions as IP decreases toward that of benzene (9.24 eV) when going from side-on to on-top orientation. The top:side ratio for E_{POL} increases for smaller interfragment orbital energy gaps because of the closer contacts. These close contacts are brought about by the potential for energetically attractive orbital interactions and introduce a stronger perturbation for intramolecular mixings. The E_{POL} ratio increases more slowly than that for $E_{\text{V-CT}}$, and that for E_{Bind} increases even more slowly because of the unfavorable frozen interactions incurred by the closer approach of the species.

however, these dative interactions can only take place if there is sufficient overlap of the relevant orbitals, as is the case for the top oriented species. A plot of the ratio of charge transfer in the top oriented complex to that of the side oriented complex for the same fragment pairs appears in Fig. (2.11). The plot shows that, for smaller inter-fragment gaps, the shift to increased charge transfer when going from the side to the top orientation is dramatically more pronounced. Additionally, the analogous plots for E_{Bind} and E_{POL} in Fig. (2.11) show that, for smaller inter-fragment gaps, the ratio of binding energies increases though not as quickly as does the ratio of polarization energy contributions and neither as quickly as the charge transfer contribution. These findings together indicate a considerable shift toward stronger binding through enhanced dative interactions when orbitals are favorably aligned and considerably more emphasis on polarization and frozen interactions (by subtraction) when orbital alignment is not optimal.

COVP analysis of the aryl radical cation complexes Fig. (2.7) shows that the charge transfer energy lowering is due to mixings between occupied donor orbitals on the nucleophile and virtual acceptor orbitals on the aryl radical cation with negligible backbonding. These mixings are primarily in the beta space for the top oriented geometries in which the nucleophile donor orbital is well aligned with the low-lying beta LUMO of the aryl radical

cation. Alternatively, the side orientations exhibit charge transfer that is quite symmetric with respect to alpha and beta despite the radical nature of the species involved, simply because the half-occupied benzene hole orbital is inaccessible.

While the binding energy of the water and aryl radical cation system is almost the same for both top and side orientations, the ALMO EDA reveals considerably different modes of interaction in the two cases. The side interaction is dominated by frozen orbital contributions while the interaction in the top orientation is more noticeably charge transfer in character (cf. Fig. (2.6)). The most important COVPs for the interaction of the aryl radical cation with water in both top and side orientations are displayed along with their corresponding energy lowerings in Fig. (2.12). These orbital plots show that the beta donation for the top case is into a π orbital which, as confirmed by the number of nodes, is lower in energy than the acceptor orbital in the alpha space, leading to the asymmetry with respect to spin in the energy lowerings. Conversely, charge donation for the side orientation is into the C-H σ^* orbital, which is very similar for both spins, and the energy lowering is roughly symmetric. The donor orbital in all cases is a non-bonding lone pair orbital on the water.

It should be noted that the β acceptor orbital does not closely resemble the benzene HOMO, because the COVP reflects the optimal compromise between large numerator (good orbital interaction) and small denominator (energy gap) to most compactly describe the interaction. Thus the β acceptor orbital also contains contributions from other, higher, empty π levels to enable spatial localization.

2.5 Conclusions

The ALMO EDA has been successfully extended to open shell systems and applied to two classes of examples. While these open shell interactions are considerably stronger than many closed shell intermolecular interactions, the ALMO-EDA continues to yield physically meaningful results. Two examples identified herein include polarization contributions that depend on the intra-fragment gap, and inter-fragment charge transfer interactions that depend on the inter-fragment orbital gap. Moreover, the ALMO EDA and COVP analysis were also able to distinguish two different interactions involving the same species, water and the aryl radical cation, with similar overall binding energies. Thus the ALMO-EDA can be useful to explore and distinguish seemingly equivalent binding sites within a given model chemistry. Here it should be noted that the ALMO EDA is contingent on the model chemistry's accurate portrayal of all relevant interactions (e.g. exchange, correlation, and dispersion).

The application of the ALMO EDA to the alkane/alkyl radical interactions with cations, and benzene cation interacting with nucleophiles has also served to illustrate some general features of open shell intermolecular interactions. First, while orbital interactions (CT) can be very important, they do depend on proper intermolecular overlap of relevant orbitals. For alkyl radicals interacting with alkali cations, CT is very small because there are no en-

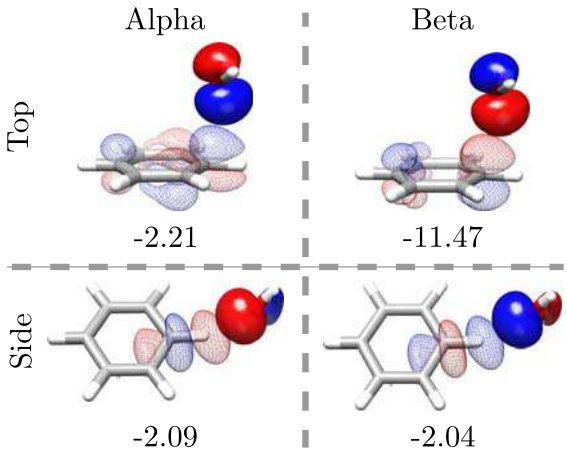

Figure 2.12: Representative COVP Images for Aryl Radical Cation Systems: The most important COVPs in the alpha and beta spaces for the interaction of water with the benzene radical cation in both the on-top and side-on orientations. The charge transfer energy lowering (kJ/mol) associated with each orbital pair is also shown. The virtual (acceptor) orbital of the pair is depicted as a mesh isosurface while that for the occupied (donor) orbital is represented with a translucent isosurface. For the side case, charge transfer is roughly symmetric with respect to spin and primarily into a C-H σ^* orbital on the aryl radical cation. For the top case, charge transfer is from a lone pair orbital on water into a somewhat localized π orbital on the aryl radical cation. In the beta space, this acceptor orbital has one fewer node (lower energy) and thus leads to greater energy lowering.

ergetically relevant acceptor orbitals. Similarly nucleophiles interact with benzene cation by other means when intermolecular orbital overlap for the most energetically relevant orbitals is poor (side-on complexes).

A second observation is that strongly unfavorable frozen interactions are typically accompanied by considerable charge transfer energy lowering. Although polarization terms are also large for systems where frozen interactions are considerably unfavorable (because fragments are close and the perturbation causing intra-fragment mixings is large) the real driving force for the close inter-fragment separations that can occur in open shell systems seems to be better orbital overlaps for charge transfer interactions. The increased polarization energy lowering largely serves to mitigate the high energetic cost incurred by the closer approach. Closer approach becomes unhelpful for overall interaction strength more rapidly when the means of lowering the system energy are restricted to polarization alone.

It is our view that there is much still to be done in unravelling intermolecular interactions, particularly when open shell fragments are involved. For instance, we intend to investigate the effects of the exclusion of different modes of interaction on the super-molecular structure so as to disentangle the considerable dependence of intermediate state energies on the ultimate geometry. Additionally, while the results of the ALMO EDA are both physically

reasonable and insightful, it is of interest to explore strict bounds on physically meaningful contributions so as to refine quantitative definitions of interactions in a subfield that can often be quite qualitative.

Chapter 3

Polarization Contributions Revisited with FERFs

3.1 Introduction

Energy decomposition analysis (EDA) methods in electronic structure theory[74] seek to partition interaction energies into physically meaningful contributions such as permanent electrostatics, induced electron polarization, dispersion interactions, charge transfer, Pauli repulsions, etc. Such contributions are useful for understanding the ways in which different components of a system interact and for determining modifications of a system that might lead to a desired outcome. While these physical concepts may be intuitive, their definitions are not unique, except in the regime where different fragments do not overlap. However, the interesting regime of intermolecular interactions is of course the overlapping regime! The goal of this work is to present a new definition of the energy lowering associated with polarization which has several desirable qualities that not all other definitions satisfy.

In the opinion of the authors, the following are attractive properties of an energy decomposition scheme and its corresponding definitions of terms:

1. Total interaction energy corresponds to a well-defined computational method. An EDA should subdivide the total intermolecular interaction energy calculated by a useful standard electronic structure method, such as a density functional theory, into physically interpretable contributions.

2. Basis function independence. The approach should not rely on the use of a particular type of basis function, such as atomic orbitals (AO's), but rather should be applicable to any convenient one-particle basis including plane waves, finite elements, etc, in addition to AO's.

3. Non-trivial basis set limit. In the overlapping regime it should be possible to converge each energy term to a stable and physically meaningful complete basis set limit.

4. Correct asymptotic behavior. The energy contributions must reproduce their known asymptotic behavior. For example, intermolecular polarization between neutral molecules with permanent dipoles yields an asymptotic R^{-6} dependence with known coefficient.

5. Quantum mechanical energies. The energy contributions should be constructed from terms that obey Fermionic quantum mechanics. For example there should be no role for the *classical* electrostatic interactions associated with the *quantum* density.

6. Continuous. The energy contributions should be continuous functions of the nuclear coordinates if the overall intermolecular interaction energy is continuous.

7. Computationally feasible. The computational cost for evaluation of each term should not be significantly greater than the direct evaluation of the entire intermolecular interaction.

8. Variational. To ensure validity in both weak and strong interaction regimes, the energy contributions should be defined as constrained variations[16, 51, 75] relative to an unconstrained calculation.

This work will focus on the construction of a definition for the polarization contribution to the interaction energy satisfying all of the above criteria but most notably the second two points, basis type independence and a non-trivial basis set limit.

There are many schemes for analyzing interaction energies that do not compute a polarization term with the meaning used in this work. The most common approach is to simply treat these two forms of relaxation, polarization and charge transfer, as inseparable, leading to the induction term in the traditional SAPT[19, 20, 22–24], the orbital term in Bickelhaupt-Baerends EDA [44, 76, 77], ETS [39–41, 78], and the CI-singles based scheme of Reinhardt et al.[79], as well as the "polarization" term in LMO-EDA [45, 80, 81] and in the deformation density based scheme of Mandado and Hermida-Ramón[82].

Our view is that the polarization contribution to interactions is a physically meaningful quantity that is closely related to isolated monomer properties, despite not being uniquely defined in the overlapping regime. There are both variational and non-variational approaches to computing polarization energies. Among the non-variational schemes are those based on symmetry adapted perturbation theory (SAPT) that either bin excitations using a basis partitioning[25, 83] to prohibit, or add potentials[84] to discourage, charge transfer contributions to the induction term. Another non-variational approach is natural energy decomposition analysis (NEDA)[34–37, 85] in which the polarization contribution is largely determined by the natural bond orbital (NBO) method's ability or lack thereof to construct monomer Lewis structures from supersystem densities. Moreover, the NEDA polarization energy is computed as a difference involving the classical interaction of monomer densities.

The pioneering Kitaura-Morokuma (K-M) EDA[38, 86, 87] can be seen as the progenitor of variational EDAs, although it has the disadvantage that the energies used to define the

polarization contribution do not correspond to the expectation values of valid wavefunctions. In much the same vein, the PIEDA[88, 89] and SCCCMS-based[90, 91] EDAs use FMO[33, 92–94] and point charges, respectively, to optimize monomer wavefunctions in the presence of the classical electrostatic potentials of all other monomers, so the polarized state energy is also not the expectation value of an antisymmetric wavefunction. The CAFI[95] method also employs FMO to relax monomer wavefunctions but then uses a basis partitioning of CI-singles to investigate the additional polarization contributions that arise together with charge transfer . A slightly different approach to polarization is taken by the CSOV[42] and RVS[43, 87] schemes in which the intermediate variational solutions come from the removal of certain orbital rotations in the optimization based on the monomer attribution of orbitals. The wavefunctions in these two methods are valid; however, subsystems are not able to relax simultaneously in contrast to the KM and related polarization schemes.

A novel method for the calculation of polarization energies is the constrained DFT approach of Wu[51, 75], which constructs a polarized wavefunction by imposing a real-space population constraint. One advantage of this variational approach is that it circumvents the partitioning of basis functions among monomers that can be problematic for other methods; however, this method is not without its drawbacks, discussed at length later. We also mention that Řezáč and de la Lande[96] have recently used a similar constraint to isolate charge transfer contributions to the interaction energy.

A fairly common approach to obtaining a variational polarization energy is to solve for a polarized state using SCF for molecular interactions (SCF-MI) SCFMI[64, 65], which both produces a valid wavefunction through constraints and allows for the simultaneous relaxation of all species. SCFMI polarization is a component of several EDA schemes including the block-localized wave function (BLW)-EDA[46–49] and the absolutely localized MO (ALMO)-EDA[15–18] schemes and the method of De Silva and Korchowiec[97]. We also note that the approach of Yamada and Koga[98] likewise uses SCF-MI to compute polarization energies; however, unlike the other three methods, the subspaces used are based on NBOs with the aim of investigating intramolecular interactions.

In the SCFMI-based schemes[15–18, 46–49, 97], the polarized state is obtained by the minimization of the single determinant electronic energy of a collection of fragments with the constraint that the AO-to-MO coefficient matrix is fragment-blocked with an integer number of electrons assigned to each fragment. The polarization energy lowering is defined as the difference between the energy of this constrained solution and that of the frozen orbital density matrix, which is the projector into the span of the occupied orbitals of the fragments computed in isolation within their subspaces. The parameters for on-fragment-subspace orbital mixings are the degrees of freedom in the constrained optimization problem. These intra-subspace occupied-virtual rotations are seen as the polarization of each fragment, an interpretation that is reinforced by the fact that displacements on this constrained surface preserve fragment populations by the Mulliken definition[17, 99]. Unlike in the KM polarization scheme, SCFMI polarization both recognizes and tries to relieve the increased kinetic energy that is a consequence of overlapping fragment occupied subspaces. The remaining

inter-subspace rotations that lead to the optimal unconstrained determinant are identified as charge transfer in character because they do allow for changes in fragment populations by the Mulliken definition. The interpretation of the partitioned singles is simple and intuitive provided that the fragment subspaces which delimit intra- from inter-fragment mixings are in fact meaningful.

The definition of the polarization energy lowering in the SCFMI-based EDA schemes has two major weaknesses. The first is that the definitions for the fragment subspaces which determine the degrees of freedom in the variational energy calculation are intrinsically tied to the use of an atom-centered basis set. This means that standard SCF-MI is not applicable to calculations involving plane-wave basis sets among others. The second weakness is the assumption that the subspaces constructed from these AO functions are fragment-ascribable. In the limit that each atom is given a complete basis set, the fragment subspaces become linearly-dependent, and the subspace rotation constraint is effectively removed so that the SCFMI energy is equal to the full SCF energy. Hence the charge transfer contribution to the interaction becomes zero, a trivial basis set limit. This lack of a meaningful basis set limit for the SCFMI-based polarization term has been discussed by several authors[84, 100, 101].

Recently[69], an approximate lower bound for the polarization contribution was computed by the same constrained optimization but using orthogonal fragment subspaces of minimal rank designed to compactly describe intra-fragment orbital relaxations. The upper bound was taken as the SCFMI-based polarization energy, which is clearly valid at the basis set limit and also very likely true for some of the larger common basis sets. Figure 3.1 demonstrates the poor basis set convergence of the polarization energy lowering in the original ALMO-EDA scheme compared to the much more quickly converged frozen and total interaction energies as a function of both basis set augmentation and basis set zeta. In practice (e.g. in using the ALMO-EDA or the BLW-EDA), the restriction to AO basis sets was simply an accepted limitation, and the lack of a useful basis set limit was tempered by the use of basis sets with function spaces that were largely fragment-ascribable (e.g. typically no larger than aug-cc-pVTZ). It is the goal of this work to overcome these weaknesses in the original definition of the polarization energy lowering in the SCFMI-based schemes by constructing new fragment subspaces.

The remainder of this paper is organized as follows. The theory, Sec. 3.2, is based on defining "fragment electric-field response functions" (FERFs) for each fragment, which form an appropriate basis for describing inductive effects. The FERFs can exactly (in a sense to be discussed) capture the response of an isolated fragment to weak electric fields. One FERF per occupied orbital is required for each independent component of a weak applied field. Thus there are 3 FERFs per occupied orbital for thee dipole (D) responses to a uniform field, 5 for the quadrupole (Q) responses to a field gradient, 7 for octupole (O) responses, etc. The polarization models we explore involve the use of D, DQ, or DQO sets of FERFs. The FERFs can be used directly as a basis for polarization, in which case they are non-orthogonal from one fragment to the next, and we will refer to such models as nD, nDQ, and nDQO. Alternatively, we next define orthogonalized FERFs, which give rise to the oD, oDQ, and

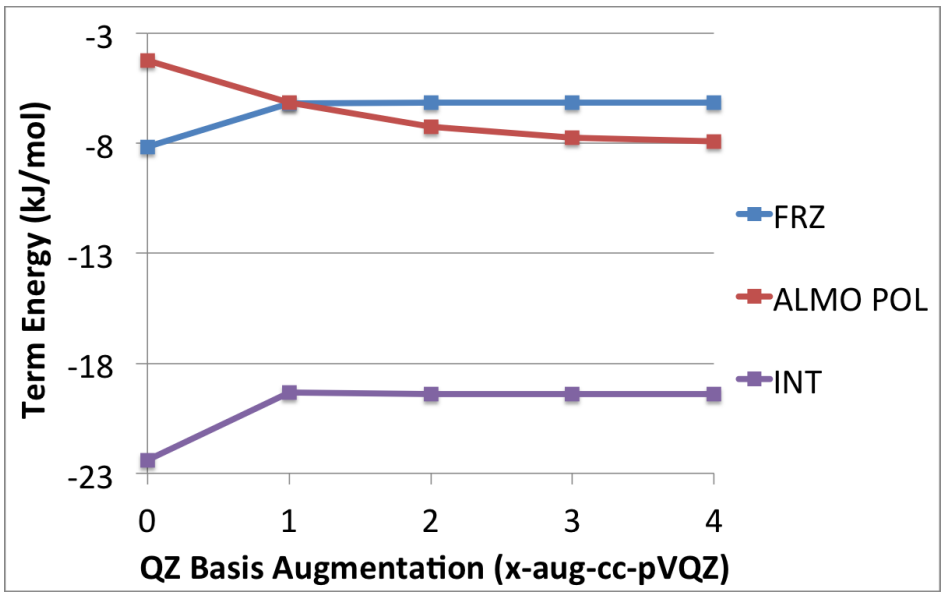

(a)

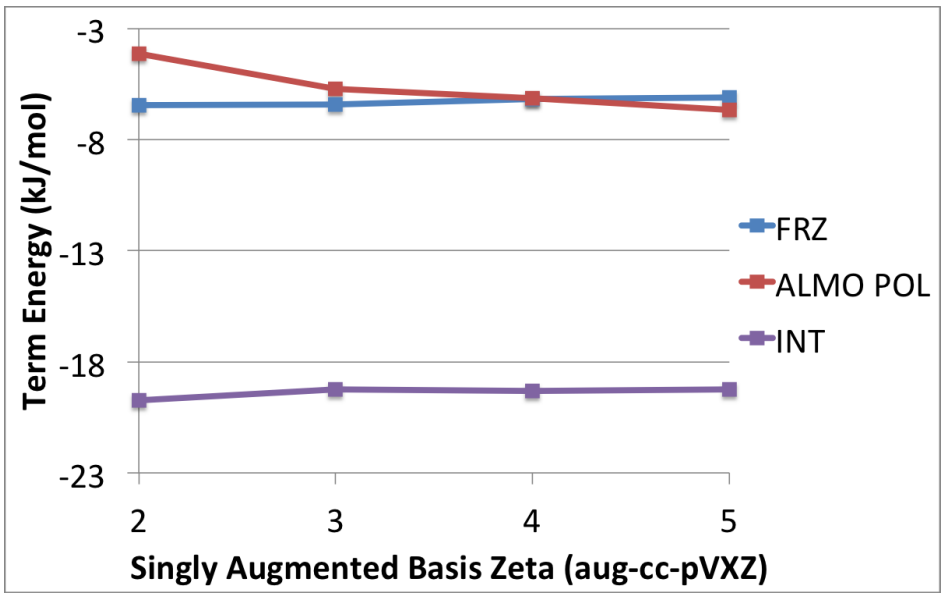

(b)

Figure 3.1: Basis set convergence of some ALMO-EDA energy terms for the aug-cc-pVQZ/B3LYP optimized water dimer with an intermolecular distance of $R_{O-H} = 1.96$Å. The upper panel shows the effect of adding diffuse functions, while the lower panel shows the effect of increasing the cardinal number, X.

oDQO models, using an importance-weighted orthogonalization that allows the FERFs that contribute most to polarization to be least distorted. Next, the interpretation of the SCFMI equations is re-evaluated in terms of orbital rotations, leading to an important distinction between some variational polarization schemes.

We then turn to the results of test calculations assessing the various FERF models on polarization contributions to a range of model intermolecular interactions. Vastly improved basis set convergence characteristics are found relative to the standard ALMO polarization model. We assess the differences in polarization energies predicted by the non-orthogonal and orthogonal models. The paper concludes with our recommendations for the use of these models, as well as some discussion of their merits relative to existing variational treatments of polarization in EDAs.

3.2 Theory

General notation in this work is as follows: subspace indices: capital Roman $X, Y...$; AO and subspace basis indices: lower case Greek μ, $\nu...$; virtual MO indices: $a, b...$; occupied MO indices: $i, j...$; generic MO indices: $r, s.....$ This work considers non-orthogonal subspaces and thus makes considerable use of tensors with both covariant (subscript) and contravariant (superscript) indices.[63] Dots are used as placeholders for clear index ordering in quantities that have both covariant and contravariant indices. For instance, the matrix $\mathbf{C}$ with matrix elements $C^{X\mu}_{\bullet Yr}$ has rows corresponding to contravariant basis vectors associated with subspace X and columns corresponding to covariant molecular orbitals associated with subspace Y, both occupied and virtual. For simplicity, matrices are generally given in spin-orbital notation, which permits simplification to any of the standard spin cases, such as either restricted or unrestricted. Exceptions will explicitly include a spin index as a subscript, as in $\mathbf{C}_\alpha$. Further notation will be introduced as needed.

3.2.1 Electric-Field Response Functions to Define Polarization Subspaces of Isolated Fragments

The role of the fragment polarization subspaces is to separate rotations that are polarization-like from those that are charge-transfer-like. An unambiguous distinction between the two only exists in the non-overlapping, well-separated, weak-field regime where charge-transfer is zero because of the lack of overlap but polarization is non-zero because of the presence of a field. In this limit, other fragments are well approximated by low-order multipole expansions, and polarization is the response to this multipole field, which, for single-determinant methods, is merely a matrix of occupied-virtual rotations.

It is preferable to consider polarization spaces that are inherent to the molecule such that they can be computed for the fragment in isolation with a sufficiently complete basis of any type. The first essential (and trivial) component of this space is the span of the occupied

orbitals of the isolated fragment. The remaining vectors must come from the fragment's virtual subspace, and it is necessary to include some portion of this space in order that the given fragment is able to relax in the presence of other perturbing species.

In order to select supersystem-independent virtual functions, we consider fragment responses to general weak fields, field gradients, and so forth such that the fragment is able to respond to the presence of some other arbitrary, well-separated fragment. This will ensure that the correct asymptotic polarization behavior is recovered to sufficient accuracy. These orbital responses are exactly those computed in the calculation of dipole, quadrupole and higher polarizabilities, which are the second derivatives of the electronic energy with respect to field perturbations.

Denoting derivatives with superscripts, the orbital response (of a fragment) to the field component F_μ is Δ^μ. It is the solution to the following (coupled perturbed SCF (CPSCF)) linear equations obtained by differentiating the zero field SCF stationarity condition, $E^\Delta = 0$, with respect to the field component F_μ, which couples to the molecule by the multipole moment matrix M_μ in the core hamiltonian, h:

$$E^{\Delta\Delta} \cdot \Delta^\mu = -E^{\Delta h} \cdot h^\mu \tag{3.1}$$

$$E^{\Delta h} \cdot h^\mu \equiv \frac{\partial^2 E}{\partial \Delta^{ai} \partial h_{\lambda\sigma}} (h^\mu)_{\lambda\sigma} = 2(M_\mu)_{ai} \tag{3.2}$$

$E^{\Delta\Delta}$ is the usual SCF orbital Hessian. In this work, the equation is solved for all RHS simultaneously using conjugate gradient preconditioned with the easily inverted $E^P \cdot P^{\Delta\Delta}$ portion of the Hessian. The fragment center of mass is taken as the origin for computing the cartesian multipole matrices, which are then transformed to the real spherical harmonic multipole matrices[102] appearing in the RHS.

The fragment orbital response matrix, Δ^μ, for a given field component, $F_\mu = F_x, F_y, F_z, \frac{\partial F_x}{\partial z}, \frac{\partial F_y}{\partial z}$, etc., which couples through the multipole moment matrix $M_\mu = \mu_x, \mu_y, \mu_z, Q_{xz}, Q_{yz}$, etc., is in general dense, describing the mixings of all occupied orbitals with all virtual orbitals. Singular Value Decomposition (SVD) of these amplitudes expressed in an orthogonal basis for a specific spin (we consider only the restricted closed-shell and unrestricted cases in this work),

$$(\Delta^\mu)_{ai} = (L_\mu)_{ab} (d_\mu)_{bj} (R_\mu^T)_{ji}, \tag{3.3}$$

yields a unitary transformation of the virtual orbitals, $(L_\mu)_{ab}$. This transformation allows for the description of the orbital response in terms of only $\min(O, V)$ virtual orbitals, which are the fragment electric-field response functions (FERFs) for field component μ:

$$(V_\mu)^\nu_{\bullet b} = C^\nu_{\bullet a} (L_\mu)_{ab} \tag{3.4}$$

FERFs are only defined for positive singular values, $(d_\mu)_{bj} \neq 0$. For basis sets that are appropriate for the calculation of polarizabilities (discussed at length later), the number of fragment virtual orbitals is considerably larger than the number of fragment occupied

orbitals, and the subspace spanned by the FERFs is a small subset of the total virtual space. The number of FERFs is no larger than one FERF per considered field component per occupied orbital. Within this subspace, the response of the fragment to a weak field component of the given type is described exactly.

In this work, we consider three non-orthogonal FERF models for the polarization subspace for each fragment, A. First, the non-orthogonal dipole type, nD:

$$\mathbf{R}^{nD}_{POL,A} = \mathbf{P}_A \oplus span\{\mathbf{V}_{\mu_x}, \mathbf{V}_{\mu_y}, \mathbf{V}_{\mu_z}\} \tag{3.5}$$

Second, the non-orthogonal dipole plus quadrupole type, nDQ (using spherical harmonic indices):

$$\begin{aligned}\mathbf{R}^{nDQ}_{POL,A} = span\{ \quad & \mathbf{R}^{nD}_{POL,A}, \mathbf{V}_{Q_{2,-2}}, \\ & \mathbf{V}_{Q_{2,-1}}, \mathbf{V}_{Q_{2,0}}, \mathbf{V}_{Q_{2,1}}, \mathbf{V}_{Q_{2,2}}\}\end{aligned} \tag{3.6}$$

Third and most demanding, the non-orthogonal dipole plus quadrupole plus octupole type, nDQO:

$$\begin{aligned}\mathbf{R}^{nDQO}_{POL,A} = span\{ \quad & \mathbf{R}^{nDQ}_{POL,A}, \mathbf{V}_{O_{3,-3}}, \\ & \mathbf{V}_{O_{3,-2}}, \mathbf{V}_{O_{3,-1}}, \mathbf{V}_{O_{3,0}}, \\ & \mathbf{V}_{O_{3,1}}, \mathbf{V}_{O_{3,2}}, \mathbf{V}_{O_{3,3}}\}\end{aligned} \tag{3.7}$$

It is clearly possible to continue this series of models, but arguments will be made for the preferred truncation later, based on test calculations. For spin unrestricted calculations, alpha and beta polarization subspaces of these types will in general be different. No reference has been made to atom-tagged AO functions in these FERF models, and the fragment SCF and CPSCF equations can be solved in an appropriately complete basis of any type.

3.2.2 Constrained Solutions for General Fragment Spans

Given vectors, $G^{\mu\,\bullet}_{\bullet\,A\lambda}$, for each fragment, A, spanning the fragment's polarization subspace, as defined by the projector $\mathbf{R}_{POL,A}$, one can obtain the polarized (SCFMI) determinant by solving one of the following slightly generalized non-linear eigenvalue problems for each fragment[64, 65] and for each spin. In the equations below, the subscript S denotes the formulation of Stoll[64]:

$$\begin{aligned}&[\mathbf{G}^T(\mathbf{1} - \mathbf{SP} + \mathbf{SP}^A_S)\mathbf{F} \\ &\times(\mathbf{1} - \mathbf{PS} + \mathbf{P}^A_S\mathbf{S})\mathbf{G}]_{AA}\mathbf{C}_A \\ &= [\mathbf{G}^T\mathbf{SG}]_{AA}\mathbf{C}_A\epsilon_A\end{aligned} \tag{3.8}$$

$$\begin{aligned}(P^A_S)^{\mu\nu} = &\sum_Z G^{\mu\,\bullet}_{\bullet\,Z\lambda}(T_Z)^{Z\lambda}_{\bullet\,Zj} \\ &\times \left((\sigma_{OO})^{-1}\right)^{ZjAi}(T^T_A)^{\bullet\,A\sigma}_{Ai\,\bullet}(G^T)^{\bullet\,\nu}_{A\sigma\,\bullet}\end{aligned} \tag{3.9}$$

and the subscript G is used to denote the Gianinetti[65] approach.

$$\begin{aligned}[\mathbf{G}^T(\mathbf{1}-\mathbf{SP}+\mathbf{SP}_G^A)\mathbf{F} \\ \times(\mathbf{1}-\mathbf{PS}+\mathbf{P}_G^A\mathbf{S})\mathbf{G}]_{AA}\mathbf{C}_A \\ =[\mathbf{G}^T(\mathbf{S}-\mathbf{SPS}+\mathbf{SP}_G^A\mathbf{S})\mathbf{G}]_{AA}\mathbf{C}_A\epsilon_A\end{aligned} \tag{3.10}$$

$$\begin{aligned}(P_G^A)^{\mu\nu}=\sum_{YZ}G^{\mu\,\bullet}_{\bullet\,Z\lambda}(T_Z)^{Z\lambda\,\bullet}_{\bullet\,Zj} \\ \times\left((\sigma_{OO})^{-1}\right)^{ZjAi}\left((\sigma_{OO})^{-1}\right)^{AiYk} \\ \times(T_Y^T)^{\bullet\,Y\sigma}_{Yk\,\bullet}(G^T)^{\bullet\,\nu}_{Y\sigma\,\bullet}\end{aligned} \tag{3.11}$$

In the above equations, the one-particle density matrix $\mathbf{P}$ is the projector into the occupied subspace,

$$\mathbf{P}=\sum_{XY}\mathbf{G}\mathbf{T}_X\left(\boldsymbol{\sigma}_{OO}\right)^{-1}\mathbf{T}_Y^T\mathbf{G}^T \tag{3.12}$$

$$\left(\boldsymbol{\sigma}_{OO}\right)_{XY}=\mathbf{T}_X^T\boldsymbol{\gamma}\mathbf{T}_Y \tag{3.13}$$

$$\boldsymbol{\gamma}=\mathbf{G}^T\mathbf{S}\mathbf{G} \tag{3.14}$$

and the Fock matrix, $\mathbf{F}$, is the derivative of the energy with respect to this occupied subspace projector:

$$F_{\mu\nu}=\frac{\partial E}{\partial P^{\mu\nu}} \tag{3.15}$$

$\mathbf{C}_A$ are the fragment coefficient matrices for the covariant molecular orbitals in the contravariant $\mathbf{G}$ basis with the occupied subset of these vectors denoted by $\mathbf{T}$ and the virtual subset denoted by $\mathbf{V}$. The $\mathbf{C}_A$ can be collected into a global matrix, $\mathbf{C}$, which is subspace-block-diagonal, analogous to the coefficient matrices in the original SCFMI scheme (for which $\mathbf{G}$, the matrix of subspace vectors in terms of the AO basis, is simply the identity matrix).

The projected Fock operators in the LHS of equations (3.8) and (3.10) can be extrapolated and diagonalized using the DIIS[67] algorithm with the following error vector for each fragment, A:

$$\begin{aligned}\mathbf{Err}_{AA}=\boldsymbol{\gamma}_{AA}\left[\boldsymbol{\gamma}^{-1}\mathbf{G}^T\mathbf{SPF}\left(\mathbf{PS}-\mathbf{1}\right)\mathbf{G}\right]_{AA} \\ -\text{Transpose}\end{aligned} \tag{3.16}$$

Alternatively, one can zero the gradient of the energy with respect to intra-subspace orbital rotation parameters, $\{\boldsymbol{\Delta}_A\}$ (which can also be collected into a global fragment-diagonal matrix, $\boldsymbol{\Delta}$):

$$\mathbf{C}_A\leftarrow\mathbf{C}_A\mathbf{U}_A=\mathbf{C}_A\,\exp\left(\boldsymbol{\Delta}_A-\boldsymbol{\Delta}_A^T\right) \tag{3.17}$$

$$
\begin{aligned}
C^{A\mu}_{\bullet\ As} \leftarrow C^{A\mu}_{\bullet\ Ar}\sigma^{A\bar{r}A\bar{t}}_{AA}[\\
+\sigma_{AtAs} + \Delta_{AtAs} - \Delta_{AsAt} \\
+\tfrac{1}{2}\Delta_{AtAu}\sigma^{A\bar{u}A\bar{v}}_{AA}\Delta_{AvAs} - \tfrac{1}{2}\Delta_{AtAu}\sigma^{A\bar{u}A\bar{v}}_{AA}\Delta_{AsAv} \\
-\tfrac{1}{2}\Delta_{AuAt}\sigma^{A\bar{u}A\bar{v}}_{AA}\Delta_{AvAs} + \tfrac{1}{2}\Delta_{AuAt}\sigma^{A\bar{u}A\bar{v}}_{AA}\Delta_{AsAv} \\
+O\left(\boldsymbol{\Delta}^3\right)]
\end{aligned}
\tag{3.18}
$$

$$
\begin{aligned}
\left.\frac{\partial E}{\partial \Delta_{ApAq}}\right|_{\boldsymbol{\Delta}=\mathbf{0}} &= \left.\frac{\partial E}{\partial P^{\mu\nu}}\frac{\partial P^{\mu\nu}}{\partial \Delta_{ApAq}}\right|_{\boldsymbol{\Delta}=\mathbf{0}} \\
&= 2[\delta^p_r\delta^q_i - \delta^p_i\delta^q_r] \\
\times \left[\sum_Z (\boldsymbol{\sigma}_{OO})^{-1}\mathbf{T}^T_Z\mathbf{G}^T\mathbf{F}\left(\mathbf{I}-\mathbf{PS}\right)\mathbf{G}\mathbf{C}_A(\boldsymbol{\sigma}_{AA})^{-1}\right]^{AiA\bar{r}}
\end{aligned}
\tag{3.19}
$$

for each subspace, A with one's non-linear solver of choice. Contravariant indices with bars ($A\overline{p}$) indicate that the index is not globally contravariant but rather contravariant with respect to the covariant metric for the given subspace (A). The gradient is subspace-blocked, and exponentiation of the corresponding displacements yields subspace-block-diagonal orthogonal (in the general non-orthogonal sense) orbital updates. We note that this gradient as written has occupied-occupied rotation dependence in addition to the usual occupied-virtual dependence if intra-subspace occupied-virtual orthogonality is not enforced (if the columns of $\mathbf{T}_A$ and $\mathbf{V}_A$ are not orthogonal). The subspace-block-diagonal vectors in $\mathbf{C}$, thus far only assumed to be intra-subspace linearly independent, can be chosen to be intra-subspace orthonormal ($\boldsymbol{\sigma}_{AA} = \mathbf{I}$) without loss of generality, resulting in slightly simpler expressions and algorithms.

In several calculations in this work, a quasi-Newton algorithm incorporating an approximate inverse Hessian (preconditioned L-BFGS)[103, 104] and the Newton-Raphson algorithm itself were employed to solve the SCFMI problem to obtain the polarized determinant. The Hessian for the SCFMI problem has been presented previously for different variables[64], and it is presented without the assumption of intra-subspace orthogonality for the orbital rotation parameters used in this work in the appendix (3.43) along with relevant intermediates. Additionally, in Section 3.5.4 we include a detailed discussion of our preconditioning strategy.

3.2.3 Orthogonal Polarization Subspaces

We next consider the construction of orthogonal fragment polarization subspaces that are based on the non-orthogonal subspaces discussed above. Orthogonalized models are a way to explore approximate bounds on the magnitude of polarization energy lowerings. They may be particularly appealing to those who, for one reason or another, consider carrying a metric to be heretical[105] and prefer instead the onus of the caveats that we now enumerate:

1. The construction of orthogonal projectors from non-orthogonal spans is not unique, and while it is possible to form these orthogonal subspaces in a way that is in some sense optimal, the corresponding merit function will always be arbitrary.

2. Orthogonal subspaces ascribed to fragments are not appropriate spans for describing the electronic structure of those fragments in isolation (except in the uninteresting limit where no orthogonalization is required).

3. If the number of degrees of freedom in the SCFMI problem is unchanged, then, while the orthogonal subspaces may seem more restrictive, all that can be said is that the degrees of freedom are *different*. SCFMI energies computed with arbitrary orthogonal subspaces therefore have no variational guarantee to be an upper bound to the energy computed with non-orthogonal subspaces of the same rank.

4. As an extreme example, the *exact* MO's (after localization) can be partitioned into orthogonal SCFMI subspaces such that the exact SCF energy could be obtained from the solution of the (albeit poorly) constrained SCFMI problem.

To avoid such pitfalls, we insist that the vectors after orthogonalization be justifiably tagged to a subspace. From the previous section, we already have a method to ascribe all polarization-relevant vectors in the system to *non-orthogonal* SCFMI subspaces. Hence an appropriately weighted symmetric orthogonalization[106] (3.20), which preserves fragment tagging by pairing each non-orthogonal vector with a single orthogonal counterpart, is a natural choice.

$$G^{\mu\,\bullet}_{\bullet\,A\lambda} \leftarrow \sum_{B} G^{\mu\,\bullet}_{\bullet\,B\rho} C^{B\rho\,\bullet}_{\bullet\,Br} \times \left[\mathbf{W}\left(\mathbf{W}\boldsymbol{\sigma}\mathbf{W}\right)^{-\frac{1}{2}}\right]^{Br\,\bullet}_{\bullet\,As} \tag{3.20}$$

For systems like water interacting with a sodium cation, minimal CT is expected, but inappropriate construction of the orthogonal subspaces could inhibit the water molecule from properly polarizing in response to the presence of the cation. The result would be an unduly large CT contribution to the interaction. To allow adequate water polarization with orthogonal subspaces, we could preserve the important water FERFs unmodified and orthogonalize the less vital sodium FERFs against them. To bring about this outcome in a black-box way, we will construct the weights such that FERFs deemed more important for polarization are given larger weights so that they are least deformed by orthogonalization. The resulting weights should create the greatest lower bound on the stabilization energy from polarization. Non-orthogonal FERFs contain exactly the degrees of freedom necessary for the fragment to relax in the presence of weak fields, and any modification of the FERF subspaces (such as orthogonalization) should impede this relaxation.

Orthogonalization necessitates that functions in one domain develop "tails" in other domains. Some systems could exploit such degrees of freedom during the polarization stage of the calculation to bring about delocalization of charge that would have otherwise occurred during the CT portion of the corresponding non-orthogonal calculation. This should only occur when there is a physical motivation for such mixings. For systems with very little CT, such as H_2O-Na^+, this premature delocalization of charge should only occur to a negligible extent even if the orthogonal subspace construction permits it. The question of whether this consequence of orthogonalization is problematic (giving overly large polarization energies when CT is important), must be assessed by test calculations.

In this work, the weight matrix is chosen to be diagonal with values between 1 and 100 to avoid poor conditioning of $\mathbf{W}\boldsymbol{\sigma}\mathbf{W}$ from an excessively large range of weights. The first step in generating the weights is the construction of intra-subspace mixing amplitudes, $(\mathbf{X}_A)_{VO}$, by considering the rotations necessary to solve the Stoll[64] equation (3.8) for each fragment and unique spin with fixed frozen orbital density and corresponding Fock operators[68, 107].

$$(\mathbf{F}_A)_{VO} + (\mathbf{F}_A)_{VV}\,(\mathbf{X}_A)_{VO} - (\mathbf{X}_A)_{VO}\,(\mathbf{F}_A)_{OO} - (\mathbf{X}_A)_{VO}\,(\mathbf{F}_A)_{OV}\,(\mathbf{X}_A)_{VO} = (\mathbf{0}_A)_{VO} \tag{3.21}$$

$$(\mathbf{F}_A)_{OO} = \left[\sum_{YZ}(\boldsymbol{\sigma}_{OO})^{-1}\mathbf{T}_Y^T\mathbf{G}^T\mathbf{F}_\mathbf{G}\mathbf{T}_Z(\boldsymbol{\sigma}_{OO})^{-1}\right]_{AA} \tag{3.22}$$

$$(\mathbf{F}_A)_{VO} = \left[\sum_{Z}\mathbf{V}_A^T\mathbf{G}^T\,(\mathbf{1}-\mathbf{SP})\,\mathbf{FGT}_Z(\boldsymbol{\sigma}_{OO})^{-1}\right]_{AA} \tag{3.23}$$

$$(\mathbf{F}_A)_{VV} = \left[\mathbf{V}_A^T\mathbf{G}^T\,(\mathbf{1}-\mathbf{SP})\,\mathbf{F}\,(\mathbf{1}-\mathbf{PS})\,\mathbf{GV}_A\right]_{AA} \tag{3.24}$$

In practice, the projected virtuals used for the amplitudes are on-fragment orthogonalized to remove any virtual vectors lying entirely in the occupied subspace. Singular value decomposition (SVD) of the amplitudes for each fragment (3.25) yields a single scalar for each orbital that describes, after transformation by the eigenvectors, the importance of that orbital for intra-subspace relaxations.

$$(\mathbf{X}_A)_{VO} = \mathbf{L}_A\mathbf{x}_A\mathbf{R}_A^T \tag{3.25}$$

In general, the amplitudes have different row and column dimensions, leaving some vectors with a weight of identically zero. In order to give all vectors non-zero weights, the non-zero singular values across all fragments are uniformly scaled such that the smallest non-zero singular value is 1. The vectors with exactly zero singular values are then given weight 1 such that they have the same importance as the least important vector with non-zero singular value. The weights are then forced to be in the range 1 to 100 while still preserving importance ordering by taking the weights associated with all vectors to the same power.

With the weights in hand, application of (3.20) is straightforward. This process is performed first for the occupied orbitals of the supersystem, providing a new definition of the occupied subspace of each fragment. The process is then repeated for the globally projected

and intra-subspace orthonormalized FERFs determined by the field responses, taking into account the newly defined, orthogonal fragment occupied subspaces in the construction of the amplitudes. The projection of virtual FERFs into the orthogonal complement of the global occupied subspace allows for the construction of orthogonal fragment subspaces without changing the supersystem occupied subspace projector from that of the frozen orbitals.

Because the occupied orbitals used to compute the weights for the virtual subspaces weighted symmetric orthogonalization are orthogonal, the linearized version of the amplitude equation (3.21) obtained by deleting the term quadratic in $(\mathbf{X}_A)_{VO}$ yields the same equation for the amplitudes used previously to construct a compact set of orthogonal functions for polarization, polMOs[69]. While the intra-subspace amplitudes are determined using the same expressions, there are important differences between the current procedure and that which defines the polMOs. Notably, in the polMO procedure, amplitudes are computed using fragment-tagged occupied and virtual vectors with a collective span equal to that of all atom-centered AO basis functions on the fragment. Moreover, only eigenvectors with non-zero singular values are included in the weighted symmetric orthogonalization, and the singular values associated with these vectors are used directly as the weights. Thus, the treatment of weights and the spans that are considered for orthogonalization are different. Furthermore, the polMO procedure relies on atom-centered basis functions to define fragment subspaces for amplitude construction.

The variational polarization of a system with orthogonal fragment subspaces can be performed using a simplified version of the Stoll[64] and Gianinetti[65] eigenvalue equations as described previously[69]. Alternatively, one can use the above gradient and Hessian equations (Section 3.5.4) for Newton or quasi-Newton methods with $\boldsymbol{\gamma} = \boldsymbol{\sigma} = \mathbf{I}$.

3.2.4 Delineation Between Polarization and Charge Transfer

One consequence of using both the general, non-orthogonal and orthogonalized versions of the FERFs is that fragment populations as computed by the traditional AO Mulliken scheme can change during self-consistent polarization. This was not the case for the original, atom-centered AO basis scheme[17, 99]. However, charges are preserved by a modified Mulliken definition where instead of tracing fragment-diagonal blocks of the contravariant-covariant density matrix in the AO basis, one instead traces the contravariant-covariant density matrix in the basis of the columns of $\mathbf{G}$ defining the polarization subspace of each fragment. Again, the original SCFMI-based EDA result is recovered for $\mathbf{G} = \mathbf{I}$.

A notable special case occurs when non-orthogonal FERFs are computed using only the AO functions from that fragment, which is the way they are later employed in production calculations. In this case, there is also no charge flow during polarization by the traditional Mulliken definition as the non-orthogonal FERF polarization subspaces are exact subsets of the original SCFMI polarization subspaces. Another special case arises when one of the orthogonal schemes is used. In this case, both the modified Mulliken and comparably modified Löwdin schemes will compute no inter-fragment charge flow during polarization.

The population conserving character of the SCFMI degrees of freedom by a modified Mulliken-like definition is the basis for the interpretation of the intra-subspace relaxations in the polarization step as excluding charge transfer interactions; however, the SCFMI-based schemes are not the only ones that can make this claim. The density-based EDA of Wu[51, 75] likewise conserves fragment populations during the polarization stage of the calculation though by a real-space partitioning of charges. We shall show that the distinction between these two flavors of variational polarization goes well beyond the definition of the chosen population scheme. SCFMI-allowed rotations are not only population conserving but also what we will refer to as charge-flow-prohibiting. Charge-flow-prohibiting rotations are a subset of the population conserving rotations, all of which are allowed in Wu's constrained-DFT-based decomposition.

The remainder of this section is structured as follows. First, we will show in a more involved but instructive way that SCFMI rotations are population conserving. Next, we will introduce the full SCF degrees of freedom into the SCFMI objective function by the construction of linearly dependent subspaces and identify the form of displacements utilizing these additional degrees of freedom that are likewise population conserving. Finally, we will discuss the interpretation of these population conserving but not charge flow prohibiting displacements as they relate to polarization and charge transfer.

The population of a domain, A, by a generalized Mulliken definition is:

$$\mathrm{Pop}_A = \left[\mathbf{S}\mathbf{P}_A\mathbf{S}\right]_{\mu\nu} P^{\mu\nu} \tag{3.26}$$

where we define:

$$P_A^{\lambda\sigma} = \sum_X M^{\lambda}_{\bullet\, A\tilde{\pi}} \mu^{A\tilde{\pi}X\tilde{\beta}} (M^T)^{\bullet\, \sigma}_{X\tilde{\beta}\, \bullet} \tag{3.27}$$

$$\mu_{A\tilde{\pi}X\tilde{\beta}} = (M^T)^{\bullet\, \lambda}_{A\tilde{\pi}\, \bullet} S_{\lambda\sigma} M^{\sigma}_{\bullet\, X\tilde{\beta}} \tag{3.28}$$

The usual AO Mulliken scheme is recovered with $\mathbf{M} = \mathbf{I}$. The operator $\hat{P}_A$ is neither a projector nor symmetric except when the columns of $\mathbf{M}$ are orthogonal. The change in the population of domain A due to SCFMI-like displacements, $\mathbf{D} = [\mathbf{D}_A, \mathbf{D}_B, ...]$, can be written as:

$$\begin{aligned} \Delta\mathrm{Pop}_A = &\sum_X \mathbf{D}_X \cdot \left.\frac{\partial \mathrm{Pop}_A}{\partial \boldsymbol{\Delta}_X}\right|_{\boldsymbol{\Delta}=\mathbf{0}} \\ &+ \sum_{XY} \frac{1}{2}\mathbf{D}_X \cdot \left.\frac{\partial^2 \mathrm{Pop}_A}{\partial \boldsymbol{\Delta}_X \partial \boldsymbol{\Delta}_Y}\right|_{\boldsymbol{\Delta}=\mathbf{0}} \cdot \mathbf{D}_Y + O(\mathbf{D}^3) \end{aligned} \tag{3.29}$$

The first (3.53) and second (3.54) derivatives of populations with respect to the SCFMI parameters, $\boldsymbol{\Delta}_X$, can be found in the appendix along with the relevant intermediates. If $\mathbf{M} = \mathbf{G}$, corresponding to the modified Mulliken definition discussed above, it can be shown that both the population gradient and Hessian with respect to SCFMI rotations are zero

(Section 3.5.5), yielding by (3.29) constant populations through second order in SCFMI displacements.

We now construct linearly dependent SCFMI subspaces, $A', B', ...$, (the above equations do not require any particular relationship among the vectors $\mathbf{G}$ defining different subspaces beyond that it be possible to construct a nonsingular occupied subspace metric) such that each occupied orbital is able to mix with every other orbital, the full degrees of freedom in unconstrained SCF. The distinction is that, in the linearly dependent SCFMI case, independent displacements are made on a number of Grassmann manifolds equal to the number of subspaces instead of only one, and the difficulties associated with these redundant and less connected degrees of freedom are shifted into the objective function with variable occupied subspace metric.

$$span\{\mathbf{G}]_{A'}\} = span\{\mathbf{M}]_A, \mathbf{M}]_B, \mathbf{M}]_C, ...\} \tag{3.30}$$

$$\begin{aligned}(C_{A'})^{\nu\,\bullet}_{\bullet\,A'r} &= G^{\nu\,\bullet}_{\bullet\,A'\pi}(C_{A'})^{A'\pi\,\bullet}_{\bullet\,A'r} \\ &= \sum_X M^{\nu\,\bullet}_{\bullet\,X\tilde{\rho}}(C_{A'})^{X\tilde{\rho}\,\bullet}_{\bullet\,A'r}\end{aligned} \tag{3.31}$$

We have used the notation $\mathbf{X}]_Y$ to indicate the columns of the matrix $\mathbf{X}$ with label Y.

For the purposes of this discussion, we will consider a specific initial condition where the orbitals in each subspace are written as follows:

$$\begin{aligned}(C_{X'})^{\mu\,\bullet}_{\bullet\,Z\hat{s}} = \\ \left[\delta^\mu_\lambda - \left(\delta^\mu_\sigma - \delta^\mu_\sigma\delta^X_Z\right)\Phi^{\sigma\nu}_X S_{\nu\lambda}\right] \\ \times M^{\lambda\,\bullet}_{\bullet\,Z\tilde{\gamma}}(C_Z)^{Z\tilde{\gamma}\,\bullet}_{\bullet\,Zs}\end{aligned} \tag{3.32}$$

$$\Phi^{\sigma\nu}_X = M^{\sigma\,\bullet}_{\bullet\,X\tilde{\alpha}}(\mu^{-1}_{XX})^{X\tilde{\alpha}X\tilde{\beta}}M^{\nu\,\bullet}_{\bullet\,X\tilde{\beta}}$$

The vectors $(C_Z)^{Z\tilde{\gamma}\,\bullet}_{\bullet\,Zs}$ span the same space as the columns $\mathbf{M}]_Z$ and are thus of the same form as the MOs for subspace Z in a $\mathbf{G} = \mathbf{M}$ SCFMI calculation. The hat notation, $Z\hat{s}$, in the coefficients, $(C_{X'})^{\mu\,\bullet}_{\bullet\,Z\hat{s}}$, has been introduced to carry along Mulliken-domain-based tags from the $\mathbf{G} = \mathbf{M}$ SCFMI subspace Z to the linearly dependent SCFMI subspace X'. The MOs in subspace X' are in general of the form (3.31), but the Mulliken-domain attribution of the columns of $(C_{\alpha,X'})^{\mu\,\bullet}_{\bullet\,X's}$ by (3.32) will allow us to identify the form and character of the new degrees of freedom in the linearly dependent SCFMI.

Vectors of the form $(C_{\alpha,X'})^{\mu\,\bullet}_{\bullet\,Z\hat{s}}$ are virtuals in linearly dependent SCFMI subspace X' if $X \neq Z$, and these vectors, by (3.32), are in the orthogonal complement of the $\mathbf{G} = \mathbf{M}$ SCFMI subspace X. This means that rotations involving the $(C_{X'})^{\mu\,\bullet}_{\bullet\,Z\hat{s}}(X \neq Z)$ are explicitly new degrees of freedom for linearly dependent subspace X' relative to those of X. A consequence of this choice is that the subspace metric for X', $\boldsymbol{\sigma}_{X'X'}$, and thus its inverse are block-diagonal:

$$(\sigma_{X'X'})_{X\hat{r}Z\hat{s}} = \delta^X_Z(\sigma_{X'X'})_{X\hat{r}X\hat{s}} \tag{3.33}$$

Moreover, by (3.32), vectors previously in subspace X are duplicated in subspace X', which means that SCFMI subspaces X and X' can and do have all occupied vectors identical at our initial condition. This establishes the connection between primed and unprimed subspace counterparts, and their indices should be assumed to be coupled in expressions in which they both appear. We note that in order to maintain these Mulliken-based labels for general Mulliken subspaces, orthogonality of the MOs in each linearly dependent SCFMI subspace, X', is not assumed.

In this notation, the degrees of freedom in A' corresponding to those in A, all of which have already been shown to be population conserving, are of the form $(\Delta_{A'})_{A\hat{p}A\hat{q}}$, and because of the way in which the vectors spanning A' were constructed ((3.32) and (3.33)), they remain population conserving by (3.29) after introducing the new degrees of freedom (Section 3.5.6). New variables are of the form $(\Delta_{A'})_{A\hat{i}B\hat{s}}$ because our parametrization has no virtual-virtual rotation dependence and because all occupied orbitals in A' at the initial condition have Mulliken-domain tag A. These new variables will be referred to as delocalization degrees of freedom. It is important to note that vectors written $B\hat{i}$ in A' are virtual vectors for subspace A' despite the occupied index.

With the form of the new degrees of freedom identified and the old degrees of freedom verified to remain population conserving, it is clearly possible to write the change in population to second order in terms of delocalizing displacements (3.29) for a general, non-orthogonal Mulliken partitioning (Section 3.5.6); however, such a cumbersome expression is not apt for the current purpose. To facilitate interpretation, we will analyze the case where the columns of $\mathbf{M}$ are orthogonal, and thus $\boldsymbol{\sigma}_{OO}$, $\boldsymbol{\sigma}_{XX}$, $\boldsymbol{\sigma}_{X'X'}$, and $\boldsymbol{\mu}$ are or can be chosen without loss of generality to be $\mathbf{I}$. In this case, the change in population to second order is:

$$\Delta\mathrm{Pop}_A = \sum_{X'} \sum_{Z\neq X} \sum_{\hat{i}\hat{a}} [(D_{X'})_{X\hat{i}Z\hat{a}}]^2 [\delta_A^Z - \delta_A^X] \tag{3.34}$$

The displacements that zero (3.34) for all A are delocalizing but also population conserving for small displacements, and it is clear from this expression that there are many delocalizing rotations that produce no net change in populations through second order. If we consider a system with only two Mulliken domains, A and B, then by conservation of total population we need only satisfy:

$$0 = \sum_{\hat{i}\hat{a}} [(D_{B'})_{B\hat{i}A\hat{a}}]^2 - [(D_{A'})_{A\hat{i}B\hat{a}}]^2 \tag{3.35}$$

and the physical interpretation is that charge flows from domain A into domain B, but an equal amount of charge flows from domain B into domain A.

We do not see these sorts of delocalizations as polarization in character but rather as contributing to the kinetic energy lowering associated with inter-fragment orbital or bonding interactions. We emphasize that methods that merely constrain populations like those based on constrained DFT allow all population conserving rotations including some of those that we

have termed delocalizing. In SCFMI-based schemes, only charge-flow-prohibiting rotations contribute to polarization, and all delocalization degrees of freedom - population conserving though they may be - are treated collectively as charge transfer contributions.

An important class of systems that highlights the difference between the two approaches to polarization are those in which all fragments are equivalent by symmetry. Meaningful population schemes should respect the point group symmetry of the system, as must the unconstrained density. Thus, if the fragments are all constrained to have the same charge, then schemes that allow all population conserving rotations must then yield identically zero "charge transfer" contribution! SCFMI-based schemes that only allow charge-flow-prohibiting rotations do not enforce this trivial solution for CT, although it may still be zero for other reasons. The case of high symmetry systems is merely an extreme example of complexes where the forward and back donation of electrons is not well described by their signed sum. Thus, this distinction between the two approaches is expected to be quite relevant beyond model systems.

We note that Misquitta[84] also discusses the imprecision of the label "CT" with a preference instead for the term delocalization. We agree with this interpretation; however, to avoid unnecessary confusion, we will continue to use the term charge transfer to describe the energy lowering associated with the delocalization degrees of freedom. Possible further decompositions along these lines within the CT term are beyond the scope of this work.

3.2.5 Treatment of Charge Transfer and Basis Set Superposition Error

With new schemes for polarization defined and the frozen energy unaltered, it remains to discuss the treatment of the final component of energy lowering, charge transfer, in light of these modifications. In this work we employ only the subtractive approach in which the charge transfer energy lowering is computed as the difference between the energy of the optimal subspace-rotation-constrained determinant and the fully optimized supersystem determinant, guaranteeing recovery of the total binding energy. Note that the tools developed for decomposing charge transfer interactions in the original ALMO[17] scheme are not directly applicable here if one seeks to recover the full binding energy or a perturbative approximation thereof because not all vectors in the supersystem have been assigned to a fragment. The development of modified approaches will be a focus of future work.

If isolated fragments are computed with only their respective AO basis sets, then there will be a non-zero basis set superposition error (BSSE) contribution to the interaction energy. BSSE was problematic for SCFMI-based EDA schemes previously because the diffuse basis sets required to make BSSE negligible had to be avoided to ensure that the polarization and CT terms remained meaningful. With these new FERF schemes, creating fragment-ascribable subspaces is no longer an issue, and large basis sets that do not require BSSE corrections can be employed. For systems with many fragments, the ability to compute

responses fragment by fragment (without using the global basis) is an immense computational advantage.

3.3 Results and Discussion

3.3.1 Computational Details

Calculations in this work were performed with a development version of QChem [70, 108], which was extensively modified to implement the non-orthogonal FERF (using fragment blocking) and orthgonalized FERF models for describing polarization. Because multiply augmented Dunning basis sets have not been defined for all of the elements used in this work, multiply augmented basis sets were constructed for all atoms systematically from Dunning[109, 110] aug-cc-pVXZ basis sets by the addition of one primitive per angular momentum with an exponent half the size of the next smallest primitive exponent for that angular momentum. Multiply augmented functions used in this work are thus slightly less diffuse than those in parametrized basis sets; however, this allows for basis sets of larger rank to be used before encountering severe linear dependencies. Though the method can be used with any density functional, the B3LYP[6–8] functional is used throughout this work as it is in common use and its second functional derivatives are available to us. Additionally its deficiencies for intermolecular interactions relate to dispersion-dominated interactions, which are not of interest here. It should be noted that, for functionals with density-independent corrections (for example, dispersion-corrected functionals of the D2 or D3 type[3, 4]), the binding energy associated with these corrections resides in the frozen orbital energy term. While the systems analyzed in this work are dimers, this method can treat a cluster of an arbitrary number of fragments either directly or by means of a many-body expansion of arbitrary order.

3.3.2 Assessment of Non-Orthogonal Fragment Electric Field Response Functions (FERFs)

The new methods for constructing the FERFs do not depend on the use of atom-centered basis functions. However, because our molecular electronic structure code[70, 108] is based on gaussian AOs, we do in fact employ these standard quantum chemistry basis sets to demonstrate basis set convergence and assess both behavior and feasibility of these models. We compute FERF spans using only the given fragment's AO functions and not the entire supersystem basis as the goal is to identify basis sets capable of describing both the ground state density as well as the field responses. Hence the FERF polarization energies are variationally guaranteed to be less than or equal in magnitude compared to the corresponding ALMO polarization energies.

Figure 3.2a shows the basis set convergence of the polarization energy of the original ALMO and the new non-orthogonal FERF models, for the water dimer. It is clear from Figure 3.2a that ALMO does not converge at all in the basis set sequences examined. By contrast, the new FERF-based models do converge towards basis set limits which are characteristic of each model. Whilst the nD model is clearly converged at the aTZ basis, larger basis sets are required to converge the higher order FERF models, particularly the nDQO model. For the smallest basis sets considered (e.g. TZ), the response schemes produce polarization energies that are quite similar to the ALMO result, primarily due to basis set deficiencies.

Some general observations about convergence of the FERF models can be made. For atoms, each multipole response order requires basis functions of one higher angular momentum relative to that of the highest momentum valence orbital (eg. p-orbitals allow s-orbitals to respond to a dipole field, and d-orbitals allow s-orbitals to respond to a quadrupole field). The analogous response pairs are less clear for molecular fragments where functions of higher angular momentum than an atom's valence are necessary to describe the chemical environment (i.e. d functions for the water molecule). However the behavior is analogous: referring again to Figure 3.2a, basis set convergence is achieved for nD at triple zeta, nDQ at quadruple zeta, and nDQO at quintuple zeta provided sufficiently diffuse functions are included.

Given the increasing difficulty in converging the nD, nDQ, and nDQO models with respect to basis set, it is preferable to use lower order models if they are qualitatively correct on approaching the non-overlapping regime. It is also clear from Figure 3.2a that the progression of FERF model subspaces to high multipole orders will eventually develop the flexibility and thus the problems of the ALMO model itself. For this reason also, we would like to choose the smallest FERF model that is capable of a correct description of long-range polarization.

To this end, we investigated the distance dependence of the polarization energy of the FERF models and the original ALMO scheme for the dissociation of the water dimer along the O-O coordinate (Figure 3.2b). The d-aug-cc-pVQZ basis was chosen because it is one of the smallest to display clear differences in polarization energies for all methods at R_e. The polarization energies all appear fairly similar past R_e and at first seem only to distinguish themselves at compressed distances where there is no a priori correct answer.

To further differentiate the models, we investigated the polynomial decay (Figure 3.3) that they yield for the polarization energy for the water dimer (asymptotically an R^{-6} dipole induced-dipole interaction). Figure 3.3a shows the polynomial decay in the overlapping regime, highlighting again the considerable differences in the models for short intermolecular distances. In the long-range (Figure 3.3b), all methods approach but do not reach the R^{-6} limit before numerical difficulties set in at large R_{OO}. Evidently higher order polarization terms (e.g. quadrupole-induced dipole) are not yet negligible at these separations. Nonetheless, the interfragment overlaps are small enough that we can view the most variationally flexible method, ALMO, as the correct answer. This is because, in the long range, charge transfer is zero, and, because our model chemistry lacks a description of long-range elec-

tron correlation, all binding beyond the permanent electrostatic interaction (described by the ALMO frozen energy term) is the exact polarization energy of the classical polarization theory within this model chemistry. In the case of a model chemistry that does include long-range electron correlation, such as in the case of the exact exchange-correlation functional itself, deviations from the classical polarization theory will arise due to ALMO's effective partitioning of the polarization-dispersion cross terms of the classical polarization theory into separate contributions. A thorough treatment of inter-fragment electron correlation contributions to binding within the framework of SCFMI-based EDA is beyond the scope of this work but will be addressed in a future publication. The inability of a FERF model to reproduce the exact ALMO result in the long range thus indicates that it is inadequate for the description of polarization in the molecular field, which is more complicated than a simple field or field gradient.

Based on Figure 3.3b, the distance dependence of the polarization energy as computed by the nDQ and nDQO models is the same as that of ALMO while nD, which has the least variational flexibility to describe polarization, behaves qualitatively differently from the rest. From this data it would seem that the nD model is potentially inadequate for describing the polarization of molecular systems, and thus nDQ is the simplest FERF model with sufficient accuracy.

We also investigated the convergence of the polarization energy computed by the various non-orthogonal models as a function of basis set cardinal number (i.e. X in aug-cc-pVXZ) for the ammonia dimer (Figure 3.4a) and methane interacting with a sodium cation (Figure 3.4b). The ammonia dimer results (Figure 3.4a) show that the nD model is acceptably converged at aug-cc-pVTZ, nDQ by aug-cc-pVQZ, and nDQO likely by aug-cc-pV5Z based on the water results above employing more diffuse functions. The angular momentum needs for the polarization of methane in response to a sodium cation (Figure 3.4b) are by comparison less severe with nD, nDQ, and nDQO all converged by aug-cc-pVQZ.

We analyzed the distance dependence of the polarization models for the qualitatively different CH_4-Na^+ interaction (Figure 3.5) in the aug-cc-pVQZ basis, which was shown to be sufficient to converge all considered FERF models at equilibrium. The polarization energies computed at compressed distances are not dramatically different for this system, likely because there is little legitimate charge transfer that unduly flexible polarization subspaces could attempt to describe. Figure 3.6 shows the exponent computed for the polynomial decay of the various polarization models throughout the C-Na coordinate. The nD model distinguishes itself from the others both in the short-range (Figure 3.6a) and in the long-range (Figure 3.6b) which asymptotes to R^{-4}, a monopole induced-dipole interaction. All models closely approach R^{-4} decay before polarization energies become too small to compute reliably. As for the water dimer, the nD model behaves qualitatively differently from the others, while both nDQ and nDQO closely track the ALMO results, which should be the correct result at these large separations. Thus, nDQ is again the simplest model with sufficient flexibility to describe the long-range polarization.

We emphasize that, unlike the original ALMO scheme, the new FERF models do have a

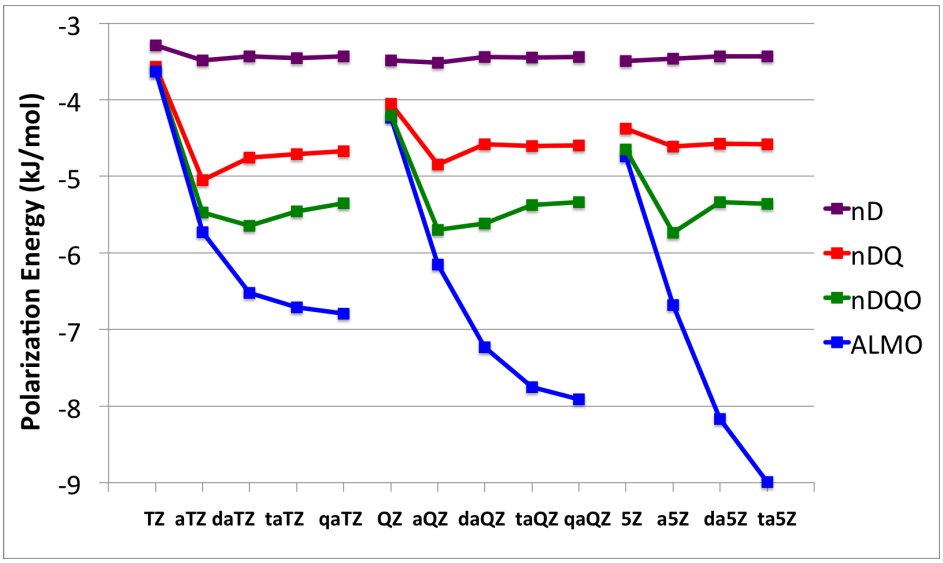

(a)

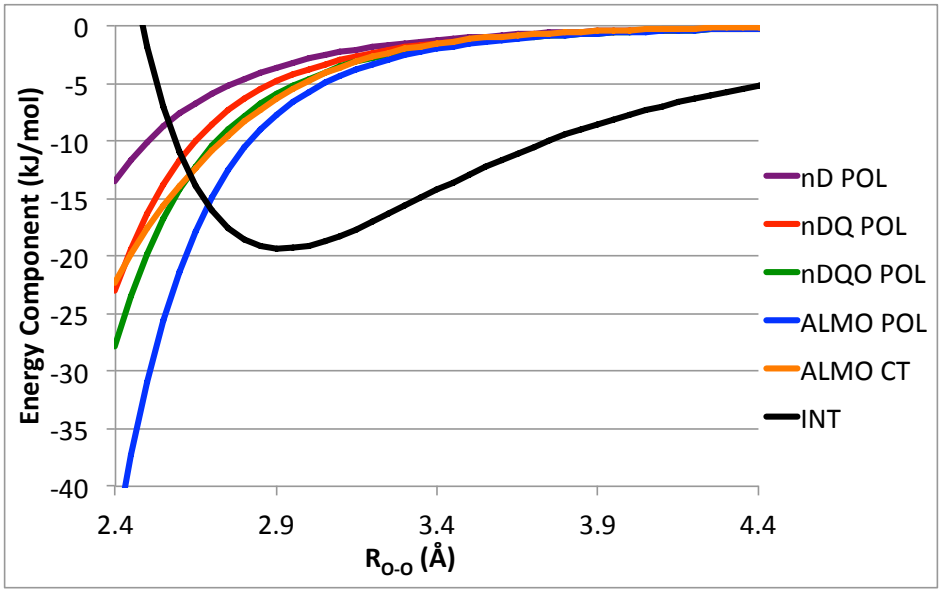

(b)

Figure 3.2: Basis set convergence (a) at R_e ($R_{O\text{-}H}$ = 1.96 Å) and distance dependence (b) of the polarization energy computed by ALMO and FERF models for the B3LYP/aug-cc-pVQZ optimized water dimer. The upper panel, (a), shows that the FERF polarization energies converge to useful basis set limits, which the ALMO model cannot achieve. The lower panel, (b), shows the distance dependence of B3LYP/d-aug-cc-pVQZ ALMO and FERF polarization energies, the total interaction energy (INT) and the ALMO charge transfer (CT) energy for rigid dissociation along the O-O coordinate. While similar at R_e and beyond, the polarization models produce considerably different results at compressed geometries.

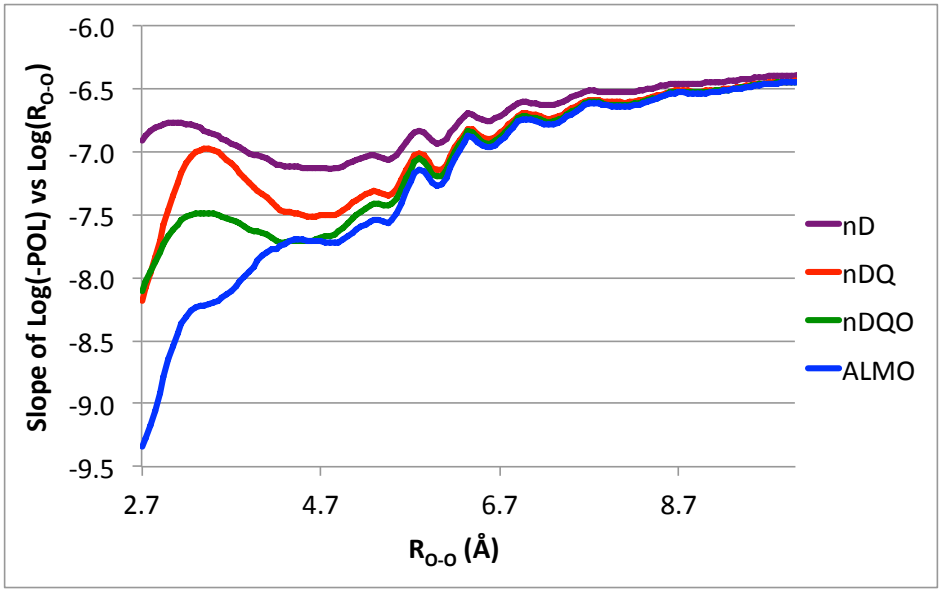

(a)

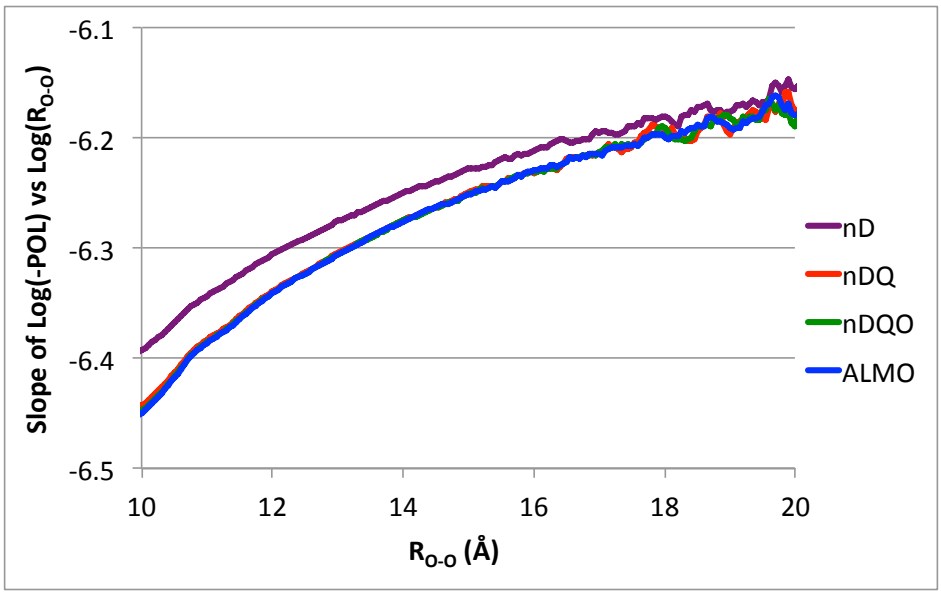

(b)

Figure 3.3: Polynomial decay of the polarization energy computed using B3LYP/d-aug-cc-pVQZ ALMO and FERF models for the rigid dissociation along the O-O coordinate of the aug-cc-pVQZ/B3LYP optimized water dimer. The slope at point R was computed by linear regression of the log(-POL) vs. $\log(R_{O\text{-}O})$ plot for the closest 11 points within 0.25Å of R_{O-O}. The upper panel (a) contains results at shorter O-O separations, demonstrating the different character of the ALMO and FERF models at these distances. The lower panel (b) shows results at longer distances, where the R_{O-O}^{-6} asymptote is approached but not reached before numerical difficulties associated with very small polarization energies arise. Only the least flexible nD model fails to achieve the correct ALMO limiting behavior.

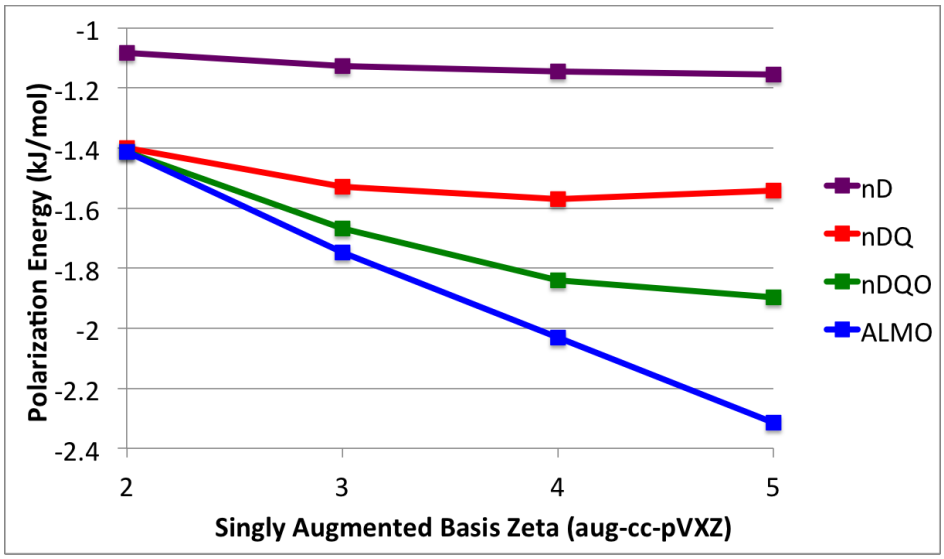

(a)

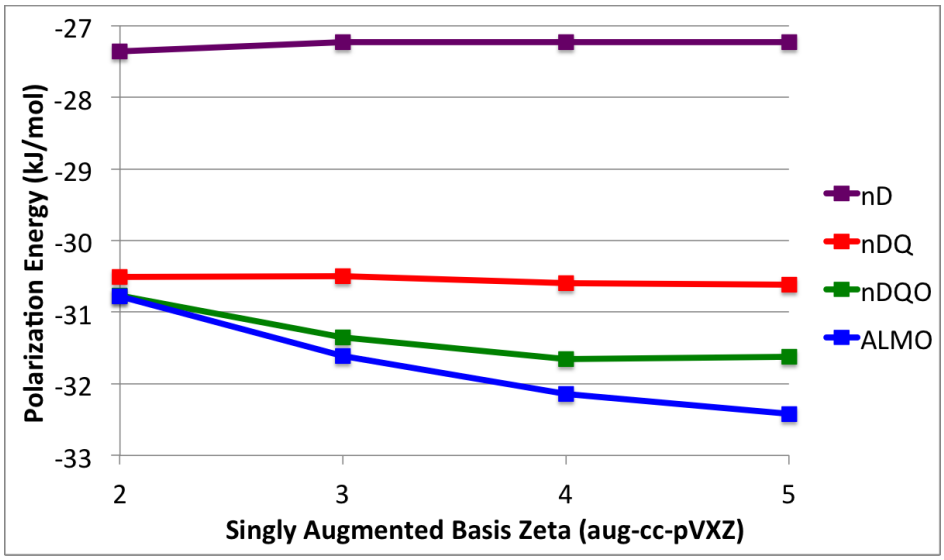

(b)

Figure 3.4: Basis set convergence of B3LYP/aug-cc-pVXZ polarization energies with respect to cardinal number, X, for the ammonia dimer (upper panel, (a)), and the methane-Na^+ complex (lower panel, (b)), both at their B3LYP/aug-cc-pVQZ optimized geometries. Due to the lack of an aug-cc-pV5Z basis set for sodium, the aug-cc-pVQZ basis was used for Na^+ only in the aug-cc-pV5Z calculations.

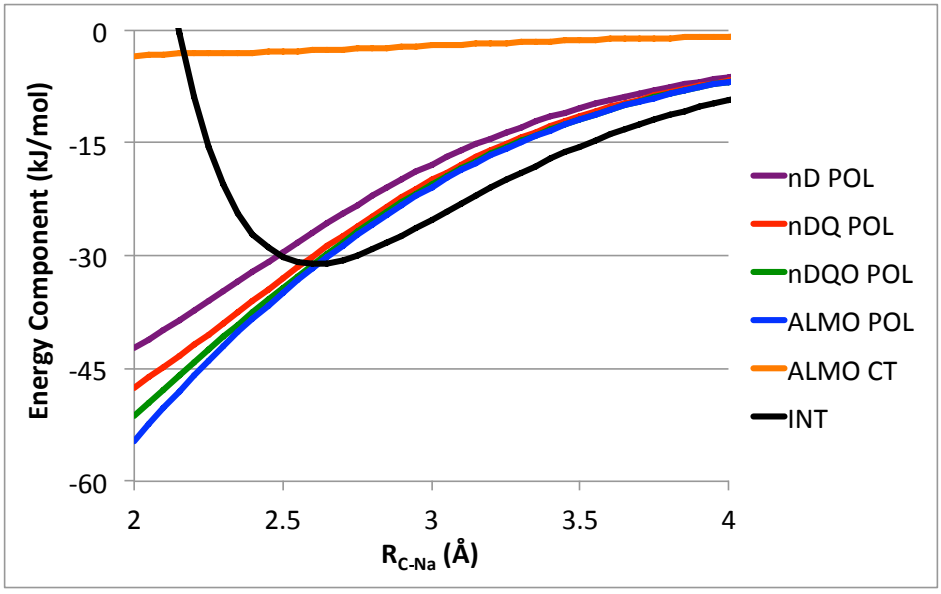

Figure 3.5: B3LYP/aug-cc-pVQZ polarization energies by ALMO and FERF models along with total interaction energy (INT) and ALMO charge transfer (CT) contributions for the rigid dissociation of methane-Na^+ along the C-Na coordinate, where the methane fragment is aug-cc-pVQZ/B3LYP optimized.

basis set limit, and it is moreover achievable. Higher order field response models partition more of the single particle space into fragment-ascribable subspaces with the unwanted consequences of (i) larger basis sets to converge these larger subspaces, as well as (ii) expected ALMO-like behavior of high order models. With this in mind, we recommend the nDQ model as the change in qualitative behavior as well as the computed polarization energy when going from nD to nDQ is palpable while the change in going from nDQ to nDQO seems insufficiently large to justify the increased ambiguity in distinguishing inter- and intra-fragment rotations or the increased cost. The aug-cc-pVQZ basis has been shown to be quite adequate for the nDQ model (aug-cc-pVTZ is nearly adequate), and so QZ basis sets will be used for the DQ models in the remainder of this work.

3.3.3 Assessment of Orthogonalized FERF Models

With a model based on responses to weak fields and field gradients decided (FERF/nDQ), we now consider the orthogonalized variant of this scheme. Our first test is the water dimer. The polarization energy lowerings as computed by the nDQ, oDQ, and ALMO models as a function of augmentation of the cc-pVQZ basis are shown in Figure 3.7. Both the nDQ and oDQ methods yield acceptably converged values at the level of single augmentation though more stringently at double augmentation. Moreover, for all levels of augmentation

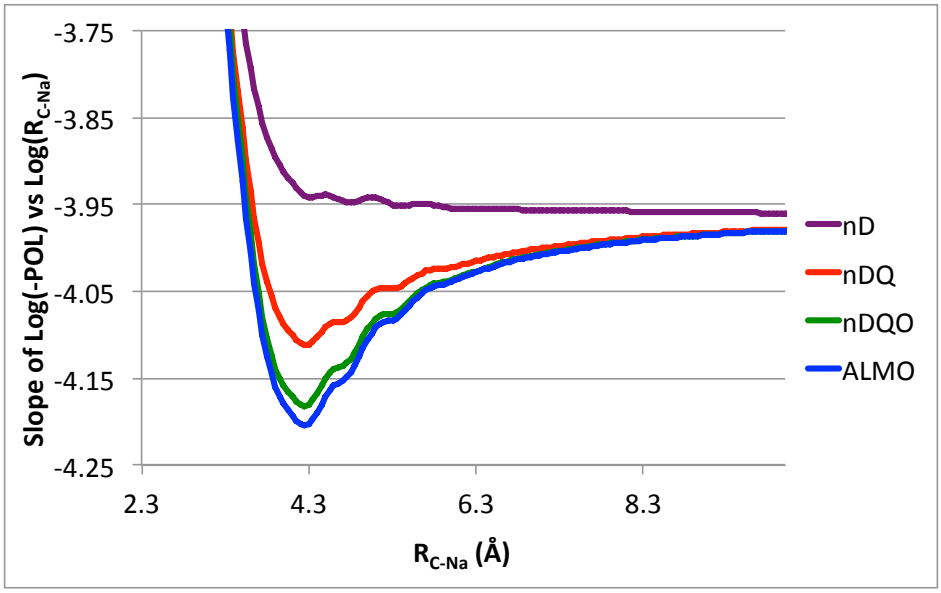

(a)

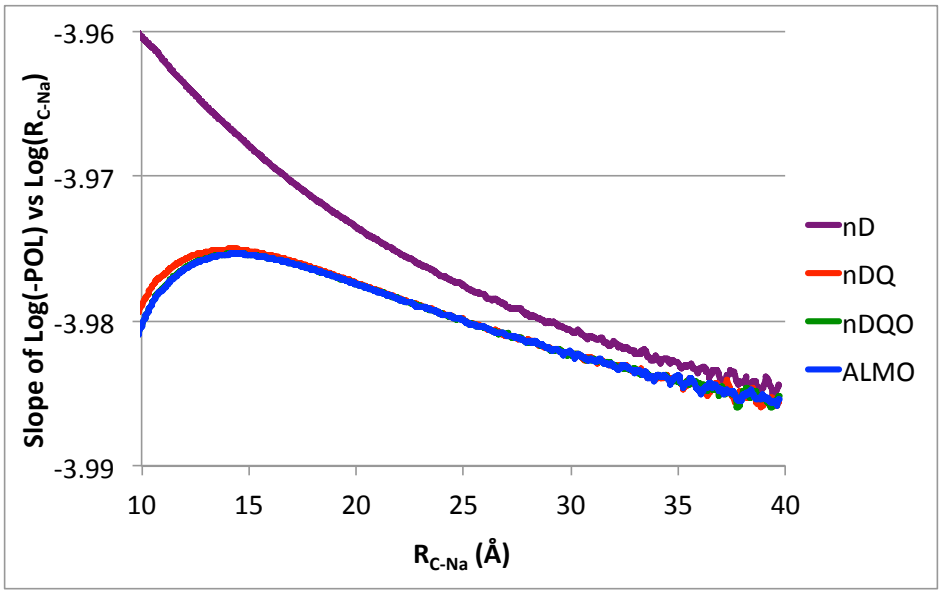

(b)

Figure 3.6: Polynomial decay of the B3LYP/aug-cc-pVQZ polarization energy computed using ALMO and FERF models for rigid dissociation of methane-Na^+ along the C-Na coordinate, as in Figure 3.5, with slopes computed as in Figure 3.3. The upper panel (a) shows polynomial decay of polarization terms for shorter C-Na separations, while the lower panel (b) contains longer range data. In both cases there is a clear difference between the nD model and all others.

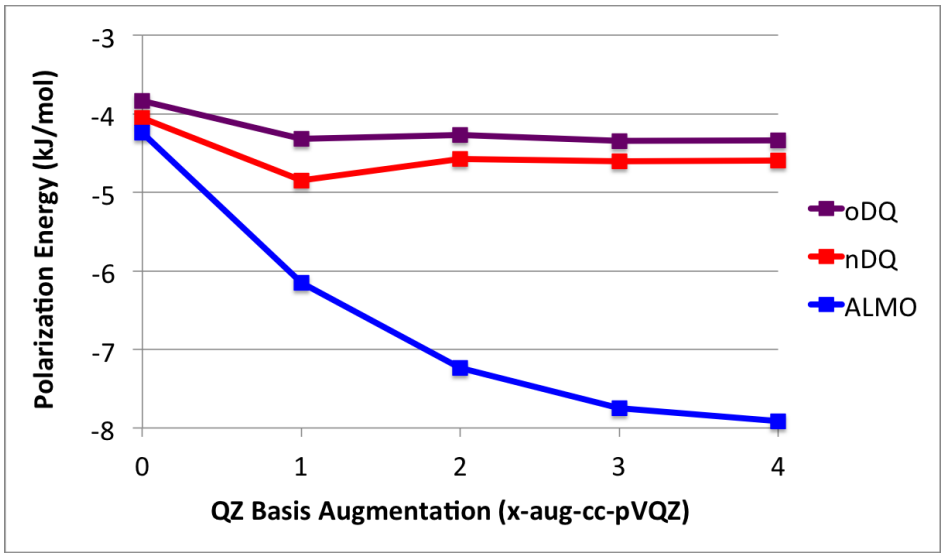

Figure 3.7: Convergence with respect to basis augmentation of ALMO and FERF polarization energies computed using B3LYP for the B3LYP/aug-cc-pVQZ optimized water dimer.

considered, the oDQ polarization energy lowering is fairly close to but never exceeds that computed by the nDQ model. The gap is less than 1kJ/mol, which may then be viewed as the difference in predictions between the orthogonalized and non-orthogonalized models in the moderately overlapping regime. It is encouraging that this difference is small compared to the magnitude of the nDQ polarization interaction (indeed it is smaller than the nD vs nDQ difference discussed in the previous section). Of course there is no difference between the orthogonal and non-orthogonal FERF variants in the non-overlapping regime.

These same methods have been applied to the water-Na^+ system that was used to motivate the weight matrix construction, (Figure 3.8a), as well as to the much stronger water-Mg^{2+} interaction (Figure 3.8b). Both systems show good convergence for the FERF models by aug-cc-pVQZ with over 90% of the nDQ polarization energy lowering recovered by the orthogonal variant, yielding a qualitatively consistent interpretation of the interactions as being polarization dominated in both schemes. While larger than the very small values seen in the ALMO scheme (ALMO E_{CT} is -2.2 kJ/mol for water-Na^+ and -6.8 kJ/mol for water-Mg^{2+} at aug-cc-pVQZ), CT values for the FERF models are still much smaller than the corresponding polarization contributions (even in the oDQ case, which has larger CT contributions than nDQ, E_{CT} is -4.4 kJ/mol for water-Na^+ and -28.3 kJ/mol for water-Mg^{2+} at aug-cc-pVQZ).

We also consider relatively strong (water-F^-, Figure 3.9a) and weak (water-Cl^-, Figure 3.9b) interactions with non-negligible CT contributions. These dimers are interesting tests to explore whether or not the energy difference between the non-orthogonal and orthogonal schemes increases in the presence of significant CT. Both figures, but particularly the

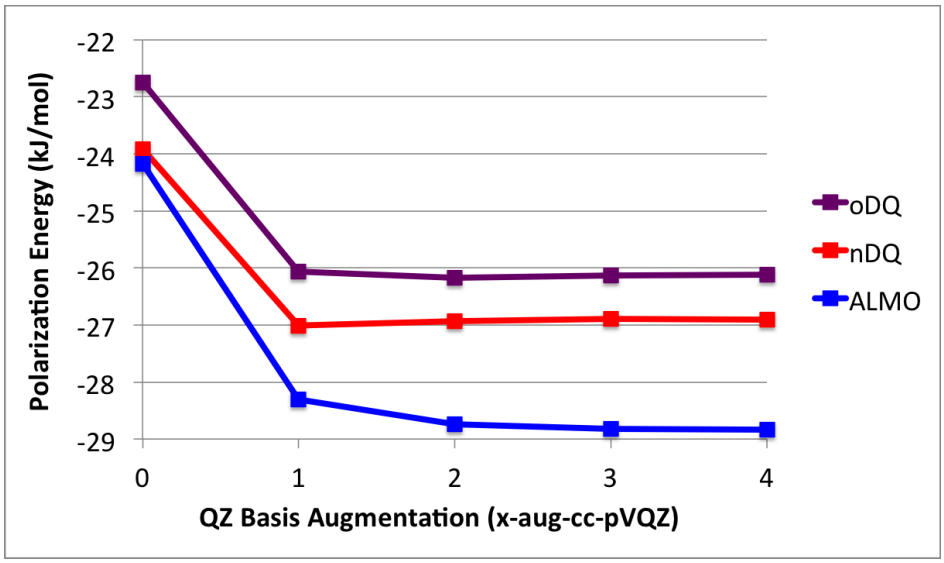

(a)

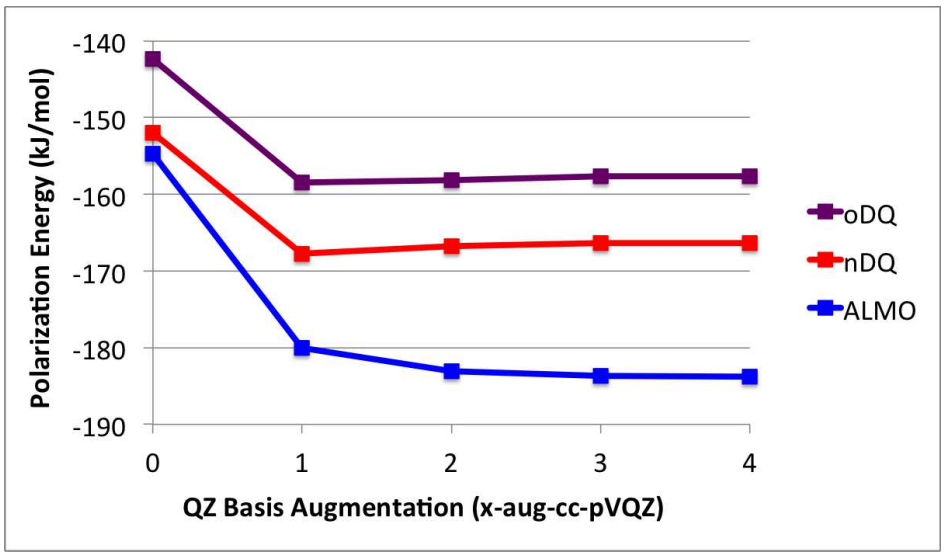

(b)

Figure 3.8: Convergence with respect to basis augmentation of ALMO and FERF polarization energies computed using B3LYP for water interacting with Na^+ (upper panel, (a)), and Mg^{2+} (lower panel, (b)) at B3LYP/aug-cc-pVQZ optimized geometries.

fluoride-water results, show the increased difficulty involved in converging DQ responses with respect to basis set augmentation for anionic systems relative to the cationic and neutral systems examined above. This is to be expected as anionic systems require more diffuse functions than the corresponding neutral system to describe the ground state density, and the prerequisites for describing the responses of this density should increase in kind. The more weakly interacting water-Cl^- system is fairly well converged at the level of double augmentation while water-F^- requires a triply augmented basis to converge the orbital response subspace.

One interesting aspect of the results shown in Figure 3.9 is the pronounced *decrease* in the magnitude of the polarization energy obtained by both the nDQ and oDQ models for the fluoride-water interaction as the degree of basis set augmentation increases. Does this mean that polarization is over-estimated in the aug-cc-pVQZ basis? We think the answer is no. Rather, we conclude that the basis set limit optimal functions for polarization of the isolated fragment (which is the basis of the FERF models) are not optimal for polarization of the fluoride anion in close contact with the water molecule and vice versa. By this argument (as well as practical imperatives), use of the singly augmented aug-cc-pVQZ basis remains a reasonable choice even for anions, in preference to multiply augmented basis sets.

The fraction of nDQ polarization energy recovered by the oDQ scheme is considerable in both cases though less impressive in the case of water-F^- when compared to the even more strongly interacting water-Mg^{2+} system investigated above. This is likely a consequence of the increased difficulty in meaningfully orthogonalizing the more diffuse functions necessary to describe the anionic system. Furthermore, despite the large CT character of these interactions and the exaggerated problem of tails when orthogonalizing diffuse functions, the oDQ polarization energy does not exceed that of the nDQ model throughout the basis augmentation series.

The last system that we examine in this section is the methyl radical interacting with sodium cation (Figure 3.10). This system, like its closed shell counterpart, methane-Na^+, discussed above, is expected to have a negligible charge transfer contribution. The occupied and nDQ virtual spans are different for the α and β one-particle subspaces of the methyl radical, and it is the goal of the orthogonalization procedure to maximize the ability of both subspaces to allow the methyl radical density to relax in the presence of the cation. The orthogonalization is quite successful to this end: the gap between nDQ and oDQ is less than 10% of the polarization interaction. In this case, the ALMO model itself is also quite well-behaved, as a consequence of the very small charge-transfer contribution.

The orthogonalization scheme largely accomplishes its aims for the systems investigated here. Should the orthogonal FERF variant, specifically oDQ, be used in practice in preference to the non-orthogonal nDQ model? Though the method is successful, it entails an additional set of arbitrary choices beyond those involved in construction of the naturally non-orthogonal FERFs. The non-orthogonal models have the tremendous advantage of being able to describe the occupied subspace of the isolated fragment, unlike any orthogonal scheme in the overlapping fragment regime. The orthogonal fragment subspaces are also necessarily

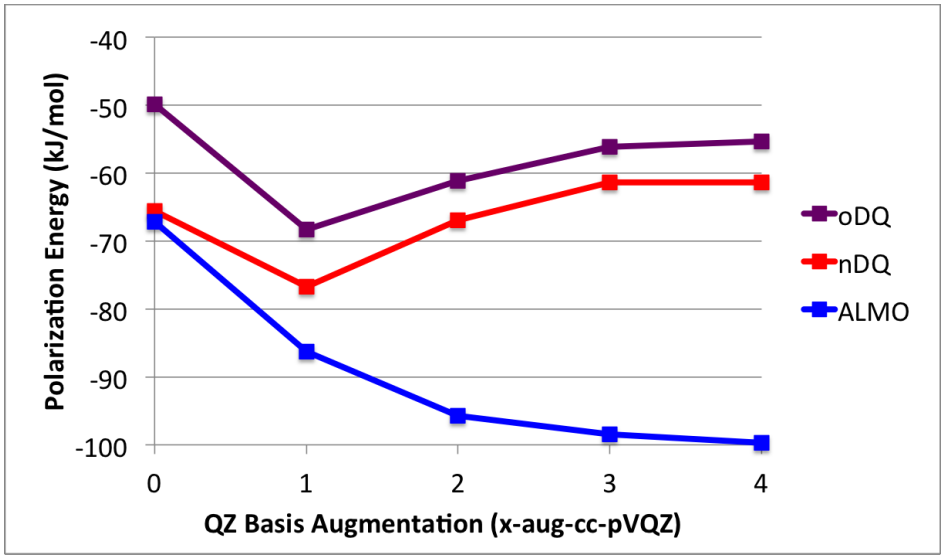

(a)

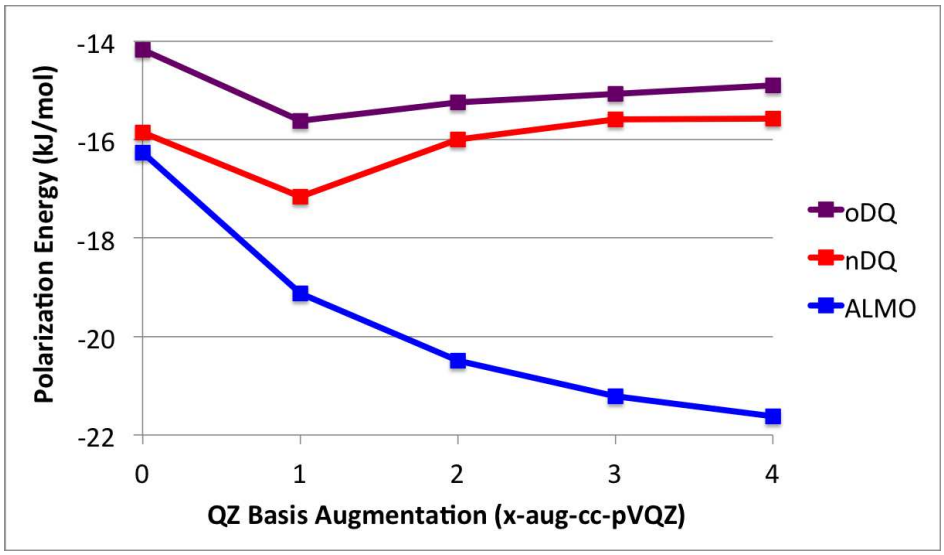

(b)

Figure 3.9: Convergence with respect to basis augmentation of ALMO and FERF polarization energies computed using B3LYP for water interacting with the F^- (upper panel, (a)), and Cl^- (lower panel, (b)) anions, at B3LYP/aug-cc-pVQZ geometries.

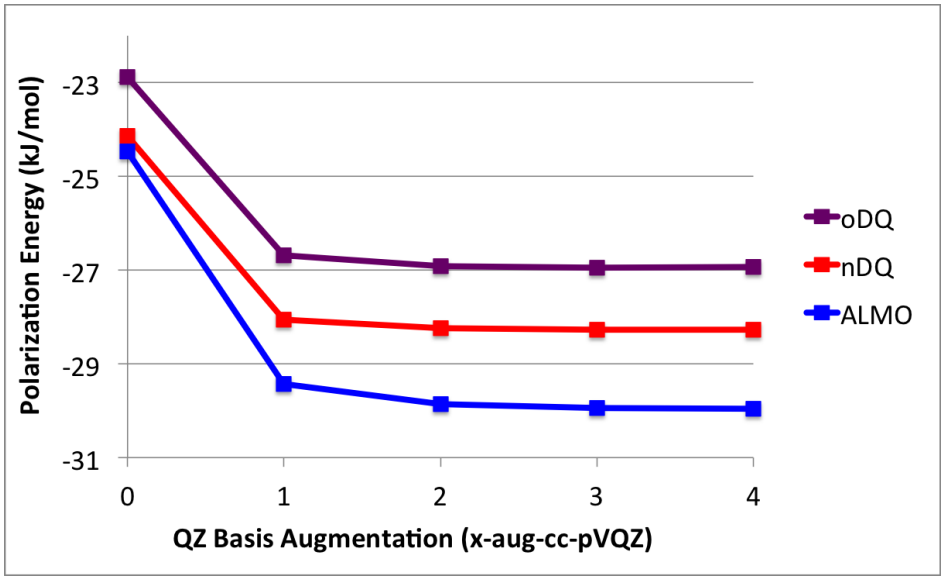

Figure 3.10: Convergence with respect to basis augmentation of ALMO and FERF polarization energies computed using B3LYP for methyl radical interacting with Na^+ at the B3LYP/aug-cc-pVQZ optimized geometry ($R_{C\text{-}Na}$ = 2.66 Å).

super-system dependent and are therefore not inherent to a single fragment. Moreover, most variational arguments are sacrificed as the orthogonal subspaces are in general subsets of only the entire one-particle span of the supersystem. However, the orthogonal schemes do have a place in assessing the uncertainty in the construction of fragment subspaces by the non-orthogonal schemes, as they provide a lower bound estimate on the magnitude of the polarization energy lowering.

3.3.4 Application of New Polarization Schemes to a Bonded Interaction

The final system that we investigate is the dissociation of ethane into two doublet methyl fragments using the aug-cc-pVQZ basis, which has been shown to be generally sufficient to describe the nDQ and oDQ models in particular. The decomposition of the binding energy using the various polarization models appears in Figure 3.11a. The considerable difference in results for the different polarization models is not surprising given both the importance of CT interactions and the overall strength of the interaction. The polarization models all give reasonable curves for the polarization energy; however, the choice of model also determines the shape of the CT energy curve (Figure 3.11b), and not all of these are so reasonable. Notably, the ALMO curve is non-monotonic! The expected CT behavior is to increase with decreasing C-C distance. While still monotonic, the nDQO curve has a similar noticeable change in curvature around the equilibrium separation, and it is not until one decreases

SCFMI flexibility to the level of nDQ subspaces that this feature is largely removed. This finding further illustrates the tendency toward spurious ALMO-like behavior for higher order FERF models (though the nDQO model at aug-cc-pVQZ may not be converged and may be somewhat biased toward ALMO-like behavior).

Figure 3.11 also contains data for the oD, oDQ, and oDQO polarization models. Unlike most of the previous cases, the oDQ polarization energy deviates appreciably from the nDQ model at compressed bond distances. This difference is larger between oDQO and nDQO and smaller between oD and nD as one might expect given the ranks of their respective polarization subspaces. We note also that the behavior of oDQ is considerably closer to that of oDQO than of oD, suggesting a rather rapid convergence of the orthogonal FERF models with respect to multipole order. The considerable difference between the non-orthogonal and orthogonal polarization models for these short C-C separations indicates a fairly large degree of uncertainty in the numerical values for the polarization and charge transfer contributions provided by each model order in the very strongly overlapping regime.

Whilst Figure 3.11b reaffirms our preference for lower order FERF models, Figure 3.12 illustrates the inadequacy of the nD model for the description of polarization in molecular systems as it fails yet again to achieve the ALMO long-range limiting behavior. The expected polarization decay for this system is R_{C-C}^{-6} for a dipole induced-dipole interaction, which is approached but not reached (Figure 3.12b). The oD, oDQ, and oDQO curves are of course equivalent to the nD, nDQ, and nDQO curves within numerical limitations for appreciable separations where orthogonalization becomes irrelevant, but it is interesting that the oDQ curve (and to a lesser extent oDQO) approximates the limiting R_{C-C}^{-6} decay at noticeably shorter distances than the other methods (Figure 3.12a). Because of the spurious, ALMO-like behavior of the nDQO model and the deficient long-range polarization in the nD model, we are once again lead to the conclusion that nDQ is the most appropriate non-orthogonal FERF model for polarization. Its orthogonalized counterpart, oDQ, has been shown to be a reasonable indicator for uncertainty, not trivially providing a very similar result to nDQ when interactions are particularly strong.

3.4 Conclusions

In this work, we have presented and applied a method of constructing non-orthogonal and orthogonal fragment electric-field response functions (FERFs) that exactly describe the polarization of a molecular fragment by an electric field and its spatial derivatives. When applied to a cluster, the FERFs define subspaces of fragment-tagged virtual functions that allow for the definition of a polarization energy (based on solving trivially modified SCFMI equations in the FERF basis) that has the desirable properties listed in the introduction. These properties include basis type independence and a non-trivial basis set limit, which were not features of the AO-subspace SCFMI-based polarization employed by several EDA methods. Our main conclusions are as follows:

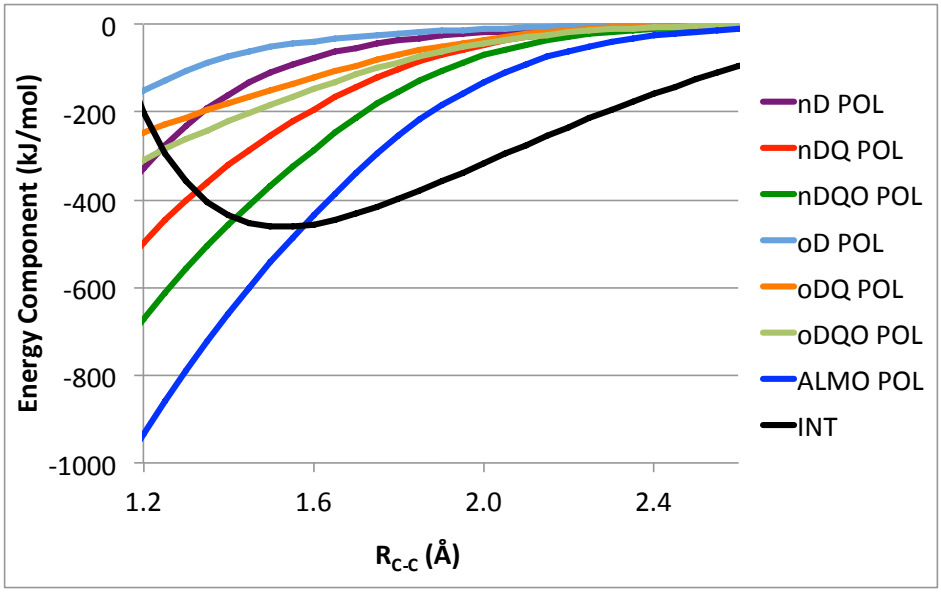

(a)

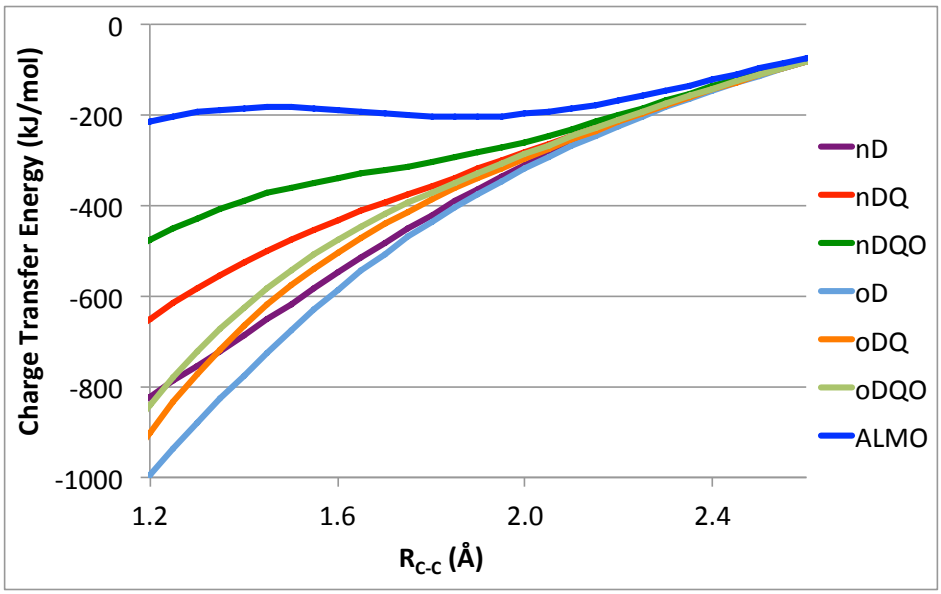

(b)

Figure 3.11: B3LYP/aug-cc-pVQZ energy components for rigid dissociation of B3LYP/aug-cc-pVTZ optimized ethane along $R_{C\text{-}C}$ to form two methyl fragments. The upper panel, (a), shows the polarization energy computed by various models along with the total interaction energy (INT). The difference between the nDQ and oDQ polarization models for compressed geometries indicates intrinsic uncertainty in the numerical values for the polarization and CT contributions provided by these models in the very strongly overlapping regime. The lower panel, (b), shows the CT contributions for ethane dissociation. The curious non-monotonic character of CT in the ALMO model due to a partial description of CT during polarization is removed by the use of the nDQ model.

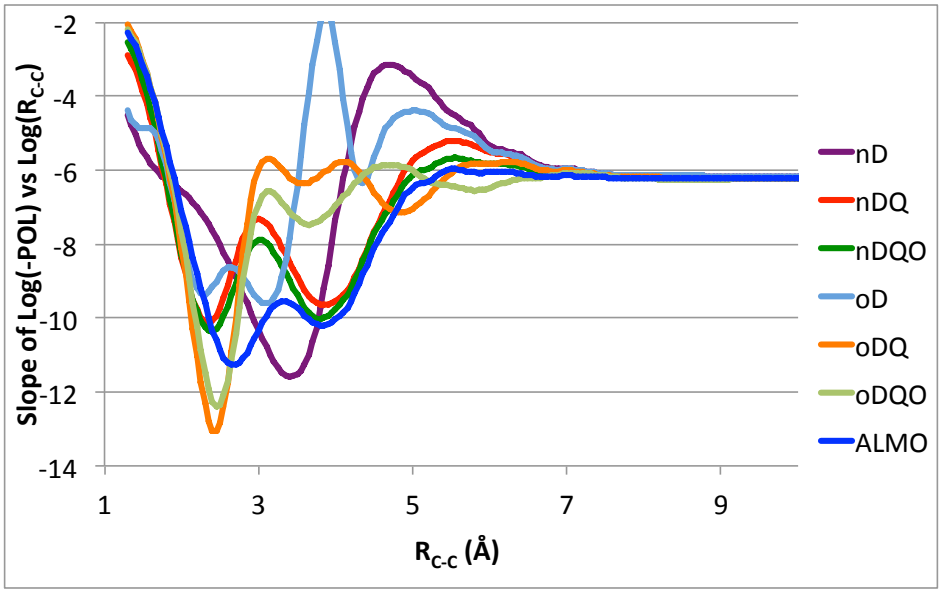

(a)

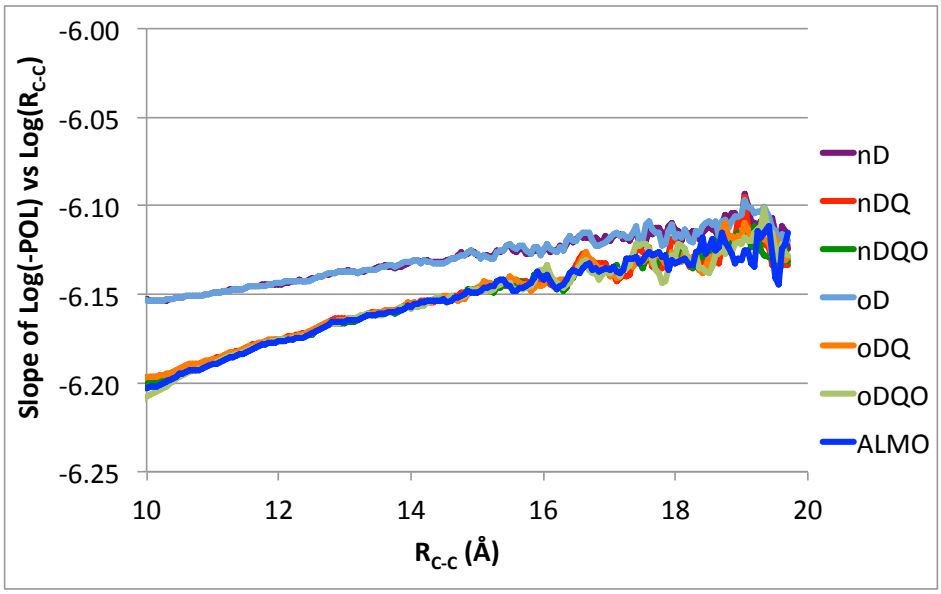

(b)

Figure 3.12: Polynomial decay of the B3LYP/aug-cc-pVQZ polarization energy using the ALMO and FERF models for dissociation of ethane, using the same level of theory as Figure 3.11, and the same protocol for tangent evaluation as Figure 3.3. The upper panel (a), shows the short-range behavior, while the lower panel, (b) shows the long-range behavior. Only the simple nD model fails to achieve the correct ALMO limiting behavior.

1. Test calculations showed that, unlike nD, the FERF nDQ model is capable of describing long-range induced electrostatic interactions in molecular systems. We recommend the smallest adequate FERF model, nDQ, over the nDQO or other higher order models because with the increased flexibility that these higher order models provide, the problems associated with separating polarization and charge transfer in large basis ALMO calculations will be reintroduced. Our investigation of ethane dissociation suggests that this unwanted behavior from undue variational flexibility is already present at the nDQO level. Moreover, it has been shown that reaching the basis set limit for the FERF/nDQ model for polarization is feasible.

2. In practice, the FERF/nDQ model can be satisfactorily employed with a basis set of aug-cc-pVQZ size, and results close to the limit are generally obtained. Even the smaller aug-cc-pVTZ basis appears to give useful results, for systems where aug-cc-pVQZ is too computationally demanding.

3. The orthogonal oDQ scheme was shown for several equilibrium structures to yield polarization energies close to but not exceeding the corresponding nDQ model, demonstrating its utility for approximating a lower bound on the magnitude of the polarization component of interactions. These orthogonalization effects were shown to be relatively small, and therefore there is no *necessity* to use orthogonal schemes, contrary to claims that have periodically been made without numerical support.

4. The only other method for computing polarization energies that meets all of the criteria in the introduction is the CDFT scheme of Wu. We have highlighted a fundamental difference between the degrees of freedom in that scheme and in the SCFMI based schemes. Only the latter are capable of properly prohibiting charge delocalization during polarization.

5. We intend to incorporate the FERF/nDQ model for describing intra-fragment polarization into a future energy decomposition analysis method, which we hope to report on in due course.

3.5 Mathematical Details

3.5.1 SCFMI Density Matrix First Derivative

Recalling the definition of the density matrix (3.12) and the SCFMI parametrization in terms of orbital rotations (3.18), the first derivative of the density matrix with respect to these degrees of freedom and the necessary partials are:

$$\left.\frac{\partial P_\alpha^{\mu\nu}}{\partial(\Delta_{\alpha,X})_{XpXq}}\right|_{\Delta_\alpha=0} = [(\mathbf{I}-\mathbf{P}_\alpha\mathbf{S})\mathbf{G}_\alpha\mathbf{C}_{\alpha,X}\boldsymbol{\sigma}_{\alpha,XX}^{-1}]^{\mu X\overline{r}}[\sum_Z \mathbf{G}_\alpha\mathbf{T}_{\alpha,Z}\boldsymbol{\sigma}_{\alpha,OO}^{-1}]^{\nu Xi}[\delta_r^p\delta_i^q-\delta_i^p\delta_r^q]+\text{Trans}[\mu\nu] \tag{3.36}$$

$$\left.\frac{\partial(\sigma^{-1}_{\alpha,OO})^{AiBj}}{\partial(\Delta_{\alpha,X})_{XpXq}}\right|_{\Delta_\alpha=0} = -\sum_{CD}(\sigma^{-1}_{\alpha,OO})^{AiCk}\left(\left.\frac{\partial(\sigma_\alpha)_{CkDl}}{\partial(\Delta_{\alpha,X})_{XpXq}}\right|_{\Delta_\alpha=0}\right)(\sigma^{-1}_{\alpha,OO})^{DlBj} \tag{3.37}$$

$$\left.\frac{\partial(\sigma_\alpha)_{CkDl}}{\partial(\Delta_{\alpha,X})_{XpXq}}\right|_{\Delta_\alpha=0} = [\mathbf{T}^T_{\alpha,D}\mathbf{\Gamma}_\alpha\mathbf{C}_{\alpha,C}\boldsymbol{\sigma}^{-1}_{\alpha,CC}]^{\bullet\ C\overline{r}}_{Dl\ \bullet}[\delta^p_r\delta^q_k - \delta^q_r\delta^p_k]\delta^X_C + \text{Trans}[CkDl] \tag{3.38}$$

3.5.2 SCFMI Density Matrix Second Derivative

The second derivative of the density matrix (3.12) with respect to SCFMI rotation parameters (3.18) is:

$$\begin{aligned}
&\left.\frac{\partial^2 P^{\mu\nu}_\alpha}{\partial(\Delta_{\alpha,X})_{XpXq}\partial(\Delta_{\alpha,Y})_{YnYo}}\right|_{\Delta_\alpha=0} = \\
&+\frac{1}{2}\delta^X_Y[+\delta^p_t\delta^q_u\delta^n_v\delta^o_k - \delta^p_t\delta^q_u\delta^o_v\delta^n_k - \delta^q_t\delta^p_u\delta^n_v\delta^o_k + \delta^q_t\delta^p_u\delta^o_v\delta^n_k \\
&+\delta^n_t\delta^o_u\delta^p_v\delta^q_k - \delta^n_t\delta^o_u\delta^q_v\delta^p_k - \delta^o_t\delta^n_u\delta^p_v\delta^q_k + \delta^o_t\delta^n_u\delta^q_v\delta^p_k] \\
&\times[(\mathbf{I}-\mathbf{P}_\alpha\mathbf{S})\mathbf{G}_\alpha\mathbf{C}_{\alpha,X}\boldsymbol{\sigma}^{-1}_{\alpha,XX}]^{\mu X\overline{t}}(\sigma^{-1}_{\alpha,XX})^{X\overline{u}X\overline{v}}[\sum_Z \mathbf{G}_\alpha\mathbf{T}_{\alpha,Z}\boldsymbol{\sigma}^{-1}_{\alpha,OO}]^{\nu Xk} \\
&+[\delta^p_l\delta^q_s\delta^n_k\delta^o_t - \delta^p_l\delta^q_s\delta^o_k\delta^n_t - \delta^q_l\delta^p_s\delta^n_k\delta^o_t + \delta^q_l\delta^p_s\delta^o_k\delta^n_t] \\
&\times\Big[[(\mathbf{I}-\mathbf{P}_\alpha\mathbf{S})\mathbf{G}_\alpha\mathbf{C}_{\alpha,X}\boldsymbol{\sigma}^{-1}_{\alpha,XX}]^{\mu X\overline{s}}(\sigma^{-1}_{\alpha,OO})^{XlYk}[(\mathbf{I}-\mathbf{P}_\alpha\mathbf{S})\mathbf{G}_\alpha\mathbf{C}_{\alpha,Y}\boldsymbol{\sigma}^{-1}_{\alpha,YY}]^{\nu Y\overline{t}} \\
&-[(\mathbf{I}-\mathbf{P}_\alpha\mathbf{S})\mathbf{G}_\alpha\mathbf{C}_{\alpha,Y}\boldsymbol{\sigma}^{-1}_{\alpha,YY}]^{\mu Y\overline{t}}[\sum_Z \mathbf{G}_\alpha\mathbf{T}_{\alpha,Z}\boldsymbol{\sigma}^{-1}_{\alpha,OO}]^{\nu Xl}[\sum_W \boldsymbol{\sigma}^{-1}_{\alpha,OO}\mathbf{T}^T_{\alpha,W}\mathbf{\Gamma}_\alpha\mathbf{C}_{\alpha,X}\boldsymbol{\sigma}^{-1}_{\alpha,XX}]^{YkX\overline{s}} \\
&-[(\mathbf{I}-\mathbf{P}_\alpha\mathbf{S})\mathbf{G}_\alpha\mathbf{C}_{\alpha,X}\boldsymbol{\sigma}^{-1}_{\alpha,XX}]^{\mu X\overline{s}}[\sum_Z \mathbf{G}_\alpha\mathbf{T}_{\alpha,Z}\boldsymbol{\sigma}^{-1}_{\alpha,OO}]^{\nu Yk}[\sum_W \boldsymbol{\sigma}^{-1}_{\alpha,OO}\mathbf{T}^T_{\alpha,W}\mathbf{\Gamma}_\alpha\mathbf{C}_{\alpha,Y}\boldsymbol{\sigma}^{-1}_{\alpha,YY}]^{XlY\overline{t}} \\
&-[\sum_Z \mathbf{G}_\alpha\mathbf{T}_{\alpha,Z}\boldsymbol{\alpha}^{-1}_{\alpha,OO}]^{\mu Xl}[\sum_W \mathbf{G}_\alpha\mathbf{T}_{\alpha,W}\boldsymbol{\alpha}^{-1}_{\alpha,OO}]^{\nu Yk}[\boldsymbol{\sigma}^{-1}_{\alpha,YY}\mathbf{C}^T_{\alpha,Y}\mathbf{G}^T_\alpha(\mathbf{S}-\mathbf{S}\mathbf{P}_\alpha\mathbf{S})\mathbf{G}_\alpha\mathbf{C}_{\alpha,X}\boldsymbol{\sigma}^{-1}_{\alpha,XX}]^{Y\overline{t}X\overline{s}}\Big] \\
&+\text{Trans}[\mu\nu]
\end{aligned} \tag{3.39}$$

The necessary partials in addition to (3.37) and (3.38) are:

$$\begin{aligned}
&\left.\frac{\partial^2(\sigma^{-1}_{\alpha,OO})^{AiBj}}{\partial(\Delta_{\alpha,X})_{XpXq}\partial(\Delta_{\alpha,Y})_{YnYo}}\right|_{\Delta_\alpha=0} = \\
&-\textstyle\sum_{CD}(\sigma^{-1}_{\alpha,OO})^{AiCk}\left(\left.\frac{\partial^2(\sigma_\alpha)_{CkDl}}{\partial(\Delta_{\alpha,X})_{XpXq}\partial(\Delta_{\alpha,Y})_{YnYo}}\right|_{\Delta_\alpha=0}\right)(\sigma^{-1}_{\alpha,OO})^{DlBj} \\
&+\textstyle\sum_{CDEF}(\sigma^{-1}_{\alpha,OO})^{AiCk}\left(\left.\frac{\partial(\sigma_\alpha)_{CkDl}}{\partial(\Delta_{\alpha,X})_{XpXq}}\right|_{\Delta_\alpha=0}\right)(\sigma^{-1}_{\alpha,OO})^{DlEe}\left(\left.\frac{\partial(\sigma_\alpha)_{EeFf}}{\partial(\Delta_{\alpha,Y})_{YnYo}}\right|_{\Delta_\alpha=0}\right)(\sigma^{-1}_{\alpha,OO})^{FfBj} \\
&+\textstyle\sum_{CDEF}(\sigma^{-1}_{\alpha,OO})^{AiEe}\left(\left.\frac{\partial(\sigma_\alpha)_{EeFf}}{\partial(\Delta_{\alpha,Y})_{YnYo}}\right|_{\Delta_\alpha=0}\right)(\sigma^{-1}_{\alpha,OO})^{FfCk}\left(\left.\frac{\partial(\sigma_\alpha)_{CkDl}}{\partial(\Delta_{\alpha,X})_{XpXq}}\right|_{\Delta_\alpha=0}\right)(\sigma^{-1}_{\alpha,OO})^{DlBj}
\end{aligned} \tag{3.40}$$

$$
\begin{aligned}
\left.\frac{\partial^2(\sigma_\alpha)_{CkDl}}{\partial(\Delta_{\alpha,X})_{XpXq}\partial(\Delta_{\alpha,Y})_{YnYo}}\right|_{\Delta_\alpha=0} = \\
+\frac{1}{2}\delta_C^X\delta_C^Y[\mathbf{T}_{\alpha,D}^T\boldsymbol{\Gamma}_\alpha\mathbf{C}_{\alpha,C}\boldsymbol{\sigma}_{\alpha,CC}^{-1}]_{Dl}^{\bullet\ C\overline{t}}{}_{\bullet}(\sigma_{\alpha,CC}^{-1})^{C\overline{u}C\overline{v}} \\
\times[+\delta_t^p\delta_u^q\delta_v^n\delta_k^o-\delta_t^p\delta_u^q\delta_k^n\delta_v^o-\delta_u^p\delta_t^q\delta_v^n\delta_k^o+\delta_u^p\delta_t^q\delta_k^n\delta_v^o \\
+\delta_t^n\delta_u^o\delta_v^p\delta_k^q-\delta_t^n\delta_u^o\delta_k^p\delta_v^q-\delta_u^n\delta_t^o\delta_v^p\delta_k^q+\delta_u^n\delta_t^o\delta_k^p\delta_v^q] \\
+\delta_C^X\delta_D^Y[\boldsymbol{\sigma}_{\alpha,XX}^{-1}\boldsymbol{\sigma}_\alpha\boldsymbol{\sigma}_{\alpha,YY}^{-1}]^{X\overline{t}Y\overline{w}} \\
\times[\delta_t^p\delta_k^q\delta_w^n\delta_l^o-\delta_k^p\delta_t^q\delta_w^n\delta_l^o-\delta_t^p\delta_k^q\delta_l^n\delta_w^o+\delta_k^p\delta_t^q\delta_l^n\delta_w^o] \\
+\mathrm{Trans}[CkDl]
\end{aligned}
\tag{3.41}
$$

3.5.3 SCFMI Energy Orbital Hessian

The second derivative of the electronic energy with respect to SCFMI orbital rotations is:

$$
\begin{aligned}
\left.\frac{\partial^2 E}{\partial(\Delta_{\alpha,X})_{XpXq}\partial(\Delta_{\beta,Y})_{YnYo}}\right|_{\Delta_\alpha=0} \\
= \frac{\partial E}{\partial P_\alpha^{\mu\nu}}\left.\frac{\partial^2 P_\alpha^{\mu\nu}}{\partial(\Delta_{\alpha,X})_{XpXq}\partial(\Delta_{\beta,Y})_{YnYo}}\right|_{\Delta_\alpha=0} \\
+\left.\frac{\partial(P_\alpha)^{\mu\nu}}{\partial(\Delta_{\alpha,X})_{XpXq}}\right|_{\Delta_\alpha=0}\frac{\partial^2 E}{\partial P_\alpha^{\mu\nu}\partial P_\beta^{\lambda\sigma}}\left.\frac{\partial(P_\beta)^{\lambda\sigma}}{\partial(\Delta_{\beta,Y})_{YnYo}}\right|_{\Delta_\alpha=0}
\end{aligned}
\tag{3.42}
$$

This expression can be simplified using (3.15), (3.49), (3.36), and (3.39) to yield the Hessian without the assumption of intra-subspace orthogonality:

$$
\begin{aligned}
\left.\frac{\partial^2 E}{\partial(\Delta_{\alpha,X})_{XpXq}\partial(\Delta_{\beta,Y})_{YnYo}}\right|_{\Delta_\alpha=0} = \\
+\delta_Y^X\delta_\beta^\alpha[+\delta_t^p\delta_u^q\delta_v^n\delta_k^o-\delta_t^p\delta_u^q\delta_v^o\delta_k^n-\delta_t^q\delta_u^p\delta_v^n\delta_k^o+\delta_t^q\delta_u^p\delta_v^o\delta_k^n \\
+\delta_t^n\delta_u^o\delta_v^p\delta_k^q-\delta_t^n\delta_u^o\delta_v^q\delta_k^p-\delta_t^o\delta_u^n\delta_v^p\delta_k^q+\delta_t^o\delta_u^n\delta_v^q\delta_k^p] \\
\times[\sum_Z\boldsymbol{\sigma}_{\alpha,OO}^{-1}\mathbf{T}_{\alpha,Z}^T\mathbf{G}_\alpha^T\mathbf{F}_\alpha(\mathbf{I}-\mathbf{P}_\alpha\mathbf{S})\mathbf{G}_\alpha\mathbf{C}_{\alpha,X}\boldsymbol{\sigma}_{\alpha,XX}^{-1}]^{XkX\overline{t}}\sigma_\alpha^{X\overline{u}X\overline{v}} \\
+2\delta_\beta^\alpha[\delta_l^p\delta_s^q\delta_k^n\delta_t^o-\delta_l^p\delta_s^q\delta_k^o\delta_t^n-\delta_l^q\delta_s^p\delta_k^n\delta_t^o+\delta_l^q\delta_s^p\delta_k^o\delta_t^n] \\
\times\Big[(\sigma_{\alpha,OO}^{-1})^{XlYk}[\boldsymbol{\sigma}_{\alpha,XX}^{-1}\mathbf{C}_{\alpha,X}^T\mathbf{G}_\alpha^T(\mathbf{I}-\mathbf{S}\mathbf{P}_\alpha)\mathbf{F}_\alpha(\mathbf{I}-\mathbf{P}_\alpha\mathbf{S})\mathbf{G}_\alpha\mathbf{C}_{\alpha,Y}\boldsymbol{\sigma}_{\alpha,YY}^{-1}]^{X\overline{s}Y\overline{t}} \\
-[\sum_Z\boldsymbol{\sigma}_{\alpha,OO}^{-1}\mathbf{T}_{\alpha,Z}^T\mathbf{G}_\alpha^T\mathbf{F}_\alpha(\mathbf{I}-\mathbf{P}_\alpha\mathbf{S})\mathbf{G}_\alpha\mathbf{C}_{\alpha,Y}\boldsymbol{\sigma}_{\alpha,YY}^{-1}]^{XlY\overline{t}}[\sum_W\boldsymbol{\sigma}_{\alpha,OO}^{-1}\mathbf{T}_{\alpha,W}^T\boldsymbol{\Gamma}_\alpha\mathbf{C}_{\alpha,X}\boldsymbol{\sigma}_{\alpha,XX}^{-1}]^{YkX\overline{s}} \\
-[\sum_Z\boldsymbol{\sigma}_{\alpha,OO}^{-1}\mathbf{T}_{\alpha,Z}^T\mathbf{G}_\alpha^T\mathbf{F}_\alpha(\mathbf{I}-\mathbf{P}_\alpha\mathbf{S})\mathbf{G}_\alpha\mathbf{C}_{\alpha,X}\boldsymbol{\sigma}_{\alpha,XX}^{-1}]^{YkX\overline{s}}[\sum_W\boldsymbol{\sigma}_{\alpha,OO}^{-1}\mathbf{T}_{\alpha,W}^T\boldsymbol{\Gamma}_\alpha\mathbf{C}_{\alpha,Y}\boldsymbol{\sigma}_{\alpha,YY}^{-1}]^{XlY\overline{t}} \\
-[\sum_{WZ}\boldsymbol{\sigma}_{\alpha,OO}^{-1}\mathbf{T}_{\alpha,Z}^T\mathbf{G}_\alpha^T\mathbf{F}_\alpha\mathbf{G}_\alpha\mathbf{T}_{\alpha,W}\boldsymbol{\sigma}_{\alpha,OO}^{-1}]^{YkXl}[\boldsymbol{\sigma}_{\alpha,YY}^{-1}\mathbf{C}_{\alpha,Y}^T\mathbf{G}_\alpha^T(\mathbf{S}-\mathbf{S}\mathbf{P}_\alpha\mathbf{S})\mathbf{G}_\alpha\mathbf{C}_{\alpha,X}\boldsymbol{\sigma}_{\alpha,XX}^{-1}]^{Y\overline{t}X\overline{s}}\Big] \\
+4[\delta_r^p\delta_i^q-\delta_i^p\delta_r^q][\delta_s^n\delta_j^o-\delta_j^n\delta_s^o](\Pi_{\alpha\beta})_{\mu\nu\lambda\sigma} \\
\times[(\mathbf{I}-\mathbf{P}_\alpha\mathbf{S})\,\mathbf{G}_\alpha\mathbf{C}_{\alpha,X}(\boldsymbol{\sigma}_{\alpha,XX})^{-1}]^{\mu X\overline{r}}[\sum_Z\mathbf{G}_\alpha\mathbf{T}_{\alpha,Z}(\boldsymbol{\sigma}_{\alpha,OO})^{-1}]^{\nu Xi} \\
\times[(\mathbf{I}-\mathbf{P}_\beta\mathbf{S})\,\mathbf{G}_\beta\mathbf{C}_{\beta,Y}(\boldsymbol{\sigma}_{\beta,YY})^{-1}]^{\lambda Y\overline{s}}[\sum_W\mathbf{G}_\beta\mathbf{T}_{\beta,W}(\boldsymbol{\sigma}_{\beta,OO})^{-1}]^{\sigma Yj}
\end{aligned}
\tag{3.43}
$$

3.5.4 SCFMI Energy Preconditioning Strategy

The SCFMI orbital Hessian in the case of intra-subspace orthogonality is as follows (where we are reverting to considering the spin cases explicitly, as indicated by the spin labels):

$$\frac{\partial^2 E}{\partial(\Delta_{\alpha,A})_{AiAa}\partial(\Delta_{\beta,B})_{BjBb}}\Big|_{\{\Delta\}=0} = \tag{3.44}$$

$$\delta^{\alpha}_{\beta} 2 \left[(\boldsymbol{\sigma}_{\alpha,OO})^{-1}\right]^{AiBj} \left[\mathbf{V}^T_{\alpha,A}\mathbf{G}^T_{\alpha}\left(\mathbf{I}-\mathbf{SP}_{\alpha}\right)\mathbf{F}_{\alpha}\left(\mathbf{I}-\mathbf{P}_{\alpha}\mathbf{S}\right)\mathbf{G}_{\alpha}\mathbf{V}_{\alpha,B}\right]_{AaBb} \tag{3.45}$$

$$-\delta^{\alpha}_{\beta} 2 \left[\sum_{Z}(\boldsymbol{\sigma}_{\alpha,OO})^{-1}\mathbf{T}^T_{\alpha,Z}\boldsymbol{\Gamma}_{\alpha}\mathbf{V}_{\alpha,B}\right]^{Ai\,\bullet}_{\bullet\,Bb} \left[\sum_{Y}(\boldsymbol{\sigma}_{\alpha,OO})^{-1}\mathbf{T}^T_{\alpha,Y}\mathbf{G}^T_{\alpha}\mathbf{F}_{\alpha}\left(\mathbf{I}-\mathbf{P}_{\alpha}\mathbf{S}\right)\mathbf{G}_{\alpha}\mathbf{V}_{\alpha,A}\right]^{Bj\,\bullet}_{\bullet\,Aa} \tag{3.46}$$

$$-\delta^{\alpha}_{\beta} 2 \left[\sum_{Z}(\boldsymbol{\sigma}_{\alpha,OO})^{-1}\mathbf{T}^T_{\alpha,Z}\boldsymbol{\Gamma}_{\alpha}\mathbf{V}_{\alpha,A}\right]^{Bj\,\bullet}_{\bullet\,Aa} \left[\sum_{Y}(\boldsymbol{\sigma}_{\alpha,OO})^{-1}\mathbf{T}^T_{\alpha,Y}\mathbf{G}^T_{\alpha}\mathbf{F}_{\alpha}\left(\mathbf{I}-\mathbf{P}_{\alpha}\mathbf{S}\right)\mathbf{G}_{\alpha}\mathbf{V}_{\alpha,B}\right]^{Ai\,\bullet}_{\bullet\,Bb} \tag{3.47}$$

$$-\delta^{\alpha}_{\beta} 2 \left[\mathbf{V}^T_{\alpha,A}\mathbf{G}^T_{\alpha}\left(\mathbf{S}-\mathbf{SP}_{\alpha}\mathbf{S}\right)\mathbf{G}_{\alpha}\mathbf{V}_{\alpha,B}\right]_{AaBb} \left[\sum_{YZ}(\boldsymbol{\sigma}_{\alpha,OO})^{-1}\mathbf{T}^T_{\alpha,Z}\mathbf{G}^T_{\alpha}\mathbf{F}_{\alpha}\mathbf{G}_{\alpha}\mathbf{T}_{\alpha,Y}(\boldsymbol{\sigma}_{\alpha,OO})^{-1}\right]^{AiBj} \tag{3.48}$$

$$+4\left[\left(\mathbf{I}-\mathbf{P}_{\alpha}\mathbf{S}\right)\mathbf{G}_{\alpha}\mathbf{V}_{\alpha,A}\right]^{\mu\,\bullet}_{\bullet\,Aa} \left[\sum_{Z}(\boldsymbol{\sigma}_{\alpha,OO})^{-1}\mathbf{T}^T_{\alpha,Z}\mathbf{G}^T_{\alpha}\right]^{Ai\nu} (\Pi_{\alpha\beta})_{\mu\nu\lambda\sigma}$$

$$\times\left[\left(\mathbf{I}-\mathbf{P}_{\beta}\mathbf{S}\right)\mathbf{G}_{\beta}\mathbf{V}_{\beta,B}\right]^{\lambda\,\bullet}_{\bullet\,Bb} \left[\sum_{Y}(\boldsymbol{\sigma}_{\beta,OO})^{-1}\mathbf{T}^T_{\beta,Y}\mathbf{G}^T_{\beta}\right]^{Bj\sigma}$$

where:

$$\left(\Pi_{\alpha\beta}\right)_{\mu\nu\lambda\sigma} \equiv \frac{\partial^2 E}{\partial P^{\mu\nu}_{\alpha}\partial P^{\lambda\sigma}_{\beta}} \tag{3.49}$$

The tensor $\mathbf{\Pi}$ involves the two electron integrals and second derivatives of the exchange correlation energy in the case of DFT. Apparent inconsistences in the covariant-contravariant notation are a consequence of the omission of metrics equivalent to the identity. The contraction of the SCFMI Hessian with a trial vector for the solution of the Newton step by conjugate gradient or MINRES is straightforward.

We have considered two levels of preconditioning for the solution of this linear equation, and we use these same approximate inverse Hessians to augment the quasi-Newton algorithm. The less expensive of the two preconditioners considers terms from $E^P \cdot P^{\Delta\Delta}$, lines (3.45) through (3.48), assuming weakly overlapping fragments such that overlap-like terms can be approximated by kronecker deltas:

$$(B_{\alpha})^{(A\bar{i}A\bar{a})\,\bullet}_{\bullet\,R} = \tag{3.50}$$
$$(H^{approx.}_{\alpha\alpha})^{(A\bar{i}A\bar{a})(A\bar{j}A\bar{b})}(X_{\alpha})_{(AjAb)R}$$

$$(H^{approx.}_{\alpha\alpha})^{(A\bar{i}A\bar{a})(A\bar{j}A\bar{b})} = \tag{3.51}$$
$$\left[\mathbf{V}^T_{\alpha,A}\mathbf{G}^T_{\alpha}\left(\mathbf{I}-\mathbf{SP}_{\alpha}\right)\mathbf{F}_{\alpha}\left(\mathbf{I}-\mathbf{P}_{\alpha}\mathbf{S}\right)\mathbf{G}_{\alpha}\mathbf{V}_{\alpha B}\right]_{AaAb}$$
$$\times 2\delta_{AiAj} - 2\delta_{AaAb}$$
$$\times\left[\sum_{YZ}(\boldsymbol{\sigma}_{\alpha,OO})^{-1}\mathbf{T}^T_{\alpha,Z}\mathbf{G}^T_{\alpha}\mathbf{F}_{\alpha}\mathbf{G}_{\alpha}\mathbf{T}_{\alpha,Y}(\boldsymbol{\sigma}_{\alpha,OO})^{-1}\right]^{AiAj}$$

B is the matrix of column vectors (R) with potentially alpha and beta portions to be preconditioned (our approximate Hessian is spin-block-diagonal), and **X** are the preconditioned vectors. The linear equation defined by (3.50) and (3.51) can easily be solved by the application of pseudocanonical-like intra-subspace occupied-occupied and virtual-virtual rotations, which bring the approximate Hessian (3.51) into diagonal form.

A more expensive but still linear scaling preconditioner which does not involve the contraction of trial vectors with two-electron integrals or XC matrix derivatives considers all subspace-diagonal blocks of terms from $E^P \cdot P^{\Delta\Delta}$, (3.45) through (3.48), which are again spin-diagonal:

$$
\begin{aligned}
&(H^{approx.}_{\alpha\alpha})^{(A\bar{i}A\bar{a})(A\bar{j}A\bar{b})} = \qquad (3.52)\\
&2\left((\sigma_{\alpha,OO})^{-1}\right)^{AiAj}\left[\mathbf{V}^T_{\alpha,A}\mathbf{G}^T_\alpha\left(\mathbf{I}-\mathbf{S}\mathbf{P}_\alpha\right)\mathbf{F}_\alpha\left(\mathbf{I}-\mathbf{P}_\alpha\mathbf{S}\right)\mathbf{G}_\alpha\mathbf{V}_{\alpha A}\right]_{AaAb}\\
&-2\left[\sum_Z(\boldsymbol{\sigma}_{\alpha,OO})^{-1}\mathbf{T}^T_{\alpha,Z}\boldsymbol{\Gamma}_\alpha\mathbf{V}_{\alpha,A}\right]^{Ai\,\bullet}_{\bullet\,Ab}\left[\sum_Y(\boldsymbol{\sigma}_{\alpha,OO})^{-1}\mathbf{T}^T_{\alpha,Y}\mathbf{G}^T_\alpha\mathbf{F}_\alpha\left(\mathbf{I}-\mathbf{P}_\alpha\mathbf{S}\right)\mathbf{G}_\alpha\mathbf{V}_{\alpha,A}\right]^{Aj\,\bullet}_{\bullet\,Aa}\\
&-2\left[\sum_Z(\boldsymbol{\sigma}_{\alpha,OO})^{-1}\mathbf{T}^T_{\alpha,Z}\boldsymbol{\Gamma}_\alpha\mathbf{V}_{\alpha,A}\right]^{Aj\,\bullet}_{\bullet\,Aa}\left[\sum_Y(\boldsymbol{\sigma}_{\alpha,OO})^{-1}\mathbf{T}^T_{\alpha,Y}\mathbf{G}^T_\alpha\mathbf{F}_\alpha\left(\mathbf{I}-\mathbf{P}_\alpha\mathbf{S}\right)\mathbf{G}_\alpha\mathbf{V}_{\alpha,A}\right]^{Ai\,\bullet}_{\bullet\,Ab}\\
&-2\left[\mathbf{V}^T_{\alpha,A}\mathbf{G}^T_\alpha\left(\mathbf{S}-\mathbf{S}\mathbf{P}_\alpha\mathbf{S}\right)\mathbf{G}_\alpha\mathbf{V}_{\alpha,A}\right]_{AaAb}\left[\sum_{YZ}(\boldsymbol{\sigma}_{\alpha,OO})^{-1}\mathbf{T}^T_{\alpha,Z}\mathbf{G}^T_\alpha\mathbf{F}_\alpha\mathbf{G}_\alpha\mathbf{T}_{\alpha,Y}(\boldsymbol{\sigma}_{\alpha,OO})^{-1}\right]^{AiAj}
\end{aligned}
$$

The solution of the linear system defined by (3.50) and (3.52) can be computed separately for each subspace by a linear solver such as conjugate gradient using a more approximate and less expensive preconditioner such as (3.51). One could continue nesting preconditioners in this way to precondition with all of $E^P \cdot P^{\Delta\Delta}$, (3.45) through (3.48), but the inclusion of inter-subspace blocks makes the matrix application to a trial vector quadratic in subspaces. This is in general an undesirable cost increase for quasi-Newton methods; however, it has been a helpful strategy in the context of preconditioning the conjugate gradient iterations for the solution of Newton steps where the expensive operation is multiplication by the entire Hessian (3.44), which requires the additional, more expensive contractions with Π. We note that other authors[111, 112] have previously employed full BFGS initialized with an approximate Hessian to solve the SCFMI problem. The approach taken in this work uses a newly calculated and thus more relevant approximate Hessian as a preconditioner at each L-BFGS iteration and requires only the application of this matrix to a vector, never its storage.

3.5.5 SCFMI Population Derivatives

The first derivative of the population of domain A with respect to SCFMI rotation parameters by (3.26) and (3.36) is:

$$\begin{aligned}\left.\frac{\partial \mathrm{Pop}_{\alpha,A}}{\partial(\Delta_{\alpha,X})_{XpXq}}\right|_{\Delta_\alpha=0} &= \frac{\partial \mathrm{Pop}_{\alpha,A}}{\partial P_\alpha^{\mu\nu}}\left.\frac{\partial P_\alpha^{\mu\nu}}{\partial(\Delta_{\alpha,X})_{XpXq}}\right|_{\Delta_\alpha=0} \\ = [\delta_r^p\delta_i^q - \delta_i^p\delta_r^q][\sum_Z(\boldsymbol{\sigma}_{\alpha,OO})^{-1}\mathbf{T}_{\alpha,Z}^T\mathbf{G}_\alpha^T\mathbf{S}(\mathbf{P}_{\alpha,A}+\mathbf{P}_{\alpha,A}^T) \\ \times\mathbf{S}(\mathbf{I}-\mathbf{P}_\alpha\mathbf{S})\mathbf{G}_\alpha\mathbf{C}_{\alpha,X}(\boldsymbol{\sigma}_{\alpha,XX})^{-1}]^{XiX\overline{r}}\end{aligned} \tag{3.53}$$

The second derivative of the population of domain A with respect to SCFMI rotation parameters by (3.26) and (3.39) is:

$$\begin{aligned}&\left.\frac{\partial^2 \mathrm{Pop}_{\alpha,A}}{\partial(\Delta_{\alpha,X})_{XpXq}\partial(\Delta_{\alpha,Y})_{YnYo}}\right|_{\Delta_\alpha=0} \\ &+\delta_Y^X\frac{1}{2}[+\delta_t^p\delta_u^q\delta_v^n\delta_k^o - \delta_t^p\delta_u^q\delta_v^o\delta_k^n - \delta_t^q\delta_u^p\delta_v^n\delta_k^o + \delta_t^q\delta_u^p\delta_v^o\delta_k^n \\ &+\delta_t^n\delta_u^o\delta_v^p\delta_k^q - \delta_t^n\delta_u^o\delta_v^q\delta_k^p - \delta_t^o\delta_u^n\delta_v^p\delta_k^q + \delta_t^o\delta_u^n\delta_v^q\delta_k^p] \\ &\times[\sum_Z\boldsymbol{\sigma}_{\alpha,OO}^{-1}\mathbf{T}_{\alpha,Z}^T\mathbf{G}_\alpha^T\mathbf{S}(\mathbf{P}_{\alpha,A}+\mathbf{P}_{\alpha,A}^T)\mathbf{S}(\mathbf{I}-\mathbf{P}_\alpha\mathbf{S})\mathbf{G}_\alpha\mathbf{C}_{\alpha,X}\boldsymbol{\sigma}_{\alpha,XX}^{-1}]^{XkX\overline{t}}\sigma_\alpha^{X\overline{u}X\overline{v}} \\ &+[\delta_l^p\delta_s^q\delta_k^n\delta_t^o - \delta_l^p\delta_s^q\delta_k^o\delta_t^n - \delta_l^q\delta_s^p\delta_k^n\delta_t^o + \delta_l^q\delta_s^p\delta_k^o\delta_t^n] \\ &\times\Big[(\sigma_{\alpha,OO}^{-1})^{XlYk}[\boldsymbol{\sigma}_{\alpha,XX}^{-1}\mathbf{C}_{\alpha,X}^T\mathbf{G}_\alpha^T(\mathbf{I}-\mathbf{S}\mathbf{P}_\alpha)\mathbf{S}(\mathbf{P}_{\alpha,A}+\mathbf{P}_{\alpha,A}^T)\mathbf{S}(\mathbf{I}-\mathbf{P}_\alpha\mathbf{S})\mathbf{G}_\alpha\mathbf{C}_{\alpha,Y}\boldsymbol{\sigma}_{\alpha,YY}^{-1}]^{X\overline{s}Y\overline{t}} \\ &-[\sum_Z\boldsymbol{\sigma}_{\alpha,OO}^{-1}\mathbf{T}_{\alpha,Z}^T\mathbf{G}_\alpha^T\mathbf{S}(\mathbf{P}_{\alpha,A}+\mathbf{P}_{\alpha,A}^T)\mathbf{S}(\mathbf{I}-\mathbf{P}_\alpha\mathbf{S})\mathbf{G}_\alpha\mathbf{C}_{\alpha,Y}\boldsymbol{\sigma}_{\alpha,YY}^{-1}]^{XlY\overline{t}}[\sum_W\boldsymbol{\sigma}_{\alpha,OO}^{-1}\mathbf{T}_{\alpha,W}^T\boldsymbol{\Gamma}_\alpha\mathbf{C}_{\alpha,X}\boldsymbol{\sigma}_{\alpha,XX}^{-1}]^{YkX\overline{s}} \\ &-[\sum_Z\boldsymbol{\sigma}_{\alpha,OO}^{-1}\mathbf{T}_{\alpha,Z}^T\mathbf{G}_\alpha^T\mathbf{S}(\mathbf{P}_{\alpha,A}+\mathbf{P}_{\alpha,A}^T)\mathbf{S}(\mathbf{I}-\mathbf{P}_\alpha\mathbf{S})\mathbf{G}_\alpha\mathbf{C}_{\alpha,X}\boldsymbol{\sigma}_{\alpha,XX}^{-1}]^{YkX\overline{s}}[\sum_W\boldsymbol{\sigma}_{\alpha,OO}^{-1}\mathbf{T}_{\alpha,W}^T\boldsymbol{\Gamma}_\alpha\mathbf{C}_{\alpha,Y}\boldsymbol{\sigma}_{\alpha,YY}^{-1}]^{XlY\overline{t}} \\ &-[\sum_{ZW}\boldsymbol{\sigma}_{\alpha,OO}^{-1}\mathbf{T}_{\alpha,Z}^T\mathbf{G}_\alpha^T\mathbf{S}(\mathbf{P}_{\alpha,A}+\mathbf{P}_{\alpha,A}^T)\mathbf{S}\mathbf{G}_\alpha\mathbf{T}_{\alpha,W}\boldsymbol{\alpha}_{\alpha,OO}^{-1}]^{YkXl}[\boldsymbol{\sigma}_{\alpha,YY}^{-1}\mathbf{C}_{\alpha,Y}^T\mathbf{G}_\alpha^T(\mathbf{S}-\mathbf{S}\mathbf{P}_\alpha\mathbf{S})\mathbf{G}_\alpha\mathbf{C}_{\alpha,X}\boldsymbol{\sigma}_{\alpha,XX}^{-1}]^{Y\overline{t}X\overline{s}}\Big]\end{aligned} \tag{3.54}$$

For the case $\mathbf{G}_\alpha = \mathbf{M}_\alpha$ we have the following intermediate results that can be used to show that both (3.53) and (3.54) are zero:

$$[\sum_{ZW}\boldsymbol{\sigma}_{\alpha,OO}^{-1}\mathbf{T}_{\alpha,Z}^T\mathbf{G}_\alpha^T\mathbf{S}(\mathbf{P}_{\alpha,A}+\mathbf{P}_{\alpha,A}^T)\mathbf{S}\mathbf{G}_\alpha\mathbf{T}_{\alpha,W}\boldsymbol{\alpha}_{\alpha,OO}^{-1}]^{XlYk} = (\boldsymbol{\sigma}_{\alpha,OO}^{-1})^{XlYk}[\delta_A^X+\delta_A^Y] \tag{3.55}$$

$$[\sum_Z\boldsymbol{\sigma}_{\alpha,OO}^{-1}\mathbf{T}_{\alpha,Z}^T\mathbf{G}_\alpha^T\mathbf{S}(\mathbf{P}_{\alpha,A}+\mathbf{P}_{\alpha,A}^T)\mathbf{S}(\mathbf{I}-\mathbf{P}_\alpha\mathbf{S})\mathbf{G}_\alpha\mathbf{C}_{\alpha,Y}\boldsymbol{\sigma}_{\alpha,YY}^{-1}]^{XlY\overline{t}} = [\boldsymbol{\sigma}_{\alpha,OO}^{-1}\boldsymbol{\sigma}_{\alpha,OY}\boldsymbol{\sigma}_{\alpha,YY}^{-1}]^{XlY\overline{t}}[\delta_A^Y-\delta_A^X] \tag{3.56}$$

$$\begin{aligned}&[\boldsymbol{\sigma}_{\alpha,XX}^{-1}\mathbf{C}_{\alpha,X}^T\mathbf{G}_\alpha^T(\mathbf{I}-\mathbf{S}\mathbf{P}_\alpha)\mathbf{S}(\mathbf{P}_{\alpha,A}+\mathbf{P}_{\alpha,A}^T)\mathbf{S}(\mathbf{I}-\mathbf{P}_\alpha\mathbf{S})\mathbf{G}_\alpha\mathbf{C}_{\alpha,Y}\boldsymbol{\sigma}_{\alpha,YY}^{-1}]^{X\overline{s}Y\overline{t}} \\ &= [\delta_A^Y+\delta_A^X][\boldsymbol{\sigma}_{\alpha,XX}^{-1}(\boldsymbol{\sigma}_{\alpha,XY}-\boldsymbol{\sigma}_{\alpha,XO}\boldsymbol{\sigma}_{\alpha,OO}^{-1}\boldsymbol{\sigma}_{\alpha,OY})\boldsymbol{\sigma}_{\alpha,YY}^{-1}]^{X\overline{s}Y\overline{t}}\end{aligned} \tag{3.57}$$

3.5.6 Linearly Dependent SCFMI Population Derivatives

The first and second derivatives of populations with respect to the degrees of freedom in the linearly dependent SCFMI subspaces, $\{X'\}$, described in the text can be obtained by replacing unprimed SCFMI subspace labels in (3.53) and (3.54) with their primed counterparts ($\mathbf{C}_{\alpha,X'} \leftarrow \mathbf{C}_{\alpha,X}$ etc). The statements made in the text assume that the vectors spanning the

primed subspaces are constructed in a specific way (3.32) from unprimed $\mathbf{G}_\alpha = \mathbf{M}_\alpha$ SCFMI subspaces. Rewriting the primed variants of (3.53) and (3.54) in terms of Mulliken-domain attributed vectors yields:

$$\left.\frac{\partial \mathrm{Pop}_{\alpha,A}}{\partial(\Delta_{\alpha,X'})_{X\hat{p}C\hat{q}}}\right|_{\Delta_\alpha=0} = \sum_E [\delta^{X\hat{p}}_{E\hat{r}}\delta^{C\hat{q}}_{X\hat{i}} - \delta^{X\hat{p}}_{X\hat{i}}\delta^{C\hat{q}}_{E\hat{r}}] \tag{3.58}$$
$$\times[\sum_{Z'}(\boldsymbol{\sigma}_{\alpha,OO})^{-1}\mathbf{T}^T_{\alpha,Z'}\mathbf{G}^T_\alpha\mathbf{S}(\mathbf{P}_{\alpha,A}+\mathbf{P}^T_{\alpha,A})\mathbf{S}(\mathbf{I}-\mathbf{P}_\alpha\mathbf{S})\mathbf{G}_\alpha\mathbf{C}_{\alpha,X'}(\boldsymbol{\sigma}_{\alpha,X'X'})^{-1}]^{X\hat{i}E\hat{r}}$$

$$\left.\frac{\partial^2 \mathrm{Pop}_{\alpha,A}}{\partial(\Delta_{\alpha,X'})_{X\hat{p}C\hat{q}}\partial(\Delta_{\alpha,Y'})_{Y\hat{n}D\hat{o}}}\right|_{\Delta_\alpha=0} \tag{3.59}$$
$$+\delta^{X'}_{Y'}\frac{1}{2}\sum_{EFG}[+\delta^{X\hat{p}}_{E\hat{t}}\delta^{C\hat{q}}_{F\hat{u}}\delta^{Y\hat{n}}_{G\hat{v}}\delta^{D\hat{o}}_{X\hat{k}} - \delta^{X\hat{p}}_{E\hat{t}}\delta^{C\hat{q}}_{F\hat{u}}\delta^{D\hat{o}}_{G\hat{v}}\delta^{Y\hat{n}}_{X\hat{k}} - \delta^{C\hat{q}}_{E\hat{t}}\delta^{X\hat{p}}_{F\hat{u}}\delta^{Y\hat{n}}_{G\hat{v}}\delta^{D\hat{o}}_{X\hat{k}} + \delta^{C\hat{q}}_{E\hat{t}}\delta^{X\hat{p}}_{F\hat{u}}\delta^{D\hat{o}}_{G\hat{v}}\delta^{Y\hat{n}}_{X\hat{k}}$$
$$+\delta^{Y\hat{n}}_{E\hat{t}}\delta^{D\hat{o}}_{F\hat{u}}\delta^{X\hat{p}}_{G\hat{v}}\delta^{C\hat{q}}_{X\hat{k}} - \delta^{Y\hat{n}}_{E\hat{t}}\delta^{D\hat{o}}_{F\hat{u}}\delta^{C\hat{q}}_{G\hat{v}}\delta^{X\hat{p}}_{X\hat{k}} - \delta^{D\hat{o}}_{E\hat{t}}\delta^{Y\hat{n}}_{F\hat{u}}\delta^{X\hat{p}}_{G\hat{v}}\delta^{C\hat{q}}_{X\hat{k}} + \delta^{D\hat{o}}_{E\hat{t}}\delta^{Y\hat{n}}_{F\hat{u}}\delta^{C\hat{q}}_{G\hat{v}}\delta^{X\hat{p}}_{X\hat{k}}]$$
$$\times[\sum_{Z'}\boldsymbol{\sigma}^{-1}_{\alpha,OO}\mathbf{T}^T_{\alpha,Z'}\mathbf{G}^T_\alpha\mathbf{S}(\mathbf{P}_{\alpha,A}+\mathbf{P}^T_{\alpha,A})\mathbf{S}(\mathbf{I}-\mathbf{P}_\alpha\mathbf{S})\mathbf{G}_\alpha\mathbf{C}_{\alpha,X'}\boldsymbol{\sigma}^{-1}_{\alpha,X'X'}]^{X\hat{k}E\hat{\bar{t}}}(\sigma^{-1}_{\alpha,X'X'})^{F\hat{u}G\hat{v}}$$
$$+\sum_{EF}[\delta^{X\hat{p}}_{X\hat{l}}\delta^{C\hat{q}}_{E\hat{s}}\delta^{Y\hat{n}}_{Y\hat{k}}\delta^{D\hat{o}}_{F\hat{t}} - \delta^{X\hat{p}}_{X\hat{l}}\delta^{C\hat{q}}_{E\hat{s}}\delta^{D\hat{o}}_{Y\hat{k}}\delta^{Y\hat{n}}_{F\hat{t}} - \delta^{C\hat{q}}_{X\hat{l}}\delta^{X\hat{p}}_{E\hat{s}}\delta^{Y\hat{n}}_{Y\hat{k}}\delta^{D\hat{o}}_{F\hat{t}} + \delta^{C\hat{q}}_{X\hat{l}}\delta^{X\hat{p}}_{E\hat{s}}\delta^{D\hat{o}}_{Y\hat{k}}\delta^{Y\hat{n}}_{F\hat{t}}]$$
$$\times\Big[(\sigma^{-1}_{\alpha,OO})^{X\hat{l}Y\hat{k}}[\boldsymbol{\sigma}^{-1}_{\alpha,X'X'}\mathbf{C}^T_{\alpha,X'}\mathbf{G}^T_\alpha(\mathbf{I}-\mathbf{S}\mathbf{P}_\alpha)\mathbf{S}(\mathbf{P}_{\alpha,A}+\mathbf{P}^T_{\alpha,A})\mathbf{S}(\mathbf{I}-\mathbf{P}_\alpha\mathbf{S})\mathbf{G}_\alpha\mathbf{C}_{\alpha,Y'}\boldsymbol{\sigma}^{-1}_{\alpha,Y'Y'}]^{E\hat{s}F\hat{\bar{t}}}$$
$$-[\sum_{Z'}\boldsymbol{\sigma}^{-1}_{\alpha,OO}\mathbf{T}^T_{\alpha,Z'}\mathbf{G}^T_\alpha\mathbf{S}(\mathbf{P}_{\alpha,A}+\mathbf{P}^T_{\alpha,A})\mathbf{S}(\mathbf{I}-\mathbf{P}_\alpha\mathbf{S})\mathbf{G}_\alpha\mathbf{C}_{\alpha,Y'}\boldsymbol{\sigma}^{-1}_{\alpha,Y'Y'}]^{X\hat{l}F\hat{\bar{t}}}$$
$$\times[\sum_{W'}\boldsymbol{\sigma}^{-1}_{\alpha,OO}\mathbf{T}^T_{\alpha,W'}\boldsymbol{\Gamma}_\alpha\mathbf{C}_{\alpha,X'}\boldsymbol{\sigma}^{-1}_{\alpha,X'X'}]^{Y\hat{k}E\hat{\bar{s}}}$$
$$-[\sum_{Z'}\boldsymbol{\sigma}^{-1}_{\alpha,OO}\mathbf{T}^T_{\alpha,Z'}\mathbf{G}^T_\alpha\mathbf{S}(\mathbf{P}_{\alpha,A}+\mathbf{P}^T_{\alpha,A})\mathbf{S}(\mathbf{I}-\mathbf{P}_\alpha\mathbf{S})\mathbf{G}_\alpha\mathbf{C}_{\alpha,X'}\boldsymbol{\sigma}^{-1}_{\alpha,X'X'}]^{Y\hat{k}E\hat{\bar{s}}}$$
$$\times[\sum_{W'}\boldsymbol{\sigma}^{-1}_{\alpha,OO}\mathbf{T}^T_{\alpha,W'}\boldsymbol{\Gamma}_\alpha\mathbf{C}_{\alpha,Y'}\boldsymbol{\sigma}^{-1}_{\alpha,Y'Y'}]^{X\hat{l}F\hat{\bar{t}}}$$
$$-[\sum_{Z'W'}\boldsymbol{\sigma}^{-1}_{\alpha,OO}\mathbf{T}^T_{\alpha,Z'}\mathbf{G}^T_\alpha\mathbf{S}(\mathbf{P}_{\alpha,A}+\mathbf{P}^T_{\alpha,A})\mathbf{S}\mathbf{G}_\alpha\mathbf{T}_{\alpha,W'}\boldsymbol{\alpha}^{-1}_{\alpha,OO}]^{Y\hat{k}X\hat{l}}$$
$$\times[\boldsymbol{\sigma}^{-1}_{\alpha,Y'Y'}\mathbf{C}^T_{\alpha,Y'}\mathbf{G}^T_\alpha(\mathbf{S}-\mathbf{S}\mathbf{P}_\alpha\mathbf{S})\mathbf{G}_\alpha\mathbf{C}_{\alpha,X'}\boldsymbol{\sigma}^{-1}_{\alpha,X'X'}]^{F\hat{\bar{t}}E\hat{\bar{s}}}\Big]$$

In these expressions, matching primed and unprimed subspace indices, X' and X, are coupled because all occupied vectors in subspace X' have Mulliken-domain labels X. This coupling of indices is also described by (3.32). The gradient and Hessian for the degrees of freedom present in the unprimed subspace SCFMI are recovered for $X = C$ and $Y = D$ in the above, and these can be shown using the results for important cases below to both be zero. The derivatives for the newly introduced delocalization degrees of freedom are given by $X \neq C$ and $Y \neq D$. Orthogonal Mulliken domains refers to the case where the columns of $\mathbf{M}_\alpha$ are orthogonal, and thus at our initial condition we can choose without loss of generality to have $\boldsymbol{\sigma}_{\alpha,OO}$, $\boldsymbol{\sigma}_{\alpha,XX}$, $\boldsymbol{\sigma}_{\alpha,X'X'}$, and $\boldsymbol{\mu}_\alpha$ all $\mathbf{I}$.

$$[\sum_{Z'W'}\boldsymbol{\sigma}^{-1}_{\alpha,OO}\mathbf{T}^T_{\alpha,Z'}\mathbf{G}^T_\alpha\mathbf{S}(\mathbf{P}_{\alpha,A}+\mathbf{P}^T_{\alpha,A})\mathbf{S}\mathbf{G}_\alpha\mathbf{T}_{\alpha,W'}\boldsymbol{\alpha}^{-1}_{\alpha,OO}]^{Y\hat{k}X\hat{l}} = (\sigma^{-1}_{\alpha,OO})^{Y\hat{k}X\hat{l}}[\delta^X_A + \delta^Y_A] \tag{3.60}$$

$$[\sum_{Z'}\boldsymbol{\sigma}^{-1}_{\alpha,OO}\mathbf{T}^{T}_{\alpha,Z'}\mathbf{G}^{T}_{\alpha}\mathbf{S}(\mathbf{P}_{\alpha,A}+\mathbf{P}^{T}_{\alpha,A})\mathbf{S}(\mathbf{I}-\mathbf{P}_{\alpha}\mathbf{S})\mathbf{G}_{\alpha}\mathbf{C}_{\alpha,Y'}\boldsymbol{\sigma}^{-1}_{\alpha,Y'Y'}]^{X\hat{l}F\hat{\tilde{t}}} \tag{3.61}$$

$$= \left[\sum_{Z}\boldsymbol{\sigma}^{-1}_{\alpha,OO}\mathbf{T}^{T}_{\alpha,Z}\boldsymbol{\mu}_{\alpha}\right]^{X\hat{l}\,\bullet}_{\bullet\,A\tilde{\gamma}}\left((\mathbf{C}_{\alpha,A})^{A\tilde{\gamma}}_{\bullet\,Aq}(\boldsymbol{\sigma}^{-1}_{\alpha,Y'Y'})^{A\hat{q}F\hat{t}}-\sum_{E}[(\mathbf{I}-\delta^{Y}_{E})\delta^{Y}_{A}\boldsymbol{\mu}^{-1}_{\alpha,YY}\boldsymbol{\mu}_{\alpha,YE}\mathbf{C}_{\alpha,E}]^{A\tilde{\gamma}}_{\bullet\,Eq}(\boldsymbol{\sigma}^{-1}_{\alpha,Y'Y'})^{E\hat{q}F\hat{t}}\right)$$

$$-\delta^{X}_{A}\left[\boldsymbol{\sigma}^{-1}_{\alpha,OO}\boldsymbol{\sigma}_{\alpha,OY'}\boldsymbol{\sigma}^{-1}_{\alpha,Y'Y'}\right]^{X\hat{l}F\hat{t}}$$

$$= (\text{CASE: } F=Y)\rightarrow[\boldsymbol{\sigma}^{-1}_{\alpha,OO}\boldsymbol{\sigma}_{\alpha,OA}]^{X\hat{l}\,\bullet}_{\bullet\,Aq}(\boldsymbol{\sigma}^{-1}_{\alpha,Y'Y'})^{A\hat{q}F\hat{t}}-\delta^{X}_{A}[\boldsymbol{\sigma}^{-1}_{\alpha,OO}\boldsymbol{\sigma}_{\alpha,OY'}\boldsymbol{\sigma}^{-1}_{\alpha,Y'Y'}]^{X\hat{l}F\hat{t}}$$

$$= (\text{CASE: } F=Y=X)\rightarrow 0$$

$$= (\text{CASE: Orthogonal Mulliken Domains})\rightarrow 0$$

$$\begin{aligned}
[\boldsymbol{\sigma}^{-1}_{\alpha,X'X'}\mathbf{C}^{T}_{\alpha,X'}\mathbf{G}^{T}_{\alpha}(\mathbf{I}-\mathbf{SP}_{\alpha})\mathbf{S}(\mathbf{P}_{\alpha,A}+\mathbf{P}^{T}_{\alpha,A})\mathbf{S}(\mathbf{I}-\mathbf{P}_{\alpha}\mathbf{S})\mathbf{G}_{\alpha}\mathbf{C}_{\alpha,Y'}\boldsymbol{\sigma}^{-1}_{\alpha,Y'Y'}]^{E\hat{\tilde{s}}F\hat{\tilde{t}}} = \\
+\sum_{G}(\boldsymbol{\sigma}^{-1}_{\alpha,X'X'})^{E\hat{s}G\hat{v}}[\mathbf{C}^{T}_{\alpha,G}(\mathbf{I}-\mathbf{S}\boldsymbol{\Phi}_{\alpha,X})\mathbf{S}(\mathbf{I}-\mathbf{PS})\mathbf{C}_{\alpha,A}]_{GvAu}(\boldsymbol{\sigma}^{-1}_{\alpha,Y'Y'})^{A\hat{u}F\hat{t}} \\
+\sum_{H}(\boldsymbol{\sigma}^{-1}_{\alpha,X'X'})^{E\hat{s}A\hat{v}}[\mathbf{C}^{T}_{\alpha,A}(\mathbf{I}-\mathbf{SP})\mathbf{S}(\mathbf{I}-\boldsymbol{\Phi}_{\alpha,Y}\mathbf{S})\mathbf{C}_{\alpha,H}]_{AvHu}(\boldsymbol{\sigma}^{-1}_{\alpha,Y'Y'})^{H\hat{u}F\hat{t}} \\
+\delta^{X}_{E}(\boldsymbol{\sigma}^{-1}_{\alpha,X'X'})^{E\hat{s}X\hat{v}}[\mathbf{C}^{T}_{\alpha,X}\mathbf{S}(\mathbf{I}-\mathbf{PS})\mathbf{C}_{\alpha,A}]_{XvAu}(\boldsymbol{\sigma}^{-1}_{\alpha,Y'Y'})^{A\hat{u}F\hat{t}} \\
+\delta^{Y}_{F}(\boldsymbol{\sigma}^{-1}_{\alpha,X'X'})^{E\hat{s}A\hat{v}}[\mathbf{C}^{T}_{\alpha,A}(\mathbf{I}-\mathbf{SP})\mathbf{SC}_{\alpha,Y}]_{AvYu}(\boldsymbol{\sigma}^{-1}_{\alpha,Y'Y'})^{Y\hat{u}F\hat{t}} \\
+\sum_{G}\delta^{Y}_{F}\delta^{Y}_{A}(\boldsymbol{\sigma}^{-1}_{\alpha,X'X'})^{E\hat{s}G\hat{v}}[\mathbf{C}^{T}_{\alpha,G}(\mathbf{I}-\mathbf{S}\boldsymbol{\Phi}_{\alpha,X})\mathbf{S}(\mathbf{I}-\mathbf{PS})\mathbf{C}_{\alpha,Y}]_{GvYu}(\boldsymbol{\sigma}^{-1}_{\alpha,Y'Y'})^{Y\hat{u}F\hat{t}} \\
+\sum_{H}\delta^{X}_{E}\delta^{X}_{A}(\boldsymbol{\sigma}^{-1}_{\alpha,X'X'})^{E\hat{s}X\hat{v}}[\mathbf{C}^{T}_{\alpha,X}(\mathbf{I}-\mathbf{SP})\mathbf{S}(\mathbf{I}-\boldsymbol{\Phi}_{\alpha,Y}\mathbf{S})\mathbf{C}_{\alpha,H}]_{XvHu}(\boldsymbol{\sigma}^{-1}_{\alpha,Y'Y'})^{H\hat{u}F\hat{t}} \\
-\sum_{H}\delta^{X}_{E}\delta^{Y}_{A}(\boldsymbol{\sigma}^{-1}_{\alpha,X'X'})^{E\hat{s}X\hat{v}}[\mathbf{C}^{T}_{\alpha,X}\mathbf{S}(\mathbf{I}-\mathbf{PS})\boldsymbol{\Phi}_{\alpha,Y}\mathbf{SC}_{\alpha,H}]_{XvHu}(\boldsymbol{\sigma}^{-1}_{\alpha,Y'Y'})^{H\hat{u}F\hat{t}} \\
-\sum_{G}\delta^{Y}_{F}\delta^{X}_{A}(\boldsymbol{\sigma}^{-1}_{\alpha,X'X'})^{E\hat{s}G\hat{v}}[\mathbf{C}^{T}_{\alpha,G}\mathbf{S}\boldsymbol{\Phi}_{\alpha,X}(\mathbf{I}-\mathbf{SP})\mathbf{SC}_{\alpha,Y}]_{GvYu}(\boldsymbol{\sigma}^{-1}_{\alpha,Y'Y'})^{Y\hat{u}F\hat{t}} \\
-\sum_{GH}(\boldsymbol{\sigma}^{-1}_{\alpha,X'X'})^{E\hat{s}G\hat{v}}[\mathbf{C}^{T}_{\alpha,G}\mathbf{S}(\delta^{X}_{A}\boldsymbol{\Phi}_{\alpha,X}(\mathbf{I}-\mathbf{SP})+\delta^{Y}_{A}(\mathbf{I}-\mathbf{PS})\boldsymbol{\Phi}_{\alpha,Y})\mathbf{SC}_{\alpha,H}]_{GvHu}(\boldsymbol{\sigma}^{-1}_{\alpha,Y'Y'})^{H\hat{u}F\hat{t}} \\
+\delta^{Y}_{F}\delta^{X}_{E}(\delta^{X}_{A}+\delta^{Y}_{A})(\boldsymbol{\sigma}^{-1}_{\alpha,X'X'})^{E\hat{s}X\hat{v}}[\mathbf{C}^{T}_{\alpha,X}(\mathbf{I}-\mathbf{SP})\mathbf{SC}_{\alpha,Y}]_{XvYu}(\boldsymbol{\sigma}^{-1}_{\alpha,Y'Y'})^{Y\hat{u}F\hat{t}} \\
+\sum_{GH}(\delta^{X}_{A}+\delta^{Y}_{A})(\boldsymbol{\sigma}^{-1}_{\alpha,X'X'})^{E\hat{s}G\hat{v}}[\mathbf{C}^{T}_{\alpha,G}\mathbf{S}\boldsymbol{\Phi}_{\alpha,X}(\mathbf{I}-\mathbf{SP})\mathbf{S}\boldsymbol{\Phi}_{\alpha,Y}\mathbf{SC}_{\alpha,H}]_{GvHu}(\boldsymbol{\sigma}^{-1}_{\alpha,Y'Y'})^{H\hat{u}F\hat{t}} \\
= (\text{CASE: } E=X, F=Y)\rightarrow \\
+\delta^{Y}_{A}(\boldsymbol{\sigma}^{-1}_{\alpha,X'X'})^{E\hat{s}X\hat{v}}[\mathbf{C}^{T}_{\alpha,X}\mathbf{S}(\mathbf{I}-\mathbf{PS})\mathbf{C}_{\alpha,A}]_{XvAu}(\boldsymbol{\sigma}^{-1}_{\alpha,Y'Y'})^{A\hat{u}F\hat{t}} \\
+\delta^{X}_{A}(\boldsymbol{\sigma}^{-1}_{\alpha,X'X'})^{E\hat{s}A\hat{v}}[\mathbf{C}^{T}_{\alpha,A}(\mathbf{I}-\mathbf{SP})\mathbf{SC}_{\alpha,Y}]_{AvYu}(\boldsymbol{\sigma}^{-1}_{\alpha,Y'Y'})^{Y\hat{u}F\hat{t}} \\
= (\text{CASE: Orthogonal Mulliken Domains})\rightarrow 2\delta^{E\hat{s}}_{A\hat{a}}\delta^{F\hat{t}}_{A\hat{a}}
\end{aligned} \tag{3.62}$$

Chapter 4

Alternative Definitions of the Frozen Energy

4.1 Introduction

An energy decomposition analysis (EDA) is a tool in electronic structure theory that partitions the interaction energy of a system of fragments, an observable, into a sum of energy terms that are not observables but carry chemical meaning. Such terms typically include polarization, charge transfer, permanent electrostatics, dispersion, and Pauli repulsion. Such decompositions can build intuition about the given system and thus inform the question of what chemical modifications of the system would produce a desired change in the interaction energy or other related observables. Because the total energy of interest is the difference between that of the supersystem and the non-interacting component subsystems, the decompositions generally involve a progression from many subsystem wavefunctions to a single, optimal supersystem wavefunction. The differences between the energies of the wavefunctions produced in this stepwise progression yield contributions that are either interaction components in themselves or sums of interaction components that need to be further decomposed.

An important but of course non-unique intermediate electronic wavefunction in this sequence is the first one in which all electrons in the system are described together. The meaning associated with the energy of such a wavefunction relative to those of the isolated subsystems is usually taken as a combination of permanent electrostatics and Pauli repulsion.[74] This initial supersystem wavefunction, and its construction in the single Slater determinant case (i.e. Kohn-Sham density functional theory, and mean-field molecular orbital theory), is the central concern of this work. A single Slater determinant wavefunction is completely defined by its one-particle density matrix, and thus density matrices and wavefunctions will be used interchangeably throughout.

There are many EDA schemes but currently only a handful of distinct ways used to

construct the initial supersystem wavefunction. The simplest choice is to throw Fermionic quantum mechanics to the wayside and adopt the Hartree product of monomer wavefunctions as the initial supersystem electronic wavefunction despite its lack of proper antisymmetry with respect to electron variables. This approach is employed by methods such as the polarization theory [20], KM EDA[38, 86, 87], PIEDA[88, 89], and CAFI[95], which are older methods or are adapted from older methods. These approaches, except for the polarization theory, which is only valid for well-separated fragments, eventually account for antisymmetry in the supersystem wavefunction but not until after a classical polarization procedure has been performed.

A majority of methods including SAPT[19, 20, 22–24], Bickelhaupt-Baerends EDA [44, 76, 77], NOCV-ETS [39–41, 78], GKS-EDA [45, 80, 81], CSOV[42], RVS[43, 87], the CI-singles based scheme of Reinhardt et al.[79], the method of De Silva and Korchowiec[97], the method of Mandado and Hermida-Ramón[82], BLW-EDA[46–48] (though not so obviously in later works[49]), and ALMO-EDA[15–18] employ the antisymmetric product of isolated monomer wavefunctions, the Heitler-London wavefunction, as the initial supersystem wavefunction. We note that some of these methods also make use of the Hartree product wavefunction to separate out a classical permanent electrostatic contribution to the Heitler-London energy, which makes it somewhat unclear whether the Hartree product or the Heitler-London wavefunction should be considered "first". Another method, NEDA [34–37, 85], also uses the antisymmetric product though not of the isolated monomer wavefunctions but rather of the NBO-determined monomer Lewis-like determinants.

A refreshingly different definition for the initial supersystem wavefunction is used in the density-based EDA (DEDA) scheme of Wu[51, 75]. The DEDA method uses constrained DFT to define the initial wavefunction as the lowest energy single Slater determinant that has a 3-space density equivalent to the sum of isolated fragment densities. Relative to other EDA's, the DEDA is the first approach to add an energetic optimality condition to the construction of the initial supersystem wavefunction while still making a connection to the properties of isolated fragments. This energetic optimality is necessary because the Kohn Sham energy depends on the non-interacting one-particle density matrix at least through the the kinetic energy operator. The mapping between one-particle density matrices and 3-space densities is many-to-one by virtue of linear dependence in the products of basis functions used to construct the density matrix[113].

For the DEDA examples presented by Wu et al[51, 75], minimization with constant sum of fragments density yielded very significant energy lowering beyond the frozen orbital energy used in EDA's such as the KM-EDA, the BLW-EDA, and the ALMO-EDA. For example, for the water dimer using B3LYP/aug-cc-pVQZ at R_e, the frozen orbital interaction energy is -5 kJ/mol, while the DEDA approach yields a frozen energy of -13 kJ/mol, relative to the total interaction energy of -19 kJ/mol. Thus the choice of frozen energy has important consequences for the interpretative purposes of the EDA.

It is accordingly important to better understand the origin of the large energetic differences between the DEDA frozen energy and the frozen orbital initial energy. Is it intra-

Method	P_{target}	**Orbitals**
P_{frz}	P_{frz}	none
ρ_{sum}-SCF	$\sum_A P_A$	SCF
ρ_{frz}-SCF	P_{frz}	SCF
ρ_{frz}-SCFMI	P_{frz}	SCFMI

Table 4.1: Summary of methods used to compute the frozen energy EDA component. P_{target} is the matrix which upon collapse defines the 3-space density constraint, and the orbital degrees of freedom specify which rotations are allowed during density matrix optimization. The frozen energy method labeled P_{frz} is equivalent to that used in ALMO-EDA among others and involves no energetic optimality component. The frozen energy method labeled ρ_{frz}-SCF is equivalent to that used in Wu's DEDA[51, 75].

fragment relaxation, corresponding to relieving steric repulsions, without changing the density? Or are there also important contributions from inter-fragment relaxation, corresponding to forward and backward charge transfer at constant density? Is there also a significant effect from the different choice of target density relative to other EDA's? Finally, since the constraint of constant density can only be approximately enforced, is it possible to measure the energetic consequences of small deviations from exact constraint satisfaction? These are the issues that this paper will attempt to address by comparing numerical results for the frozen orbital model, the DEDA frozen density model, and two other related methods.

4.2 Models for the initial supersystem wavefunction

General notation in this work is as follows: subspace indices: capital Roman $X, Y...$; AO basis indices: lower case Greek μ, $\nu...$; virtual MO indices: $a, b...$; occupied MO indices: $i, j...$; generic MO indices: $r, s.....$ This work considers non-orthogonal subspaces and thus makes use of tensors with both covariant (subscript) and contravariant (superscript) indices.[63] Dots are used as placeholders for clear index ordering in quantities that have both covariant and contravariant indices. For instance, the matrix $\mathbf{C}_\alpha$ with matrix elements $(C_\alpha)^{X\mu}_{\bullet\ \bullet}{}_{Yr}$ has rows corresponding to contravariant basis vectors associated with subspace X and columns corresponding to covariant molecular orbitals associated with subspace Y, both occupied and virtual. Further notation will be introduced as needed.

Given subsystem single determinant wavefunctions optimized in isolation, there is no unique way to construct an initial supersystem single determinant wavefunction, unless one simply performs the full optimization, which includes all interactions. With unfettered energetic optimality eliminated, we are left with constructing an initial supersystem wavefunction for the supersystem that in some specified sense closely resembles the isolated subsystems' wavefunctions. There are four alternatives considered in this work, which are summarized in Table 4.1 and outlined in detail below.

4.2.1 The Frozen Orbital Model ($P_{\mathbf{frz}}$)

To guarantee a valid single Slater determinant wavefunction from which a valid energy can be evaluated, the most basic model simply uses the frozen orbitals of each fragment. They are non-orthogonal from one fragment to the next, and therefore a valid one-particle density matrix must include the appropriate metric:

$$P_{\alpha}^{\mu\nu} = \sum_{AB} (C_{\alpha})^{\mu}_{\bullet\ Ai} (\sigma^{-1}_{\alpha,OO})^{AiBj} (C_{\alpha})^{\nu}_{\bullet\ Bj} \tag{4.1}$$

where the isolated fragment MO coefficient matrices, $\{\mathbf{C}_A\}$, employed to compute the frozen orbital density matrix, $\mathbf{P}_{frz}$, by (4.1) are those with columns spanning the optimal occupied subspaces of all subsystems in isolation. In previous works on SCFMI-based EDA, this projector has been referred to as the frozen orbital density matrix, and it is equivalent to the density matrix for the single determinant Heitler-London wavefunction built as the antisymmetric product of subsystem Slater determinants. The frozen orbital density matrix in turn yields a frozen density as $\rho_{\text{frz}}(\mathbf{r}) = P_{\text{frz}}(\mathbf{r}, \mathbf{r})$, as well as the energy corresponding to the frozen orbital initial supersystem wavefunction: $E^{\text{frz}}_{\text{initial}} = E(\mathbf{P}_{frz})$.

An equivalent derivation of the projector corresponding to Eq. 4.1 is to form the sum of the occupied subspace projectors for the isolated subsystems, $\mathbf{P}_{\text{sum}}$. $\mathbf{P}_{\text{sum}}$ is not generally a valid projector, as the sum of projectors is not a projector when they are non-orthogonal (i.e. its eigenvalues deviate from 0 and 1). The idempotent projector that is closest to this simple sum may be found by successive applications of the well-known McWeeny purification[114] beginning with $\mathbf{P}^{(0)} = \mathbf{P}_{\text{sum}}$:

$$\mathbf{P}^{(i+1)} = \mathbf{3P}^{(i)}\mathbf{SP}^{(i)} - \mathbf{2P}^{(i)}\mathbf{SP}^{(i)}\mathbf{SP}^{(i)} \tag{4.2}$$

It has been proven that the final result of that sequence, $\mathbf{P}^{(\infty)}$, is geometrically optimal, in the sense of being the closest valid projector to $\mathbf{P}_{\text{sum}}$ in the space of matrices [115]. It is moreover straightforward to prove that under mild conditions $\mathbf{P}_{frz} = \mathbf{P}^{(\infty)}$.

The frozen orbital density matrix thus defines a geometrically optimal initial supersystem wavefunction, and its corresponding $\rho(r)$ will be in non-trivial cases different from the sum of subsystem densities. The distortion of this density relative to the simple sum is a consequence of the requirement for an antisymmetric electronic wavefunction, and its qualitative features been discussed in detail by other authors[44]. Briefly, the distortions include a depletion of electron density in the overlapping region and an increase in electron density near nuclei, resulting in higher electron kinetic energy and lower electron-nuclear potential energy.

4.2.2 Energy minimization with sum of fragment densities ($\rho_{\mathbf{sum}}$-SCF)

This approach is the basis of Wu's Density-based Energy Decomposition Analysis (DEDA). Imagine translating the electron densities of the subsystems along with their respective nu-

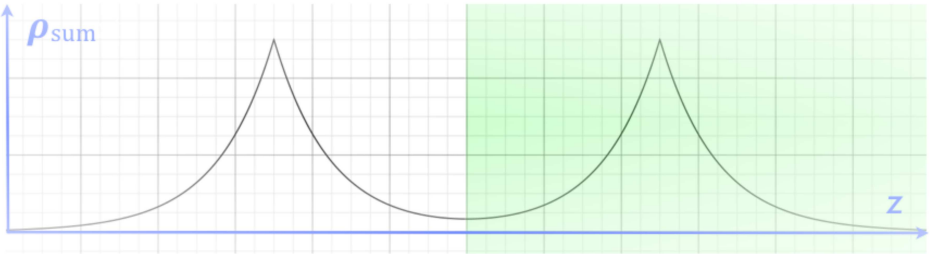

Figure 4.1: Sum of densities, ρ_{sum}, for a helium dimer system, showing a sharp division into two fragment quantities in the overlapping regime. This sharp division is a feasible point, in the sense that it can be represented by two localized orthogonal orbitals, in a complete basis set. It is not a feasible point in a finite basis set, such as a minimal basis, composed of smooth functions.

clei from infinitely far away to the supersystem geometry, resulting in a supersystem 3-space electron density, $\rho_{\text{sum}}(\mathbf{r})$, that is the sum of subsystem densities:

$$\rho_{\text{sum}}(\mathbf{r}) = \sum_A \rho_A(\mathbf{r}) \tag{4.3}$$

The correct number of electrons is obtained. This method appears classical both because it discounts electronic wavefunction antisymmetry and because the classical electrostatic interaction between these translated nuclei and electron densities is used to define the permanent electrostatic interaction energy component in some EDAs.

Is there, by extension, a valid supersystem occupied subspace "projector" that is a sum of subsystem occupied subspace projectors? The sum of projectors is only a projector if the respective vectors defining the spans are orthogonal from one span to the next or equivalently if the metric for the collection of these vectors is subspace-block-diagonal. This is trivially true for non-overlapping (i.e. weakly interacting) fragments and *can* also be true in the strongly interacting case. For example one could re-partition $\rho_{\text{sum}}(\mathbf{r})$ into *non-overlapping* spatial domains corresponding to each fragment, with each having its original number of electrons, as illustrated schematically for a symmetric helium-dimer-like system in Figure 4.1. This will enable subsystem projectors to be strongly orthogonal, and is a feasible point, at least in a complete basis set. By contrast, in a minimal basis for two overlapping He atoms, such a feasible point does not exist. We believe the question of whether or not feasible points strictly exist in larger finite basis sets is open.

Wu employs constrained DFT to compute the lowest energy single Slater determinant for the supersystem with the constraint that its corresponding $\rho(r)$ equals the sum of isolated fragment densities:

$$E_{\text{initial}}^{(\text{sum,SCF})} = \underset{\rho_{\text{sum}} \leftarrow \mathbf{P}}{\text{minimize}}\, E[\mathbf{P}] \tag{4.4}$$

There are two interesting issues with this approach. The first, already discussed above, is that if a feasible solution does not exist, then constrained DFT algorithm does not impose a constraint, but instead adds an energetic penalty that enforces similarity between the actual 3-space density of the wavefunction and $\rho_{\text{sum}}(\mathbf{r})$.

The second interesting issue concerns the interpretation of the energy lowering associated with a wavefunction optimized in such a way. Neglecting numerical challenges discussed later, the energy is lowered from an initial feasible point (such as $\mathbf{P}_{frz}$) by constant density orbital mixings between occupied and empty orbitals that are either on the same fragment or on different fragments. For EDA purposes, it is desirable to distinguish these two cases, since the latter is essentially constant density charge transfer (CT), which is typically separated from the electrostatic, Pauli and dispersion interactions associated with the frozen energy. The fourth method discussed below preserves this separation. On the other hand, there are other applications of the frozen energy, such as parameterizing force field models that lack explicit CT terms, where it may be desirable to include the constant density CT in the frozen energy. Thus the merit of a particular frozen energy definition must be assessed on the basis of the intended application.

4.2.3 Energy minimization with the constraint of frozen orbital density (ρ_{frz}-SCF)

The issue of existence or non-existence of valid projectors yielding ρ_{sum} in Wu's density matching constraint can be circumvented by instead requiring the density to match the frozen orbital density, ρ_{frz}, in a constrained minimization of the frozen energy:

$$E_{\text{initial}}^{(\text{frz,SCF})} = \underset{\rho_{\text{frz}} \leftarrow \mathbf{P}}{\text{minimize}} E\left[\mathbf{P}\right] \tag{4.5}$$

The result of this minimization is necessarily an energy lowering relative to the frozen orbital energy, and various numerical tests of this energy difference will be presented later. Relative to energy minimization constrained to ρ_{sum}, the optimized energy, $E_{\text{initial}}^{(\text{frz,SCF})}$, could be either higher or lower, a fact that will be confirmed with numerical examples. In both cases, the constant density relaxation must be viewed as including both intra-fragment and inter-fragment contributions.

4.2.4 Energy minimization with constrained density and without charge transfer (ρ_{frz}-SCFMI)

Constant density minimization requires an additional constraint to formally prohibit CT between fragments. There is a long history [15, 64, 65, 99, 116, 117] of using the constraint of a fragment-blocked MO coefficient matrix to describe polarization and exclude CT, defining the so-called self-consistent field method for molecular interactions (SCF-MI). SCF-MI in the

AO basis is used to describe polarization in the widely used BLW-EDA and ALMO-EDA methods. Fragment-blocking retains the form of the MO coefficients associated with the frozen-orbital density matrix, (4.1), which is therefore the natural initial guess. Use of ρ_{frz} for the density constraint is also natural, since we are guaranteed the initial feasible point, $\mathbf{P}_{\text{frz}}$.

It is important to note that the SCF-MI method in the AO basis does not converge to a useful basis set limit for polarization. This is because more and more of the CT contribution can be captured by SCF-MI as the AO basis set size is increased [69](Chapter 3). To address this problem, as well as to permit the SCF-MI method to be applied to systems where the underlying basis may not be fragment-blocked, we recently developed a polarization basis composed of fragment electrical response functions (FERFs) (Chapter 3). We showed that the FERFs that describe the fragment linear response to a uniform electric field comprise 3 dipolar (D) functions per occupied fragment orbital. Similarly, 5 additional quadrupolar (Q) FERFs describe the fragment linear response to an electric field gradient. Numerical tests showed that the non-orthogonal D+Q polarization model (nDQ) satisfactorily reproduced exact results for polarization in the non-overlapping limit, as well as having a non-trivial basis set limit in the overlapping regime.

While there is no unique separation of polarization and CT in overlapping systems, the SCF-MI/nDQ model is a clearly better choice than use of SCF-MI in the AO basis, and so we choose it as the model that excludes CT. A doubly constrained energy is defined by performing density constrained minimization within the SCF-MI/nDQ model:

$$E_{\text{initial}}^{(\text{frz,SCFMI})} = \underset{\rho_{\text{frz}} \leftarrow \mathbf{P};\ \text{SCFMI/nDQ}}{\text{minimize}} E\left[\mathbf{P}\right] \tag{4.6}$$

The 3-space density constraint employed is the total spinless density. It is the simplest option and it allows the method to be defined for all single Slater determinant methods, though we only employ RKS and UKS in this work.

Defining the initial supersystem wavefunction via (4.6) removes constant density CT via the SCF-MI constraint, and the restriction of collapse to $\rho_{Frz}(r)$ enforces a constant 3-space density on this already restricted surface. As a consequence of this combination of constraints, the following inequalities are true:

$$E_{\text{initial}}^{\text{frz}} \leq E_{\text{initial}}^{(\text{frz,SCF-MI})} \leq E_{\text{pol}}^{\text{SCF-MI}} \tag{4.7}$$

Thus (i) the energy of this determinant is lower than or equal to frozen orbital energy, and (ii) the SCF-MI energy without the density constraint is equal or lower than this determinant. Property (ii) ensures a negative semi-definite value for the polarization energy, which is now computed as the change in the supersystem energy upon the release of the constant 3-space density constraint but with the SCFMI constraint still in place.

4.3 Implementation

4.3.1 Methodology for Computing the Initial Supersystem Wavefunction

The nonlinear problem defined by (4.6) is a minimization of the single determinant electronic energy of a system with both SCFMI and constant density constraints. Methods for optimization on the surface of SCFMI-allowed one-particle density matrices are known[64, 65, 111, 112](Chapter 3); however, the proper parameters for optimization on the surface of constant $\rho(r)$ let alone those for the surface defined by the intersection of the two constraints are not known. We thus resort to the use of Lagrange multipliers and define the following penalty function:

$$E_{\text{penalty}}\left[\delta\mathbf{P}\right] = \frac{1}{2}\delta P^{\mu\nu}\left(\mu\nu|\lambda\sigma\right)\delta P^{\lambda\sigma} \tag{4.8}$$

$$\left(\mu\nu|\lambda\sigma\right) = \iint \omega_\mu(1)\omega_\nu(1)r_{12}^{-1}\omega_\lambda(2)\omega_\sigma(2)d\mathbf{r}_1 d\mathbf{r}_2 \tag{4.9}$$

Here the deviation in the density matrix, $\mathbf{P}$, is defined as $\delta\mathbf{P} = \mathbf{P} - \mathbf{P}_{target}$, where the target density matrix, $\mathbf{P}_{target}$, produces the target density, $\rho_{\text{target}}\left(\mathbf{r}\right) = P_{\text{target}}\left(\mathbf{r},\mathbf{r}\right)$. The energy penalty is the coulomb interaction of the density error, $\delta\rho(\mathbf{r})$ with itself, and will be zero when the densities are identical.

We can thus write a Lagrangian for this constrained optimization problem with a single Lagrange multiplier, λ, as:

$$\mathcal{L}\left[\mathbf{P},\lambda\right] = E\left[\mathbf{P}\right] + \lambda E_{\text{penalty}}\left[\delta\mathbf{P}\right] \tag{4.10}$$

where E is the usual electronic energy as defined by HF or some KS density functional with at most one-particle density matrix dependence. Stationarity with respect to λ enforces (4.8) to be zero. We can solve this optimization problem using an outer loop that monotonically increases λ, which is ideally infinite but is in practice chosen to be sufficiently large such that the penalty function (4.8) is zero to within tolerance, and an inner loop that solves for the optimal $\mathbf{P}$ by (4.10) at fixed λ and of course fixed $\mathbf{P}_{\text{target}}$.

The relevant partial derivatives for the optimization at fixed λ are:

$$\left(F_\lambda\right)_{\mu\nu} \equiv \frac{\partial\mathcal{L}}{\partial P^{\mu\nu}} = F_{\mu\nu} + \lambda\left(F_{\text{penalty}}\right)_{\mu\nu} \tag{4.11}$$

$$\left(F_{\text{penalty}}\right)_{\mu\nu} = \left(\mu\nu|\lambda\sigma\right)\delta P^{\lambda\sigma} \tag{4.12}$$

The above expression for $\mathbf{F}_\lambda$, (4.11), can be used in place of the normal density derivative of the electronic energy, $\mathbf{F}$, in standard gradient- or eigenvalue-based nonlinear solvers to obtain the optimal $\mathbf{P}$ at fixed λ where $\mathbf{P}$ has either full SCF[67, 104] or SCF-MI[64, 65] (Chapter 3) degrees of freedom.

Because of the difficulty in converging the constant λ problem for λ large, the protocol employed in this work consists of a combination of two algorithms. The first is preconditioned L-BFGS[103] using orbital rotation parameters[104, 118] (Chapter 3) and employing a robust line search[119]. The preconditioner used for both surfaces considered is all of $\mathbf{F}_\lambda \cdot \mathbf{P}^{\Delta\Delta}$, which in the case of SCF can be written in terms of $\mathbf{F}_\lambda$ occupied-virtual eigenvalue differences after pseudocanonical transformation and in the case of SCFMI involves a series of nested preconditioned linear equations that have been described previously (Chapter 3). The second algorithm, used ideally for only a single step after the first algorithm has converged to a modest tolerance, is Newton-Raphson. Even when the first algorithm is converged fairly tightly, the objective function is such that the linear equation for the solution of the Newton step by conjugate gradient is generally poorly conditioned, and even with the preconditioning described above the best that can be obtained is an approximate Newton step; however, this is often sufficient.

The Hessian-vector-product needed in the conjugate gradient iterations for the solution of the Newton step (as well as in the determination of the FERF subspaces) can either be computed analytically or by finite difference[120] (with an orbital displacement of order 1.0×10^{-4}) when second functional derivatives are not available. In the former case, the second density derivative of the Lagrangian (4.10) with respect to the density matrix is needed.

$$\frac{\partial^2 \mathcal{L}}{\partial P_\alpha^{\mu\nu} \partial P_\beta^{\pi\sigma}} = \left(\Pi_{\alpha\beta}\right)_{\mu\nu\pi\sigma} + \lambda \left(\mu\nu|\pi\sigma\right) \tag{4.13}$$

$$\left(\Pi_{\alpha\beta}\right)_{\mu\nu\lambda\sigma} \equiv \frac{\partial^2 E}{\partial P_\alpha^{\mu\nu} \partial P_\beta^{\lambda\sigma}} \tag{4.14}$$

The tensor $\mathbf{\Pi}$ involves the two electron integrals and second functional derivatives of the exchange correlation energy in the case of DFT. In practice, the Lagrangian first ((4.11)), and second, ((4.13)) density derivatives are simply used in place of $\mathbf{F}$ and $\mathbf{\Pi}$ respectively in the usual expressions for the Hessians of electronic degrees of freedom.[121] (Chapter 3)

We have chosen to use this method based on the coulomb interaction of the density error with itself instead of the constrained DFT approach[51] to the constant $\rho(r)$ constraint both because it is straightforward to implement and because it has a single parameter, λ, which can be used to increase the fidelity of the 3-space density matching as opposed to the many parameters present in the additional basis expansion of the constraint potential that are necessary in DEDA. In principle it does not matter which approach is used to enforce the constraint as both have the potential to enforce it exactly either with an infinite Lagrange multiplier, λ, or with an infinite potential basis set and all expansion coefficients infinite such that the constraint potential is infinite at all grid points.

There are several measures of the deviation of the optimized density from the constant $\rho(r)$ surface. One possibility is of course the penalty function itself (4.8) though this has little physical relevance. Another with the meaning of displaced electrons[75] is the integral

of the absolute value of the deviation in the density:

$$\epsilon_\rho = \int_{\mathbf{r}} |\rho(\mathbf{r}) - \rho_{\text{target}}(\mathbf{r})| \tag{4.15}$$

This is the measure used by Wu[75] and is thus useful for comparison. However, what is perhaps most meaningful in assessing constant $\rho(r)$ relaxation is a measure with units of energy. Both the electron-nuclear attraction and electron-electron repulsion (coulomb) energies should remain constant during constant $\rho(r)$ density relaxation. Thus, the changes in these contributions can give an estimate of the portion of the energy change upon relaxation that is illegitimate, deriving from changes in $\rho(r)$, small though they may be, instead of changes in the density matrix alone.

The frozen energy for all methods involving energetic criteria is defined as the energy of the electronic wavefunction (plus nuclear repulsion) from the optimization of (4.10) less the sum of the energies of the fully optimal isolated fragments. We stress that, unlike Wu, we will not use the value of the Lagrangian itself, which will include a non-zero contribution from the unphysical penalty term that is approximately (but not exactly) enforcing the constant density constraint.

4.3.2 Computational Details

Calculations in this work were performed with a development version of QChem[70, 108]. The SCFMI subspaces used throughout this work are non-orthogonal FERF DQ subspaces, which have been described previously (Chapter 3) and which do not have the weakness of a trivial basis set limit that simple fragment-AO-blocked SCFMI schemes possess. The aug-cc-pVQZ basis of Dunning[109, 110] is used for all single point calculations both because it allows direct comparison with previously reported results of Wu in some cases and because this basis has been shown to be adequate for the construction of FERF DQ subspaces. All single point calculations similarly employ the B3LYP[6–8] functional likewise for direct comparison but also because it is in common use with deficiencies mainly in its description of dispersive intermolecular interactions, which are not of primary interest in this work. The methods for the optimization of the nuclear coordinates of each investigated system will be given for each system in turn. No corrections for basis set superposition error were performed in this work. For calculations involving constant density constraints, the energy values reported are for $\lambda = 2000$ a.u. unless otherwise indicated.

4.4 Results and Discussion

4.4.1 Neon Dimer

The first system to be examined is the neon dimer because both large potential basis set as well as basis set limit extrapolated potential basis DEDA results at two internuclear distances

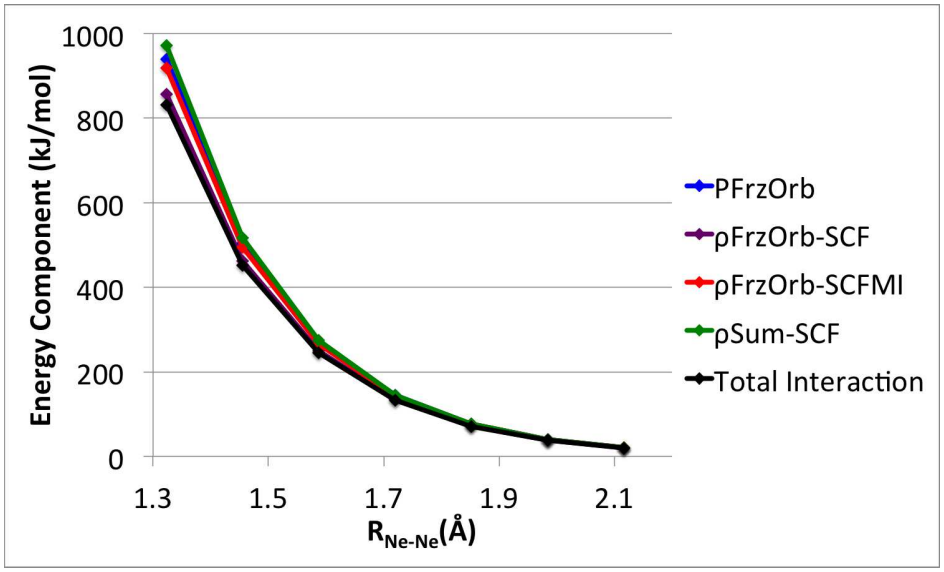

(a) Frozen energy component as computed by various methods along with the total interaction energy for the neon dimer at compressed distances.

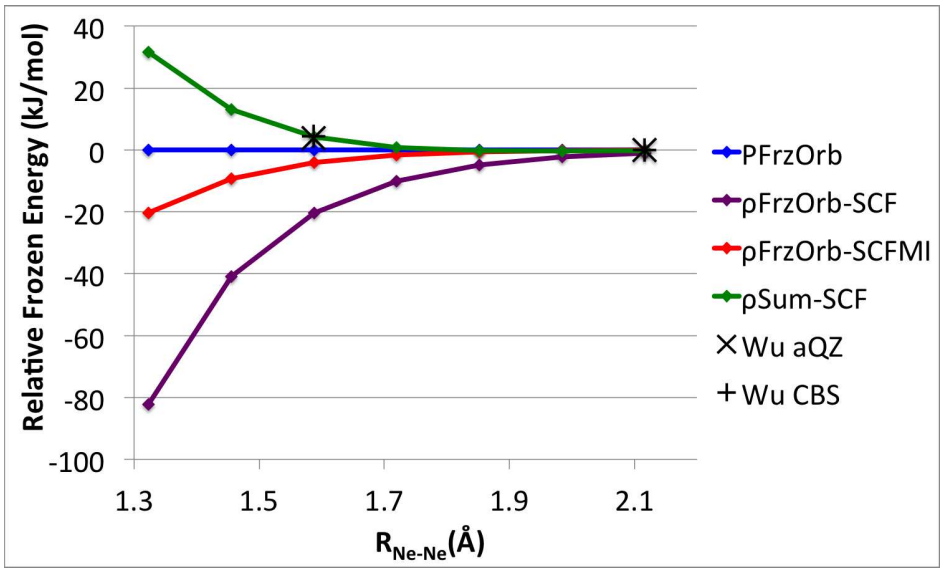

(b) Frozen energy component deviations from that of the frozen orbital density matrix for several methods. ρ_{frz}-SCF and ρ_{frz}-SCFMI both correspond to relaxed wavefunctions relative to P_{frz}, whilst ρ_{sum}-SCF does not admit an unrelaxed analog.

Figure 4.2: Comparison of frozen energy components for B3LYP/aug-cc-pVQZ neon dimer at various internuclear distances in the repulsive part of the potential energy curve (MP2/aug-cc-pVQZ $\text{R}_{Ne-Ne} = 3.10$Å). The data labeled Wu aQZ correspond to previous results[75] in which the aug-cc-pVQZ basis is used as the potential basis set as well as the orbital basis set in a DEDA calculation, while Wu CBS indicates Wu's complete penalty basis extrapolated results[75].

exist for comparison[75]. Figure 4.2 shows the frozen energy computed for the neon dimer at various repulsive inter-atomic distances using B3LYP/aug-cc-pVQZ by various methods both in absolute terms (Figure 4.2a) and relative to the energy of the frozen orbital density matrix, P_{frz}, for clearer illustration of differences (Figure 4.2b). The total interaction energy for the neon dimer at these separations is also included in Figure 4.2a both to give perspective for the portion of the internuclear coordinate considered and to highlight the considerable range in the computed sum of non-frozen contributions to the interaction energy.

The non-frozen contributions are polarization and charge transfer, and their sum within each method is the difference between the total interaction energy and the frozen energy component as determined by the given method. We do not separate the sum of polarization and charge transfer here as this is done differently in SCFMI-based and constrained-DFT-based schemes and also because not all pairs of initial wavefunction definitions and POL/CT delineations are commensurate. The non-frozen interaction components vary by more than a factor of five depending on which constraints are chosen for the initial wavefunction optimization at the most compressed geometry considered though, as expected, it is in all cases dwarfed by the corresponding frozen energy itself.

From Figure 4.2b it is clear that the different constraints lead to quite different frozen energies for highly compressed geometries. One can also see that despite the energetic optimality criterion present in the ρ_{sum}-SCF method, this energy is still considerably higher than that of the unoptimized frozen orbital density matrix, P_{frz}, for the repulsive coordinate values considered. ρ_{frz}-SCF and ρ_{frz}-SCFMI both correspond to relaxed wavefunctions relative to P_{frz} and are thus variationally guaranteed to have corresponding frozen energies that lie below that of P_{frz}, whilst ρ_{sum}-SCF does not have a meaningful unrelaxed analog and thus can be either higher or lower than P_{frz} in the overlapping regime. Indeed, the energetic ordering of the P_{frz} and ρ_{sum}-SCF methods is reversed at greater separations where the differences between the computed frozen energies drop below 0.5 kJ/mol.

Another clear conclusion that can be drawn from Figure 4.2b is that the restriction of the density matrix to the SCFMI surface even with a constant density constraint already in place is significant. Comparing the ρ_{frz}-SCF and ρ_{frz}-SCFMI curves shows that the inclusion of delocalization degrees of freedom in the density matrix optimization at constant $\rho = \rho_{frz}$ results in more than four times the initial wavefunction energy relaxation relative to the energy of P_{frz}, which likewise has 3-space density ρ_{frz}.

Figure 4.2b also includes the B3LYP/aug-cc-pVQZ neon dimer DEDA frozen energy as computed by Wu[75] with aug-cc-pVQZ as the potential basis set (PBS) as well the complete (potential) basis set (CBS) extrapolated result. The difference between Wu's aug-cc-pVQZ PBS result and that obtained using the finite Lagrange multiplier method with identical constraints, ρ_{sum}-SCF, for λ=2000 is 0.53 kJ/mol at 1.59 Å (3.0 Bohr) with our computed frozen energy slightly higher. This would suggest that we have done a slightly better job of enforcing the constant density constraint in this case. Indeed, Wu's purported complete potential basis set extrapolated result is only 0.18 kJ/mol higher in energy than this quite achievable finite λ value.

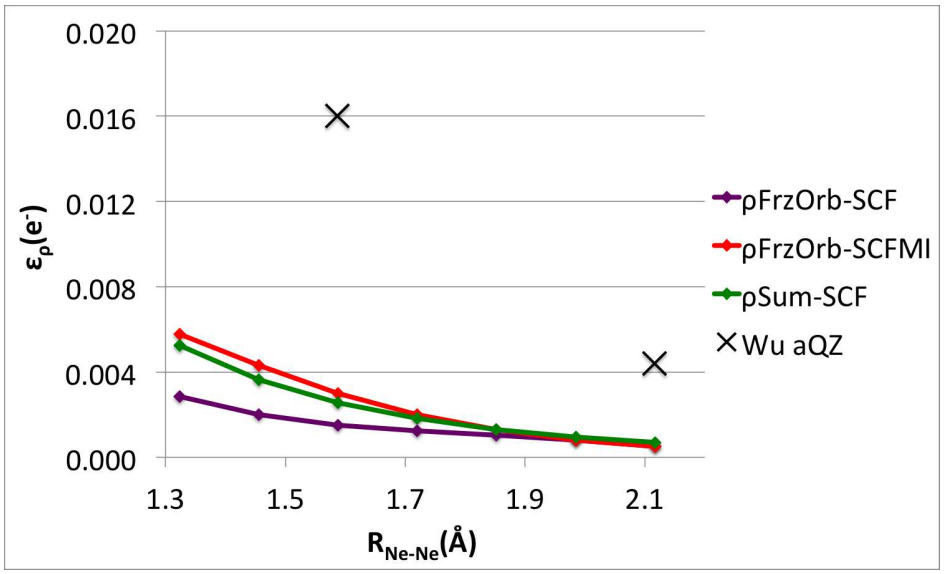

Figure 4.3: Integrated absolute value of 3-space density deviation of the optimized initial wavefunction from the target 3-space density of the given method for B3LYP/aug-cc-pVQZ neon dimer at various internuclear distances. Results with the label Wu aQZ are from earlier work[75] in which the aug-cc-pVQZ basis is used as the potential basis set as well as the orbital basis set in a DEDA calculation.

Figure 4.3 shows the integrated 3-space density error, ϵ_ρ (4.15), of the optimized density relative to the target density as defined by each of the given initial wavefunction methods for the neon dimer. Fairly similar fidelity is achieved for all finite λ methods across the R_{Ne-Ne} coordinate. ρ_{frz}-SCF and ρ_{frz}-SCFMI have the potential to achieve $\epsilon_\rho = 0$ though this is clearly not achieved with finite λ. ρ_{sum}-SCF on the other hand is not guaranteed to be able to reach $\epsilon_\rho = 0$ but has a quite small electron error nonetheless. The general trend in Figure 4.3 is that ϵ_ρ decreases with increasing internuclear separation. This is likely because of the increased relative importance of the penalty term in the Lagrangian, (4.10), compared to the physical driving forces for supersystem density relaxation, which decrease with increasing internuclear separation.

For ρ_{sum}-SCF, the ϵ_ρ error measures that we compute for our finite λ calculations are more than five times smaller than the same values reported by Wu[75] based on his constrained DFT method with an aug-cc-pVQZ PBS. Based on these results as well as the energies (Figure 4.2b) discussed above, we conclude that our methodology for performing optimizations with constant 3-space density constraints is capable of at least the same accuracy as Wu's scheme with the largest potential basis set that he has employed.

We now turn to the energetic consequences of not exactly enforcing constant $\rho(\mathbf{r})$ during initial wavefunction optimization for the neon dimer. Figure 4.4 shows the relaxation relative to the P_{frz} wavefunction for the ρ_{frz}-SCF (Figure 4.4a) and ρ_{frz}-SCFMI (Figure 4.4b)

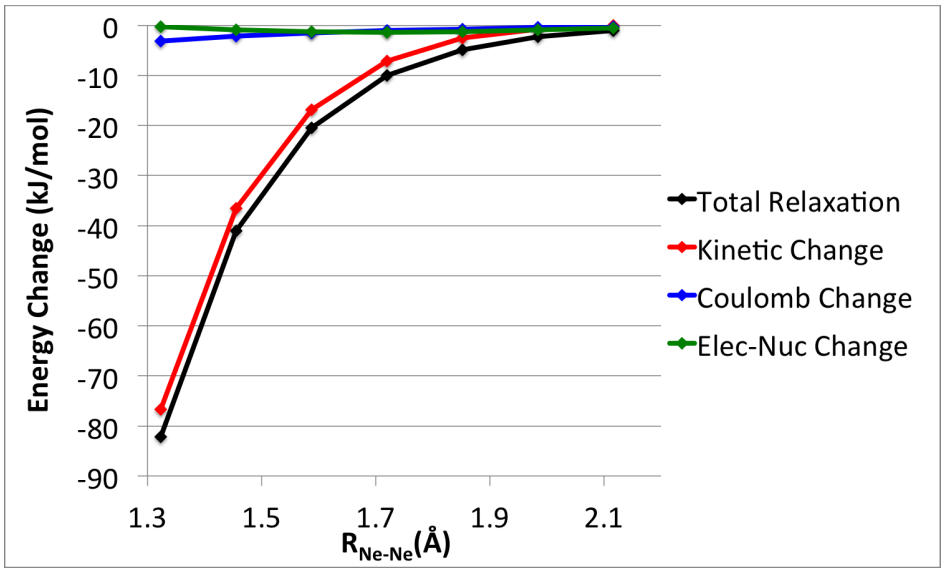

(a) Changes in energy components upon initial wavefunction optimization by the ρ_{frz}-SCF method with finite λ.

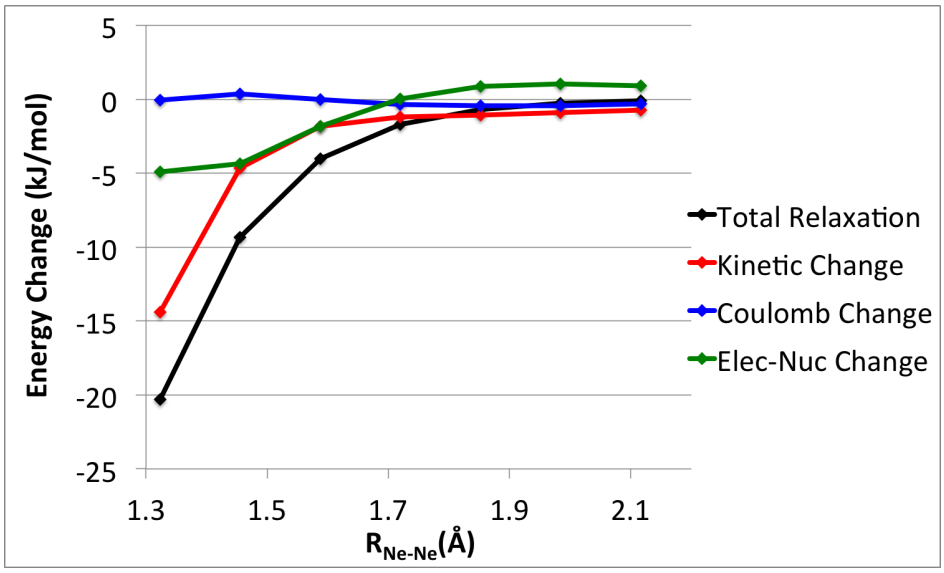

(b) Changes in energy components upon initial wavefunction optimization by the ρ_{frz}-SCFMI method with finite $\lambda = 2000$ for all calculations.

Figure 4.4: Energetic assessment of errors resulting from deviations from the target 3-space density during constant 3-space density initial wavefunction determination for B3LYP/aug-cc-pVQZ neon dimer at various internuclear distances. The target density for both methods show is ρ_{frz}, which is a feasible point by construction. Changes in coulomb and electron-nuclear contributions to the interaction energy are thus ideally zero because they depend only on the 3-space density of the supersystem, while the kinetic energy is expected to change. Changes in the exchange-correlation contribution to binding are not shown but can be inferred as the remaining contribution to the total relaxation.

wavefunctions along with a basic decomposition of this energy change based on electronic Hamiltonian terms. Coulomb repulsion and electron-nuclear attraction are functions of the 3-space density alone, and therefore should not change upon initial wavefunction relaxation. This is not the case with finite λ values, but the illegitimate energetic deviations are typically fairly small ($<$ 5 kJ/mol for the internuclear distances examined here. The change in the coulomb interaction is considerably smaller than the change in the electron-nuclear attraction in many cases, probably because the penalty term is in fact the coulomb interaction of density deviations. The total relaxation is generally well described by the change in the kinetic energy, which does have density matrix dependence and is thus (at least in part) legitimate energy lowering. The remaining relaxation not displayed here is relatively small and corresponds to changes in the exchange-correlation energy, which in the case of B3LYP is a mix of legitimate energy lowering from the density-matrix-dependent exact exchange and illegitimate energy lowering associated with the GGA exchange and correlation functionals.

In the case of ρ_{frz}-SCF (Figure 4.4a), relaxation is quite large, and the energy changes from electron-electron and electron-nuclear interactions are negligibly small for much of the coordinate. This is however not the case for the ρ_{frz}-SCFMI (Figure 4.4b) method, for which the clearly illegitimate energy changes are a large fraction of the relatively minor total relaxation. Thus it would seem that unless relaxation relative to P_{frz} is appreciable, then not only is it unlikely to be worthwhile to expend the computational effort to solve the constant 3-space density problem, but also the limited relaxation that is computed is likely to incorporate a large fraction of illegitimate energy lowering. In particular, the removal of constant density polarization by the relaxation of P_{frz} to ρ_{frz}-SCFMI does not appear to be essential for the Ne dimer.

The Lagrange multiplier of $\lambda = 2000$ is used throughout this work (with a few noted exceptions) as it is a fairly large value for which the optimization problem at fixed λ could be reliably converged for all methods for most of the systems investigated here. We now consider convergence of the initial wavefunction energies with respect to λ at a single point (R_{Ne-Ne} = 1.59 Å= 3.0 Bohr) on the neon dimer potential energy surface to place this computational limitation into perspective. Figure 4.5 shows both integrated absolute density errors, ϵ_ρ, (Figure 4.5a) and relative initial wavefunction energies (Figure 4.5b) for a range of λ values between 500 and 7000. ρ_{sum}-SCF values for large λ were considerably more computationally demanding in no small part due to the fact that a feasible point is not available as a guess, and so density errors and relative energies were only computed up to $\lambda = 3000$ for this method.

Figure 4.5a illustrates the painfully slow convergence of the integrated density error with respect to λ with all methods exhibiting a polynomial decay of roughly $\lambda^{-0.5}$. Using Figure 4.5b we can see the energetic consequences of our failures to exactly enforce the constant density constraint. Each method's frozen energy is offset by the value obtained with the modest $\lambda = 500$ optimization, and Wu's aug-cc-pVQZ and (potential) CBS extrapolated results are offset by the ρ_{sum}-SCF frozen energy at $\lambda = 500$. We can see from Figure 4.5b that like ϵ_ρ, the initial wavefunction energies also converge quite slowly with respect to λ.

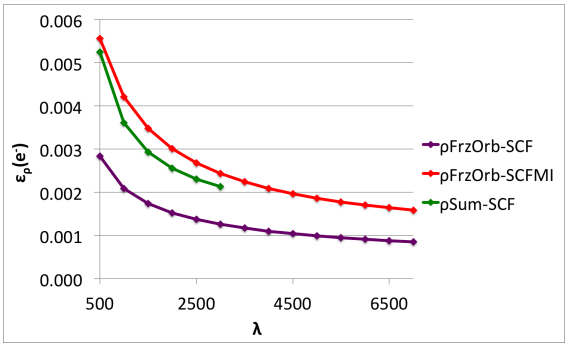

(a) Integrated absolute value of the deviation of the 3-space density of the optimized initial wavefunction from the target 3-space density for the given method computed for multiple values of λ.

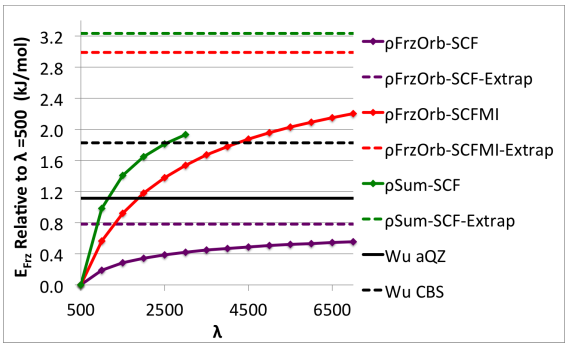

(b) Frozen energy as computed by various methods relative to that for the same constrained optimization with λ=500 for multiple values of λ.

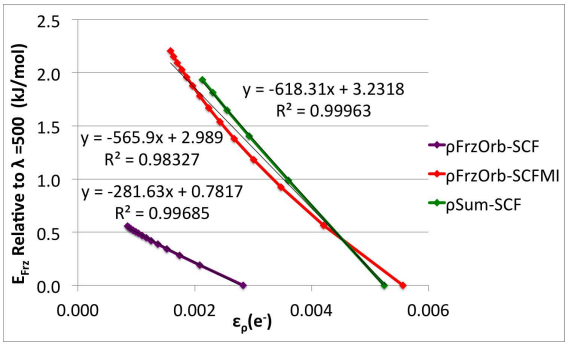

(c) Plots of frozen energy contributions relative to the λ=500 computed value versus the corresponding ϵ_ρ value with linear fits for the purpose of estimating the relative frozen energy at the ideal case of ϵ_ρ=0.

Figure 4.5: Convergence of ϵ_ρ and the frozen energy contribution as computed by various methods for multiple values of λ in the Lagrangian at fixed R_{Ne-Ne} = 1.59 Å= 3.0 Bohr.

We note also that our ρ_{sum}-SCF value with a λ value of only 3000 has already passed Wu's extrapolated value for the same optimization problem, and we expect, based on results below that it will go quite a bit farther.

Finally, we consider an extrapolation of the frozen energy for each method to the $\epsilon_\rho = 0$ limit (even though it is not necessarily possible for ρ_{sum}-SCF) for the purpose of assessing errors in our finite $\lambda = 2000$ calculations. The results of applying linear regression to relative E_{frz} vs ϵ_ρ curves for each of the optimized initial wavefunction methods are displayed in Figure 4.5c. The corresponding $\epsilon_\rho = 0$ extrapolated values relative to the respective offsets are given by the intercepts and are displayed as dashed lines in Figure 4.5b for perspective. From at least the ρ_{frz}-SCFMI curve it seems like the linear fit will result in a rather crude underestimate of the effect of strict enforcement of the constant ρ constraint just as Wu's extrapolated value for the ρ_{sum}-SCF optimization problem was an underestimate. However, we find it difficult to justify introducing additional degrees of freedom into these fits and will use these intercepts as our best guess at the limiting behavior, crude though they may be. Returning to Figure 4.5b, we see that choosing λ=2000 roughly halves the difference between the fairly easily obtained λ=500 value and the estimated $\epsilon_\rho = 0$ or equivalently the $\lambda = \infty$ limit (this is rather generous in the case of ρ_{frz}-SCFMI which would ideally use a larger λ value than the other methods). λ =2000 thus seems like a reasonable compromise as the returns on accuracy for increasing λ diminish quite rapidly, and converging the calculations becomes increasingly difficult. We stress that these energy errors are quite small compared both to the absolute frozen energies and to the differences in the frozen energies produced by the various methods at this neon dimer geometry.

4.4.2 Water Dimer

The next system that we investigate is the water dimer, a fairly weakly interacting system for the displacements considered and for which charge transfer is important to bonding, highlighting the importance of the orbital degrees of freedom employed during initial wavefunction optimization. Moreover, this system has also been investigated by Wu using DEDA[51], allowing again for a comparison of constraint methodology. The water dimer investigated here is rigidly displaced along the hydrogen bond coordinate relative to the MP2/aug-cc-pVQZ optimized structure (equilibrium $R_{\text{O-H}} = 1.93$ Å).

Figure 4.6 shows the frozen energy components both absolute (Figure 4.6a) and relative to that of P_{frz} (Figure 4.6b) computed using the various initial wavefunction schemes. Included also are results from Wu's DEDA using the same aug-cc-pVQZ basis to construct the density matrix but the cc-pVTZ basis to expand the constraint potential. We notice in this case that there is relatively little difference between the ρ_{sum}-SCF and ρ_{frz}-SCF results, suggesting that the target 3-space densities are roughly the same. Moreover, Wu's TZ PBS result lies quite close to but below our ρ_{sum}-SCF, illustrating again that the two methods of enforcing the constant density constraint, the finite λ coulomb penalty and finite potential basis CDFT, are comparable.

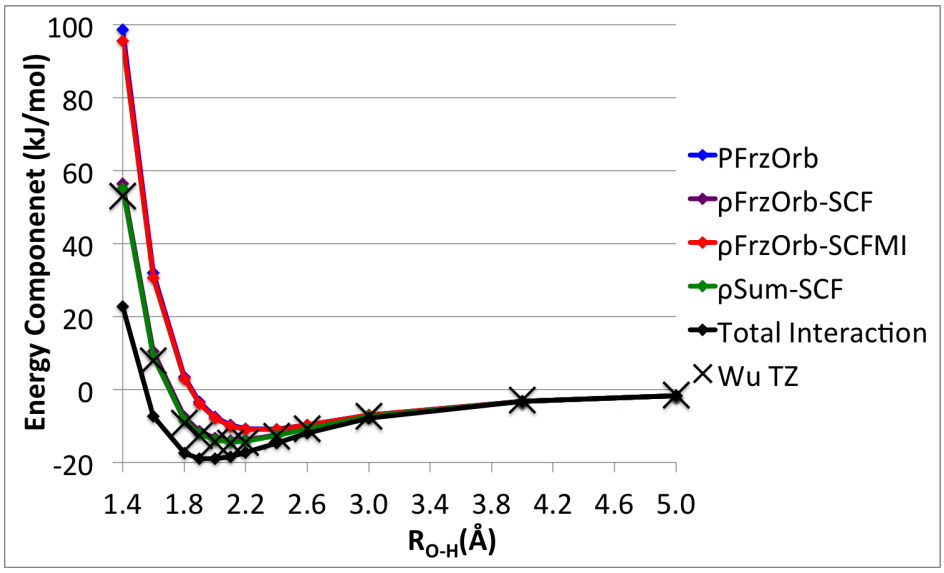

(a) Frozen energy component as computed by various methods along with the total interaction energy for the water dimer at various hydrogen bond distances.

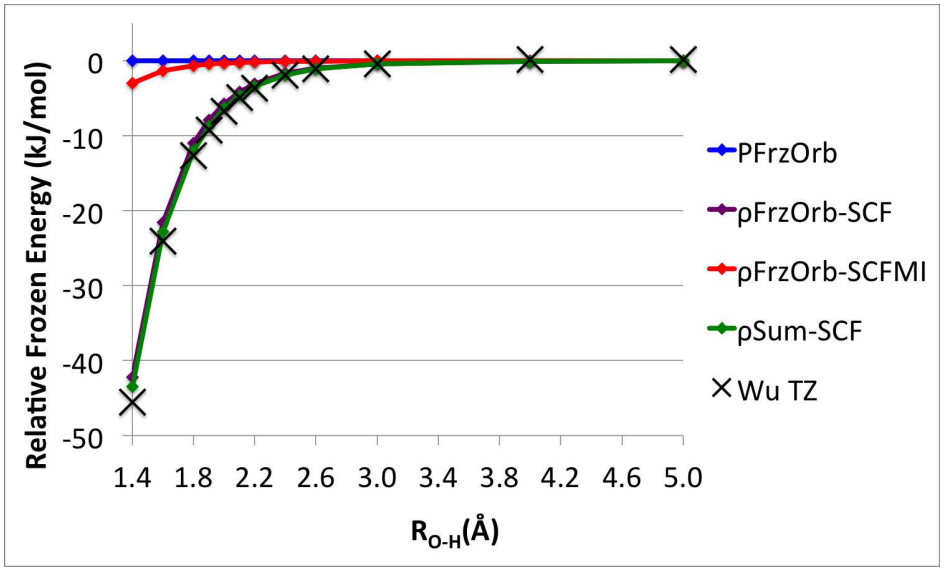

(b) Frozen energy component deviations from that of the frozen orbital density matrix for several methods for the water dimer.

Figure 4.6: Comparison of frozen energy components for the MP2/aug-cc-pVQZ optimized and rigidly displaced water dimer at various hydrogen bond ($R_{O\text{-}H}$) distances with B3LYP/aug-cc-pVQZ single points. Curves with the label Wu TZ correspond to earlier DEDA B3LYP/aug-cc-pVQZ calculations[51] in which the cc-pVTZ basis is used as the potential basis set.

There is however a clear distinction between the ρ_{frz}-SCF and ρ_{frz}-SCFMI schemes, indicating that whilst the choice of target density is not important here, the choice of orbital degrees of freedom is crucial. The ρ_{frz}-SCFMI scheme permits almost no relaxation relative to P_{frz}, but the relaxation when all SCF orbital degrees of freedom are included is substantial on the scale of the interaction energy, approximately halving the non-frozen contribution to the interaction out to 2.6 Å and at roughly equilibrium separation ($\text{R}_{\text{O-H}} = 2.0$ Å) decreasing it from 11.16 to 5.76 kJ/mol.

We turn again to an assessment of our methodology's ability to enforce the constant density constraint. Figure 4.7a shows the degree to which the constant density constraint is violated by Equation 4.15 in terms of number of displaced electrons, ϵ_ρ, for each of the finite λ initial wavefunction optimization methods. All methods maintain approximately the same fidelity. The errors are noticeably smaller than many observed for the compressed neon dimer (Figure 4.3), likely due to decreased impetus for relaxation associated with near-equilibrium water dimer geometries.

Figure 4.7b shows the total relaxation of the initial wavefunction from P_{frz} by the ρ_{frz}-SCFMI method along with the corresponding components of the electronic Hamiltonian. Again, the terms should be zero if $\rho(\mathbf{r})$ has not changed, but this is not the case; though the illegitimate energy changes in coulomb and electron-nuclear terms are considerably smaller than in the case of the much more strongly interacting neon dimer investigated above (Figure 4.4b). Relaxation for the water dimer by ρ_{frz}-SCFMI seems largely legitimate for compressed hydrogen bond distances though the relaxation itself is actually quite negligible. We do not show the corresponding results for the ρ_{frz}-SCF or ρ_{sum}-SCF methods because, as was seen in the neon dimer case, illegitimate energy lowerings are quite a small fraction of the total relaxation when the magnitude of the relaxation itself is large.

The water dimer example demonstrates the importance of the SCFMI constraint during initial wavefunction optimization as it eliminates the substantial energy lowering associated with electron delocalization that is allowed in the ρ_{frz}-SCF and ρ_{sum}-SCF methods and thus the DEDA scheme. This contribution is properly part of CT in an EDA. This example also illustrates that for weakly interacting systems near or beyond the equilibrium separation, the energy lowering from constant density polarization, the difference between the frozen energy as computed by the P_{frz} and ρ_{frz}-SCFMI schemes, is negligible. It thus seems unnecessary to perform the ρ_{frz}-SCFMI initial wavefunction optimization for the water dimer. The ρ_{frz}-SCF and ρ_{sum}-SCF methods may be useful for applications such as force field development where it is desirable to combine CT with steric interactions as part of a frozen energy term.

4.4.3 Ammonia Borane Complex

The third closed-shell system that we investigate is the very strongly interacting ammonia borane complex, which has a large charge transfer component to its interaction energy. This will test whether constant density relaxation is non-negligible even with the important SCFMI orbital rotation constraint in place. The ammonia borane structures considered are

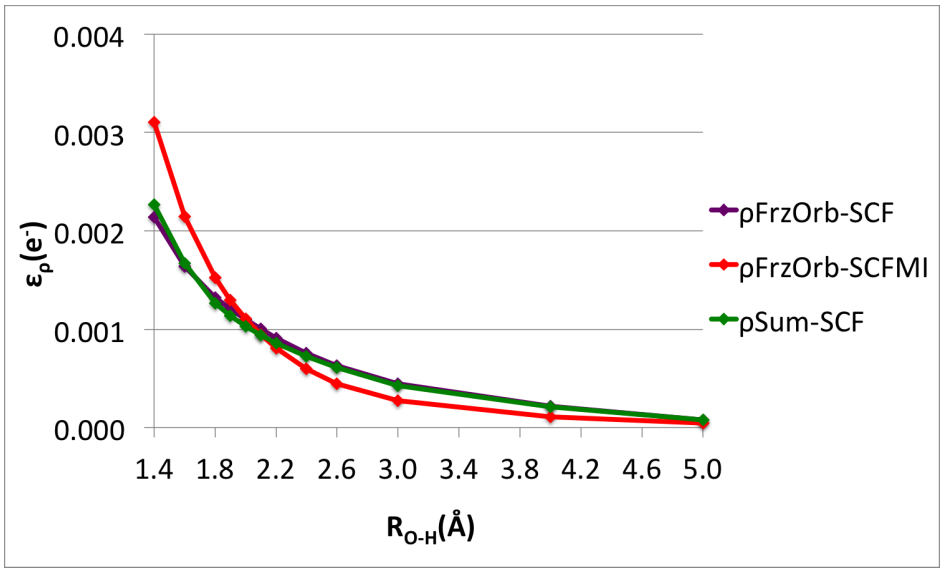

(a) Integrated absolute value of 3-space density deviation of the optimized initial wavefunction from the target 3-space density of the given method.

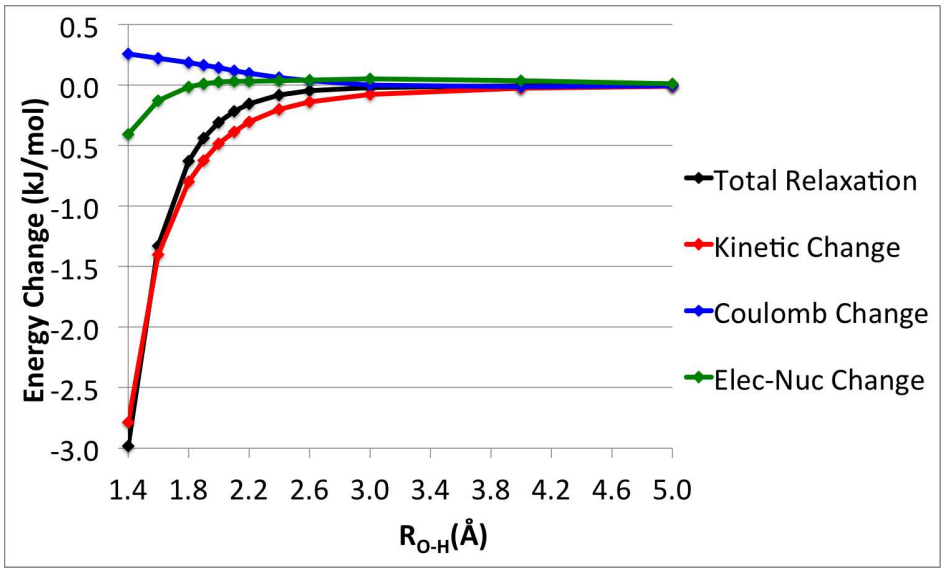

(b) Changes in energy components upon initial wavefunction optimization by the ρ_{frz}-SCFMI method with finite λ. The target density is ρ_{frz}, which is a feasible point by construction. Changes in coulomb and electron-nuclear contributions to the interaction energy are ideally zero, while the kinetic energy is expected to change. Changes in the exchange-correlation contribution to binding are not shown but can be inferred as the remaining contribution to the total relaxation.

Figure 4.7: Quantities for the assessment of the enforcement of the constant 3-space density constraint in initial wavefunction optimization by several methods for the MP2/aug-cc-pVQZ optimized and rigidly displaced water dimer at various hydrogen bond (R_{O-H}) distances with B3LYP/aug-cc-pVQZ single points.

obtained by a B3LYP/aug-cc-pVTZ relaxed scan of the $R_{N\text{-}B}$ coordinate (equilibrium $R_{N\text{-}B}$ = 1.66 Å at this level of theory). A value of 1500 instead of 2000 was used for the ρ_{sum}-SCF method for $R_{N\text{-}B} \leq 1.2$ Å due to difficulties associated with converging larger λ values.

Figure 4.8 shows absolute (Figure 4.8a) and relative (Figure 4.8b) frozen energies as computed by the various initial wavefunction methods. The relaxation relative to the frozen orbital energy, P_{frz} is considerably larger for the methods that allow all orbital rotations, ρ_{frz}-SCF and ρ_{sum}-SCF, than for ρ_{frz}-SCFMI, showing again the importance of the SCFMI orbital rotation constraint even past the equilibrium separation and strengthening the claim that much of the difference between the frozen energy of P_{frz} and that of ρ_{sum}-SCF used by DEDA is due to what SCFMI-based EDA schemes would consider charge transfer. This electron delocalization makes the computed frozen interaction attractive by 1.55 Å for ρ_{sum}-SCF and by 1.70 Å for ρ_{frz}-SCF. The frozen energy would otherwise be repulsive until beyond 2.20 Å separation by the P_{frz} and ρ_{frz}-SCFMI schemes.

While the effect of constant density polarization (the energy difference between P_{frz} and ρ_{frz}-SCFMI) is a quite substantial 50 kJ/mol for the most compressed coordinate values, it is still small compared to the magnitude of both the frozen and non-frozen EDA contributions and thus has little effect on the interpretation of the interaction. We see that for larger ammonia borane separations, the ρ_{sum}-SCF and ρ_{frz}-SCF results converge to the same value as the target densities become more similar. However, at closer separations, the energetic ordering of the two is not guaranteed, and the two curves cross at 1.0 Å. This may be due in part to the smaller value of λ that was used for the ρ_{sum}-SCF calculations.

Our assessment of errors in the density constrained optimizations performed for the ammonia borane complex appear in Figure 4.9. Integrated density errors (Figure 4.9a) are noticeably worse than those observed for the neon dimer (Figure 4.3) because the frozen energies are considerably more repulsive, and suppressing the erroneous relaxation should be more difficult. The jump in ϵ_ρ observed at 1.2 Å for ρ_{sum}-SCF is a consequence of using λ=1500 instead of the otherwise uniform λ=2000 for $R_{N\text{-}B} \leq 1.2$ Å.

The ϵ_ρ error measure for ρ_{frz}-SCFMI is substantially larger than those for the other methods, indicating that perhaps ρ_{frz}-SCFMI needs in general a larger λ value. More importantly, it also suggests that the relaxation relative to P_{frz} computed for the ρ_{frz}-SCFMI method (Figure 4.8b) while modest when compared to the other two methods is in fact a substantial overestimate of the true "constant density polarization". Figure 4.9b shows that clearly illegitimate energy changes occur for the ρ_{frz}-SCFMI at compressed distances, which is also the only region where initial wavefunction relaxation is significant on the scale of the total interaction. By contrast with the previous examples, the change in the electron-nuclear interaction leads to a net destabilizing contribution, which means that erroneous changes in $\rho(\mathbf{r})$ lead to even larger stabilizing changes in the kinetic and XC contributions to the energy that ought to be prohibited. The change in the total coulomb interaction is as in several past examples generally more subdued likely stemming from the closer relation to the penalty function employed.

For the ammonia borane complex we conclude that the removal of constant density

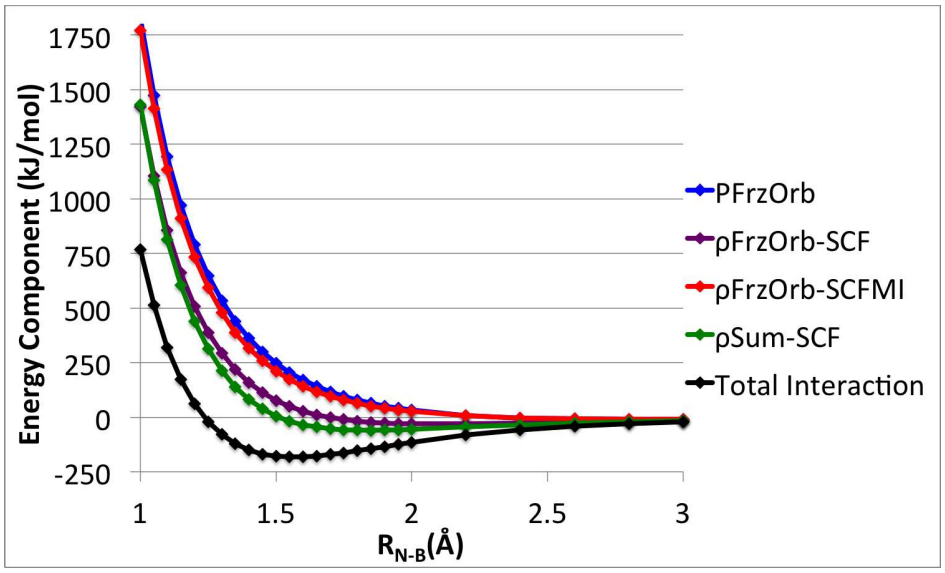

(a) Frozen energy component as computed by various methods along with the total interaction energy for NH_3-BH_3 at various interfragment (R_{N-B}) distances.

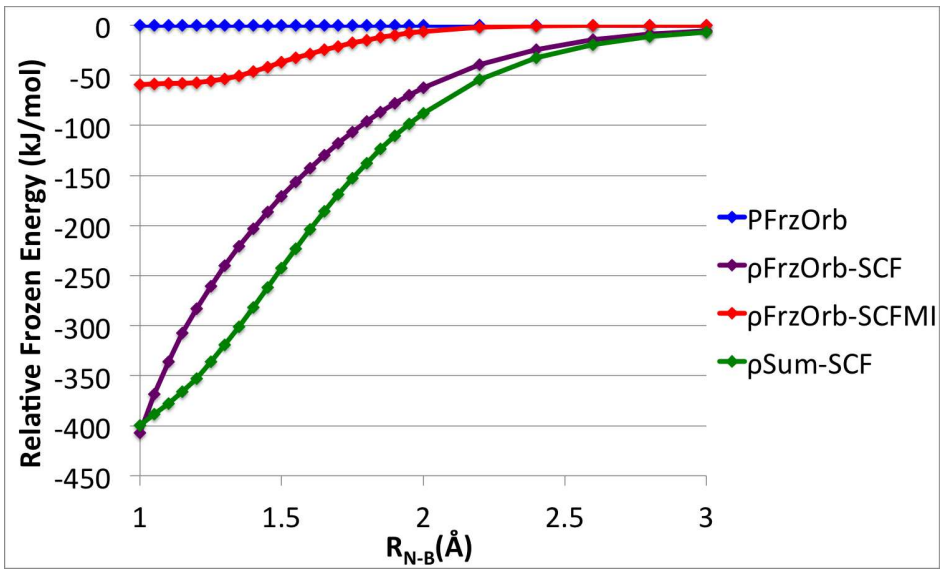

(b) Frozen energy component deviations from that of the frozen orbital density matrix for several methods for NH_3-BH_3 at various interfragment (R_{N-B}) distances.

Figure 4.8: Comparison of frozen energy components for the relaxed R_{N-B} scan of NH_3-BH_3 at B3LYP/aug-cc-pVTZ with B3LYP/aug-cc-pVQZ single points.

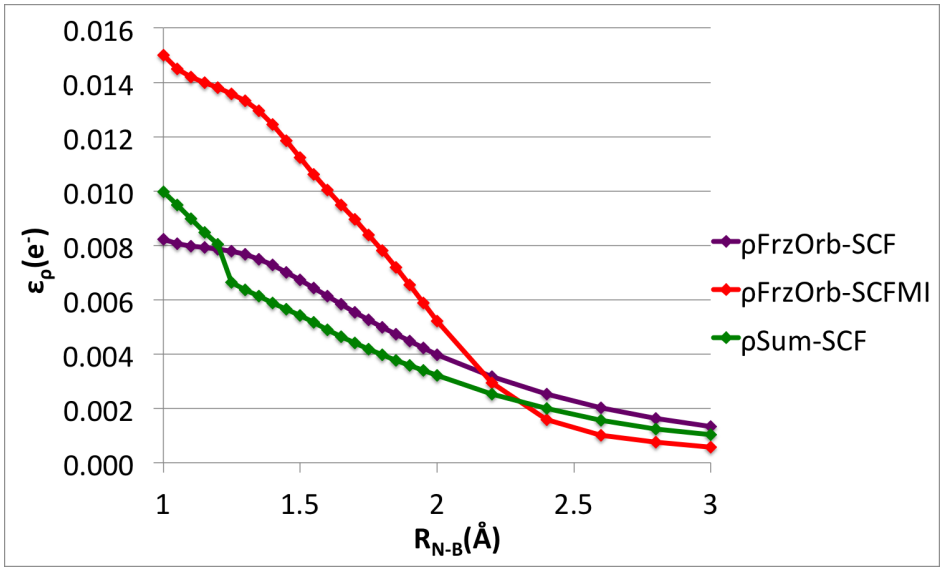

(a) Integrated absolute value of 3-space density deviation of the optimized initial wavefunction from the target 3-space density of the given method.

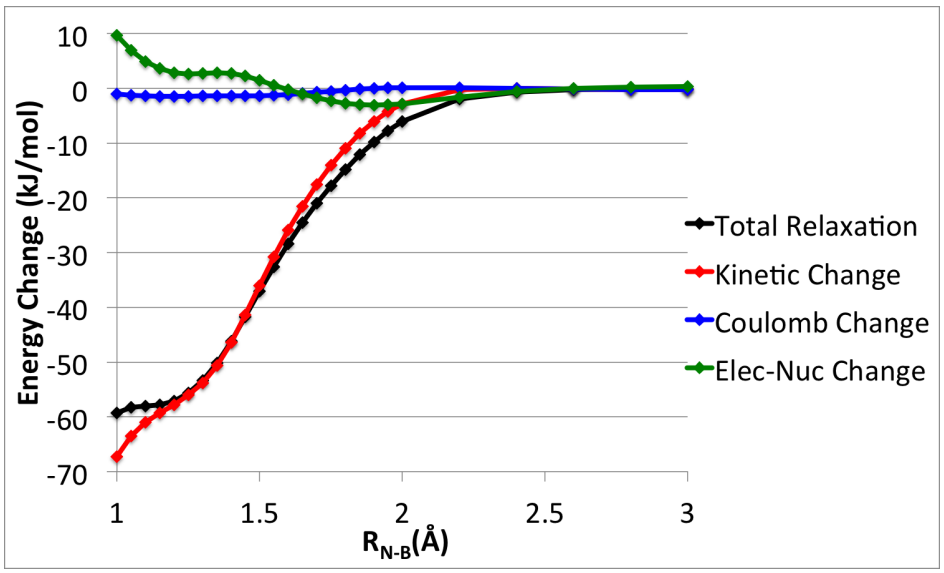

(b) Changes in energy components upon initial wavefunction optimization by the ρ_{frz}-SCFMI method with finite λ, in the same format as Figure 4.7b.

Figure 4.9: Assessment of the enforcement of the constant 3-space density constraint in initial wavefunction optimization at B3LYP/aug-cc-pVQZ by several methods for the relaxed B3LYP/aug-cc-pVTZ $R_{N\text{-}B}$ scan of NH_3-BH_3.

polarization seems to be irrelevant for qualitative understanding but arguably worthwhile for generating quantitative results with the caveat of the presence of clearly erroneous energy lowering in the initial wavefunction relaxation. The ρ_{frz}-SCF and ρ_{sum}-SCF methods on the other hand produce both quantitatively and qualitatively different results from P_{frz}, approximately halving the non-frozen contribution in the equilibrium region. From the SCFMI-based EDA viewpoint, this change is unwanted, because it originates largely from electron delocalization (i.e. the difference between ρ_{frz}-SCFMI and ρ_{frz}-SCF), which, in the EDA view, does not belong in the initial supersystem wavefunction.

4.4.4 Ethane Dissociation

We investigate the interaction of two methyl radicals, one of net alpha and one of net beta spin, to form the ethane molecule. The coordinate that we consider is R_{C-C} of rigidly dissociated D_{3d} (staggered) B3LYP/aug-cc-pVTZ optimized ethane (equilibrium $\text{R}_{\text{C-C}} = 1.53$ Å at this level of theory).

It should at this point be no surprise that that the ρ_{frz}-SCF and ρ_{sum}-SCF curves track each other fairly closely especially in this case where the spatial orbitals that are most strongly overlapping between the two fragments are spin orthogonal, thus not distorting each other in the formation of the frozen orbital density matrix. We again see a dramatic difference in the frozen energy computed by schemes that include electron delocalization degrees of freedom, ρ_{frz}-SCF and ρ_{sum}-SCF, and those that do not. At equilibrium, the methods including the full SCF degrees of freedom during constant density optimization both suggest that bonding in ethane can be predominantly described by the frozen interaction term with minimal contributions from polarization or charge transfer. On the other hand, both the P_{frz} and ρ_{frz}-SCFMI schemes suggest that the frozen contribution at this separation is destabilizing and that bonding is brought about by the stabilizing and collectively much larger non-frozen contributions. Indeed, ρ_{frz}-SCF and ρ_{sum}-SCF both suggest an attractive frozen interaction by $\text{R}_{\text{C-C}} = 1.28$ Å while neither P_{frz} nor ρ_{frz}-SCFMI yield an attractive frozen interaction until beyond 2.0 Å.

We do not constrain the spin densities separately but only the total spinless density, which allows spin polarization to occur. If $\langle S^2 \rangle$ values do not change appreciably during initial wavefunction optimization, then spin polarization has not occurred, and the choice of total spinless density or separate spin density constraints is of little consequence. Figure 4.11 shows $\langle S^2 \rangle$ for each of the initial supersystem wavefunctions for ethane along the carbon-carbon bond breaking coordinate. All methods of course go to $\langle S^2 \rangle = 1.0$, the value for a spin-symmetry broken open shell singlet, at large methyl fragment separations; however, the behaviors are quite different in the overlapping regime. ρ_{frz}-SCFMI is a relaxed wavefunction relative to P_{frz}, and the $\langle S^2 \rangle$ for these two methods are quite similar. Conversely, the ability to change the extent of spin polarization is taken advantage of in both the ρ_{frz}-SCF and ρ_{sum}-SCF initial wavefunctions at short carbon-carbon distances where the two spins couple to form a closed shell singlet. Thus, a constant density constraint based on spin densities

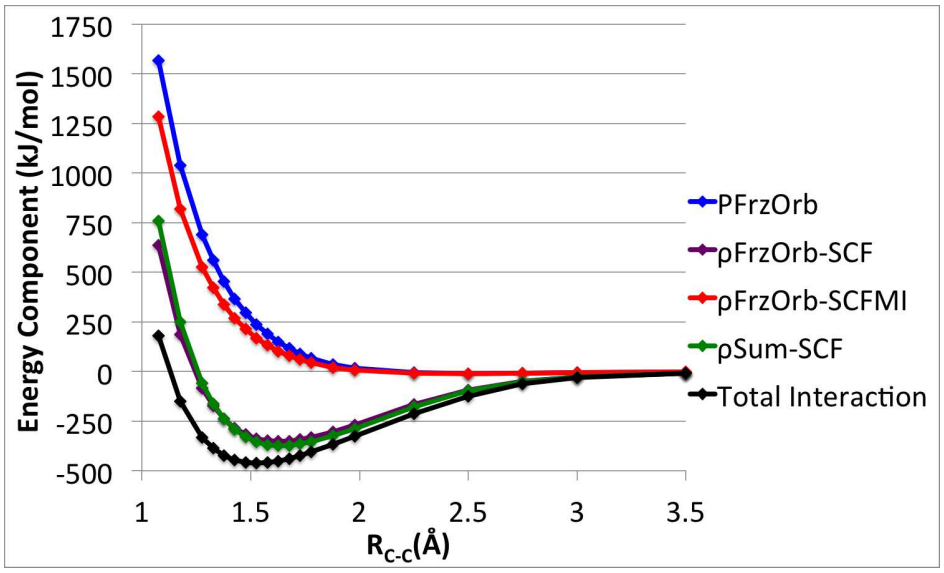

(a) Frozen energy contributions by the various methods along with the total interaction energy of the fragmented ethane molecule for comparison.

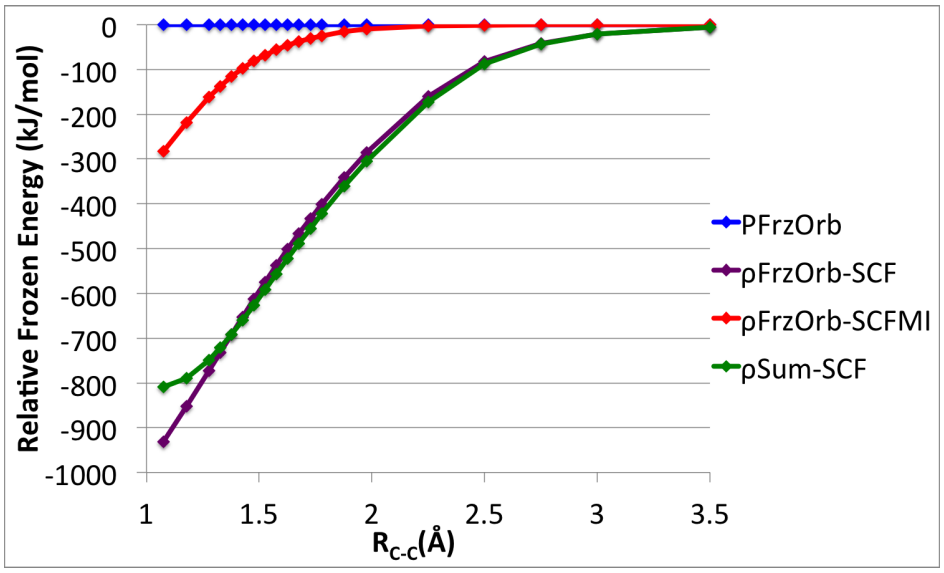

(b) Frozen energy contributions by the various methods relative to that of P_{frz}.

Figure 4.10: B3LYP/aug-cc-pVQZ frozen energy models for the rigidly $R_{C\text{-}C}$ dissociated net alpha and net beta spin methyl fragments of B3LYP/aug-cc-pVTZ optimized D_{3d} (staggered) ethane.

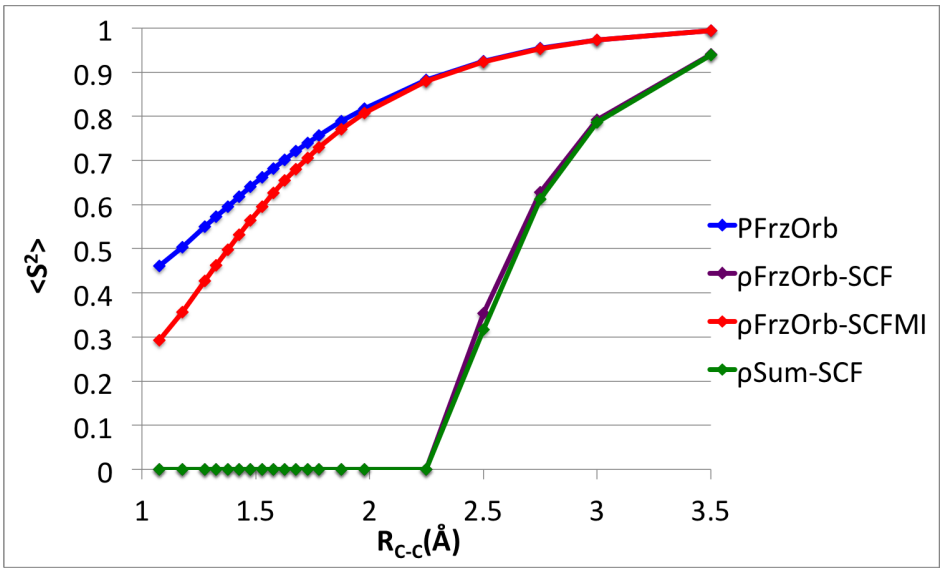

Figure 4.11: B3LYP/aug-cc-pVQZ calculations of $\langle S^2 \rangle$ for initial supersystem wavefunctions of the rigidly dissociated B3LYP/aug-cc-pVTZ optimized D_{3d} staggered ethane molecule built from net alpha and net beta spin methyl fragments. Deviations from the $\langle S^2 \rangle$ value for P_{frz} signify orbital relaxation that changes the extent of spin polarization, which is quite significant in the SCF-based methods.

instead of the total spinless density seems to be an unnecessary additional restriction in the case of ρ_{frz}-SCFMI optimization. It may be relevant for the ρ_{frz}-SCF and ρ_{sum}-SCF methods, but this will depend on the purpose of the calculation.

Figure 4.12 describes the extent of constant density constraint violation of the ethane dissociation. It is clear from Figure 4.12a that the extent of spin recoupling that occurs in ρ_{frz}-SCF and ρ_{sum}-SCF is largely legitimate (given the spin-blind density constraint) as these ϵ_ρ errors are comparable to those seen previously for other systems; however, the ϵ_ρ error associated with the ρ_{frz}-SCFMI is quite large, suggesting that much of the change in energy relative to P_{frz} and what change in $\langle S^2 \rangle$ was observed for this method upon initial wavefunction relaxation may have been due to violations of the constant ρ constraint. However, Figure 4.12b indicates that only about 15% of the relaxation brought about during the ρ_{frz}-SCFMI optimization is illegitimate at the most compressed distance and that only about 30% is illegitimate around the equilibrium separation. While not ideal, these energetic errors are not as serious as Figure 4.12a might lead one to expect, though the corresponding impact on the $\langle S^2 \rangle$ of the relaxed wavefunction is unclear.

While not particularly relevant near equilibrium, the relaxation brought about by ρ_{frz}-SCFMI initial wavefunction optimization is quite substantial for short carbon-carbon distances. The effect of the removal of constant density polarization will thus be a change in shape for the polarization contribution in SCFMI-based EDA schemes in the repulsive

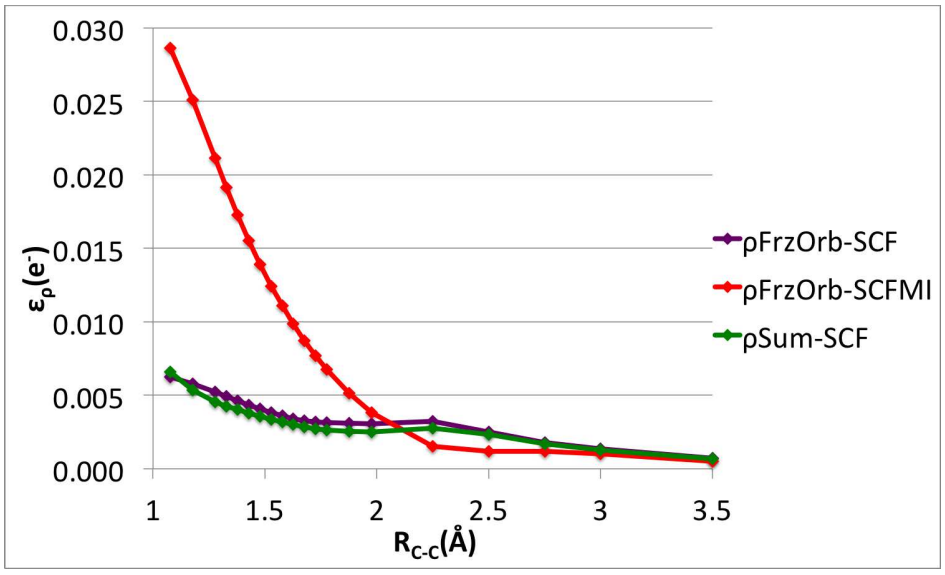

(a) Integrated absolute value of 3-space density deviation of the optimized initial wavefunction from the target 3-space density of the given method.

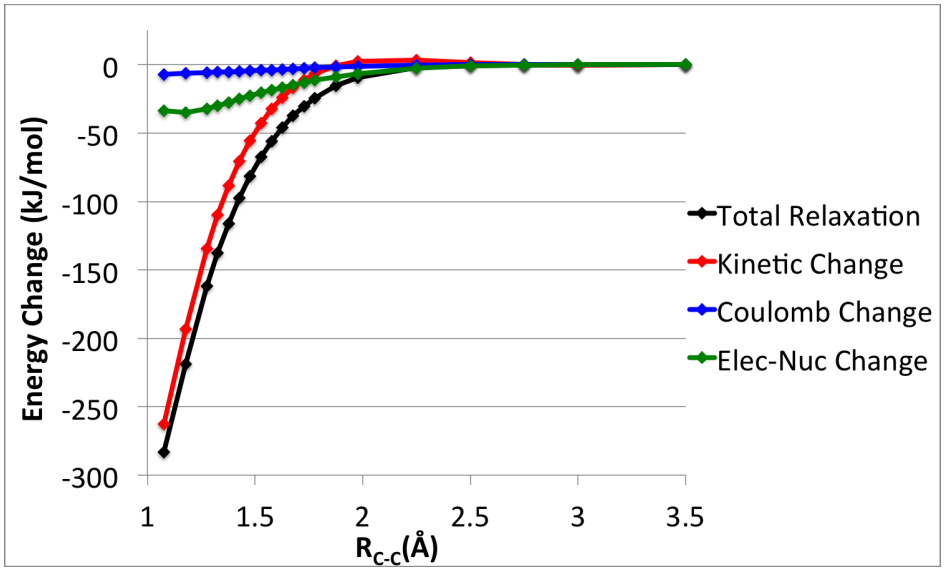

(b) Changes in energy components upon initial wavefunction optimization by the ρ_{frz}-SCFMI method with finite λ, in the same format as Figure 4.7b.

Figure 4.12: Quantities for the assessment of the enforcement of the constant 3-space density constraint in B3LYP/aug-cc-pVQZ initial wavefunction optimization by several methods for the rigidly $R_{C\text{-}C}$ dissociated net alpha and net beta spin methyl fragments of the B3LYP/aug-cc-pVTZ optimized D_{3d} staggered ethane.

	Be^+ H_2O		CO^+ HF	
	P_{frz}	ρ_{frz}-SCFMI	P_{frz}	ρ_{frz}-SCFMI
$\mathbf{E_{frz}}$	63.57	51.63	61.13	48.51
$\mathbf{E_{pol}}$	-256.55	-244.61	-95.12	-82.50
$\mathbf{E_{VCT}}$		-81.67		-126.43
$\mathbf{E_{Int}}$		-274.65		-160.42
$\Delta\mathbf{E_{relax}}$		-11.94		-12.62
$\Delta\mathbf{E}_{KE}$		-16.13		-11.34
$\Delta\mathbf{E}_{EE}$		-1.38		2.34
$\Delta\mathbf{E}_{EN}$		4.86		-3.52
$\boldsymbol{\epsilon}_\rho$		0.0052		0.0045

Table 4.2: B3LYP/aug-cc-pVQZ calculations of interaction energy contributions in kJ/mol, and $\boldsymbol{\epsilon}_\rho$ is in units of electrons for complexes of water with Be^+ and HF with CO^+. Be^+-H_2O is C_{2v} B3LYP/aug-cc-pVTZ optimized with $R_{Be\text{-}O} = 1.56$ Å, and CO^+-HF is C_s B3LYP/aug-cc-pVTZ optimized with $R_{C\text{-}F} = 1.86$ Å.

portion of the ethane potential. In this case, for compressed geometries, it is preferable to incorporate constant density relaxation using the ρ_{frz}-SCFMI initial wavefunction optimization, provided that errors stemming from the violation of the constant $\rho(\mathbf{r})$ constraint can be made sufficiently small.

4.4.5 Be^+ H_2O and CO^+ HF Complexes

Lastly we turn to two radical intermolecular interactions, which, while strongly interacting, are quite different from the covalent bond breaking in ethane examined above. The intent is to probe the importance of removing constant density polarization in equilibrium structures. The systems investigated are C_{2v} symmetry Be^+-H_2O and C_s symmetry CO^+-HF optimized using B3LYP/aug-cc-pVTZ, which have total interaction energies at the B3LYP/aug-cc-pVQZ level of -274.65 kJ/mol and -160.42 kJ/mol respectively.

The SCFMI-based EDA energy components computed with and without the ρ_{frz}-SCFMI initial wavefunction relaxation are reported in Table 4.2. From these results we see that the relaxation changes the frozen energy by only about 20% and the polarization contribution by even less, suggesting that the relaxation is qualitatively irrelevant. Moreover, at least at λ=2000, the changes in the coulomb and electron-nuclear energies upon relaxation are together a sizeable fraction of the total relaxation, indicating, as seen before, that the constant density polarization is overestimated due to these illegitimate contributions. We conclude that constant density polarization is a small effect for intermolecular interactions near equilibrium separations, which does not qualitatively change the results of the simple unrelaxed P_{frz} model.

4.5 Conclusions

In this work we have focused on comparing four possible initial supersystem wavefunctions for energy decomposition analysis. Each is optimal in some sense: solely geometric optimality in the case of P_{frz}, the initial wavefunction of ALMO-EDA among others, and both geometric and energetic optimality in the case of ρ_{frz}-SCFMI, ρ_{frz}-SCF, and ρ_{sum}-SCF, the last of which is used in DEDA. P_{frz} and ρ_{sum}-SCF differ in their form of geometric optimality; however, neither is guaranteed to be energetically superior, and feasible points for the latter are not guaranteed to exist with finite orbital basis sets.

We have also presented an algorithm for solving orbital optimizations with constant 3-space density constraints using the coulomb interaction of the density error with itself. We demonstrated that this method is capable of at least the same accuracy as constrained DFT based algorithms employing finite potential basis sets. While both approaches have the potential to enforce the constraint exactly, this goal has not yet been achieved for either one. We presented detailed tests to show that the approximately constrained results are nonetheless accurate enough, in the sense of showing sufficiently small deviations from formally conserved quantities such as the coulomb interaction, and electron nuclear attraction, to permit useful conclusions to be drawn.

Our main conclusions concerning the extent and the nature of the large energy lowering that can be obtained in the DEDA frozen energy (computed via the ρ_{sum}-SCF method) relative to the frozen orbital energy (computed via the P_{frz} approach) are as follows:

1. The large majority of the energy lowering is associated with the presence of electron delocalization (charge transfer) relaxations in the DEDA frozen energy. This is made quantitative by the dramatic energy difference observed between the ρ_{frz}-SCFMI and ρ_{frz}-SCF methods which use the same target density, but where inter-fragment relaxation is excluded by design in the former. It is our view that this constant ρ CT should not be a part of the frozen energy in an EDA composed of physically well-defined terms. It may nonetheless be valuable in other contexts such as the development of force fields that have no explicit CT terms.

2. There is a much smaller effect from the choice between using ρ_{frz} or ρ_{sum} in the overlapping regime where they differ. The latter does not necessarily admit feasible points in finite basis sets.

3. The removal of constant ρ polarization in the initial supersystem wavefunction, via the ρ_{frz}-SCFMI method, is an advance over the simple unrelaxed P_{frz} approach in an EDA, at least in principle. However, in practice, we have shown that the relaxation is inconsequential for qualitative interpretation in most of the examples presented here.

4. The merits of permitting orbital relaxation at constant density must be weighed against some illegitimate energy lowering introduced by imperfect constraint satisfaction. With

our present methods, tests of the results suggested this is not a serious problem when the relaxation is itself large, such as in the SCF methods or the SCFMI approach in the strongly overlapping regime.

Regarding future work, it may be worthwhile, though it is clearly difficult, to further develop algorithms for more accurately enforcing constant density constraints. After all, the primary argument against the removal of constant density polarization from the initial supersystem wavefunction is the computational effort that must currently be expended for modest improvements.

Chapter 5

Decomposition of the Frozen Energy

5.1 Introduction

The calculation of an interaction energy of a system of fragments is a well-defined computational procedure yielding a single scalar that, after accounting for the geometric distortions of fragments and entropic effects, can be used to compute how likely it is to find the species in question in the given configuration. What is also often of interest to chemists is the decomposition of the interaction energy into several other scalars corresponding to physical concepts that unfortunately lack unique mathematical definitions but may be useful in determining important parameters in the space of potential chemical modifications to the system. Some of the quantities that chemists consider to be important include charge transfer, permanent electrostatics, induced electrostatics, dispersion, and Pauli repulsion contributions to the interaction energy. When we say that these quantities have no unique definition we mean in the interesting part of the supersystem potential corresponding to strongly to moderately interacting fragment. In the very weakly interacting, non-overlapping portion of the potential, these physical concepts are effectively defined by matching terms in polarization theory[20], a perturbative approach to intermolecular interactions and the predecessor of SAPT[20], or they are strictly zero in the case of Pauli repulsion and charge transfer.

Because none of these terms have a unique definition in the overlapping portion of the potential, there exist many schemes for performing an energy decomposition analysis (EDA) of the interaction energy. A problem with many of the existing definitions is the neglect of proper antisymmetry in the electronic wavefunction when computing the expectation values that are used to define various terms, and this fundamental shortcoming is particularly prominent in the calculation of the Pauli repulsion and permanent electrostatic contributions to the interaction energy. The purpose of this work is to construct new definitions for the permanent electrostatic, Pauli repulsion, and what is asymptotically dispersion contributions that abide by fermionic quantum mechanics and which have other important formal properties lacking in other schemes.

We now consider the physical content of the contributions of interest. The term Pauli repulsion is often used to refer to steric or volume-exclusion effects, the marked increase in energy when two atoms are forced to occupy the same space. While certainly not hard spheres, atoms can be seen as having effective volumes that are the consequence of the "kinetic energy pressure"[13] exerted by electrons. The smaller the available volume as determined by the electron-nuclear potential of the complex, the higher the total kinetic energy of the electrons contained within. Each electron can be seen as occupying a finite volume because of the antisymmetry of fermions, expressed in the Pauli principle as the fact that electrons of the same spin cannot have the same position. Thus, when atoms are brought into close contact, the average volume available to each electron decreases, increasing the kinetic energy of the system. Pauli repulsion is sometimes referred to as exchange repulsion because the exchange terms in electronic energy expressions are likewise a consequence of the antisymmetry of the electronic wavefunction; however, this seems to us a misnomer as these exchange terms account for a degree of same spin electron correlation, an effect that is hardly repulsive in nature. One thing is clear irrespective of one's preferred formulation or name for this concept, and that is that the term should be positive semidefinite, never attractive.

The permanent electrostatic contribution describes the mean-field coulomb interaction between the electrons and nuclei of each fragment with the electrons and nuclei of all others where the electronic structure of each species has not been allowed to relax in response to the presence of the other fragments. Differences in definitions can be seen to arise from this last but important qualification about relaxation. This term is important because it reduces to the easily understood classical electrostatic interaction between fragment charge distributions in the well-separated portion of the potential.

While the permanent electrostatic term describes a large portion of the interfragment coulombic contributions to the interaction energy particularly for strongly interacting species or for species with permanent moments, that term alone does not describe the interfragment electron-electron interactions in full as it neglects their correlated motions. While it may seem almost as strange to think of electrons that are not and then suddenly are correlated as it is to think of electrons that are not and then suddenly are fermions, the former thought process is common in chemistry in no small part due to the way in which electronic structure methods themselves are constructed. Ultimately, electron-electron correlation is simply part of the accurate description of a system of electrons; however, its separation from mean-field behavior has proven conceptually advantageous in understanding the way in which molecules interact.

Indeed, it is known from polarization theory that asymptotically the distance dependence of the energetic contribution of inter-fragment electron correlation to the interaction energy is usually distinct (R^{-6}) from that of the mean-field coulomb interaction, which can be readily determined from classical electrostatics. This long-range inter-fragment dynamic correlation is known as dispersion, and while generally small in magnitude, it can be a comparatively significant component of weak intermolecular interactions. Dispersion is moreover manifestly

attractive, corresponding to the interaction of favorably aligned instantaneous multipole moments on different fragments. While dispersion must also play an important role in the overlapping regime, it, like the other EDA terms that have been discussed, lacks a unique definition in such a case. Moreover, it is incorrect that *all* correlation contributions to binding should be called dispersion, especially since such contributions can be net repulsive.[14] Thus, we will seek a term that describes non-mean-field electron-electron contributions to binding and contains within it the dispersion contribution which is of particular conceptual significance.

With the physical content of the terms of interest established, we introduce a common scheme for their calculation. The majority of EDA methods base their definitions of terms on what we will refer to as the classical approach in which the permanent electrostatic term is defined as the classical electrostatic interaction of the 3-space charge distributions (including nuclei) of fragments computed in isolation, $\{\rho_A^{tot}(\mathbf{r})\}$, and then translated to their respective positions in the complex.

$$E_{elec}^{cls} = \sum_{A<B} \int_{r_1} \int_{r_2} \rho_A^{tot}(\mathbf{r}_1) \frac{1}{\mathbf{r}_{12}} \rho_B^{tot}(\mathbf{r}_2) \tag{5.1}$$

$$\rho_A^{tot}(\mathbf{r}) = \rho_A(\mathbf{r}) + \rho_A^{nuc}(\mathbf{r}) \tag{5.2}$$

where ρ_A is the total spinless 3-space density for the electrons of fragment A only. The Pauli repulsion term in this approach is then computed as the remainder of the interaction energy for the unrelaxed complex, the simple difference between the energy of the initial supersystem wavefunction, $E_{initial}$, and the sum of isolated fragment energies, $\{E_A\}$, less the classical electrostatic interaction.

$$E_{Pauli}^{cls} = E_{initial} - \sum_A E_A - E_{elec}^{cls} \tag{5.3}$$

The initial supersystem energy depends on this choice of the initial supersystem wavefunction, which is meant to correspond to a complex in which electronic relaxation relative to the isolated fragment wavefunctions due to the presence of new species has not yet occurred, and we will see that the antisymmetric product of monomer wavefunctions is a common choice. Exchange-correlation or dispersion terms on the other hand are not treated in such a uniform way across EDA methods though it is not uncommon for an EDA to assign the contribution to binding from a density functional's dispersion correction as the dispersion term itself especially in the case of Grimme's density independent corrections[3, 4].

We now turn to the methods themselves. Bickelhaupt-Baerends EDA [44, 76, 77], KM EDA[38, 86, 87], and the CI-singles based scheme of Reinhardt et al.[79] all use the classical approach directly with the antisymmetric product of monomer wavefunctions, the Heitler-London wavefunction, as the initial supersystem wavefunction. These methods do not contain separate exchange-correlation terms. The method of Mandado and Hermida-Ramón[82],

SRW-EDA[98], and ETS-NOCV [39–41, 78] all similarly use the classical electrostatic term and the Heitler-London wavefunction though with a slight twist on the classical approach outlined above. Mandado and Hermida-Ramón[82] further decompose the Pauli term from the classical approach into an exchange term and a repulsion term where the latter is computed as the interaction of the 3-space density deformation upon going from the simple sum of fragment densities to that of the Heitler-London wavefunction with both the isolated fragment densities and itself plus its associated kinetic energy contribution. Likewise, SRW-EDA[98] and ETS-NOVC[39–41, 78] can both optionally separate the classical Pauli term into a Pauli term and an electron-exchange or exchange-correlation term, respectively, where the separated Pauli term is defined as the energy change upon going from the sum of fragment densities matrix to that of the Heitler-London wavefunction.

There are also several other methods that use the classical approach with the antisymmetric product of monomer wavefunctions as the initial wavefunction to describe permanent electrostatic and Pauli repulsion effects such as SAPT[19, 20, 22–25, 83, 84], BLW-EDA[46–49], and PIEDA[88, 89], but these methods also include separate dispersion terms. SAPT computes dispersion contributions by considering certain classes of excitations in evaluating the energetic contributions of the intermolecular interaction operator at each perturbation order, including exchange-dispersion corrections for proper wavefunction antisymmetry and coupling terms with the induction (polarization and charge transfer) interaction at third and higher orders. Within SAPT theories based on density functional theory, dispersion is included with a generalization of the above employing frequency dependent density susceptibilities. SAPT methods are anomalous in the current context as they do not decompose the same total interaction energy as computed by a given approximate Kohn-Sham model chemistry or the exact functional itself at finite order. PIEDA decomposes the energetic contributions from all pairs of monomers in a complex and adopts the approach of assigning the entire correlation energy contribution to the binding energy for each dimer as computed by a post-HF wavefunction method to dispersion. BLW-EDA on the other hand opts to exploit the structure of specific density functionals that include a non-local correlation functional (dDXDM[122–126] is used as the example) designed to capture long-range dispersion effects. It is suggested by Steinmann et al.[49] that the long-range dispersion energy be defined as the difference in the non-local correlation functional's contribution to the total energy upon going from isolated monomer wavefunctions to the Heitler-London wavefunction.

The GKS-EDA[45, 80, 81] scheme likewise uses the classical electrostatic term; however, the Pauli repulsion term in this method is computed quite differently. The energy difference from which the electrostatic interaction is subtracted to determine the Pauli term is computed using the usual monomer KS wavefunctions and their antisymmetric product, but the energies of these wavefunctions are evaluated with full exact exchange only (the Hartree-Fock functional). The contribution to this energy difference from the exchange matrix itself can also be separated out to yield an exchange term and by subtraction a repulsion term. The GKS-EDA scheme also computes a correlation term that is the exchange-correlation functional's contribution to the total binding energy relative to that of a full exact exchange

treatment. From this correlation term, a functional-form-specific dispersion contribution (such as from Grimme's -D[3, 4]) can also be separated.

There are also a number of methods that do not make use of the antisymmetric product of monomer wavefunctions in the calculation of a Pauli term. In DEDA[51, 75, 127], the electrostatic interaction is computed as in the classical approach; however, the initial wavefunction used to compute the Pauli repulsion term by difference is the lowest energy single Slater determinant that has 3-space density equivalent to the sum of non-interacting fragment densities. The authors of this method point out that what we have referred to as the Pauli repulsion term contains contributions from both Pauli repulsion and attractive vdW interactions. They do not attempt to separate the two but do suggest that a scheme based on contributions from specific density functional components could be used. The method of de Silva and Korchowiec[97] uses the standard classical electrostatic term but computes the Pauli-repulsion-like term, called exchange, as the difference between the energy of a determinant describing the polarized supersystem and the energy of the sum of polarized fragments' densities matrix.

NEDA[34–36], which is based on the construction of supersystem NBOs[37, 85], uses the classical approach to compute the electrostatic interaction but then defines its Pauli-repulsion-like term, core, as the energy cost to go from isolated monomers to the polarized monomer Lewis structures identified from analysis of the converged supersystem density matrix plus the electrostatic consequence of each monomer density polarizing in the field of the other already polarized monomers. To this is usually added an exchange-correlation term, which is the exchange-correlation functional's contribution to the interaction of these polarized monomer lewis structures. Natural Steric Analysis[128–130] is likewise based on NBO analysis and draws heavily from the orbital orthogonality interpretation of antisymmetry. A common notion is that antisymmetry and thus Pauli repulsion is closely related to the requirement of orthogonality of the occupied molecular orbitals because, unlike the energy of the symmetric Hartree product wavefunction, the energy of the antisymmetric Slater determinant wavefunction depends only on the span of the occupied orbitals, which is most conveniently expressed in terms of a set of orthogonal vectors. Moreover, this orthogonality of occupied orbitals that is effectively brought about by electronic wavefunction antisymmetry or rather the constraint on the rank of the projector into the occupied subspace can be seen as enforcing the volume exclusion effects expressed in the Pauli principle. In Natural Steric Analysis, the steric energy is defined as the difference in the exchange energy of the supersystem and the sum of exchange energies of the monomers where the exchange energies are computed as the difference in the trace of the Fock matrix in the basis of NBOs and in the basis of their non-orthogonal counterparts, ignoring metrics. This scheme also allows for an approximate decomposition into pairwise local orbital contributions which can be intramolecular.

In DFTs-EDA[131, 132], a separate steric term is computed as the Weizsäcker kinetic energy contribution to total binding, which is correct for bosonic systems, and a Pauli term is computed as the difference between this and the contribution to binding from the usual

non-interacting kinetic energy of Kohn-Sham. The remaining binding energy is divided into exchange-correlation functional contributions and electrostatics.

We now mention the methods that do not attempt to separate out permanent electrostatic, Pauli repulsion, or exchange-correlation effects. These methods are RVS[43, 87], CSOV[42], and ALMO[15–18]. Instead, these methods all use a frozen or steric energy that is the sum of the classical electrostatic and classical Pauli repulsion terms, the difference between the energy of the antisymmetric product of monomer wavefunctions and the sum of isolated monomer energies. At least in the case of ALMO, the pervasive classical approach is avoided due to its reliance on a classical charge distribution that does not correspond to the charge distribution of the unrelaxed supersystem. However, the authors agree[74] that the absence of distinct terms describing permanent electrostatics and Pauli repulsion that are present in other decomposition schemes is a deficiency of the ALMO-EDA because the related concepts are each in their own right important to the understanding of intermolecular interactions. It is thus the goal of this work to construct a more satisfying decomposition of the initial supersystem wavefunction interaction energy for use in SCFMI-based EDA schemes such as ALMO.

5.2 Theory

5.2.1 Decomposition of the Initial Supersystem Energy

A major disadvantage of the classical approach is that it relies on the use of fragment charge distributions translated from infinitely far away to the finite separation cluster geometry where they do not necessarily collectively describe the charge distribution of a valid initial electronic wavefunction of the supersystem within the given finite basis set model chemistry. This is because the sum of projectors is only a projector itself if the projection operators are orthogonal, corresponding to a rather uninteresting complex in which all of the constituent fragments are well-separated. It is also well known that the 3-space density of the antisymmetric product of monomer wavefunctions, shown in the introduction to be a very common choice for the initial supersystem wavefunction, is distorted relative to the simple sum. The classical electrostatic energy thus computes the coulomb interaction between charge distributions that not only aren't there in the initial state but moreover could possibly never be! The mean-field electrostatic interactions between the charge distributions of monomeric units is precisely what the permanent electrostatic term seeks to describe; however, upon formation of the complex, the monomer densities have changed relative to those computed in isolation to account for proper antisymmetry. Our first task in computing a more reasonable permanent electrostatics term will thus be to identify a portion of the supersystem electron density that can be justifiably tagged to each monomer, its properly distorted density in the complex.

We note that the above argument depends on the initial wavefunction employed and thus

only applies to most methods. The only exception that we know of is the initial supersystem wavefunction in DEDA, which is constructed to be the lowest energy single determinant wavefunction with 3-space density equivalent to the sum of fragment 3-space densities. The monomer charge distributions in this case are thus undistorted if the chosen model chemistry permits such a supersystem density. However, the DEDA initial wavefunction is not without issues related not only to this formal feasibility but also to the interpretation of energy terms, discussed at length in a previous work (Chapter 4). In short, the initial supersystem wavefunction in DEDA in many cases permits considerable interfragment electron delocalization, interactions associated with charge transfer in ALMO. Another disadvantage of DEDA relative to the scheme that we propose in this work is that while fragment contributions to the supersystem 3-space density are defined, fragment contributions to the supersystem density matrix are not.

The only way to guarantee that a sum of newly identified fragment densities ($\{\tilde{\rho}_A\}$) will yield a given initial supersystem density (ρ_{init}) is for the new fragment occupied subspace projectors ($\{\tilde{\mathbf{P}}_A\}$) to be orthogonal with a collective span equal to that of the initial supersystem wavefunction ($\mathbf{P}_{init}$). The problem of identifying monomer wavefunctions is thus reduced to an appropriate subspace orthogonalization, which, while not unique, can be made optimal in a sense that connects the necessarily distorted densities to those of unrelaxed fragments. The way that fragment subspaces are chosen initially is of course with energetic optimality in isolation, without the contributions of other fragments' electrons or nuclei in the energy expression. We propose that the optimal fragment subspaces within the initial supersystem wavefunction be chosen similarly but with a collective energetic optimality condition and the constraint that these subspaces are orthogonal and sum to the initial supersystem occupied subspace projector,

$$E_{frag}^{ortho} = \underset{\{\tilde{\mathbf{P}}_{\alpha,A}\},\{\tilde{\mathbf{P}}_{\beta,A}\}}{\text{minimize}} \sum_A E_A[\tilde{\mathbf{P}}_{\alpha,A}, \tilde{\mathbf{P}}_{\beta,A}] \tag{5.4}$$

where:

$$\text{Tr}\left[\tilde{\mathbf{P}}_{\sigma,A}\mathbf{S}\tilde{\mathbf{P}}_{\sigma,B}\mathbf{S}\right] = \begin{cases} 0 & B \neq A \\ \text{Tr}\left[\tilde{\mathbf{P}}_{\sigma,A}\mathbf{S}\right] & B = A \end{cases} \tag{5.5}$$

$$\mathbf{P}_{\sigma,init} = \sum_A \tilde{\mathbf{P}}_{\sigma,A} \tag{5.6}$$

It is assumed that the rank of $\mathbf{P}_{\sigma,init}$ for each spin space, σ, is such that the new fragment projectors, $\{\tilde{\mathbf{P}}_{\sigma,A}\}$, can be chosen to have the same rank as the corresponding $\mathbf{P}_{\sigma,A}$ computed for the fragment in isolation without any orthogonality constraints. This is an appropriate approach for identifying monomeric units in the case of the initial supersystem wavefunction but not for instance in the case of the polarized wavefunction because the former still carries the meaning of unrelaxed fragments while the later includes explicit supersystem-specific relaxation that an optimization without knowledge of the electrons or nuclei of all fragments would in some sense try to reverse. The new definition of the permanent electrostatic

interaction based on this simple optimization problem is then:

$$E_{elec} = \sum_{A<B} \int_{r_1} \int_{r_2} \tilde{\rho}_A^{tot}(\mathbf{r}_1) \frac{1}{\mathbf{r}_{12}} \tilde{\rho}_B^{tot}(\mathbf{r}_2) \tag{5.7}$$

This expression is very similar to the classical expression (5.1); however, unlike in the classical case, this expression can also be written in terms of matrix elements computed from antisymmetric electronic wavefunctions:

$$\begin{aligned} E_{elec} = \quad & \mathrm{Tr}\left[(\mathbf{J}[\mathbf{P}_{init}] + \mathbf{V}_{total})\mathbf{P}_{init}\right] \\ & - \textstyle\sum_A \mathrm{Tr}\left[(\mathbf{J}[\tilde{\mathbf{P}}_A] + \mathbf{V}_A)\tilde{\mathbf{P}}_A\right] + \Delta E_{NN} \end{aligned} \tag{5.8}$$

where ΔE_{NN} is the energy change derived from changes in nuclear-nuclear interactions upon formation of the complex, an entirely classical quantity within the Born-Oppenheimer approximation.

There is an additional interpretation of the orthogonality constraint in this optimization problem, and that is the inclusion of volume exclusion effects in fragment wavefunction determination. In the interest of lowering the potential energy of the system, the density tagged to each fragment will be closest to the only nuclei that are known to it, those composing the fragment itself, and though interpenetrating function tails must occur to some degree, this density will be expelled from the region closest to other fragments' nuclei by the presence of the other fragments' electrons, which are in turn most energetically suited to be near their respective nuclei. The partitioning of the valence space of different fragments is determined by overall energetic importance of that portion of Hilbert space to each fragment. Not least because of this volume exclusion interpretation of the constrained fragment solutions, we put forward the following definition for the Pauli repulsion term:

$$E_{Pauli} = \sum_A E_A[\tilde{\mathbf{P}}_A] - E_A[\mathbf{P}_A] \tag{5.9}$$

This term as defined moreover contains within it all kinetic energy differences between the sum of isolated fragments and the initial supersystem wavefunction, thus accounting entirely for the effects of the "kinetic energy pressure." It is furthermore a formally positive semidefinite quantity due to the variational determination of the two states considered in its calculation. We note that in practice if the unconstrained isolated fragment calculations are performed in the usual way with a subset of the entire supersystem basis, then this expression can be negative due to basis set superposition error (BSSE); however, as we have in the past (Chapter 3), we suggest the use of basis sets that can properly describe the monomers in the system such that BSSE is negligibly small. There are many other possible orthogonal decompositions of the initial supersystem density matrix that could be performed, but the solution to (5.4) not only uses energetic optimality to associate fragment subspaces with their respective fragment nuclei, the only particles with unambiguous fragment tagging, but

also minimizes the Pauli repulsion contribution as defined by (5.9). While the magnitude of this Pauli term has no guaranteed value relative to its classical analog, this optimality serves to reduce as much as possible the presence of large, canceling terms in our decomposition.

The sum of the above two terms does not account for the entire energy difference between the sum of isolated fragments and the initial supersystem wavefunction. The remainder is precisely the exchange-correlation interaction between what we have identified as the properly deformed monomer densities:

$$\begin{aligned} E_{xc} &= E_{XC}[\mathbf{P}_{init}] - \textstyle\sum_A E_{XC}[\tilde{\mathbf{P}}_A] \\ &= E_{Frz} - E_{elec} - E_{Pauli} \end{aligned} \tag{5.10}$$

$E_{XC}[\mathbf{P}]$ is the exchange-correlation functional for our given model chemistry that is assumed to have at most density matrix dependence, which includes Hartree-Fock itself as well as meta and hybrid functionals but unapologetically excludes double-hybrids. Because $\sum_A \tilde{\mathbf{P}}_A = \mathbf{P}_{init}$, this expression stands in sharp contrast to similar expressions in other methods that merely compute the change in the contribution of the exchange-correlation functional in its entirety or a functional-specific portion thereof to the energy difference between some supersystem wavefunction and the isolated monomers. Moreover, because not only 3-space densities but density matrices have been imputed to each fragment, this approach can be used to decompose interaction energies computed by density functionals incorporating more than simply ρ dependence.

We chose not to separate out an explicitly dispersion-like component from this exchange-correlation energy term even when the form of the functional might suggest it because, at least in the best performing functionals, the dispersion-like component is optimized together with the rest of the exchange-correlation functional, which makes their contributions far from independent. Another important reason for this choice is that the exact functional will almost certainly not permit such a separation. While the exchange-correlation functional clearly contributes to the polarization and charge transfer terms as well, we separate out the exchange-correlation contributions only for the initial supersystem wavefunction and consider all energy lowering associated with wavefunction relaxations to be polarization or charge transfer as appropriate. This choice is similar to those that are made in higher order SAPT expansions where terms such as induction-dispersion arise and must be combined if one wishes to avoid an ever increasing number of mixed terms.

While the Heitler-London wavefunction was mentioned as the initial supersystem wavefunction in the description above, using this wavefunction is not explicitly necessary. The only requirement on the supersystem occupied subspace projector in order to maintain the meaning of the new electrostatic, Pauli repulsion, and exchange-correlation terms is that it must correspond to a supersystem is which the relaxation of fragments due to their new chemical environment has not yet occurred. Thus one could alternatively employ an initial wavefunction that has been made energetically optimal in a sense such as by the removal of constant density polarization (Chapter 4).

We note that a different approach in which orthogonal fragment occupied subspaces were optimized not in the span of the initial occupied subspace projector as described above but in the span of the entire supersystem basis was considered. Indeed, the equations below can be easily adapted to include a global virtual subspace that does not contribute to the energy expression but permits additional degrees of freedom. The initial supersystem wavefunction in this case would then be chosen as the antisymmetric product of the so optimized isolated but constrained monomer wavefunctions; however, we thought the diminished connection to the truly isolated monomers in this approach to be undesirable.

5.2.2 Expected Behavior of Terms

When the occupied subspaces of fragments computed in isolation are not overlapping and the basis is such that there is no BSSE, then the orthogonal fragment subspaces that are the solution to (5.4) are precisely the occupied subspaces computed in isolation. This fact has several important consequences and guarantees the polarization theory limiting behavior of terms. For well-separated fragments, the Pauli repulsion term (5.9) vanishes, and the electrostatic term (5.8) is identical to the classical electrostatic term for equivalently treated fragments and will decay as classical electrostatics predicts. In the short-range, for which there is no exact answer, we expect the Pauli term to decay exponentially just as hydrogenic orbital overlap decays. If the underlying model chemistry is capable of describing dispersive interactions, then the exchange-correlation term will contain the dispersion contribution to the interaction, decaying as R^{-6} in the long range. The exact exchange contribution to binding decays exponentially as well, and so an exponential decay of the exchange-correlation term is expected for the Hartree-Fock functional if not for other functionals at short range where exchange contributions are relevant. The exchange-correlation term is thus expected to transition from approximately exponential decay (there are short-range contributions from correlation as well as from exchange) to polynomial R^{-6} decay for accurate density functionals.

5.2.3 Solution of the Optimization Problem for Monomer Subspace Determination

We now turn to the solution of the optimization problem from which the three newly defined EDA terms, E_{elec}, E_{Pauli}, and E_{xc}, follow. The structure of the problem (5.4) is very similar to that of ROSCF in that only inter-subspace rotations are energetically relevant, and the subspaces are constrained to be orthogonal. For simplicity and without loss of generality we also assume intra-subspace orthogonality. We parametrize the vectors, $\mathbf{T}$, defining the new orthogonal fragment subspaces in terms of orbital rotation parameters, $\mathbf{\Delta}$, as:

$$\mathbf{T} \leftarrow \mathbf{T}\, \mathbf{e}\exp\left(\mathbf{\Delta} - \mathbf{\Delta}^T\right) \tag{5.11}$$

$$T^{\mu}_{\bullet\, Ai} \leftarrow \sum_B T^{\mu}_{\bullet\, Bj} \big[\delta_{BjAi} + \Delta_{BjAi} \tag{5.12}$$
$$-\Delta_{AiBk} + \tfrac{1}{2}\sum_D (\Delta_{BjDl}\Delta_{DlAi} - \Delta_{BjDl}\Delta_{AiDl}$$
$$-\Delta_{DlBj}\Delta_{DlAi} + \Delta_{DlBj}\Delta_{AiDl}) + O\left(\boldsymbol{\Delta}^3\right)\big]$$

$$\tilde{P}^{\mu\nu}_A = T^{\mu}_{\bullet\, Ai} T^{\nu}_{\bullet\, Ai} \tag{5.13}$$

The gradient of the objective function (5.4) with respect to orbital rotation parameters is thus:

$$\left.\frac{\partial E^{ortho}_{frag}}{\partial \Delta_{CkDl}}\right|_{\boldsymbol{\Delta}=0} = 2\left[\mathbf{T}^T(\mathbf{F}_D - \mathbf{F}_C)\mathbf{T}\right]_{CkDl} \tag{5.14}$$

where:

$$(F_A)_{\mu\nu} = \frac{\partial E_A[\tilde{\mathbf{P}}_A]}{\partial \tilde{P}^{\mu\nu}_A} \tag{5.15}$$

Iterations for this optimization problem are fairly expensive, requiring number of fragments full Fock matrix builds in the supersystem basis. With this in mind, we now present a preconditioning strategy for this problem that has proven effective within a preconditioned L-BFGS[103, 104, 118] algorithm incorporating a robust line search[119]. As in past work[104](Chapters 3 and 4), we invert the portion of the Hessian that does not require the evaluation of new two-electron integrals or second functional derivatives of the exchange-correlation energy, which in this case is:

$$\sum_A \frac{\partial E^{ortho}_{frag}}{\partial \tilde{P}^{\mu\nu}_A} \left.\frac{\partial^2 \tilde{P}^{\mu\nu}_A}{\partial \Delta_{CkDl}\partial \Delta_{XiYj}}\right|_{\boldsymbol{\Delta}=0} \tag{5.16}$$
$$\begin{aligned} = \quad & \left[\mathbf{T}^T(\mathbf{F}_D - 2\mathbf{F}_C + \mathbf{F}_X)\mathbf{T}\right]_{XiDl}\delta_{CkYj} \\ & - \left[\mathbf{T}^T(\mathbf{F}_C - 2\mathbf{F}_D + \mathbf{F}_X)\mathbf{T}\right]_{XiCk}\delta_{DlYj} \\ & + \left[\mathbf{T}^T(\mathbf{F}_C - 2\mathbf{F}_D + \mathbf{F}_Y)\mathbf{T}\right]_{YjCk}\delta_{DlXi} \\ & - \left[\mathbf{T}^T(\mathbf{F}_D - 2\mathbf{F}_C + \mathbf{F}_Y)\mathbf{T}\right]_{YjDl}\delta_{CkXi} \end{aligned}$$

We compute the inverse of this approximate Hessian applied to a vector iteratively using conjugate gradient, which itself requires only the contraction of (5.16) with a trial vector. This conjugate gradient algorithm is in turn preconditioned with the inverse of an even more approximate form of the Hessian that incorporates only subspace-pair diagonal blocks:

$$\sum_A \frac{\partial E^{ortho}_{frag}}{\partial \tilde{P}^{\mu\nu}_A} \left.\frac{\partial^2 \tilde{P}^{\mu\nu}_A}{\partial \Delta_{CkDl}\partial \Delta_{CiDj}}\right|_{\boldsymbol{\Delta}=0} \tag{5.17}$$
$$\begin{aligned} = \quad & -2\left[\mathbf{T}^T(\mathbf{F}_C - \mathbf{F}_D)\mathbf{T}\right]_{CkCi}\delta_{DlDj} \\ & +2\left[\mathbf{T}^T(\mathbf{F}_C - \mathbf{F}_D)\mathbf{T}\right]_{DlDj}\delta_{CkCi} \end{aligned}$$

These blocks can be easily inverted after pseudocanonical-like transformations within subspaces. Our guess for the problem (5.4) is the symmetric orthogonalization of the occupied subspace vectors computed for the fragments in isolation, and it has proven to be a good guess in practice, corresponding to the geometrically optimal instead of the energetically optimal choice for the fragment subspace orthogonalization.

5.3 Results and Discussion

5.3.1 Computational Details

Calculations in this work were performed with a development version of QChem [70, 108]. Except in the investigation of the dissociation of ethane, the initial supersystem wavefunction used in all calculations in this work is the antisymmetric product of monomer wavefunctions, the Heitler-London or frozen orbital wavefunction, both because it allows direct comparison of the new approach to the common classical approach described in the introduction and because the removal of constant density polarization (Chapter 4) is of minimal importance for most systems investigated here.

The fragment subspaces that we use both to delimit polarization and charge transfer contributions to the interaction energy as well as to remove constant density polarization from the initial supersystem wavefunction of ethane are based on fragment electric-field response functions (FERFs)(Chapter 3). Specifically, in this work, we use the non-orthogonal dipole plus quadrupole (nDQ) subspaces, which contain the degrees of freedom necessary for fragments to respond exactly to weak electric fields and field gradients. These subspaces allow us to avoid the weaknesses of traditional fragment-AO-subspace schemes that overestimate polarization contributions in large basis sets and have a trivial basis set limit of zero for charge transfer contributions.

To explore the behavior of the newly defined exchange-correlation term, we make use of both standard Hartree-Fock for which results are in the SI for comparison and the ωB97X-V[11] density functional, which includes the VV10[5] non-local correlation functional for the treatment of dispersion. For want of analytic second derivatives for VV10 and thus ωB97X-V, steps involving application of the orbital Hessian to vectors as in the calculation of FERF nDQ subspaces are performed using finite difference matrix-vector products as described previously[120]. Basis sets used in this work are quadruple zeta with diffuse functions, aug-cc-pVQZ[109, 110] and def2-QZVPPD[133], as such basis sets are large enough to mitigate BSSE effects and have also been shown to produce valid FERF nDQ polarization subspaces (Chapter 3).

Unless otherwise noted, the coordinates investigated correspond to the rigid displacement of monomers relative to the ωB97X-V/aug-cc-pVQZ equilibrium structure. No corrections for BSSE were performed in this work. We note that the methods described can be applied to the decomposition of the interaction energy of a system of an arbitrary number of fragments

as well as the many-body expansion thereof; however, we restrict ourselves at present to dimer applications where chemical intuition is strongest.

5.3.2 Ammonia Borane

The first system that we examine is the ammonia borane complex, which is interesting in the current context because both monomers have permanent dipole moments, which should make a considerable contribution to the interaction energy in both permanent and induced electrostatics terms; however, charge transfer to the electron-poor borane molecule is also significant and leads to quite strong total binding, -189.22 kJ/mol at the close to equilibrium $R_{N\text{-}B}$=1.65Å separation. With such a short inter-monomer contact and thus large inter-monomer occupied orbital overlaps, we expect considerable differences between the new and classical approaches to the frozen orbital energy decomposition. Figure 5.1a shows that charge transfer is indeed important in this complex though it is nearly matched by the polarization contribution, which is similarly more favorable at compressed distances as it corresponds to the relaxation of each monomer in response both to the increasingly more perturbing field of the other and to the greater density deformations occurring upon formation of the initial supersystem wavefunction. While the charge transfer and polarization terms are both very favorable to binding, the frozen orbital term does not become attractive until almost $R_{N\text{-}B}$=2.00Å despite the presence of favorably aligned permanent moments.

The decomposition of the frozen orbital interaction by both the new and classical schemes appears in Figure 5.1b, and the two methods offer qualitatively different descriptions of the permanent electrostatic interaction at compressed distances. The new electrostatic term is less attractive by 153.00 kJ/mol at $R_{N\text{-}B}$=1.65Å and becomes repulsive at $R_{N\text{-}B}$=1.00Å while the classical electrostatic term is still becoming more attractive upon compression at that separation. To better understand the origin of this dramatic difference in permanent electrostatic contributions to binding we plot (Figure 5.2) the differences in the densities that are used to compute the new and classical electrostatic terms. This plot displays the characteristic density deformations that occur upon formation of the antisymmetric product of monomer wavefunctions that have been discussed extensively by others[44], depletion of density in the region of space between monomers and an increase in density near nuclei; however, because we have divided the initial supersystem wavefunction into monomer contributions, we are able to visualize the deformation undergone by each monomer instead of merely the net change for the supersystem. While there is some increase in ammonia density (red) near the borane nuclei, the major effect is the relocation of ammonia charge from near the boron nucleus to a region much closer to the nitrogen atom. The result is greatly diminished charge interpenetration and increased shielding of nuclei relative to the classical approach with the consequence of an overall diminished electrostatic interaction. We note that like the new electrostatic term, the classical electrostatic term will also ultimately become repulsive at short inter-nuclear distances where nuclear-nuclear repulsion will begin to dominate; however, where this transition from attractive to repulsive occurs is clearly quite

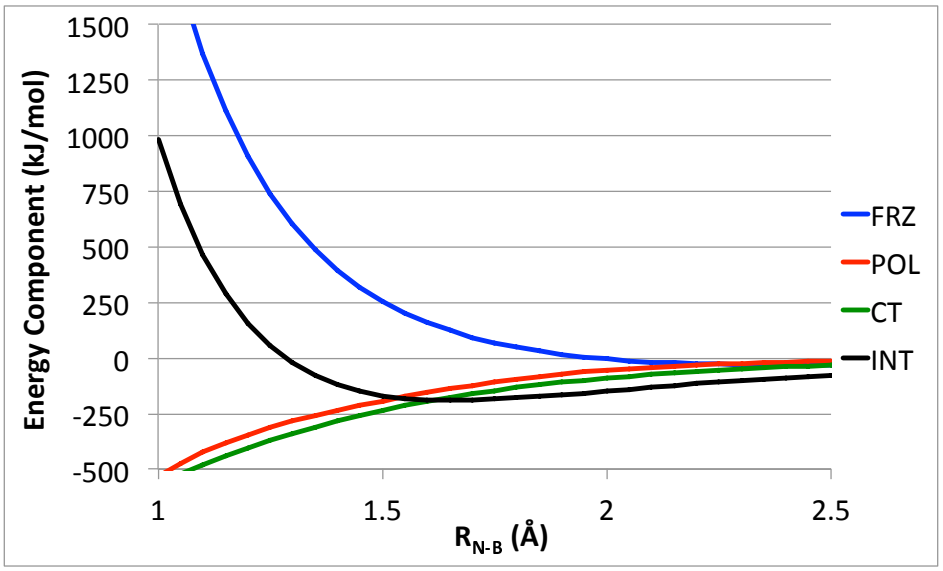

(a) Basic energy decomposition terms (FRZ, POL, CT) as well as the total interaction energy (INT) along the coordinate.

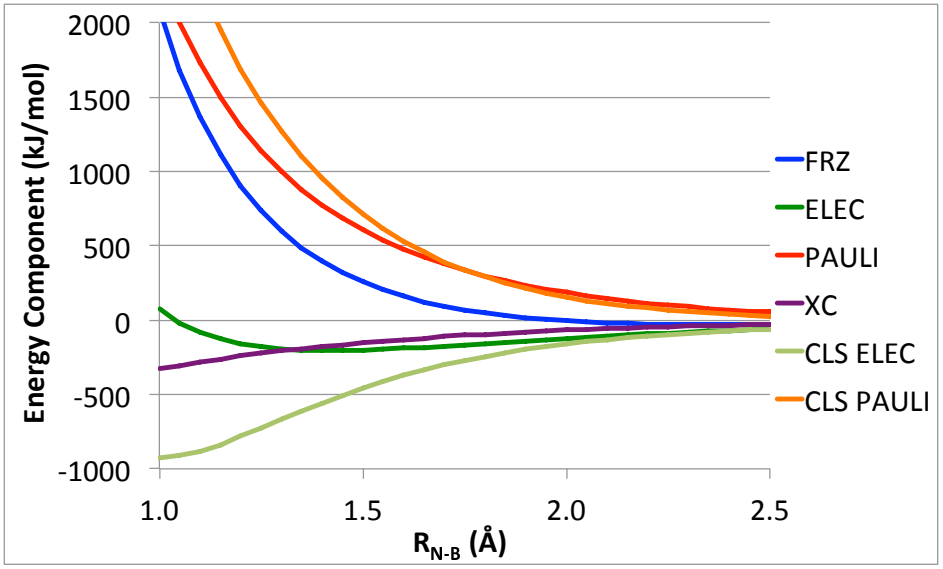

(b) Further decomposition of the frozen energy (FRZ) based on the new scheme presented in this work (ELEC, PAULI, XC) and based on the classical approach (CLS ELEC, CLS Pauli).

Figure 5.1: Energy terms computed with ωB97X-V/aug-cc-pVQZ for the rigid dissociation along the N-B coordinate of the ammonia borane complex relative to the C_{3v} ωB97X-V/aug-cc-pVQZ optimized geometry (equilibrium $R_{N\text{-}B} = 1.65$Å).

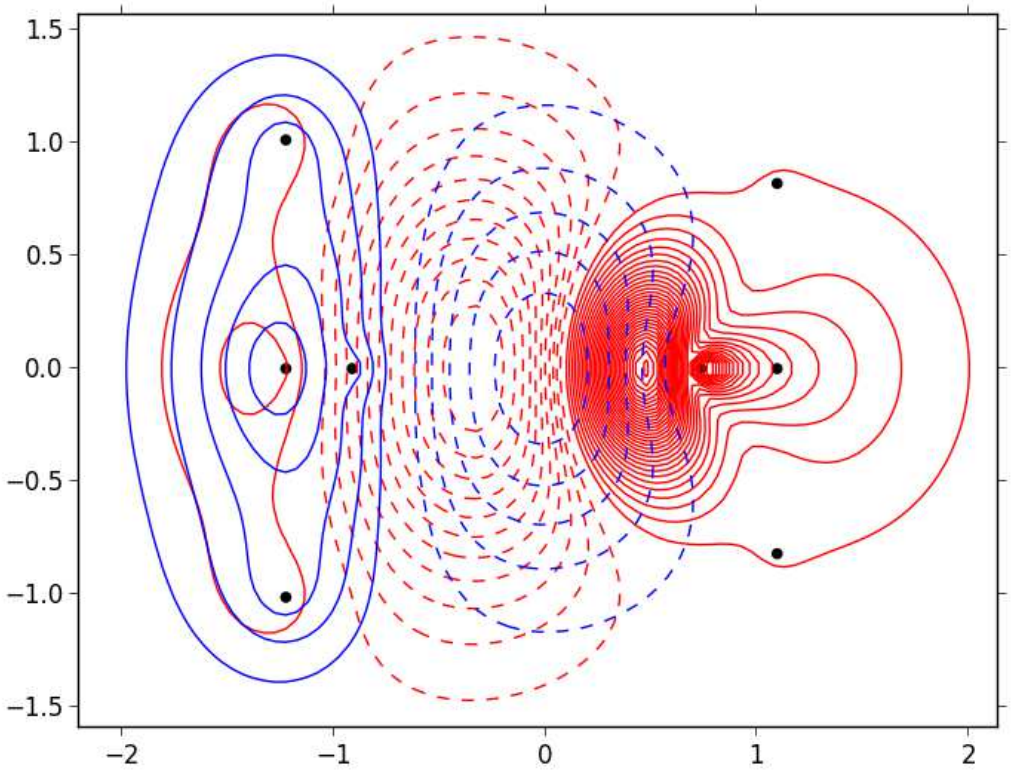

Figure 5.2: Contour plot of the change in density for NH_3 (red) and BH_3 (blue) in the ωB97X-V/aug-cc-pVQZ optimized ammonia borane complex rigidly translated to the essentially equilibrium $R_{N\text{-}B} = 1.65$Å. Single points were performed with ωB97X-V/aug-cc-pVQZ. Values plotted are the differences in the 3-space total spinless density, integrated to a plane ($\Delta_A(x,y) = \int dz \Delta\rho_A(x,y,z)$), for each fragment, A, upon going from the optimal isolated fragment density matrix to that assigned to the fragment within the initial supersystem wavefunction. Contours are evenly spaced at 0.2 $e^-/Å^3$ with positive contours solid and negative contours dashed. Dots indicate the positions of nuclei.

different between the new and classical schemes due to differences in the treatment of charge penetration effects and thus the shielding of nuclei by electrons. Due to the appreciably more attractive classical electrostatic interaction, the corresponding classical Pauli repulsion term is also much larger in magnitude despite its inclusion of exchange-correlation contributions to binding, which, by the new scheme, are computed to be quite stabilizing at compressed distances.

In order to identify the characteristic distance dependence of the terms that are produced

by the new and classical approaches to the decomposition of the frozen orbital energy we plot the log of the interaction terms with respect to both the interfragment separation (Figure 5.3a) and the log of the interfragment separation (Figure 5.3b). The latter shows that the XC term's long range decay is approximately $R_{N\text{-}B}^{-6}$, the polynomial dependence on distance expected for dispersion interactions, and both the new and classical electrostatic terms decay as approximately $R_{N\text{-}B}^{-3}$ with some contributions from higher order moments in agreement with the expected limiting behavior for a permanent dipole-dipole interaction. We see from the near linear behavior in Figure 5.3a that the new Pauli term decays exponentially throughout the coordinate while the classical Pauli becomes attractive at $R_{N\text{-}B}$=3.30Å and tracks the new exchange-correlation term, thus acquiring the meaning of dispersion in the long range. This spurious attractive contribution in the classical Pauli term is not present for example when the model chemistry does not include dynamic correlation as in the case where Hartree-Fock is used. Indeed, the corresponding curves for Hartree-Fock (See SI) indicate exponential decay of the two Pauli terms, which are both uniformly repulsive. In this case, the long range behavior of the exchange-correlation term, which includes only exact exchange, is approximately exponential as well.

5.3.3 Water-Na^+

The next system that we examine is the neutral water molecule interacting with a sodium cation, and EDA results for this system rigidly dissociated along the $R_{O\text{-}Na}$ coordinate appear in Figure 5.4. From Figure 5.4a we see that the binding is dominated by the frozen orbital contribution, which is the primary attractive interaction near equilibrium and beyond. Contributions to binding from polarization become increasingly important at short separations as the intermolecular perturbation increases, and charge transfer is shown to be negligible except at the most compressed geometries. Figure 5.4b shows the decomposition of the frozen orbital energy both by the new scheme for computing electrostatic, Pauli repulsion, and exchange-correlation contributions and by the classical approach described in the introduction. For this cationic system with a fairly compact density and thus minimal expected density distortion due to monomer occupied orbital overlap, there is a minimal difference in the new and classical electrostatic terms around the equilibrium separation (12.85 kJ/mol at $R_{O\text{-}Na}$ = 2.25Å). The difference between these two terms increases to a maximum of 42.69 kJ/mol at 1.70Å. At separations less than this, the classical electrostatic term becomes increasingly attractive more rapidly due to the increased charge penetration permitted in the model. The differences in the densities used to compute the new and classical electrostatic terms appear in Figure 5.5, and we note for this system the density difference contours are drawn at intervals of one quarter the size compared to those used for ammonia borane above, highlighting the diminished charge rearrangement in this case. Again, density is generally relocated from the inter-monomer region closer to the nuclei with some tails developing near other nuclei. The increase in sodium density (red) both near the oxygen atom of water (blue) as well as on the opposite side of the sodium atom from water may be the reason for a

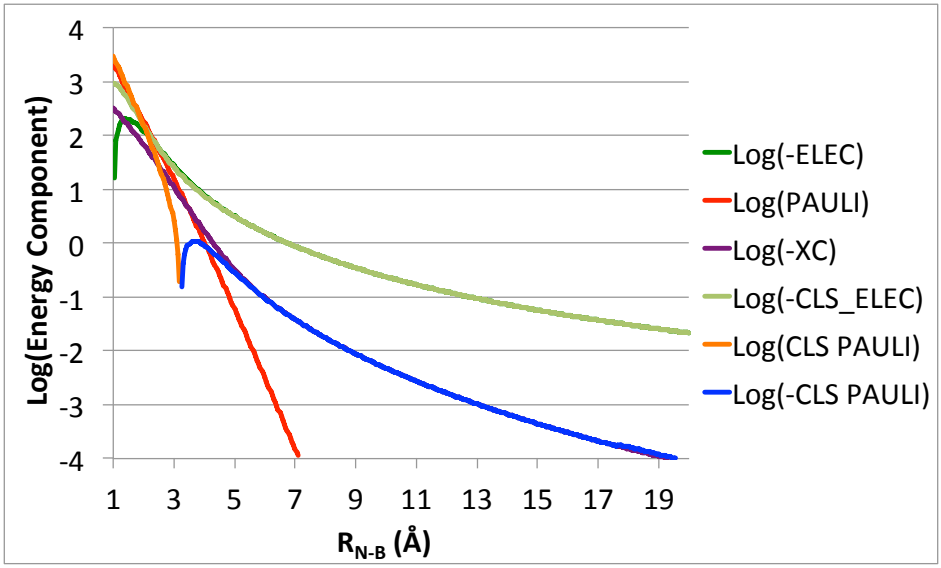

(a) Plot of log(±TERM) vs. $R_{N\text{-}B}$ for terms summing to the frozen energy as computed by the newly introduced and classical approaches. Linear relationships in this plot indicate an exponential decay of the given interaction with distance.

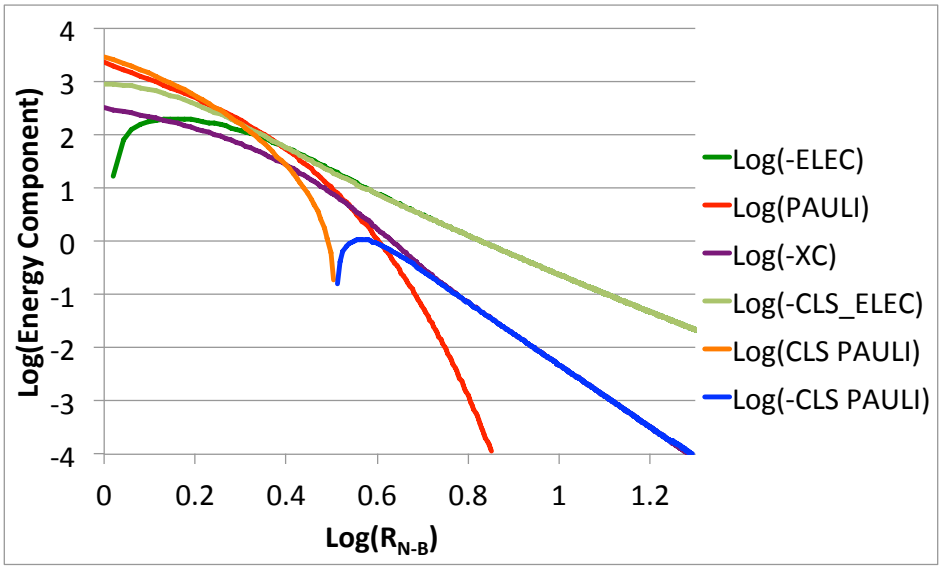

(b) Plot of log(±TERM) vs. log($R_{N\text{-}B}$) for terms summing to the frozen energy as computed by the newly introduced and classical approaches. Linear relationships in this plot indicate a polynomial decay of the given interaction with distance.

Figure 5.3: Plots for the assessment of rate of decay of EDA terms computed with ωB97X-V/aug-cc-pVQZ for the rigid dissociation along the N-B coordinate of the ammonia borane complex relative to the C_{3v} ωB97X-V/aug-cc-pVQZ optimized geometry (equilibrium $R_{N\text{-}B}$ = 1.65Å). Terms that are not uniformly signed throughout the coordinate are split into attractive(-) and repulsive(+) portions.

more favorable electrostatic interaction energy as computed by the new scheme around the equilibrium separation. The decrease in the difference between the two electrostatic energies for very compressed geometries can be seen as the negation of this effect by the generally increased shielding of nuclei in the new scheme relative to the classical approach. Due to the minimal distortion of the density in the supersystem relative to the isolated subsystems, the differences in the new and classical Pauli repulsion terms are likewise not appreciable with approximately half of the difference in the short range and the entire difference in the long range explained by the presence of exchange-correlation contributions in the latter.

From Figure 5.6 one can identify the characteristic decay behavior of each of the terms in the new and classical frozen energy decomposition schemes. Both the new and classical electrostatic terms approximately display the expected $R_{\text{O-Na}}^{-2}$ decay of a permanent monopole dipole interaction as demonstrated by the linear relationship in Figure 5.6b. From Figure 5.6a we see that the new Pauli repulsion term looks to decay roughly exponentially until the corresponding energy values themselves become quite small while the classical Pauli term looks exponential only very briefly before becoming attractive and describing the new exchange-correlation component in the long range. The exchange-correlation term transitions from roughly exponential decay in the short range to the expected approximate $R_{\text{O-Na}}^{-6}$ polynomial decay in the long range due to the ability of the ωB97X-V exchange-correlation functional to describe dispersion interactions. For comparison, we include the Hartree-Fock results for this system in the SI. Because of the lack of dynamic correlation in this case case, the classical Pauli repulsion remains repulsive for all points with values of meaningful magnitude, and classical Pauli, new Pauli, and XC all decay approximately exponentially as is expected based on overlap and exact exchange distance dependence.

5.3.4 Water-Cl^-

We now investigate neutral water interacting with chloride. This anionic system contains a monomer with a considerably more diffuse density than those in the cationic system investigated above, and so we expect a larger deviation from the decomposition produced by the classical approach due to the greater inter-fragment occupied orbital overlap and thus the more considerable 3-space density distortion upon formation of the antisymmetric initial supersystem wavefunction. The overall energy decomposition of the total interaction energy of this system for dissociation along the H-Cl coordinate is shown in Figure 5.7a. The relative importance of both polarization and charge transfer is greatly increased in this anionic system relative to the cationic system investigated above; however, the frozen interaction is still the most favorable at equilibrium and beyond. The decomposition of the frozen orbital energy by the new and classical schemes appears in Figure 5.7b. We see that indeed the electrostatic terms are further differentiated in this more diffuse system especially when one considers also the diminished scale of the total interaction energy. The electrostatic terms differ by 40.21 kJ/mol at 2.15Å, approximately the equilibrium separation, and by a maximum of 66.40 kJ/mol at 1.65Å. The fact that the new electrostatic term is more attractive

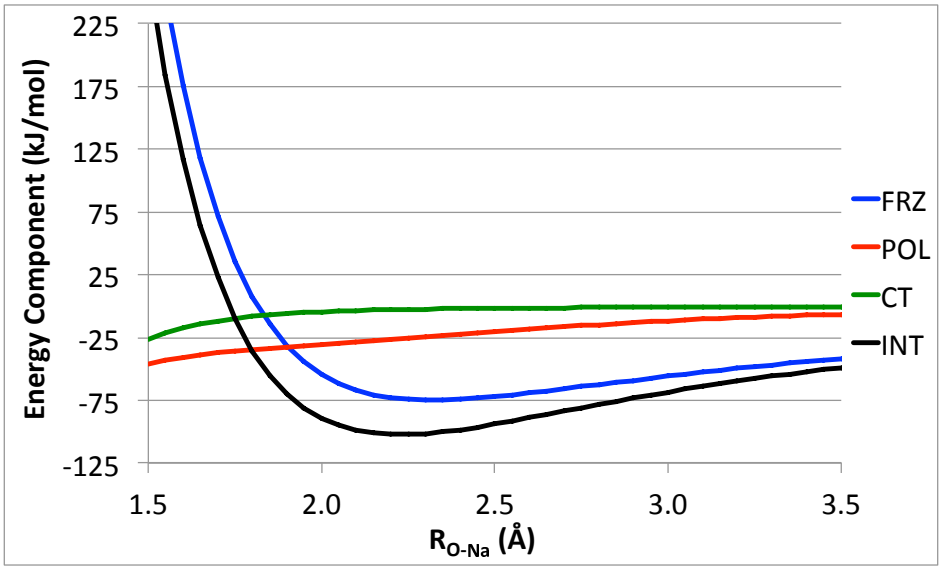

(a) Basic energy decomposition terms (FRZ, POL, CT) as well as the total interaction energy (INT) along the coordinate.

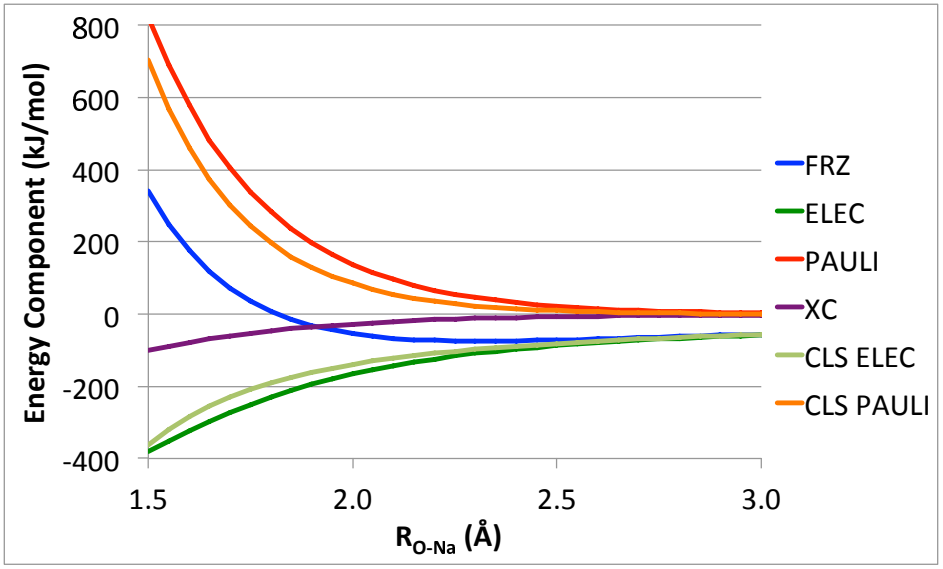

(b) Further decomposition of the frozen energy (FRZ) based on the new scheme presented in this work (ELEC, PAULI, XC) and based on the classical approach (CLS ELEC, CLS Pauli).

Figure 5.4: Energy terms computed with ωB97X-V/aug-cc-pVQZ for the rigid dissociation along the O-Na coordinate of water interacting with a sodium cation relative to the C_{2v} ωB97X-V/aug-cc-pVQZ optimized geometry (equilibrium $R_{O\text{-}Na} = 2.23$Å).

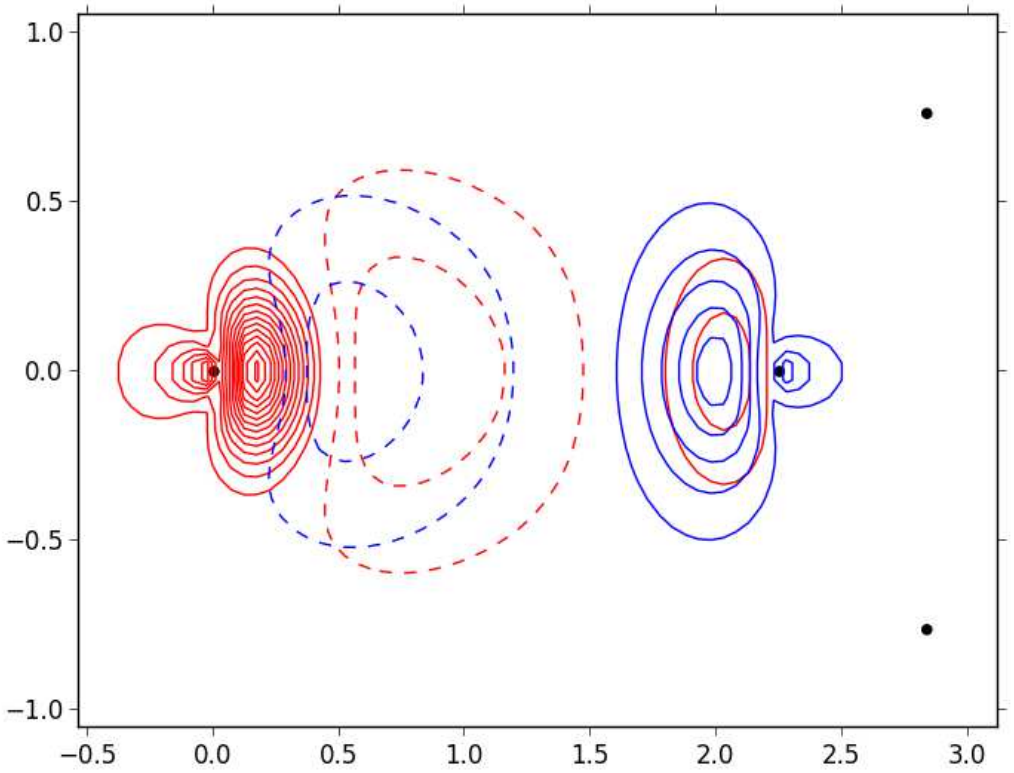

Figure 5.5: Contour plot of the change in density for Na^+ (red) and H_2O (blue) in the ωB97X-V/aug-cc-pVQZ optimized water sodium cation complex rigidly translated to $R_{O\text{-}Na}$ = 2.25Å. Contours are evenly spaced at 0.05 $e^-/Å^3$, and other details are as in Figure 5.2.

near equilibrium separations can be explained by the fragment density changes occurring on formation of the initial supersystem wavefunction as illustrated in Figure 5.8. The usual density depletion in the inter-fragment region occurs; however, the water density (blue) primarily increases between the hydrogen and oxygen atoms, leaving the proton generally less shielded from the anion. Again, the difference between the terms decreases at very compressed geometries where the new electrostatic term becomes less attractive faster due to the different treatment of the interpenetration of charge in the two methods. Again, approximately half of the difference in Pauli repulsion terms at short and mid range and the entire difference in the long range can be can be explained by the newly separated exchange-correlation term.

For water interacting with the chloride anion, the plots (Figure 5.9) for determination of the distance dependence of terms from the new and classical decompositions of the frozen orbital interaction are unsurprising. Figure 5.9b reveals approximate $R_{H\text{-}Cl}^{-2}$ decay for both

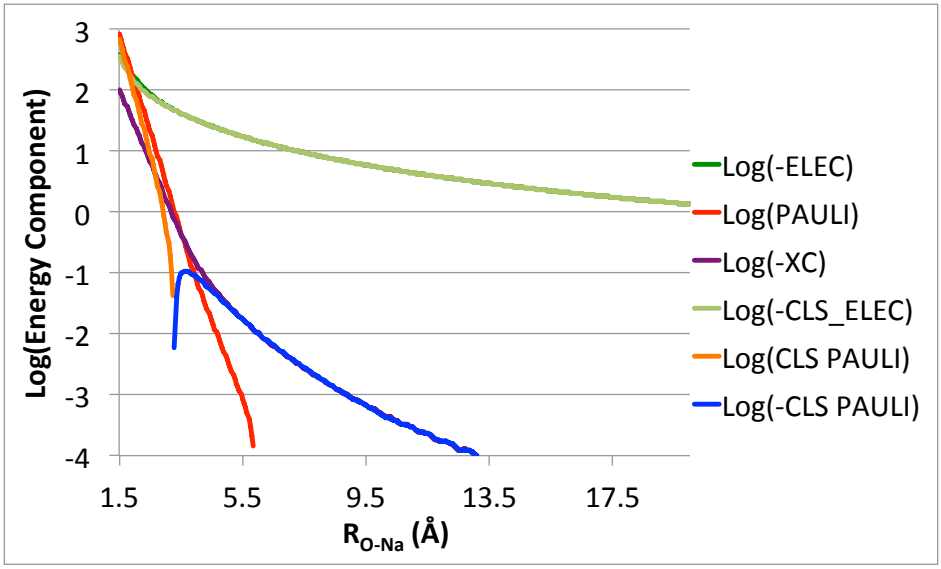

(a) Plot of log(±TERM) vs. $R_{O\text{-}Na}$ for terms summing to the frozen energy as computed by the newly introduced and classical approaches. Linear relationships in this plot indicate an exponential decay of the given interaction with distance.

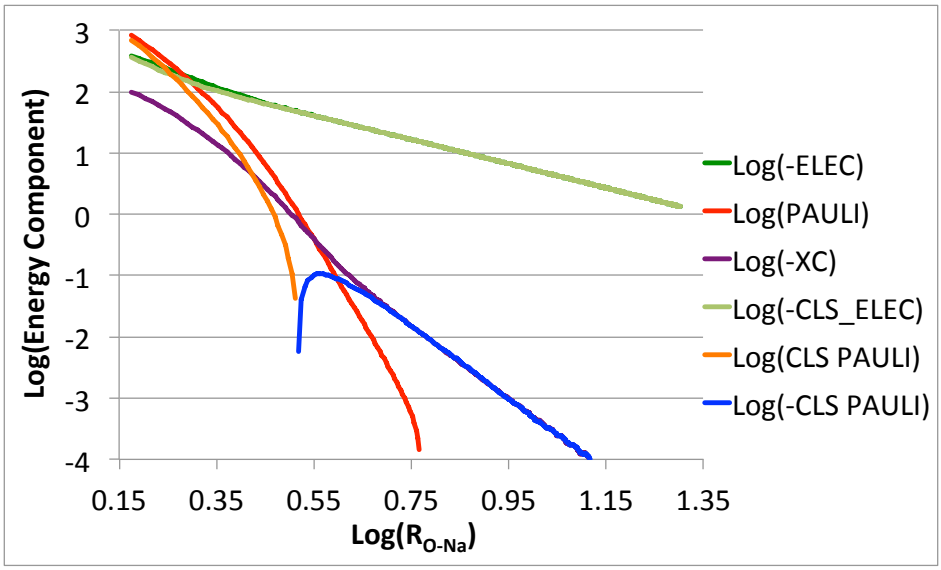

(b) Plot of log(±TERM) vs. log($R_{O\text{-}Na}$) for terms summing to the frozen energy as computed by the newly introduced and classical approaches. Linear relationships in this plot indicate a polynomial decay of the given interaction with distance.

Figure 5.6: Plots for the assessment of rate of decay of EDA terms computed with ωB97X-V/aug-cc-pVQZ for the rigid dissociation along the O-Na coordinate of water interacting with a sodium cation relative to the C_{2v} ωB97X-V/aug-cc-pVQZ optimized geometry (equilibrium $R_{O\text{-}Na}$ = 2.23Å). Terms that are not uniformly signed throughout the coordinate are split into attractive(-) and repulsive(+) portions.

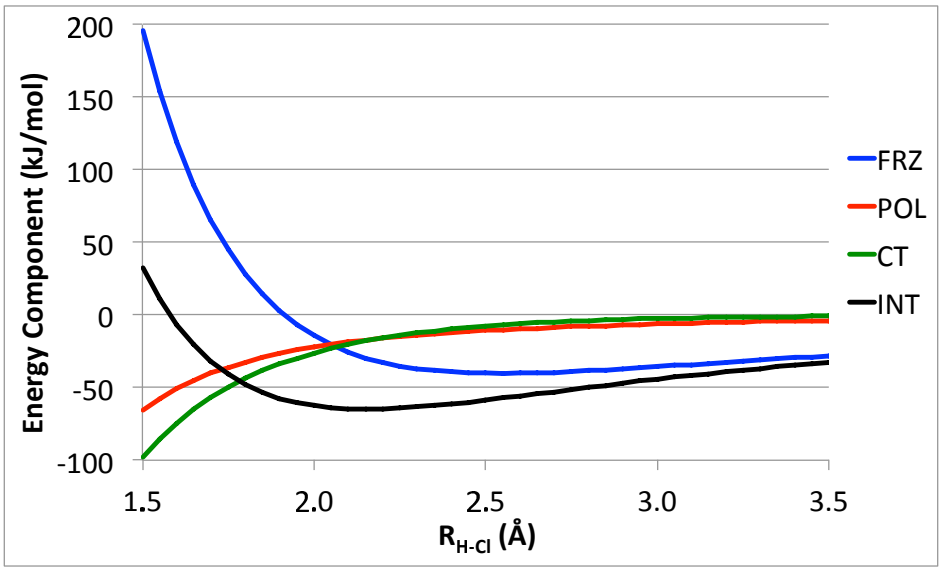

(a) Basic energy decomposition terms (FRZ, POL, CT) as well as the total interaction energy (INT) along the coordinate.

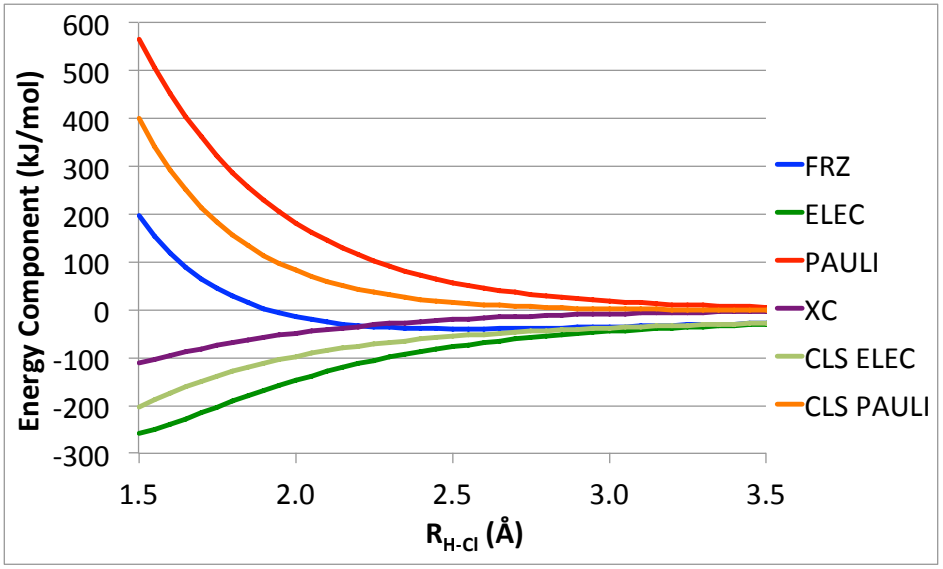

(b) Further decomposition of the frozen energy (FRZ) based on the new scheme presented in this work (ELEC, PAULI, XC) and based on the classical approach (CLS ELEC, CLS Pauli).

Figure 5.7: Energy terms computed with ωB97X-V/aug-cc-pVQZ for the rigid dissociation along the H-Cl coordinate of water interacting with a chlorine anion relative to the C_s ωB97X-V/aug-cc-pVQZ optimized geometry (equilibrium $R_{H\text{-}Cl} = 2.15$Å).

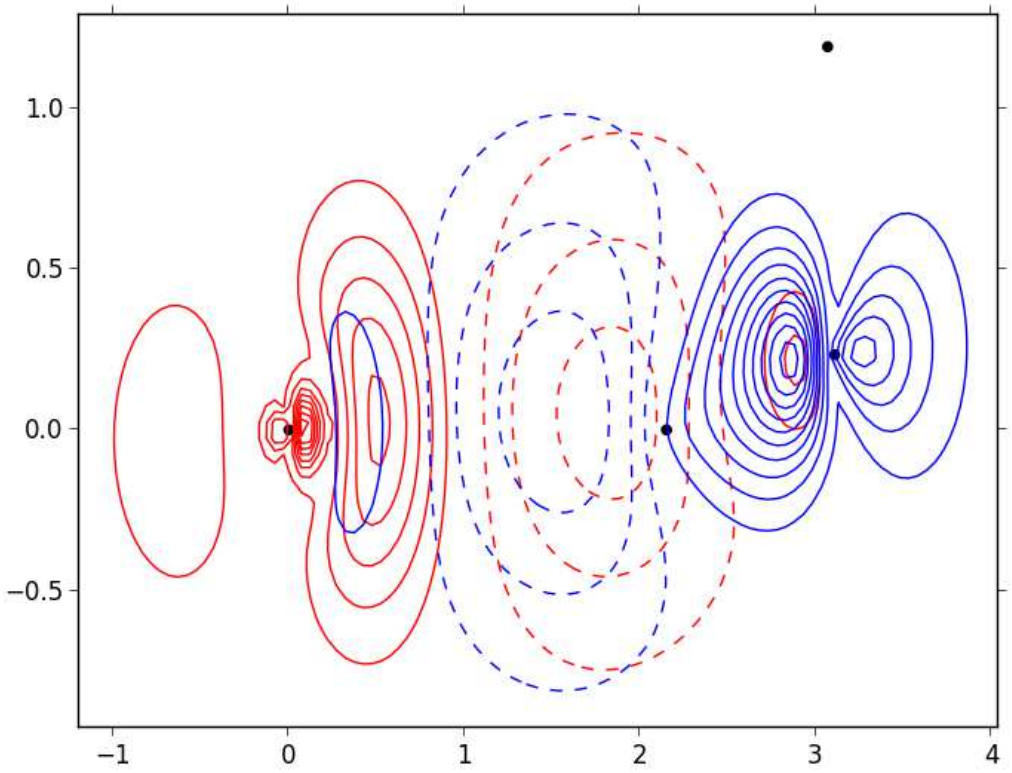

Figure 5.8: Contour plot of the change in density for Cl^- (red) and H_2O (blue) in the ωB97X-V/aug-cc-pVQZ optimized water chloride complex rigidly translated to the essentially equilibrium $R_{H\text{-}Cl} = 2.15$Å. Contours are evenly spaced at 0.1 $e^-/Å^3$, and other details are as in Figure 5.2.

electrostatic terms as expected for a permanent monopole dipole interaction, and the XC term in the long range decays approximately as $R_{H\text{-}Cl}^{-6}$, corresponding to dispersion. The classical Pauli term likewise describes this dispersion interaction in the long range. From Figure 5.9a we see that the new Pauli repulsion term exhibits essentially exponential decay throughout the coordinate while the classical Pauli term decays exponentially only briefly before ultimately becoming attractive due to the inclusion of exchange-correlation contributions to binding. The short range behavior of the XC term is likewise approximately exponential decay with distance though it is by contrast uniformly attractive. With the Hartree-Fock functional (See SI), both Pauli terms are consistently repulsive and like the corresponding XC term display roughly exponential decay along the coordinate.

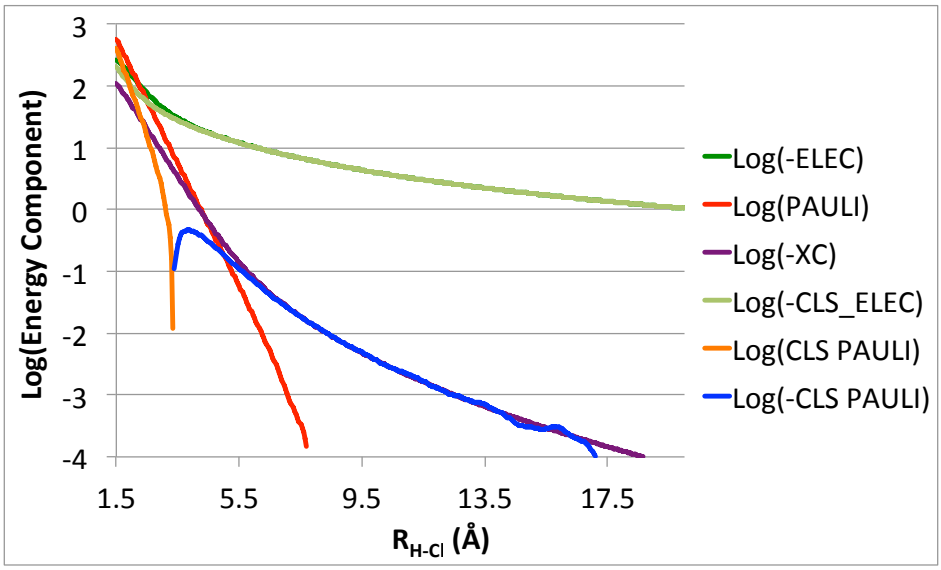

(a) Plot of log(±TERM) vs. $R_{H\text{-}Cl}$ for terms summing to the frozen energy as computed by the newly introduced and classical approaches. Linear relationships in this plot indicate an exponential decay of the given interaction with distance.

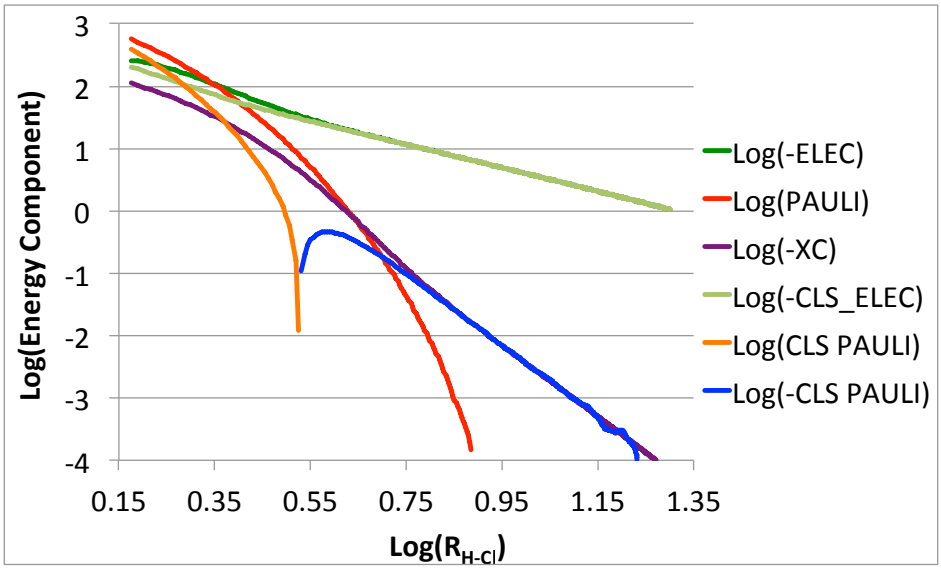

(b) Plot of log(±TERM) vs. log($R_{H\text{-}Cl}$) for terms summing to the frozen energy as computed by the newly introduced and classical approaches. Linear relationships in this plot indicate a polynomial decay of the given interaction with distance.

Figure 5.9: Plots for the assessment of rate of decay of EDA terms computed with ωB97X-V/aug-cc-pVQZ for the rigid dissociation along the H-Cl coordinate of water interacting with a chlorine anion relative to the C_s ωB97X-V/aug-cc-pVQZ optimized geometry (equilibrium $R_{H\text{-}Cl}$ = 2.15Å). Terms that are not uniformly signed throughout the coordinate are split into attractive(-) and repulsive(+) portions.

5.3.5 Ethane Dissociation

The next system that we investigate is the interaction of two methyl fragments of opposite net spin to form the ethane molecule in the staggered conformation. Corresponding to the formation of a covalent bond, this is a very strong interaction with close fragment contacts (-489.71kJ/mol at $R_{C\text{-}C}$=1.55Å), and thus we expect large differences in the decomposition of the frozen orbital energy as compute by the new and classical schemes. The primary terms from the energy decomposition for the interaction appear in Figure 5.10a. As expected for a covalent bond, charge transfer makes the dominant favorable contribution to the interaction energy. Polarization becomes more important at very compressed distances where it serves to relax some of the very repulsive frozen orbital interaction. As was the case for the strongly interacting ammonia borane complex investigated above, the decomposition of the frozen orbital energy for the dissociation of the ethane molecule is qualitatively different in the new and classical schemes (Figure 5.10b). The most striking difference is in the behavior of the electrostatic term, which reaches a minimum at only slightly less than equilibrium separation in the new scheme and is even repulsive by $R_{C\text{-}C}$=1.00Å while the classical electrostatic term has yet to reach its minimum at that compression. The less attractive electrostatic interaction in the new scheme can be understood in terms of the density distortions upon formation of the initial supersystem wavefunction, which are shown for the alpha spin density in Figure 5.11. The plot is quite similar to that for the change in total spinless density for the closed shell ammonia borane complex (Figure 5.2), which likewise showed a depletion of charge in the bonding region and a marked increase in charge near the more electron rich species. The methyl fragment with more alpha electrons necessarily has the less strongly bound alpha electrons, and thus energetic optimality determines that this fragment should be the one most distorted. The difference in the Pauli repulsion terms is largely a consequence of these different electrostatic terms in the short range as the exchange-correlation term has an uninteresting distance dependence here.

More insight into the distance dependence of terms can be gained from Figure 5.12. From Figure 5.12b we see that both electrostatic terms transition from attractive around equilibrium to repulsive decaying asymptotically approximately as $R_{C\text{-}C}^{-3}$ corresponding to unfavorably aligned permanent dipoles. As was the case for the other systems investigated, the new Pauli term decays approximately exponentially throughout the coordinate (Figure 5.12a) while both the new exchange-correlation term and the classical Pauli term are both attractive decaying as approximately $R_{C\text{-}C}^{-6}$ in the long range corresponding to the dispersion interaction between the two methyl fragments. Prior to this transition to polynomial dependence in the long range, the new XC term is shown to decay approximately exponentially in the short range. Hartree-Fock results for this system are also provided in the SI and offer no surprises.

In the context of the ethane dissociation problem, we also consider a different initial supersystem wavefunction in which not only geometric optimality but also energetic optimality (Chapter 4) is included. This wavefunction is constrained to have the same 3-space

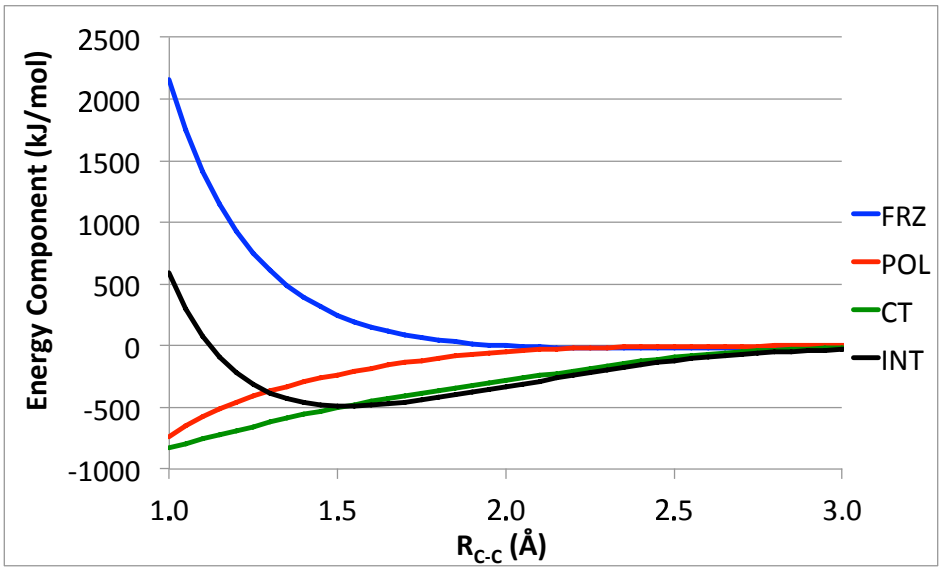

(a) Basic energy decomposition terms (FRZ, POL, CT) as well as the total interaction energy (INT) along the coordinate.

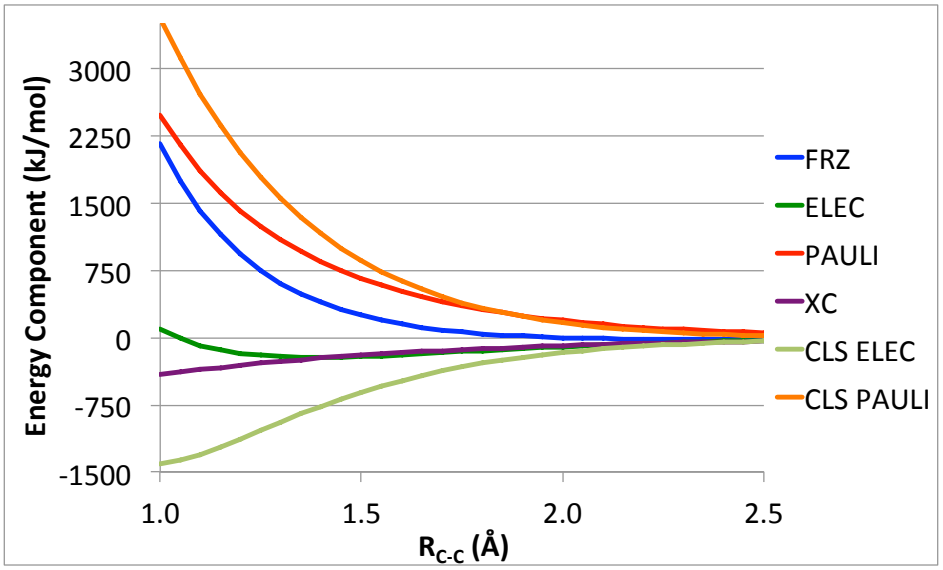

(b) Further decomposition of the frozen energy (FRZ) based on the new scheme presented in this work (ELEC, PAULI, XC) and based on the classical approach (CLS ELEC, CLS Pauli).

Figure 5.10: Energy terms computed with ωB97X-V/aug-cc-pVQZ for the rigid dissociation along the C-C coordinate of ethane relative to the D_{3d} (staggered) ωB97X-V/aug-cc-pVQZ optimized geometry (equilibrium $R_{C\text{-}C} = 1.53$Å) to form two methyl radicals of opposite net spin.

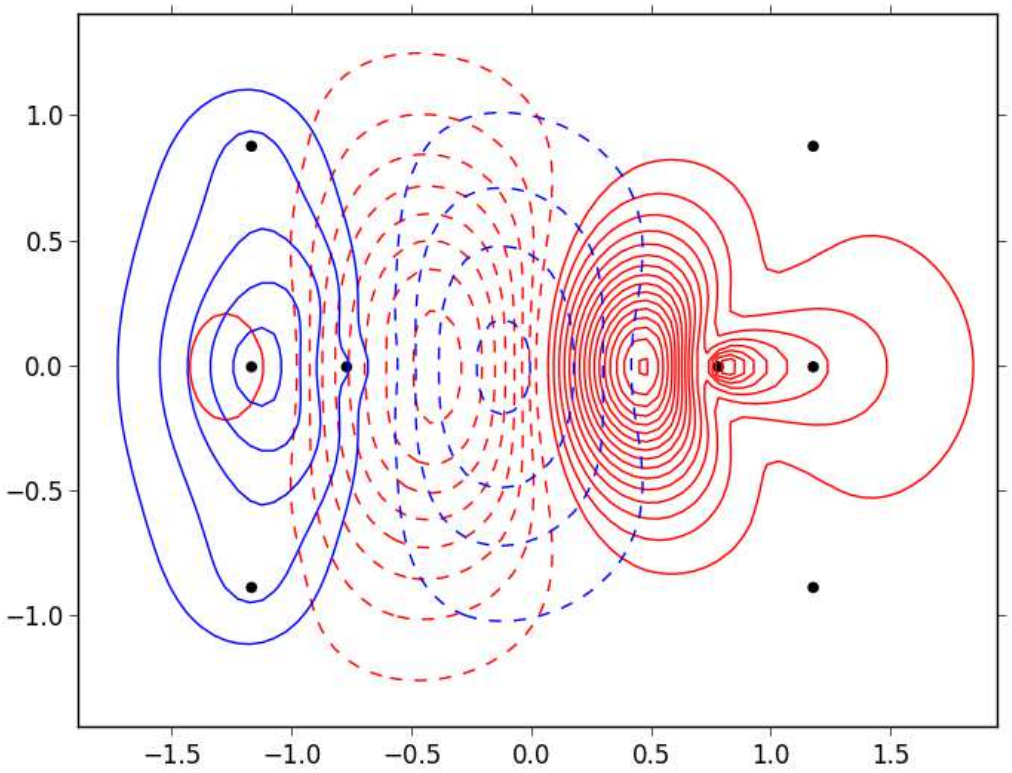

Figure 5.11: Contour plot of the change in alpha density for two methyl fragments in the ωB97X-V/aug-cc-pVQZ optimized staggered ethane rigidly translated to $R_{C\text{-}C}$ = 1.55Å. Contours are evenly spaced at 0.2 $e^-/Å^3$, and other details are as in Figure 5.2.

density as the geometrically optimal antisymmetric product of monomer wavefunctions, but intra-fragment relaxations of the supersystem density matrix are allowed to occur so as to remove what would otherwise be constant 3-space density polarization, correcting for energetic deficiencies in the initial supersystem wavefunction. The removal of constant density polarization, which one might expect to be generally small due to its seemingly paradoxical name, is only relevant to interpretation in the case of strongly interacting complexes such as the bond breaking in ethane as analyzed in a previous work (Chapter 4) with a different model chemistry, and we use the same $\lambda = 2000$ Lagrange multiplier here. The major effect of this relaxation is to reduce the kinetic energy of the electrons in the initial supersystem wavefunction though legitimate changes in the exchange-correlation energy can occur if the exchange-correlation functional itself has more than 3-space density dependence. Because of its connection with the kinetic energy, we expect the energy difference between the two

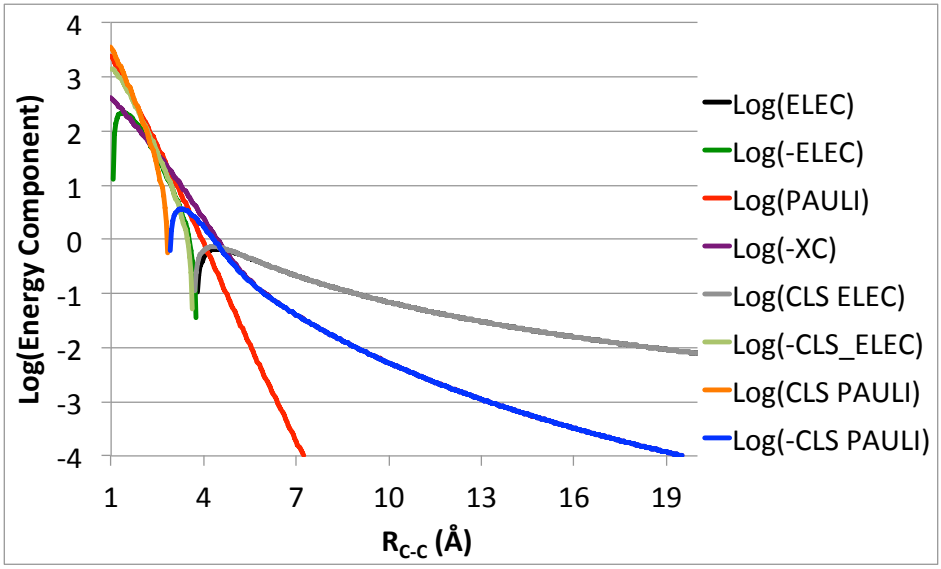

(a) Plot of log(±TERM) vs. $R_{C\text{-}C}$ for terms summing to the frozen energy as computed by the newly introduced and classical approaches. Linear relationships in this plot indicate an exponential decay of the given interaction with distance.

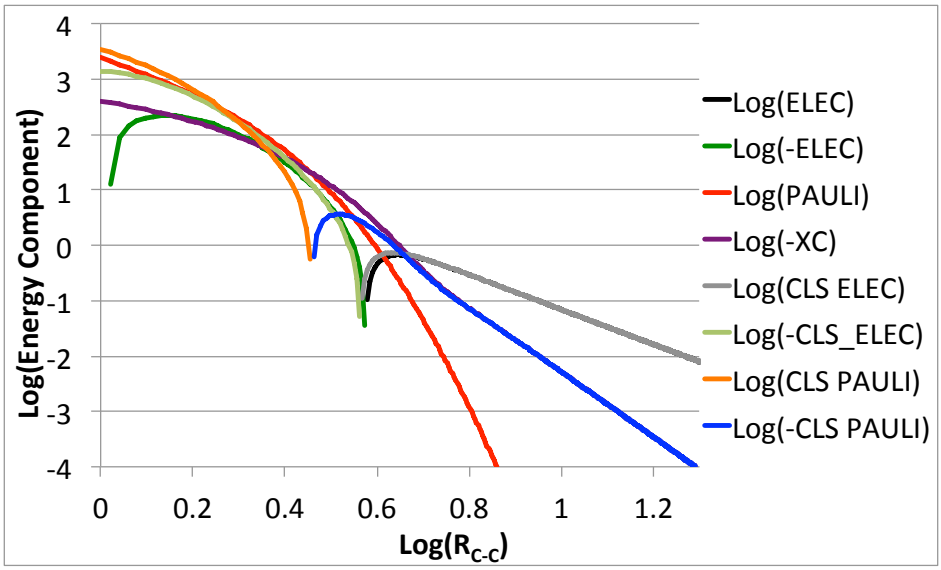

(b) Plot of log(±TERM) vs. log($R_{C\text{-}C}$) for terms summing to the frozen energy as computed by the newly introduced and classical approaches. Linear relationships in this plot indicate a polynomial decay of the given interaction with distance.

Figure 5.12: Plots for the assessment of rate of decay of EDA terms computed with ωB97X-V/aug-cc-pVQZ for the rigid dissociation along the C-C coordinate of ethane relative to the D_{3d} (staggered) ωB97X-V/aug-cc-pVQZ optimized geometry (equilibrium $R_{C\text{-}C}$ = 1.53Å) to form two methyl radicals of opposite net spin. Terms that are not uniformly signed throughout the coordinate are split into attractive(-) and repulsive(+) portions.

wavefunctions to be described largely by a change in the Pauli repulsion energy though this is not variationally guaranteed as the Pauli repulsion is not simply the kinetic energy contribution to binding though it does contain it.

Figure 5.13a shows the basic energy decomposition with (solid) and without (dashed) removal of constant density polarization from the antisymmetric product of monomer wavefunctions. Only the FRZ and POL terms are affected with the former lowered as much as the later is raised because only the energies of these terms are defined with respect to the initial supersystem wavefunction. While changes in the larger-in-magnitude frozen energy are not particularly dramatic, the change in the polarization term is substantial, altering the qualitative behavior of this term at compressed distances and thus its importance relative to the charge transfer contribution.

Because the constant density constrained optimization in principle (exact enforcement of constraints) only adjusts the particular details of the collective orbital shape distortions that energy-blind antisymmetrization brought about, we still see it as a valid initial supersystem wavefunction in which fragments have not been able to truly respond to the presence of others. We thus feel justified in the application of the new decomposition of this modified frozen energy, and the results appear in Figure 5.13b with the explicit changes in the terms computed using the two different wavefunctions illustrated in Figure 5.14. Figure 5.14 also shows changes in energy contributions derived from terms in the electronic Hamiltonian as a means of assessing the energetic consequences of the inexact enforcement of the constant 3-space density constraint. The energy lowering from electron-nuclear attraction and electron-electron Coulomb repulsion is clearly illegitimate as these quantities are functions of the 3-space density alone. The kinetic energy of the system can change during optimization due to its dependence on the details of the density matrix; however, when such relaxation is clearly accompanied by 3-space density changes, it cannot be said to be entirely legitimate. With these caveats in mind, we see that the change in the frozen energy (Figure 5.14) is largely described by the change in the Pauli repulsion term beyond equilibrium as expected. However, this is not the case at more compressed distances where changes in the electrostatic term become appreciably more important though with accompanying changes in the 3-space density as demonstrated by the increasingly large change in the electron-nuclear attraction. The primary change of note between the decompositions computed with the two wavefunctions is that in the case of the initial wavefunction with constant density polarization removed, the point at which the electrostatic term becomes repulsive is pushed back (Figure 5.13b), although this is also the region where the constraint is least well enforced. These details will need to be further examined when and if optimizations with accurately enforced constant 3-space density constraints become feasible.

5.3.6 Naphthalene Dimer

The systems examined to this point have been either charged with large permanent and induced electrostatic interactions or strongly bound with considerable charge transfer compo-

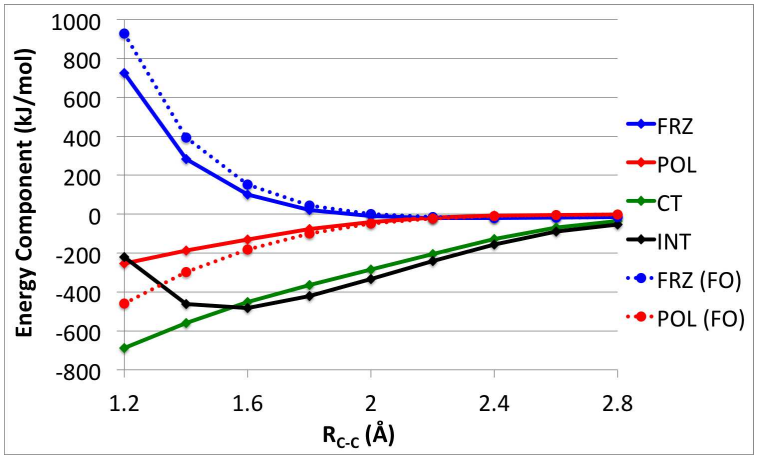

(a) Basic energy decomposition terms (FRZ, POL, CT) as well as the total interaction energy (INT) along the coordinate. The charge transfer and total interaction energies are unchanged by the removal of constant density polarization from the initial supersystem wavefunction.

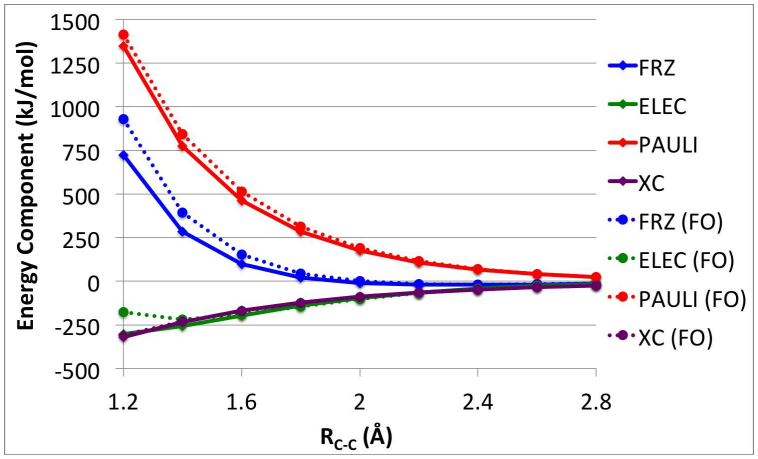

(b) Further decomposition of the frozen energy (FRZ) based on the new scheme presented in this work (ELEC, PAULI, XC).

Figure 5.13: Energy terms computed with ωB97X-V/aug-cc-pVQZ for the rigid dissociation along the C-C coordinate of ethane relative to the D_{3d} (staggered) ωB97X-V/aug-cc-pVQZ optimized geometry (equilibrium $R_{C\text{-}C} = 1.53$Å) to form two methyl radicals of opposite net spin. Values computed with the initial supersystem wavefunction where constant density polarization has been removed appear with solid lines. Values obtained with the antisymmetric product of monomer wavefunctions, the frozen orbital (FO) wavefunction, are the same as those presented above and are shown with dashed lines for comparison.

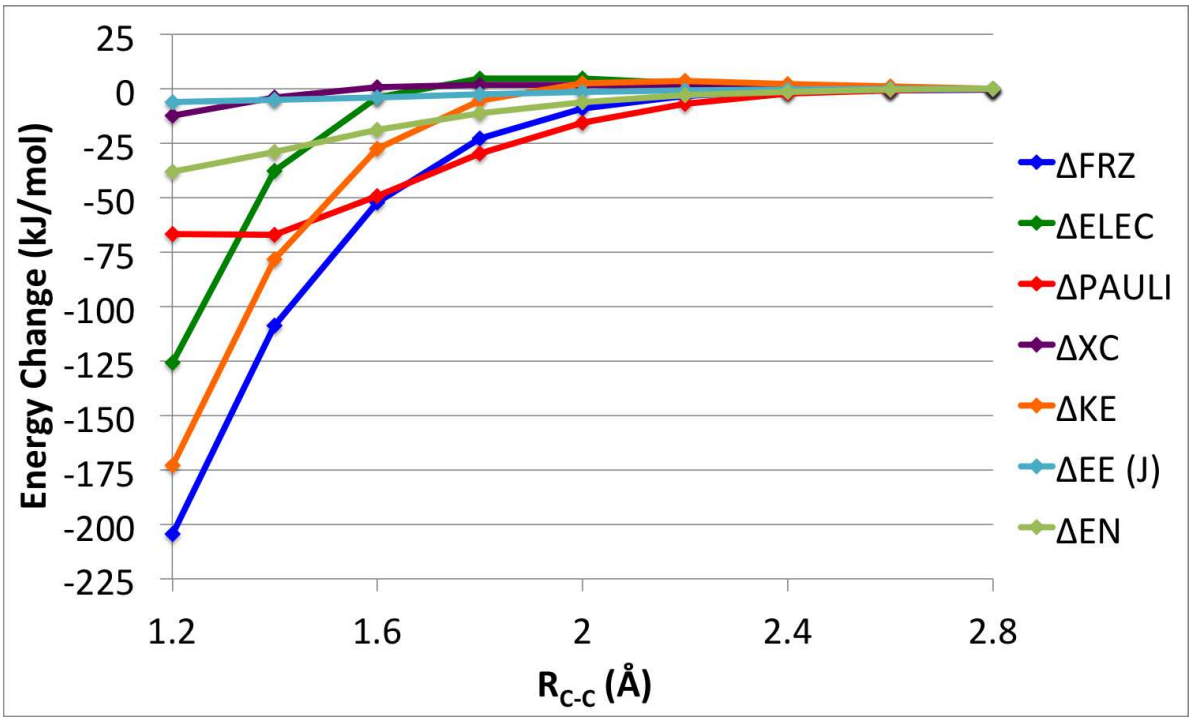

Figure 5.14: Changes in the frozen energy (FRZ) and its components (ELEC, PAULI, XC) upon going from the frozen orbital wavefunction to an initial wavefunction from which constant density polarization has been removed within a tolerance for constant 3-space density constraint violation. The changes in electronic hamiltonian energy contributions are also shown as a means of assessing the energetic consequences of constraint violation. The kinetic energy (KE) of the system is expected to change as it depends on the density matrix while the electron-nuclear attraction (EN) and electron-electron (EE) Coulomb (J) repulsion depend on the 3-space density alone and should not change during initial wavefunction optimization.

nents among others. In each, the attractive dispersion contribution to binding was identified by the characteristic R^{-6} decay in the long range within the new exchange-correlation term and the classical Pauli repulsion term. While present in the short range and necessary for the accurate calculation of interaction energies, the dispersion interaction was not essential to qualitatively describe these interactions near equilibrium. In contrast, the graphite-like, parallel displaced naphthalene dimer is bound almost entirely due to dispersion. The overall energy decomposition for the naphthalene dimer using a structure from another work[134] at the equilibrium interplanar separation (R = 3.511Å) as well as at compressed and extended separations appears in Table 5.1. Polarization and charge transfer contributions are minor at equilibrium and beyond with somewhat increased importance at compressed interplanar distances. The main contribution to binding is contained within the frozen orbital energy, and

R (Å)	3.250	3.511	3.750
ELEC	-70.05	-36.47	-18.97
PAULI	156.72	81.99	44.74
XC	-99.06	-67.07	-46.97
CLS ELEC	-27.32	-10.19	-2.94
CLS PAULI	14.93	-11.35	-18.27
FRZ	-12.39	-21.55	-21.20
POL	-3.17	-1.91	-1.28
CT	-7.57	-3.57	-1.87
INT	-23.13	-27.02	-24.36

Table 5.1: Energy terms in kJ/mol computed with ωB97X-V/def2-QZVPPD for the parallel displaced naphthalene dimer rigidly translated along the inter-planar distance coordinate, R, relative to the equilibrium structure taken from another work[134] (equilibrium R = 3.51Å).

its further decomposition by the new and classical schemes also appears in Table 5.1. We see that the new exchange-correlation term is the most important stabilizing interaction at all three separations as we might expect because it subsumes the dispersion interaction. With so many atoms in close contact in this parallel configuration, the new Pauli repulsion is also quite large though appropriately repulsive at all separations. The classical Pauli term on the other hand is unsurprisingly attractive at equilibrium due to its inclusion of the correlation effects that are the primary source of binding in this system. The two electrostatic terms are both attractive at all separations and have the same trend of increasing magnitude with decreasing distance though the differences between the two terms are most exaggerated also at compressed distances where density deformations upon initial supersystem wavefunction formation are also largest.

5.4 Conclusions

We have presented a new scheme for the identification of permanent electrostatic, Pauli repulsion, and exchange-correlation contributions to binding and have compared results for this new approach to what we have termed the classical approach that is employed with or without nuanced variations in several energy decomposition methods. A notable difference between this scheme and the classical approach is that antisymmetric electronic wavefunctions are used for the evaluation of all terms. This is accomplished by identifying fragment contributions to the initial supersystem wavefunction based on a constrained sum-of-fragments energetic optimality criterion.

The new electrostatic term properly matches the classical electrostatic term in the non-overlapping regime, and this is variationally guaranteed by the approach provided basis set superposition error is absent. The energetic ordering of the two is not guaranteed in the

overlapping regime though we have shown that the trend is for the new electrostatic term to be more repulsive at short inter-fragment separations due to decreased charge penetration and thus increased shielding of nuclei compared to the classical scheme.

We have shown that the new Pauli repulsion term is indeed repulsive when basis set superposition error is minimized with the use of an appropriate basis for monomers and also that it decays roughly exponentially as expected. A major difference between the new and classical Pauli terms is that the former includes contributions from what we have separated out as the exchange-correlation term, which notably caused the classical Pauli term to become attractive and describe dispersive interaction in the long range. The new exchange correlation term is attractive, decaying close to exponentially in the short range and transitioning to polynomial R^{-6} decay characteristic of dispersion in the long range when functionals that can describe these interactions such as ωB97X-V are employed.

The obvious errors of the classical approach that we mention are not apparent when using Hartree-Fock though a repulsive classical Pauli term is not guaranteed in this case either; however, is is clear that the classical approach is not appropriate when performing accurate calculations of intermolecular interactions with modern density functionals. The decision against separating dispersion contributions from other dynamic correlation and exchange effects was made because we see no satisfying solution to this problem though it may be an interesting topic for future work.

Chapter 6

A New EDA Applied to Chemical Interactions

6.1 Introduction

Energy decomposition methods are tools for the analysis of often nuanced intermolecular interactions and can reveal chemically useful information that can guide future investigations or shed light on a surprising result. The terms in these methods correspond to useful chemical concepts that unfortunately do not have unique definitions in the chemically interesting overlapping regime. Due to this non-uniqueness, many methods have been developed[74] to perform such decompositions, which vary both in their level of description of the interactions and in their formal properties.

KM-EDA[38, 86, 87] is one of the oldest such methods and divides the interaction energy of a cluster of monomers into electrostatic, exchange repulsion, polarization, charge transfer, and unascribable mixed interaction components. The electrostatic and polarization terms are both defined using electronic wavefunctions that are not properly antisymmetric, leading to potentially unphysical terms. This method also depends on a basis partitioning to separate polarization and charge transfer.

Bickelhaupt-Baerends EDA[44, 76, 77] (BB-EDA) divides the interaction energy into electrostatic, Pauli, and orbital contributions. Contained unseparated within the orbital term are all contributions from wavefunction relaxation, which other schemes associate with charge transfer and polarization. As in KM-EDA, the electrostatic interaction is evaluated as the classical Coulomb interaction between monomer charge distributions computed in isolation and translated to the monomer positions in the cluster geometry. The Pauli repulsion term in this method furthermore does not have a definite sign, leading to an attractive Pauli repulsion interaction for some model chemistries.

The ALMO-EDA[15–18] and BLW-EDA[46–49] methods are SCFMI-based[64, 65] EDA methods that decompose the interaction energy into frozen orbital, polarization, and charge

transfer contributions. The delineation between inter-fragment charge transfer and intra-fragment polarization, which together sum to the orbital term in BB-EDA, depends on the assignment of a portion of the single-particle space to each monomer. Traditionally these are taken as the spans of the Gaussian AO basis functions centered at the nuclei of each monomer, a partitioning that is basis type specific and lacks a meaningful basis set limit. A separation of the frozen orbital interaction into classical electrostatic and Pauli repulsion contributions (as well as a dispersion contribution if the form of the exchange-correlation functional permits it)[49] is sometimes performed in BLW EDA just as it is performed in BB-EDA. This separation is explicitly avoided in the ALMO EDA due to the improper treatment of electron antisymmetry in such decompositions.

DEDA[51, 75] similarly decomposes an interaction energy into frozen, polarization, and charge transfer contributions; however, unlike in the SCFMI-based schemes, a portion of real space instead of the single-particle space is ascribed to each monomer to define the separation of charge transfer wavefunction relaxations from those due to polarization. This choice makes the troublesome partitioning of the single-particle space needed in SCFMI-based EDA schemes unnecessary but also changes the physical content of the polarization and charge transfer terms. In DEDA, wavefunction relaxations that delocalize electrons over multiple monomers are considered to be polarization in character provided that these delocalizations do not cause a net flow of charge between the monomers; however, these delocalizations are strictly charge transfer in character in SCFMI-based schemes[**POL**]. The frozen term in DEDA is also unique because it employs an initial supersystem wavefunction that is not simply the antisymmetric product of monomer wavefunctions used by most other schemes but rather the lowest energy wavefunction that does not change the 3-space density from the simple sum of monomer densities. The separation of this frozen energy into electrostatic and Pauli repulsion terms is also possible, and, due to the way in which the initial wavefunction is constructed, the electrostatic contribution is computed with valid antisymmetric electronic wavefunctions. However, We have shown[**FRZ**] that much of the energy lowering in this initial wavefunction optimization is associated with the delocalization of electrons across monomers. Such a treatment may be beneficial in the construction of force fields, but its utility for the identification of physical contributions to quantum-mechanical interaction energies is questionable.

NEDA[34–36] decomposes an interaction energy into contributions from electrostatics, polarization, charge transfer, a self-energy term, and a core term describing Pauli repulsion and exchange-correlation effects. Separation of permanent electrostatics from polarization depends on the same calculation of classical electrostatic interactions between monomer charge distributions described above. Unlike the above methods that separate a charge transfer component, NEDA is not variational due to its dependence on the NBO[37, 85] procedure to identify polarized monomer lewis-like determinants in the supersystem wavefunction. The charge transfer contribution is then identified as all energy lowering from non-lewis wavefunction components, and it is often computed to be several times larger than the interaction energy itself.

SAPT[19, 20, 22–25, 83, 84] does not decompose the interaction energy of a Kohn-Sham model chemistry but rather computes its own perturbative expansion of the interaction energy, which includes terms describing electrostatics, exchange, induction, dispersion, and various exchange, induction, and dispersion cross terms. The electrostatic contribution is equivalent to the classical electrostatic interaction of monomers discussed above. The exchange terms enter in at all orders of the expansion as corrections to enforce proper antisymmetry of the SAPT wavefunction. Induction, like the orbital term of BB-EDA, contains both polarization and charge transfer contributions to wavefunction relaxation. Some variants of SAPT separate the induction energy into polarization and charge transfer contributions either using a partitioning of the one-particle space[25], a scheme which suffers from the same weaknesses as ALMO-EDA and BLW-EDA, or by adding additional potentials to discourage charge transfer[84].

6.2 Theory

Our new scheme (Chapters 2-5) is an enhancement of the SCFMI-based ALMO-EDA discussed above and decomposes interaction energies from Kohn-Sham density functional theory and Hartree-Fock calculations into five contributions: permanent electrostatics (ELEC), Pauli repulsion (PAULI), exchange-correlation (XC), polarization (POL), and charge transfer (CT).

$$E_{INT} = E_{ELEC} + E_{PAULI} + E_{XC} + E_{POL} + E_{CT}$$

The physical content of each of the terms in our decomposition is as follows:

1. The permanent electrostatics (ELEC) term describes the contribution from the interaction of isolated monomer monopole, dipole, and higher moments to binding. This term reduces to the simple classical electrostatic interactions of monomer charge distributions at long range but at short range is modified to account for the electronic density deformation that accompany the construction of a properly antisymmetric electronic wavefunction for the complex.

2. The positive-semidefinite Pauli repulsion (PAULI) term accounts for volume exclusion effects, the dramatic increase in energy observed when two molecules are compressed. Electronic wavefunction antisymmetry requires that electrons of the same spin not occupy the same space, an expression of the Pauli principle, and the repulsive character of this term is due to the increase in kinetic energy associated with decreasing the volume available to each electron due to the presence of all others.

3. The negative semi-definite exchange-correlation (XC) term is included to isolate the contributions of the correlated motions of electrons that are not captured in the mean-field permanent electrostatics term but are essential to the accurate description of intermolecular interactions. Contained within this term is the well-known dispersion

interaction deriving from favorably aligned instantaneous multipole moments provided that the functional itself is capable of describing these non-local correlation effects.

4. The negative polarization (POL) term describes the induced electrostatic interactions resulting from the intra-fragment density relaxation of each monomer in response to all other perturbing monomers in the cluster. Polarization is a response not only to the electric fields produced but other fragments' electrons and nuclei but also, at short inter-fragment separations, to the kinetic energy pressure exerted by the electrons of other fragments due to electronic wavefunction antisymmetry.

5. The negative charge transfer (CT) term accounts for donor-acceptor inter-fragment orbital interactions that bring about energy lowering in the system not only by allowing for net charge flow between fragments but also by allowing electrons to delocalize across fragments. This term also includes the secondary intra-fragment relaxations that occur in response to the redistribution of charge brought about by these inter-fragment orbital interactions.

We now highlight some of the features of our approach and their consequences. This EDA delimits intra-fragment polarization-like relaxations from inter-fragment charge transfer relaxations by the construction of subspaces from fragment electric-field response functions (FERFs, Chapter 3), which allow a fragment to respond exactly to weak electric fields. These are reasonable spans for intra-fragment relaxation that can be constructed from a sufficiently complete basis of any type and have meaningful complete basis set limits. These subspaces are used in a variational calculation allowing only intra-fragment relaxation to determine the energetic contributions of polarization and, by difference, charge transfer. Our scheme also computes an energetically optimal orthogonal fragment decomposition of the wavefunction of the complex prior to any relaxation due to polarization or charge transfer, the initial supersystem wavefunction, and these fragment densities are used to compute contributions from permanent electrostatics, Pauli repulsion, and exchange-correlation (Chapter 5). The Pauli repulsion term is variationally guaranteed to be positive-semidefinite, and the exchange-correlation term does not depend on a specific form of exchange-correlation functional. All three terms are moreover computed using valid antisymmetric wavefunctions. The scheme can also optionally employ a variationally determined initial supersystem wavefunction that has the same 3-space density as the commonly used antisymmetric product of monomer wavefunctions but has been relaxed to remove what would otherwise be constant density polarization (Chapter 4). We do not perform any optimization of the initial supersystem wavefunction in this work as it is unnecessary for the fairly weak interactions that we will examine; however, this relaxation has been shown to be significant in the context of breaking covalent bonds.

Ultimately, decomposition schemes must be judged by their utility in elucidating chemical phenomena. To this end, we apply our new EDA scheme to the description of interactions

in several chemically interesting examples including one that has recently been quite controversial.

6.3 Results and Discussion

6.3.1 Computational Details

Calculations in this work were performed with a development version of QChem [70, 108]. The ωB97X-V[11] functional, which includes the VV10[5] non-local correlation functional for the description of dispersion, and the def2-QZVPPD[133] basis were used to compute all interaction energies and their decompositions in this work. Polarization subspaces are FERF nDQ (Chapter 3) unless otherwise stated. We also use the antisymmetric product of monomer wavefunctions as the initial supersystem wavefunction throughout this work. Structures come from other works and will be described in turn. Images of molecular structures were generated with the help of IQmol.

6.3.2 Anti-Electrostatic Hydrogen Bonding

The first system that we investigate is the p-biphthalate dimer, one of the several controversial[135–137] anti-electrostatic hydrogen bonding interactions. It is called as such because, in addition to the presence of the usual hydrogen bonding motif, both monomers are monoanionic, and the stationary points identified along the dissociation coordinate are higher in energy than the isolated monomers due to these net charges. This anti-electrostatic interaction is seen by Weinhold and Klein[135] (WK) as an indicator of the profound importance of quantum-mechanical orbital interactions in hydrogen bonding complexes. Such interactions are not accounted for in the most simplistic electrostatic models, which would suggest a purely repulsive interaction.

We take the two hydrogen-bonding minima (HB1 and HB2) and transition structures (TS1 and TS2) from WK, unmodified, for direct comparison (Figure 6.1). The binding energies (Figure 6.2a) are quite similar to those presented previously despite the change in model chemistry, and the relative energetics are well described by changes in the interaction energies alone, allowing us to largely neglect geometric distortions in this analysis.

Because our EDA scheme shares a common intermediate state, the initial supersystem wavefunction, with BB-EDA employed by Frenking and Caramori[136] (FC) to analyze another anti-electrostatic hydrogen bonding complex, we will discuss the results of this scheme as well as our own. BB-EDA includes three terms that sum to the interaction energy, E_{Coul}, E_{Pauli}, and E_{Orb} in FC, which we will refer to as CLS ELEC, CLS PAULI, and ORB respectively.

We first address the question of why there is a minimum at all. The interaction energy for TS1, the final barrier to dissociation, is described almost entirely by the electrostatic term

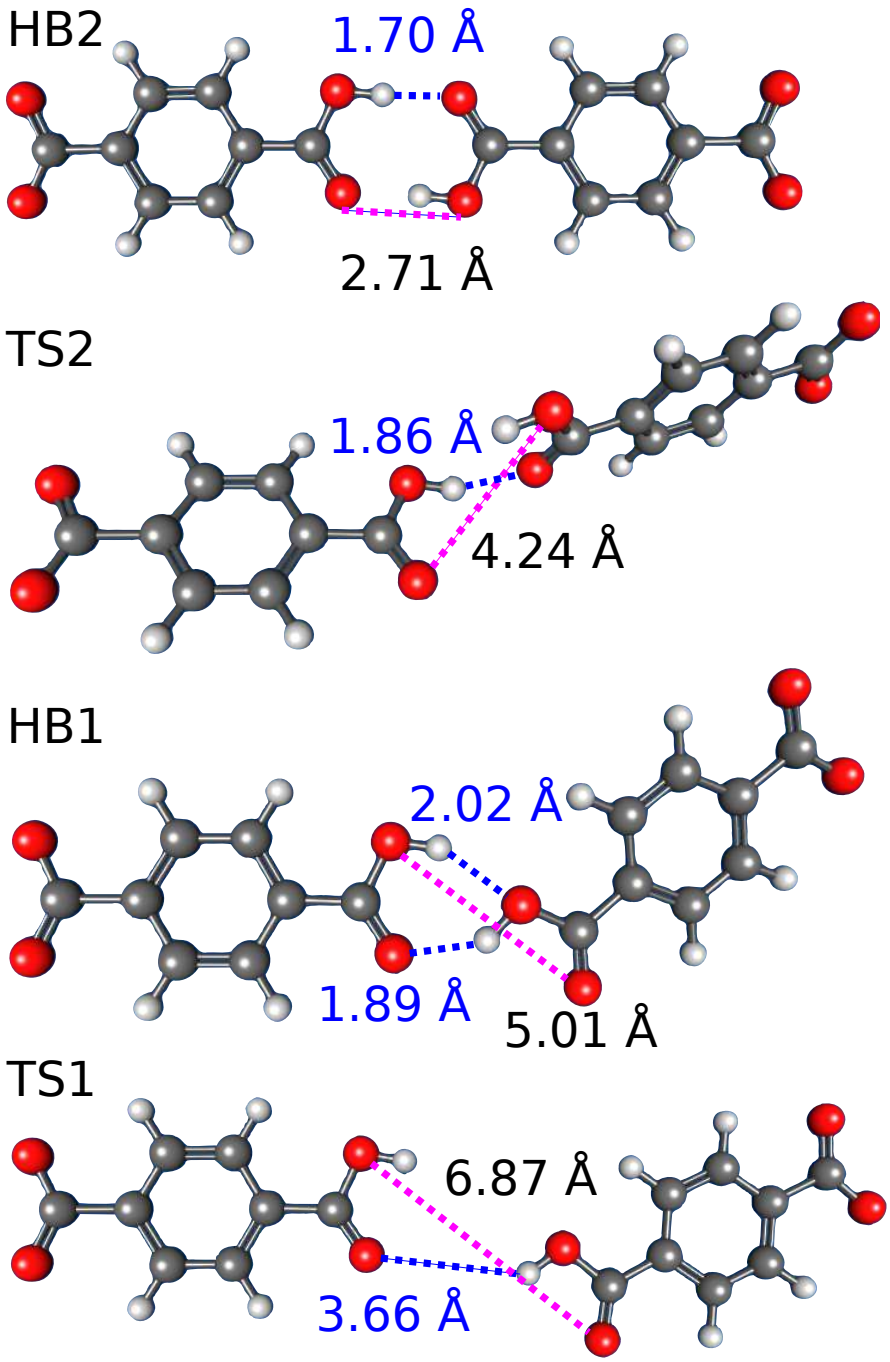

Figure 6.1: Structures at minima (HB2 and HB1) and transition states (TS2 and TS1) for the dissociation of the p-biphthalate di-anionic dimer as as given by WK[135].

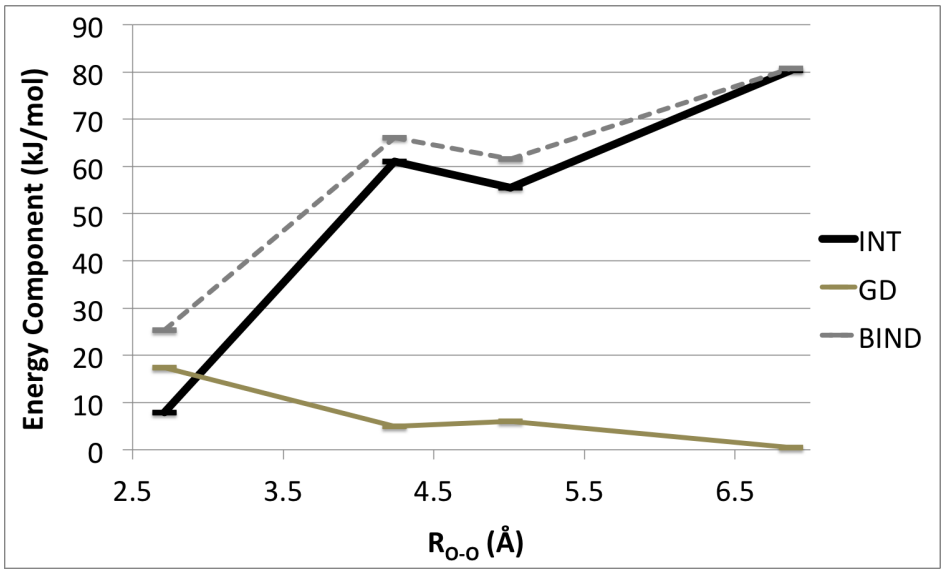

(a) Binding energy (BIND), the sum of the interaction energy (INT) and monomer geometric distortions (GD), computed for the stationary points along the coordinate. The binding energy is largely described by the interaction energy alone.

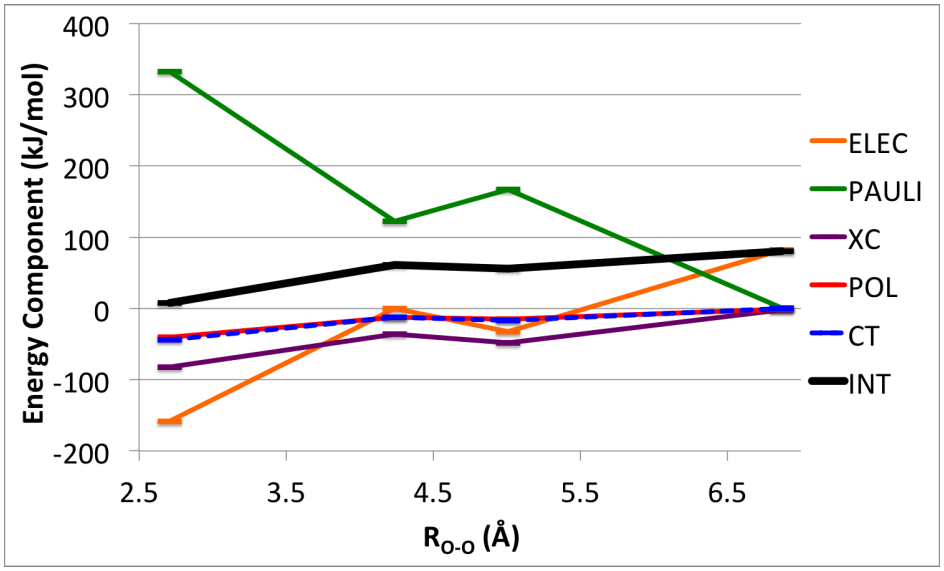

(b) Decomposition of the interaction energy (INT) into electrostatic (ELEC), Pauli repulsion (PAULI), exchange-correlation (XC), polarization (POL), and charge transfer (CT) contributions.

Figure 6.2: Energies relative to dissociated monomers and the decompositions thereof computed for the p-biphthalate di-anionic dimer dissociation coordinate minima (HB2 $R_{O\text{-}O}$ = 2.71 Å, HB1 $R_{O\text{-}O}$ = 5.01 Å) and transition structures (TS2 $R_{O\text{-}O}$ = 4.24 Å, TS1 $R_{O\text{-}O}$ = 6.87 Å) as given by WK[135].

(ELEC) with negligible contributions from other terms, which all decay more rapidly with increasing inter-monomer distance (Figure 6.2b). The electrostatic term at this separation is moreover almost identical to the analogous CLS ELEC term due to weakly overlapping fragments (Figure 6.3b). We infer that it is dominated by the repulsive monopole-monopole interaction as the monopole-dipole couplings will be attractive. Past TS1, the interaction energy decays because of the decrease in this unfavorable electrostatic interaction with increasing inter-monomer distance.

Inside of TS1, ELEC, XC, POL, and CT all become more favorable, and only the PAULI term becomes more repulsive due to increased inter-fragment overlap. All favorable terms follow the same energetic ordering as the interaction energy itself, and the Pauli repulsion term progresses in the opposite way. The HB2, TS2, and HB1 stationary points are thus the result of a delicate balance of many interactions.

We note first that the electrostatic term at HB2, HB1, and TS2 not only becomes more attractive than at TS1 but is net attractive at the minima, HB1 and HB2. To understand this effect, we consider Figure 6.4, which depicts the change in fragment densities upon going from those optimal for the fragments in isolation (and used to compute CLS ELEC) to those assigned to the fragments in the properly antisymmetric initial supersystem wavefunction (and used to compute ELEC). The effect of the antisymmetrization of monomer wavefunctions is, as always, a depletion of charge in the inter-fragment region, which in this case both deshields the hydrogen nuclei and increases density at the oxygen nuclei that are participating in hydrogen bonding. An additional consequence of this antisymmetrization is the seemingly inevitable development of small orthogonalization tails near the nuclei of other fragments. The resulting short-range electrostatic interactions are enough to overcome the repulsions between the excess electrons on the anionic fragments that are roughly located on opposite ends of the complex. The classical electrostatic (CLS ELEC) interactions are likewise more attractive than in the TS1 structure though not to the same degree; however, this is not due to the deshielding and orthogonalization tails produced by antisymmetrization but rather due to the classically permitted interpenetration of fragment charge densities.

The density rearrangements that brought about attractive electrostatic contributions for HB1 and HB2 and an only mildly repulsive electrostatic interaction for TS2 were the results of considerable inter-fragment overlaps, which have energetic costs in the form of quite unfavorable Pauli repulsion contributions for all three structures. However, these compressed configurations also bring more electrons from the two fragments into close proximity, increasing the energetic importance of their correlated motions and leading to a more attractive exchange-correlation contribution. The sum of ELEC, PAULI, and XC is termed the frozen orbital (FRZ) interaction, and despite the large changes in electrostatic and Pauli repulsion terms in particular across the coordinate, the frozen orbital energy is nearly constant (Figure 6.3b). The energetic benefits in ELEC and XC afforded by shorter separations are largely canceled by the concomitant cost. The frozen orbital interaction is equivalent to the sum of CLS ELEC and CLS PAULI in BB-EDA.

The remaining portion of the interaction energy is derived from intra-fragment polariza-

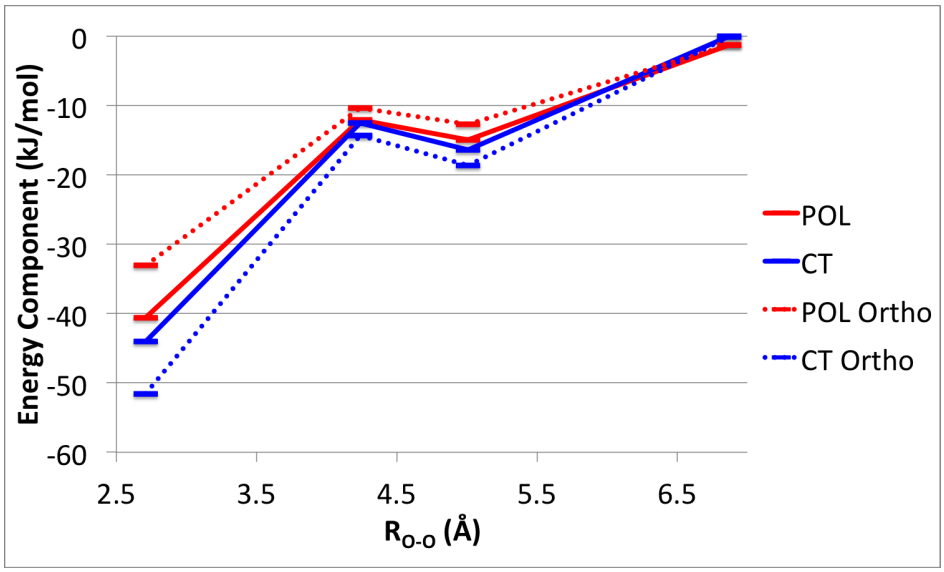

(a) Comparison of results produced by using orthogonal (oDQ, POL Ortho and CT Ortho) and non-orthogonal (nDQ, POL and CT) polarization subspaces. Differences are minor and do not alter the qualitative description of the interaction.

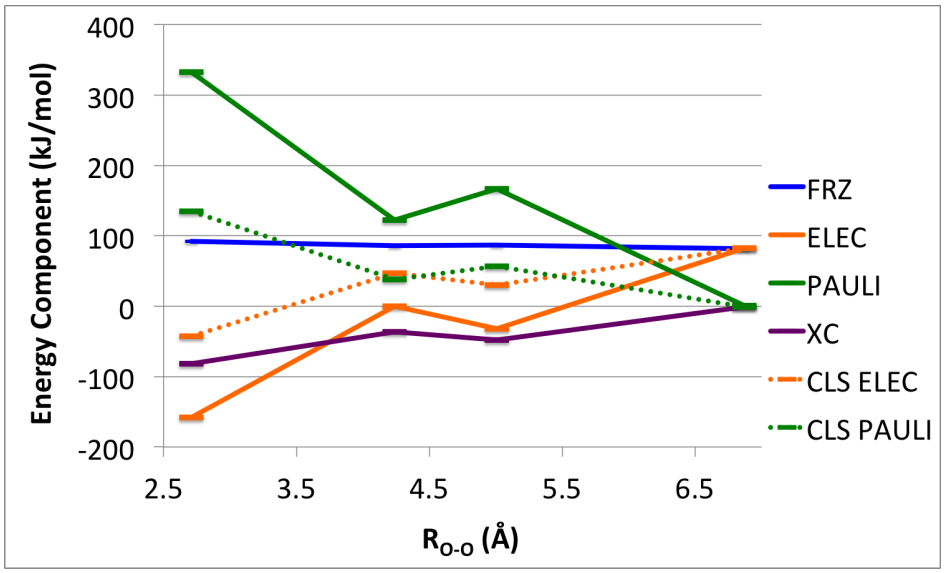

(b) Results for the decomposition of the frozen orbital energy (FRZ), which is nearly unchanged throughout the coordinate, by the scheme used in this work (ELEC, PAULI, XC) and that used in BB-EDA[44, 76, 77] (CLS ELEC, CLS PAULI) employed by FC[136].

Figure 6.3: Results for different choices in EDA term definitions computed for the p-biphthalate di-anionic dimer dissociation coordinate minima (HB2 $R_{O\text{-}O}$ = 2.71 Å, HB1 $R_{O\text{-}O}$ = 5.01 Å) and transition structures (TS2 $R_{O\text{-}O}$ = 4.24 Å, TS1 $R_{O\text{-}O}$ = 6.87 Å) as given by WK[135].

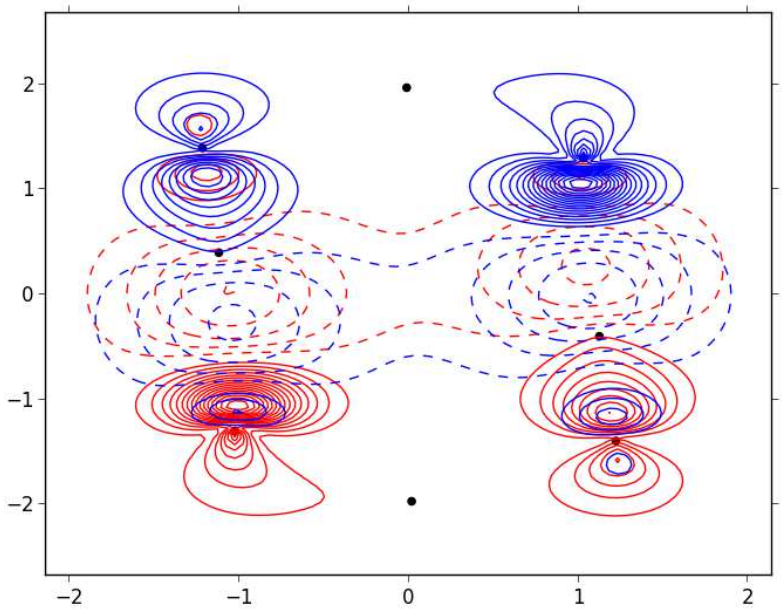

Figure 6.4: Contour plot of the change in density for the two (Red and Blue) p-biphthalate monomers in the HB2 complex of WK[135] with inter-fragment hydrogen bond lengths of $R_{O\text{-}H} = 1.70$ Å. Values plotted are the differences in the 3-space total spinless density, integrated to a plane ($\Delta_A(x,y) = \int dz \Delta\rho_A(x,y,z)$), for each fragment, A, upon going from the optimal isolated fragment density matrix to that assigned to the fragment within the initial supersystem wavefunction. Contours are evenly spaced at 0.1 $e^-/Å^3$ with positive contours solid and negative contours dashed. Dots indicate the positions of nuclei. We note the presence of seemingly unavoidable minor orthogonalization tails.

tion (POL) and inter-fragment charge transfer (CT), and these contributions have roughly the same energetic significance in each of the structures considered (Figure 6.2b). These two terms sum to the ORB term discussed by FC; however, the further decomposition into POL and CT is of interest here because one of the purposes of the work of WK was to draw attention to the importance of inter-fragment donor-acceptor orbital interactions in hydrogen bonded complexes, notably the canonical lone-pair to σ^* charge transfer interaction. We do not deny that there are contributions from inter-fragment electron delocalization in this complex, and they likely play an important role in determining the details of the fragment orientations in HB1 and HB2 due to the directional nature of orbital interactions. However, the closer contacts needed for stronger inter-fragment donor-acceptor interactions cannot occur to the same degree without an increased reliance on intra-fragment relaxation to relieve the accompanying larger electrostatic and kinetic perturbations from the presence of other

fragments, and one must remember that these Pauli repulsion effects are further offset by the ELEC and XC terms discussed above. Charge transfer is an important component of the interaction, but our results would indicate that it is no more privileged than the others. Indeed, for an interaction involving monomers with net charges, it is particularly surprising to the authors that induced electrostatic effects would not be considered significant components of the interaction from the start.

Because of the insistence by some[105] for treatments involving only orthogonal one-particle spaces, we clarify here that the POL and CT results discussed above are computed using non-orthogonal fragment subspaces for polarization. However, we also include results for another polarization model (Figure 6.3a) that employs subspaces produced by an energetically cognizant orthogonalization of these same non-orthogonal subspaces. The differences between the two sets of results for polarization and charge transfer is minor and certainly does not influence the qualitative interpretation of the interaction.

We now consider briefly the differences between the HB2, HB1, and TS2 structures. The full extent of the charge transfer interaction in the well-aligned cyclic hydrogen bonding HB2 is not possible in the more poorly aligned, strained, cyclic hydrogen bonding HB1 structure. This means that there is also a decreased motivation for adopting short inter-fragment separations, with the result that all EDA terms for HB1 are diminished in magnitude relative to those for HB2. The hydrogen bonding interactions that differentiate the cyclic configuration of HB2 from the more strained configuration of HB1 are broken in TS2, leaving only a single hydrogen bond in this structure. With only one major point of inter-fragment contact, the stabilization of TS2 relative to TS1 and the destabilization of TS2 due to Pauli repulsion relative to HB1 and HB2 are both diminished. While TS2 and HB1 have fairly similar interaction energies, the quite different electrostatic and Pauli repulsion contributions in their energy decompositions reveal the qualitative differences in the interactions that we have similarly identified by inspecting the structures.

6.3.3 Adenine Thymine Complexes

We now turn to the biologically relevant interactions between adenine and thymine base pairs with the aim of characterizing the qualitative differences between the Watson-Crick and stacked conformations (Figure 6.5) of this system taken from the S22[138] dataset. The results for the energy decomposition analysis of these two interaction energies appear in Table 6.1. Unlike in the more similar set of structures investigated above, the more strongly bound complex does not simply have all attractive terms more favorable than those of the less strongly bound complex. We note in particular that the exchange-correlation term, which contains within it the contribution to binding from dispersive interactions, is more favorable for the stacked complex than for the Watson-Crick complex, which makes sense in light of the larger number of inter-fragment contacts in the stacked structure. However, the XC contribution in the Watson-Crick complex is still appreciable due to closer contacts, which, though fewer in number, bring considerable density from the two fragments into close

	Watson-Crick	Stacked
ELEC	-183.45	-100.22
PAULI	245.64	164.05
XC	-71.10	-98.23
POL	-24.15	-6.79
CT	-34.04	-7.26
INT	-67.10	-48.45
CLS ELEC	-112.67	-45.36
CLS PAULI	103.76	10.96

Table 6.1: Energy decomposition analysis results for the interaction of adenine with thymine in the Watson-Crick and stacked configurations with corresponding structures taken from the S22[138] dataset. The shortest inter-fragment heavy-heavy distance in the stacked structure is $R_{C\text{-}N}$ = 3.09 Å. Results for the classical decomposition (ELEC + PAULI + XC = CLS ELEC + CLS PAULI) are shown for comparison.

proximity. The Pauli repulsion term in the stacked complex is large and repulsive for a similar reason though not as repulsive as in the Watson-Crick complex where the closer approach of a smaller number of atoms in hydrogen bonding motifs is motivated by an increased ability to participate in charge transfer interactions and facilitated by increased intra-fragment polarization as well as more favorable electrostatic interactions with deshielded hydrogen atoms. Charge transfer and polarization make only minor contributions to the stabilization of the stacked complex.

The lack of a separate exchange-correlation term in the classical decomposition makes the origin of the small CLS PAULI term for the stacked structure unclear (Table 6.1). It could be small either due to very weakly overlapping fragments or due to largely canceling contributions from dispersion, which is contained at least in part within CLS PAULI (it is contained entirely in CLS PAULI at long range). Indeed, the only contribution large enough to describe the interaction energy in the classical decomposition of the stacked structure is CLS ELEC. We know that the large electrostatic term in our decomposition (ELEC) is due to considerable density rearrangement during antisymmetrization as indicated by the large PAULI term; however, without prior knowledge of this system, we may be lead by the classical decomposition to believe that the interaction is almost entirely electrostatic in character instead of containing a large dispersive contribution. We note that these difficulties in the classical decomposition can be addressed in part by separating out a functional-form-specific dispersion contribution.

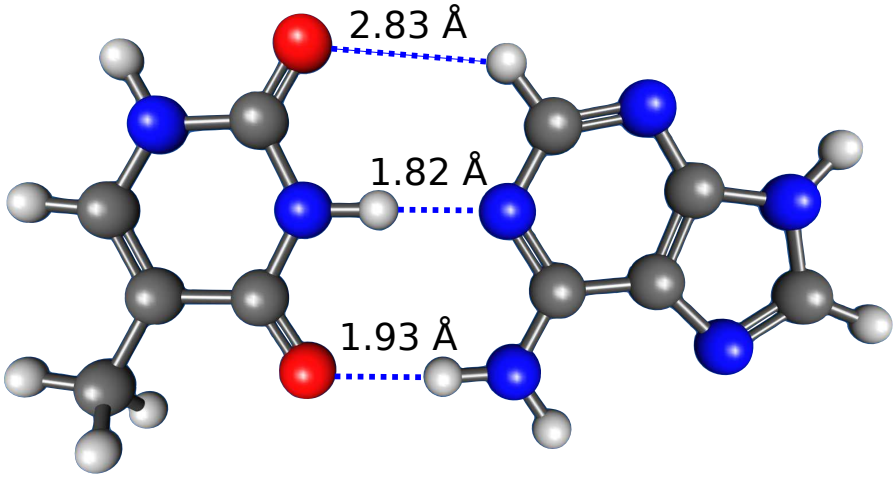

(a) Adenine thymine Watson-Crick structure.

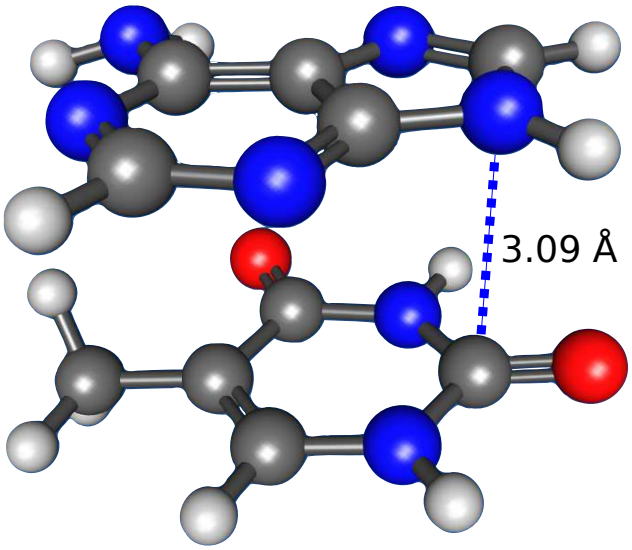

(b) Adenine thymine stacked structure.

Figure 6.5: The adenine thymine complex in the hydrogen-bonding Watson-Crick and stacked configurations from the S22[138] dataset with inter-fragment contacts shown.

6.3.4 $Cr(CO)_5$-CO

The next system that we investigate is a simple transition metal complex, $Cr(CO)_6$. The interaction of interest is the binding of the final CO ligand to the otherwise optimal complex. A plot of the energy decomposition of the interaction energy for the rigid dissociation of a carbonyl ligand along the Cr-C coordinate relative to the octahedral crystal structure[139] appears in Figure 6.6a. As expected for the σ donating and π accepting carbonyl ligand, charge transfer makes considerable contributions to binding throughout the coordinate, much more than polarization at equilibrium and shorter distances. The destabilizing Pauli repulsion contribution is mitigated to some degree by stabilizing exchange-correlation and electrostatic interactions, which are comparable in magnitude to the stabilizing charge transfer interaction near equilibrium but are of diminished importance at very compressed distances. We note also the dramatic difference in the character of the ELEC and CLS ELEC interpretations of the electrostatic contribution to binding is due to the different treatment of charge penetration effects and shielding in the two models with the ELEC term transitioning toward a repulsive interaction at the shortest coordinate values considered while CLS ELEC becomes increasingly attractive (Figure 6.6b).

6.3.5 Ionized Glycerol Complex

The final complex that we analyze is a radical cationic cluster of three fragments (Figure 6.7) that was identified by Bell et al.[140] as an important intermediate in the dissociative photoionization of glycerol and designated as COM1 in that work. We decompose the interaction energy for this structure, unmodified, by a complete many-body expansion of the interaction energy in Table 6.2. We note that a similar analysis was performed in the original work[140] though with a different model chemistry and an older version of the current decomposition scheme (ALMO-EDA) that notably lacks the decomposition of the frozen orbital interaction and the bounded treatment of polarization. As a result of the basis set choice in the earlier study, the change in model chemistry and polarization methodology has no qualitative impact on the interpretation of the interaction components analyzed in that work.

The two-body term between the vinyl alcohol radical cation (A) and water (W), E_2[AW], is the strongest interaction in the many-body expansion. The electrostatic term is large and attractive here as we have seen in other hydrogen bonding systems above; however, in this case there is a favorably aligned monopole-dipole interaction in the absence of a repulsive monopole-monopole interaction. The large, repulsive PAULI term is explained by the short ($R_{O\text{-}H}$ = 1.38 Å) hydrogen bond length between these two monomers, which was likely motivated by a combination of not only stronger inter-fragment orbital interactions (CT) but also favorable permanent (ELEC) and induced (POL) electrostatic interactions with the electron-poor vinyl alcohol radical cation. The exchange-correlation term makes a stabilizing contribution comparable to both POL and CT, which is not surprising again

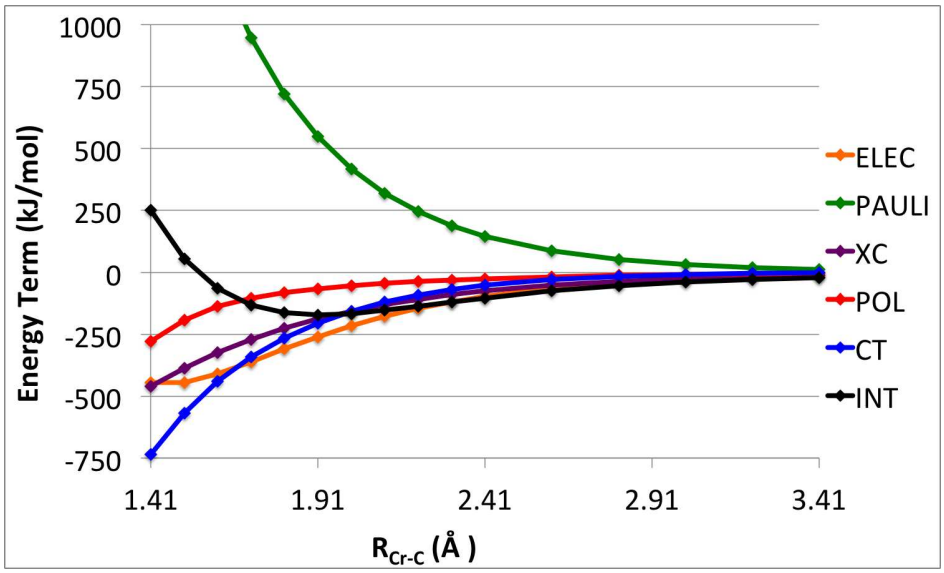

(a) Decomposition of the interaction energy (INT) into electrostatic (ELEC), Pauli repulsion (PAULI), exchange-correlation (XC), polarization (POL), and charge transfer (CT) components.

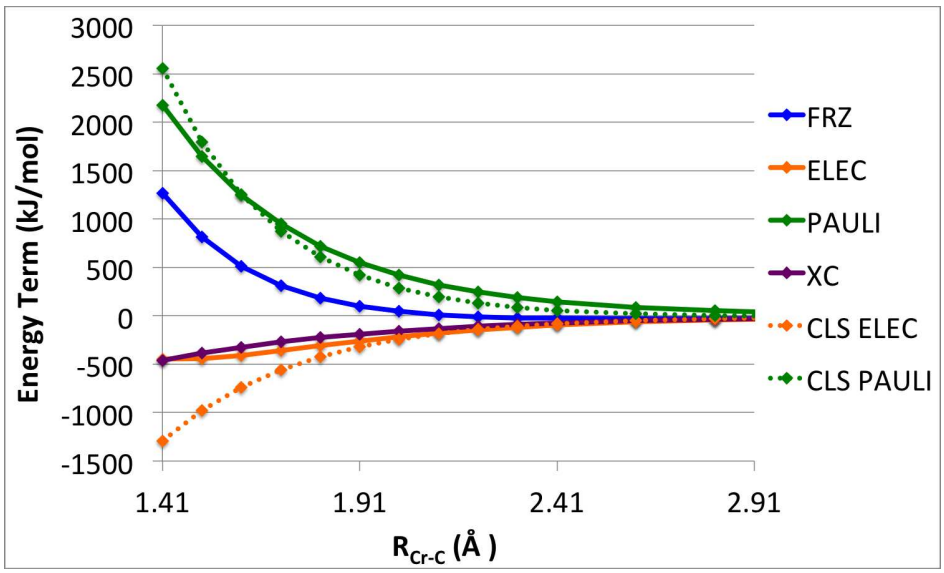

(b) Results for the decomposition of the frozen orbital energy (FRZ), by the scheme used in this work (ELEC, PAULI, XC) and that used in BB-EDA[44, 76, 77] (CLS ELEC, CLS PAULI).

Figure 6.6: Energy decomposition analysis results for the rigid dissociation of a single carbonyl ligand along the $R_{Cr\text{-}C}$ coordinate relative to the $R_{C\text{-}O}$ = 1.14 Å and $R_{Cr\text{-}C}$ = 1.91 Å octahedral $Cr(CO)_6$ crystal structure[139].

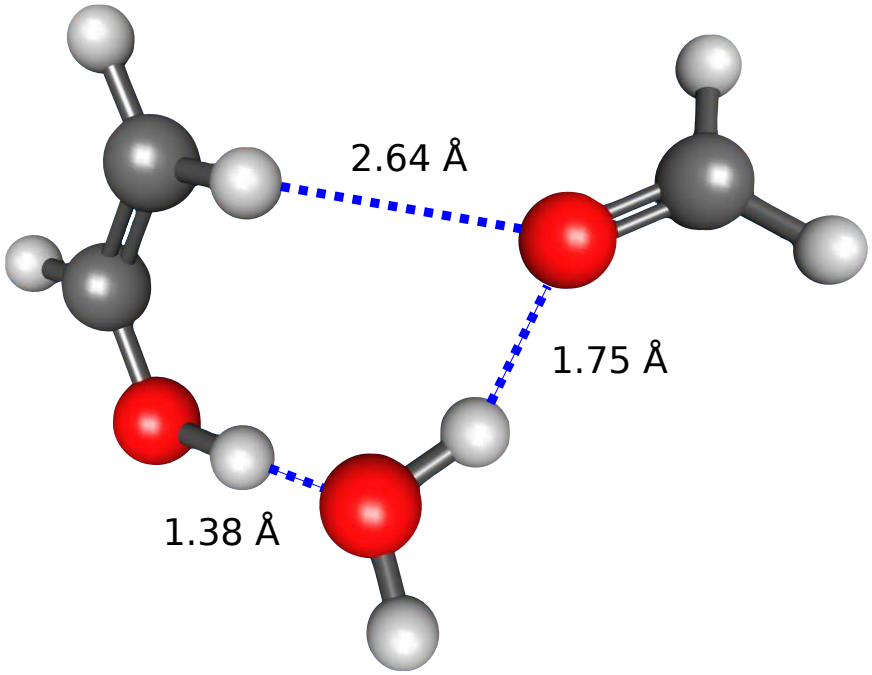

Figure 6.7: The COM1 complex from Bell et al.[140] that has been identified as an important intermediate in the dissociative photoionization of glycerol with inter-fragment contacts shown.

	E_2[AW]	E_2[AF]	E_2[WF]	E_3[AWF]	Total[AWF]
ELEC	-215.49	-47.82	-80.24	-1.28	-344.84
PAULI	300.04	12.38	121.66	-0.67	433.41
XC	-63.79	-6.85	-30.49	0.81	-100.31
POL	-66.16	-9.05	-7.17	-8.22	-90.60
CT	-72.20	-1.25	-13.62	-5.43	-92.50
INT	-117.60	-52.59	-9.87	-14.78	-194.84

Table 6.2: Energy decomposition analysis of the many-body expansion of the strongly-bound, radical, cationic COM1 complex from Bell et al.[140]. E_2 and E_3 denote two- and three-body terms in the expansion. A, W, and F indicate the vinyl alcohol radical cation, water, and formaldehyde respectively.

because of the short inter-fragment contacts.

The two-body term between the vinyl alcohol radical cation (A) and formaldehyde (F), E_2[AF], describes primarily the electrostatic interaction between the cation and favorably aligned dipole of formaldehyde with minor additional stabilization from POL and XC. Compared to the other two-body term, PAULI and CT contributions are very small in magnitude for E_2[AF] due to the distance between these two monomers.

The two-body term between water (W) and formaldehyde (F), E_2[WF], is the weakest as it involves no permanent monopoles. The hydrogen bond length in this case is slightly compressed ($R_{O\text{-}H} = 1.75$ Å) compared to the ωB97X-V/def2-QZVPPD optimal bond length ($R_{O\text{-}H} = 2.03$ Å). While not optimal for this pair interaction, it is optimal for the cluster as a whole within the model chemistry of the original work.[140] The consequence of this shorter bond is a fairly repulsive PAULI term and larger magnitude stabilizing interactions across the board relative to an equilibrium water-formaldehyde interaction, though, by definition, they do not quite match the energy increase due to Pauli repulsion.

The three-body term, E_3[AWF], is, as in our past analysis[140], dominated by POL and CT contributions owing to the presence of multiple permanent moments and to the concerted charge donation from formaldehyde to water to the vinyl alcohol radical cation. Classical electrostatic interactions are pairwise additive; however, our electrostatic term accounts for the non-additive density deformations accompanying the formation of the initial supersystem wavefunction, and so the three-body electrostatic term is not explicitly zero though in this case it is quite small. As are PAULI and XC.

6.4 Conclusions

We have introduced a new eda with the following key properties:

1. The EDA can work with any accurate single determinant Kohn-Sham model chemistry including the exact functional in a complete basis set.

2. It produces physically meaningful terms with correct sign and asymptotic behavior.

3. It is maximally descriptive, avoiding terms containing multiple distinct physical contributions.

4. The EDA is variational and optionally fully variational for extremely strong interactions where removal of constant density polarization (Chapter 4) from the initial supersystem wavefunction is necessary.

We have employed this new EDA to analyze several different intermolecular interactions including an anti-electrostatic hydrogen bond, which we revealed to be a balance of several contributions and not as counterintuitive or surprising as the name might suggest. The examination of two configurations of adenine and thymine demonstrated that our EDA is

capable of discerning between two qualitatively different types of interactions, made possible in large part by the new decomposition of the frozen energy, which separates out an exchange-correlation contribution subsuming dispersion interactions and gives physical values for Pauli repulsion. In the case of $Cr(CO)_6$ ligand dissociation, we obtained the expected result of large, favorable donor acceptor interactions and illustrated a qualitative difference between ELEC and the corresponding electrostatic term used by several other EDA schemes. In our analysis of the ionized glycerol complex, we demonstrated the utility of the combination of many-body expansions and EDA, and, taking advantage of the additional information provided by the newly added ELEC, PAULI, and XC terms, we enhanced our previous description of this interaction, while validating the earlier computational protocol.

Appendix A

Additional Data for Unrestricted ALMO-EDA

Table A.1: ALMO EDA Data for Various Functionals and Basis Sets: The systems included are a subset of the alkyl radical plus cation systems. The Density functionals presented are B3LYP, M06, M062X, ωB97, ωB97X, and ωB97X-D. The basis sets are 6-31+G(d,p) and 6-311++G(3df,3pd).

Alkyl Species	Cation	Functional	Basis	GD	FRZ	POL	V-CT	Bind
(CH3)3CH	H3O+	b3lyp	6-31+Gdp	11.3	48.2	-52.7	-55.6	-48.8
(CH3)3CH	H3O+	b3lyp	6-311++G3df3pd	11.9	48.0	-72.3	-39.4	-51.8
(CH3)3CH	H3O+	m06	6-31+Gdp	11.6	41.6	-53.1	-52.9	-52.9
(CH3)3CH	H3O+	m06	6-311++G3df3pd	12.3	41.6	-71.7	-36.0	-53.8
(CH3)3CH	H3O+	m062x	6-31+Gdp	12.1	46.5	-51.2	-58.2	-50.8
(CH3)3CH	H3O+	m062x	6-311++G3df3pd	12.6	46.1	-67.2	-47.0	-55.5
(CH3)3CH	H3O+	omegaB97	6-31+Gdp	12.0	37.0	-52.4	-47.4	-50.9
(CH3)3CH	H3O+	omegaB97	6-311++G3df3pd	12.4	36.6	-71.1	-33.0	-55.1
(CH3)3CH	H3O+	omegaB97x	6-31+Gdp	12.4	38.5	-52.5	-48.7	-50.3
(CH3)3CH	H3O+	omegaB97x	6-311++G3df3pd	12.9	38.2	-71.5	-33.8	-54.3
(CH3)3CH	H3O+	omegaB97x-D	6-31+Gdp	12.6	37.6	-52.6	-50.9	-53.4
(CH3)3CH	H3O+	omegaB97x-D	6-311++G3df3pd	13.1	37.4	-72.3	-35.2	-57.0
(CH3)3CH	K+	b3lyp	6-31+Gdp	1.8	10.4	-27.6	-5.6	-21.0
(CH3)3CH	K+	b3lyp	6-311++G3df3pd	2.0	10.8	-32.5	-1.5	-21.2
(CH3)3CH	K+	m06	6-31+Gdp	1.9	7.0	-27.6	-6.1	-24.9
(CH3)3CH	K+	m06	6-311++G3df3pd	2.1	7.3	-32.3	-2.8	-25.7
(CH3)3CH	K+	m062x	6-31+Gdp	2.0	6.1	-26.9	-8.5	-27.3
(CH3)3CH	K+	m062x	6-311++G3df3pd	2.3	6.1	-31.7	-5.3	-28.6
(CH3)3CH	K+	omegaB97	6-31+Gdp	2.0	4.0	-27.8	-4.5	-26.3
(CH3)3CH	K+	omegaB97	6-311++G3df3pd	2.1	4.4	-33.2	-1.4	-28.1
(CH3)3CH	K+	omegaB97x	6-31+Gdp	2.1	4.9	-27.5	-4.5	-25.0
(CH3)3CH	K+	omegaB97x	6-311++G3df3pd	2.3	5.3	-32.8	-1.4	-26.6
(CH3)3CH	K+	omegaB97x-D	6-31+Gdp	2.2	2.1	-27.2	-4.4	-27.4
(CH3)3CH	K+	omegaB97x-D	6-311++G3df3pd	2.4	2.6	-32.3	-1.4	-28.7
(CH3)3CH	Na+	b3lyp	6-31+Gdp	3.8	12.4	-49.4	-8.5	-41.6
(CH3)3CH	Na+	b3lyp	6-311++G3df3pd	4.3	12.2	-60.5	-1.1	-45.0
(CH3)3CH	Na+	m06	6-31+Gdp	3.9	10.6	-47.4	-8.4	-41.4
(CH3)3CH	Na+	m06	6-311++G3df3pd	4.4	11.6	-56.2	-1.6	-41.8
(CH3)3CH	Na+	m062x	6-31+Gdp	4.3	9.4	-47.6	-12.6	-46.5
(CH3)3CH	Na+	m062x	6-311++G3df3pd	4.7	9.0	-57.5	-5.9	-49.7
(CH3)3CH	Na+	omegaB97	6-31+Gdp	4.1	9.8	-47.7	-7.9	-41.7

Alkyl Species	Cation	Functional	Basis	GD	FRZ	POL	V-CT	Bind
(CH3)3CH	Na+	omegaB97	6-311++G3df3pd	4.4	9.4	-58.8	-0.8	-45.8
(CH3)3CH	Na+	omegaB97x	6-31+Gdp	4.2	12.5	-47.1	-7.5	-37.9
(CH3)3CH	Na+	omegaB97x	6-311++G3df3pd	4.5	12.3	-57.9	-0.8	-41.8
(CH3)3CH	Na+	omegaB97x-D	6-31+Gdp	4.2	4.7	-46.8	-6.8	-44.8
(CH3)3CH	Na+	omegaB97x-D	6-311++G3df3pd	4.6	4.7	-57.2	-0.7	-48.6
(CH3)3CH	NH4+	b3lyp	6-31+Gdp	2.0	18.5	-26.4	-16.3	-22.2
(CH3)3CH	NH4+	b3lyp	6-311++G3df3pd	2.3	18.7	-33.8	-12.0	-24.7
(CH3)3CH	NH4+	m06	6-31+Gdp	2.1	13.7	-27.0	-17.5	-28.8
(CH3)3CH	NH4+	m06	6-311++G3df3pd	2.4	13.7	-34.3	-12.3	-30.6
(CH3)3CH	NH4+	m062x	6-31+Gdp	2.3	14.9	-25.8	-18.4	-27.0
(CH3)3CH	NH4+	m062x	6-311++G3df3pd	2.6	15.0	-32.4	-15.3	-30.0
(CH3)3CH	NH4+	omegaB97	6-31+Gdp	2.2	9.2	-26.8	-12.9	-28.3
(CH3)3CH	NH4+	omegaB97	6-311++G3df3pd	2.5	9.5	-34.4	-8.9	-31.3
(CH3)3CH	NH4+	omegaB97x	6-31+Gdp	2.4	10.3	-26.7	-13.4	-27.5
(CH3)3CH	NH4+	omegaB97x	6-311++G3df3pd	2.6	10.6	-34.2	-9.3	-30.3
(CH3)3CH	NH4+	omegaB97x-D	6-31+Gdp	2.4	8.6	-26.7	-14.3	-30.0
(CH3)3CH	NH4+	omegaB97x-D	6-311++G3df3pd	2.7	9.0	-34.3	-10.0	-32.6
CH3$^\bullet$	H3O+	b3lyp	6-31+Gdp	13.5	21.4	-32.6	-70.9	-68.5
CH3$^\bullet$	H3O+	b3lyp	6-311++G3df3pd	14.3	27.7	-53.2	-58.2	-69.4
CH3$^\bullet$	H3O+	m06	6-31+Gdp	13.2	19.2	-31.7	-65.4	-64.8
CH3$^\bullet$	H3O+	m06	6-311++G3df3pd	14.1	25.8	-51.5	-53.4	-65.1
CH3$^\bullet$	H3O+	m062x	6-31+Gdp	13.5	25.4	-32.6	-72.1	-65.7
CH3$^\bullet$	H3O+	m062x	6-311++G3df3pd	14.1	30.8	-48.2	-63.1	-66.4
CH3$^\bullet$	H3O+	omegaB97	6-31+Gdp	14.3	11.9	-32.9	-64.5	-71.2
CH3$^\bullet$	H3O+	omegaB97	6-311++G3df3pd	14.9	18.0	-54.9	-52.5	-74.4
CH3$^\bullet$	H3O+	omegaB97x	6-31+Gdp	14.8	12.8	-32.6	-65.6	-70.6
CH3$^\bullet$	H3O+	omegaB97x	6-311++G3df3pd	15.4	18.7	-54.3	-53.2	-73.4
CH3$^\bullet$	H3O+	omegaB97x-D	6-31+Gdp	15.2	15.2	-32.7	-67.5	-69.8
CH3$^\bullet$	H3O+	omegaB97x-D	6-311++G3df3pd	15.8	21.5	-54.5	-55.1	-72.3
CH3$^\bullet$	K+	b3lyp	6-31+Gdp	1.4	-12.0	-9.4	-5.0	-25.0
CH3$^\bullet$	K+	b3lyp	6-311++G3df3pd	1.6	-10.3	-14.5	-1.3	-24.5
CH3$^\bullet$	K+	m06	6-31+Gdp	0.8	-12.2	-9.1	-5.1	-25.6
CH3$^\bullet$	K+	m06	6-311++G3df3pd	0.9	-9.9	-14.7	-2.0	-25.7
CH3$^\bullet$	K+	m062x	6-31+Gdp	0.9	-14.3	-8.9	-7.4	-29.7
CH3$^\bullet$	K+	m062x	6-311++G3df3pd	1.1	-13.1	-14.3	-4.3	-30.6
CH3$^\bullet$	K+	omegaB97	6-31+Gdp	1.5	-13.7	-9.0	-3.8	-25.0
CH3$^\bullet$	K+	omegaB97	6-311++G3df3pd	1.6	-11.6	-14.8	-1.2	-26.0
CH3$^\bullet$	K+	omegaB97x	6-31+Gdp	1.4	-14.3	-8.9	-4.0	-25.9
CH3$^\bullet$	K+	omegaB97x	6-311++G3df3pd	1.5	-12.5	-14.5	-1.1	-26.6
CH3$^\bullet$	K+	omegaB97x-D	6-31+Gdp	1.4	-14.8	-8.7	-4.0	-26.1
CH3$^\bullet$	K+	omegaB97x-D	6-311++G3df3pd	1.5	-13.0	-14.0	-1.1	-26.5
CH3$^\bullet$	Na+	b3lyp	6-31+Gdp	1.6	-18.9	-17.6	-7.4	-42.3
CH3$^\bullet$	Na+	b3lyp	6-311++G3df3pd	1.8	-16.2	-27.9	-1.5	-43.7
CH3$^\bullet$	Na+	m06	6-31+Gdp	0.9	-17.2	-16.6	-6.1	-39.0
CH3$^\bullet$	Na+	m06	6-311++G3df3pd	1.1	-12.9	-26.1	-1.6	-39.6
CH3$^\bullet$	Na+	m062x	6-31+Gdp	1.1	-19.4	-16.6	-10.4	-45.3
CH3$^\bullet$	Na+	m062x	6-311++G3df3pd	1.3	-16.8	-26.3	-4.6	-46.4
CH3$^\bullet$	Na+	omegaB97	6-31+Gdp	1.6	-18.0	-16.3	-5.6	-38.4
CH3$^\bullet$	Na+	omegaB97	6-311++G3df3pd	1.8	-15.2	-26.4	-0.6	-40.4
CH3$^\bullet$	Na+	omegaB97x	6-31+Gdp	1.6	-17.7	-16.0	-5.8	-37.9
CH3$^\bullet$	Na+	omegaB97x	6-311++G3df3pd	1.8	-15.1	-25.8	-0.7	-39.8
CH3$^\bullet$	Na+	omegaB97x-D	6-31+Gdp	1.6	-20.6	-15.8	-5.2	-40.0
CH3$^\bullet$	Na+	omegaB97x-D	6-311++G3df3pd	1.7	-17.7	-25.2	-0.6	-41.8
CH3$^\bullet$	NH4+	b3lyp	6-31+Gdp	3.3	2.8	-14.1	-28.8	-36.7
CH3$^\bullet$	NH4+	b3lyp	6-311++G3df3pd	3.8	6.1	-24.0	-23.2	-37.3
CH3$^\bullet$	NH4+	m06	6-31+Gdp	2.7	0.1	-13.6	-27.7	-38.6
CH3$^\bullet$	NH4+	m06	6-311++G3df3pd	3.1	3.5	-24.2	-22.3	-39.9
CH3$^\bullet$	NH4+	m062x	6-31+Gdp	2.8	3.0	-13.7	-30.8	-38.7
CH3$^\bullet$	NH4+	m062x	6-311++G3df3pd	3.2	5.5	-22.3	-26.1	-39.6
CH3$^\bullet$	NH4+	omegaB97	6-31+Gdp	3.5	-4.7	-14.7	-24.1	-40.0
CH3$^\bullet$	NH4+	omegaB97	6-311++G3df3pd	4.0	-1.1	-26.0	-18.6	-41.8

Alkyl Species	Cation	Functional	Basis	GD	FRZ	POL	V-CT	Bind
$CH3^{\bullet}$	NH4+	omegaB97x	6-31+Gdp	3.6	-4.3	-14.3	-25.1	-40.2
$CH3^{\bullet}$	NH4+	omegaB97x	6-311++G3df3pd	4.0	-1.1	-25.3	-19.3	-41.7
$CH3^{\bullet}$	NH4+	omegaB97x-D	6-31+Gdp	3.6	-2.9	-14.2	-26.3	-39.9
$CH3^{\bullet}$	NH4+	omegaB97x-D	6-311++G3df3pd	4.0	0.5	-25.1	-20.6	-41.2
$(CH3)3C^{\bullet}$	H3O+	b3lyp	6-31+Gdp	81.8	76.1	-118.2	-164.4	-124.7
$(CH3)3C^{\bullet}$	H3O+	b3lyp	6-311++G3df3pd	82.1	83.3	-159.0	-130.6	-124.2
$(CH3)3C^{\bullet}$	H3O+	m06	6-31+Gdp	84.4	70.5	-117.7	-154.3	-117.1
$(CH3)3C^{\bullet}$	H3O+	m06	6-311++G3df3pd	85.2	80.4	-152.7	-124.2	-111.2
$(CH3)3C^{\bullet}$	H3O+	m062x	6-31+Gdp	83.8	83.0	-114.8	-169.3	-117.3
$(CH3)3C^{\bullet}$	H3O+	m062x	6-311++G3df3pd	83.8	89.9	-145.9	-145.9	-118.1
$(CH3)3C^{\bullet}$	H3O+	omegaB97	6-31+Gdp	84.2	56.9	-114.7	-152.3	-125.9
$(CH3)3C^{\bullet}$	H3O+	omegaB97	6-311++G3df3pd	84.4	64.9	-154.4	-121.7	-126.7
$(CH3)3C^{\bullet}$	H3O+	omegaB97x	6-31+Gdp	86.0	58.8	-115.4	-153.7	-124.4
$(CH3)3C^{\bullet}$	H3O+	omegaB97x	6-311++G3df3pd	86.2	66.5	-155.5	-121.9	-124.7
$(CH3)3C^{\bullet}$	H3O+	omegaB97x-D	6-31+Gdp	86.8	56.8	-117.0	-156.8	-130.3
$(CH3)3C^{\bullet}$	H3O+	omegaB97x-D	6-311++G3df3pd	87.0	64.4	-157.9	-123.5	-130.0
$(CH3)3C^{\bullet}$	K+	b3lyp	6-31+Gdp	1.1	-11.5	-27.3	-6.2	-43.8
$(CH3)3C^{\bullet}$	K+	b3lyp	6-311++G3df3pd	1.4	-9.6	-31.0	-2.4	-41.6
$(CH3)3C^{\bullet}$	K+	m06	6-31+Gdp	1.4	-15.9	-27.4	-7.2	-49.0
$(CH3)3C^{\bullet}$	K+	m06	6-311++G3df3pd	1.7	-12.8	-31.5	-3.9	-46.4
$(CH3)3C^{\bullet}$	K+	m062x	6-31+Gdp	0.9	-17.0	-25.1	-11.3	-52.5
$(CH3)3C^{\bullet}$	K+	m062x	6-311++G3df3pd	1.1	-16.0	-29.2	-8.2	-52.3
$(CH3)3C^{\bullet}$	K+	omegaB97	6-31+Gdp	1.2	-18.8	-26.8	-4.7	-49.2
$(CH3)3C^{\bullet}$	K+	omegaB97	6-311++G3df3pd	1.4	-16.5	-31.4	-2.0	-48.4
$(CH3)3C^{\bullet}$	K+	omegaB97x	6-31+Gdp	1.3	-18.5	-26.5	-4.9	-48.6
$(CH3)3C^{\bullet}$	K+	omegaB97x	6-311++G3df3pd	1.5	-16.3	-31.0	-1.9	-47.7
$(CH3)3C^{\bullet}$	K+	omegaB97x-D	6-31+Gdp	1.2	-22.6	-26.2	-5.0	-52.6
$(CH3)3C^{\bullet}$	K+	omegaB97x-D	6-311++G3df3pd	1.4	-20.2	-30.6	-2.0	-51.4
$(CH3)3C^{\bullet}$	Na+	b3lyp	6-31+Gdp	2.0	-22.4	-46.5	-2.4	-69.3
$(CH3)3C^{\bullet}$	Na+	b3lyp	6-311++G3df3pd	2.3	-19.7	-52.8	-0.7	-71.0
$(CH3)3C^{\bullet}$	Na+	m06	6-31+Gdp	2.3	-22.2	-44.7	-3.6	-68.1
$(CH3)3C^{\bullet}$	Na+	m06	6-311++G3df3pd	2.6	-16.8	-50.1	-1.8	-66.2
$(CH3)3C^{\bullet}$	Na+	m062x	6-31+Gdp	1.6	-25.2	-42.8	-8.5	-75.0
$(CH3)3C^{\bullet}$	Na+	m062x	6-311++G3df3pd	1.7	-23.2	-48.3	-6.6	-76.3
$(CH3)3C^{\bullet}$	Na+	omegaB97	6-31+Gdp	1.9	-24.8	-42.4	-2.6	-67.9
$(CH3)3C^{\bullet}$	Na+	omegaB97	6-311++G3df3pd	2.2	-21.9	-49.6	-0.3	-69.7
$(CH3)3C^{\bullet}$	Na+	omegaB97x	6-31+Gdp	2.0	-23.7	-41.8	-2.6	-66.0
$(CH3)3C^{\bullet}$	Na+	omegaB97x	6-311++G3df3pd	2.3	-20.9	-48.8	-0.4	-67.8
$(CH3)3C^{\bullet}$	Na+	omegaB97x-D	6-31+Gdp	1.9	-32.9	-41.6	-2.0	-74.7
$(CH3)3C^{\bullet}$	Na+	omegaB97x-D	6-311++G3df3pd	2.2	-29.8	-48.4	-0.3	-76.2
$(CH3)3C^{\bullet}$	NH4+	b3lyp	6-31+Gdp	9.2	19.4	-41.2	-52.1	-64.8
$(CH3)3C^{\bullet}$	NH4+	b3lyp	6-311++G3df3pd	9.9	22.8	-54.8	-42.7	-64.9
$(CH3)3C^{\bullet}$	NH4+	m06	6-31+Gdp	9.8	12.6	-40.7	-49.6	-67.8
$(CH3)3C^{\bullet}$	NH4+	m06	6-311++G3df3pd	10.3	17.3	-52.7	-40.4	-65.5
$(CH3)3C^{\bullet}$	NH4+	m062x	6-31+Gdp	8.8	18.6	-39.1	-57.0	-68.6
$(CH3)3C^{\bullet}$	NH4+	m062x	6-311++G3df3pd	9.3	21.5	-49.5	-50.1	-68.8
$(CH3)3C^{\bullet}$	NH4+	omegaB97	6-31+Gdp	9.6	3.6	-40.9	-43.8	-71.5
$(CH3)3C^{\bullet}$	NH4+	omegaB97	6-311++G3df3pd	10.1	8.2	-54.3	-35.8	-71.8
$(CH3)3C^{\bullet}$	NH4+	omegaB97x	6-31+Gdp	9.9	5.2	-40.8	-45.2	-70.9
$(CH3)3C^{\bullet}$	NH4+	omegaB97x	6-311++G3df3pd	10.5	9.5	-54.3	-36.6	-71.0
$(CH3)3C^{\bullet}$	NH4+	omegaB97x-D	6-31+Gdp	9.8	2.7	-41.1	-47.5	-76.1
$(CH3)3C^{\bullet}$	NH4+	omegaB97x-D	6-311++G3df3pd	10.4	6.9	-55.1	-38.2	-75.9

Appendix B

Frozen Energy Decomposition Hartree-Fock Data

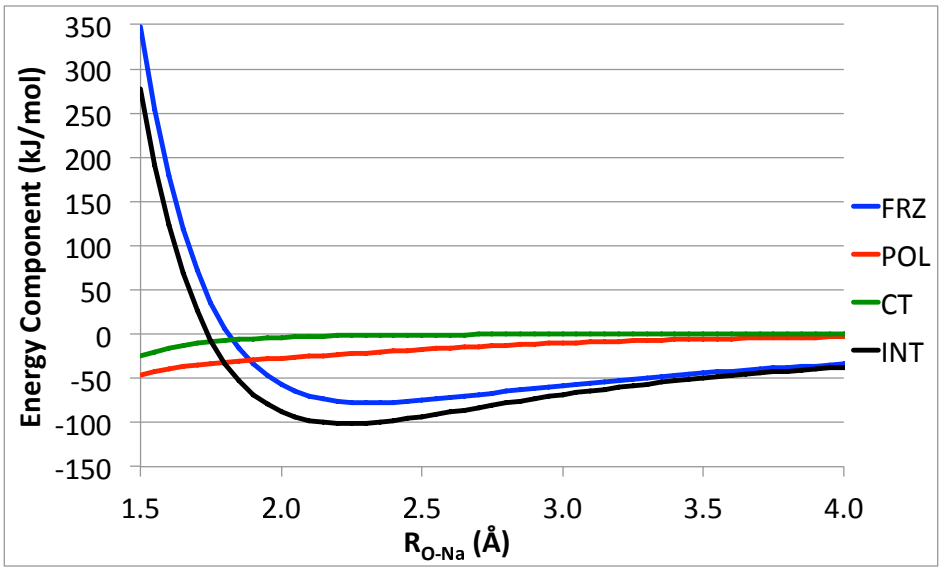

(a) Basic energy decomposition terms (FRZ, POL, CT) as well as the total interaction energy (INT) along the coordinate.

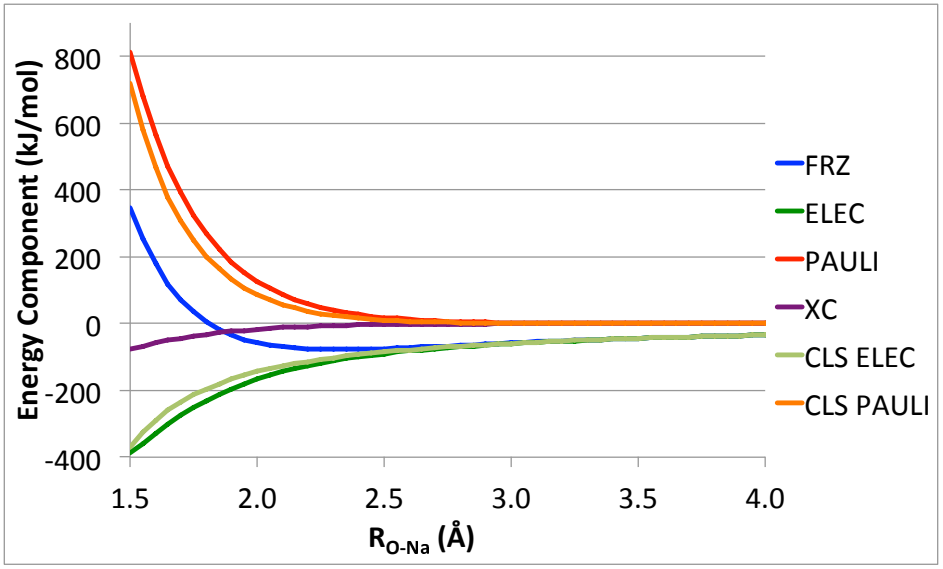

(b) Further decomposition of the frozen energy (FRZ) based on the new scheme presented in this work (ELEC, PAULI, XC) and based on the classical approach (CLS ELEC, CLS Pauli).

Figure B.1: Energy terms computed with HF/aug-cc-pVQZ for the rigid dissociation along the O-Na coordinate of water interacting with a sodium cation relative to the C_{2v} ωB97X-V/aug-cc-pVQZ optimized geometry (equilibrium $R_{O\text{-}Na}$ = 2.23Å).

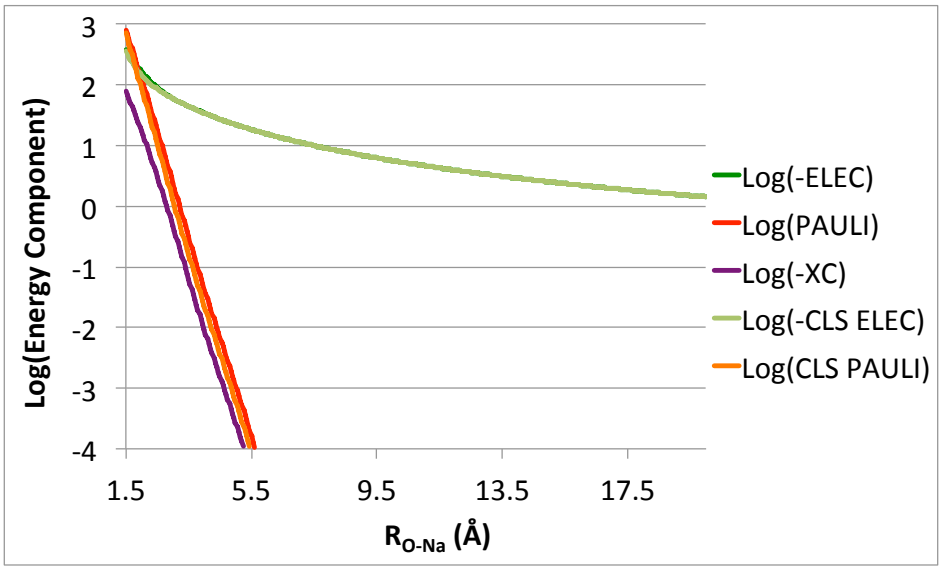

(a) Plot of log(±TERM) vs. $R_{O\text{-}Na}$ for terms summing to the frozen energy as computed by the newly introduced and classical approaches. Linear relationships in this plot indicate an exponential decay of the given interaction with distance.

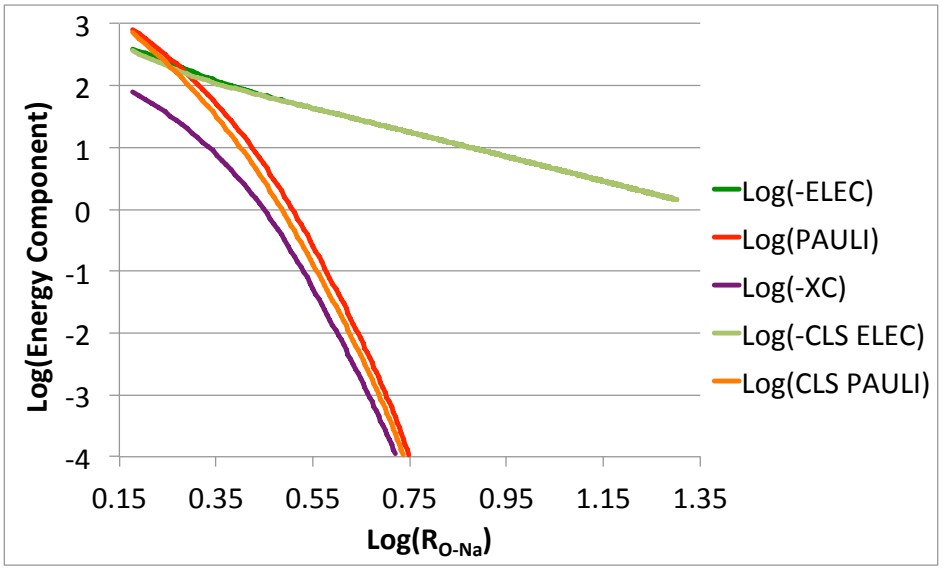

(b) Plot of log(±TERM) vs. log($R_{O\text{-}Na}$) for terms summing to the frozen energy as computed by the newly introduced and classical approaches. Linear relationships in this plot indicate a polynomial decay of the given interaction with distance.

Figure B.2: Plots for the assessment of rate of decay of EDA terms computed with HF/aug-cc-pVQZ for the rigid dissociation along the O-Na coordinate of water interacting with a sodium cation relative to the C_{2v} ωB97X-V/aug-cc-pVQZ optimized geometry (equilibrium $R_{O\text{-}Na}$ = 2.23Å). Terms that are not uniformly signed throughout the coordinate are split into attractive(-) and repulsive(+) portions.

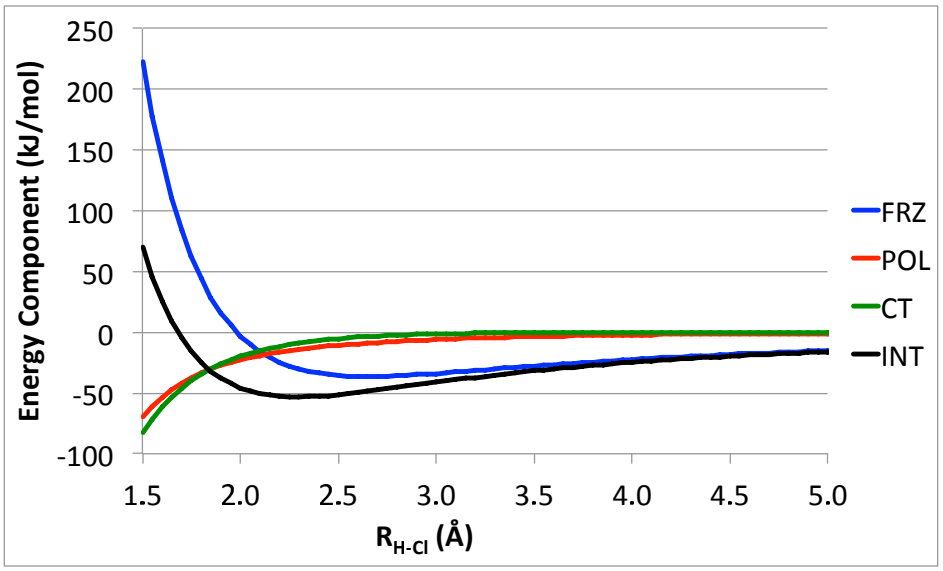

(a) Basic energy decomposition terms (FRZ, POL, CT) as well as the total interaction energy (INT) along the coordinate.

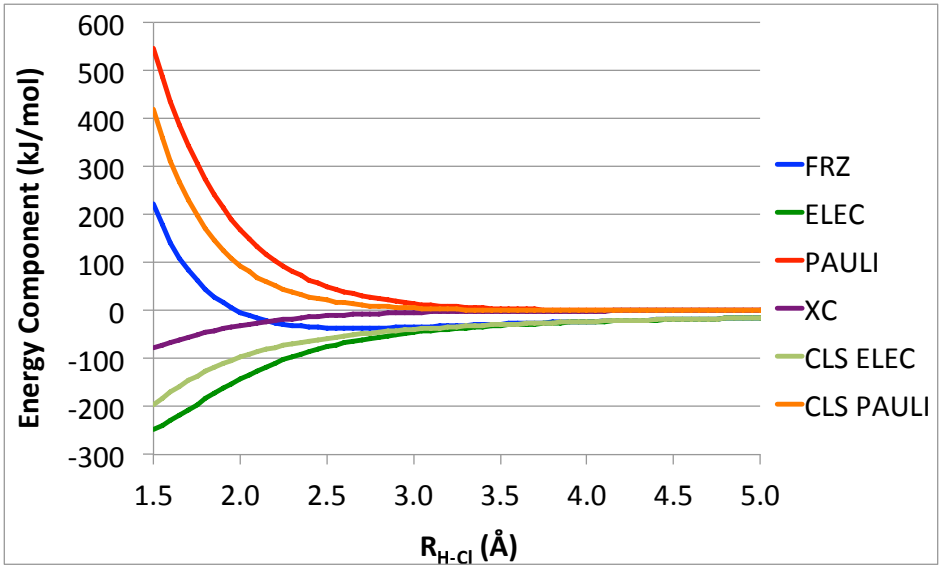

(b) Further decomposition of the frozen energy (FRZ) based on the new scheme presented in this work (ELEC, PAULI, XC) and based on the classical approach (CLS ELEC, CLS Pauli).

Figure B.3: Energy terms computed with HF/aug-cc-pVQZ for the rigid dissociation along the H-Cl coordinate of water interacting with a chlorine anion relative to the C_s ωB97X-V/aug-cc-pVQZ optimized geometry (equilibrium $R_{H\text{-}Cl} = 2.15$Å).

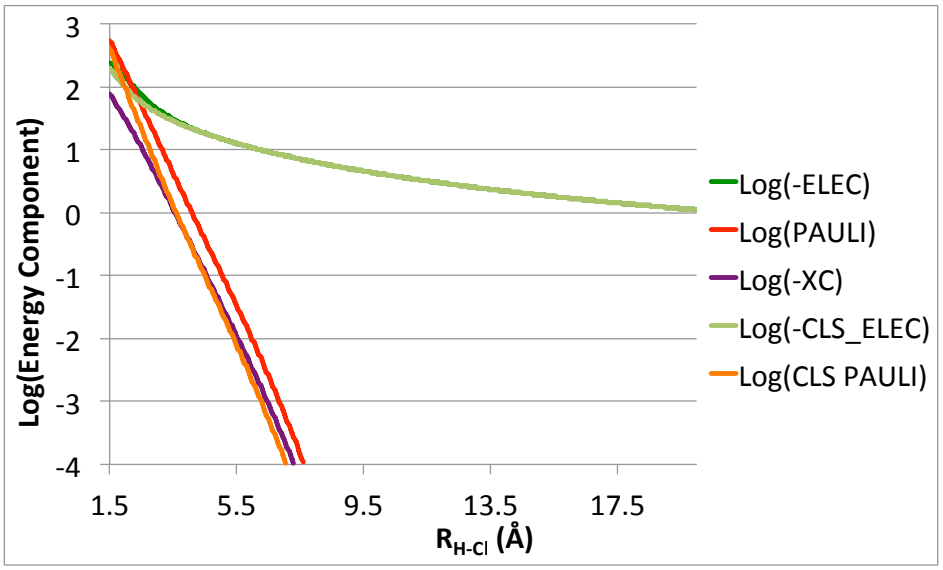

(a) Plot of log(±TERM) vs. $R_{H\text{-}Cl}$ for terms summing to the frozen energy as computed by the newly introduced and classical approaches. Linear relationships in this plot indicate an exponential decay of the given interaction with distance.

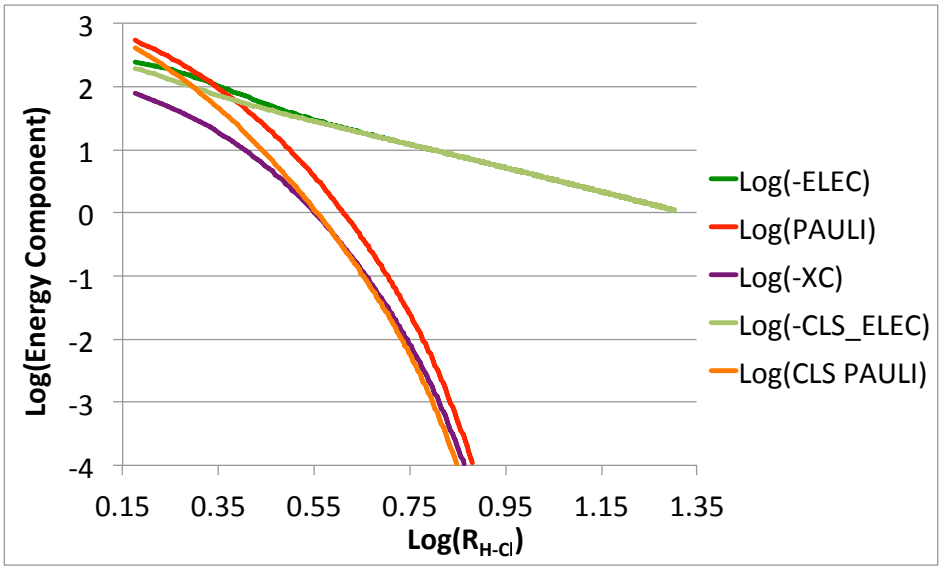

(b) Plot of log(±TERM) vs. log($R_{H\text{-}Cl}$) for terms summing to the frozen energy as computed by the newly introduced and classical approaches. Linear relationships in this plot indicate a polynomial decay of the given interaction with distance.

Figure B.4: Plots for the assessment of rate of decay of EDA terms computed with HF/aug-cc-pVQZ for the rigid dissociation along the H-Cl coordinate of water interacting with a chlorine anion relative to the C_s ωB97X-V/aug-cc-pVQZ optimized geometry (equilibrium $R_{H\text{-}Cl}$ = 2.15Å). Terms that are not uniformly signed throughout the coordinate are split into attractive(-) and repulsive(+) portions.

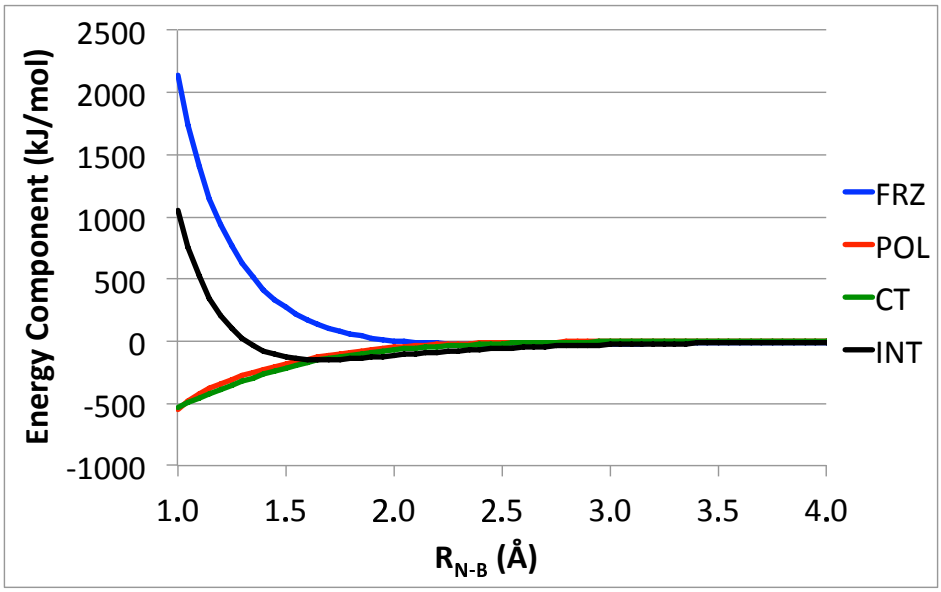

(a) Basic energy decomposition terms (FRZ, POL, CT) as well as the total interaction energy (INT) along the coordinate.

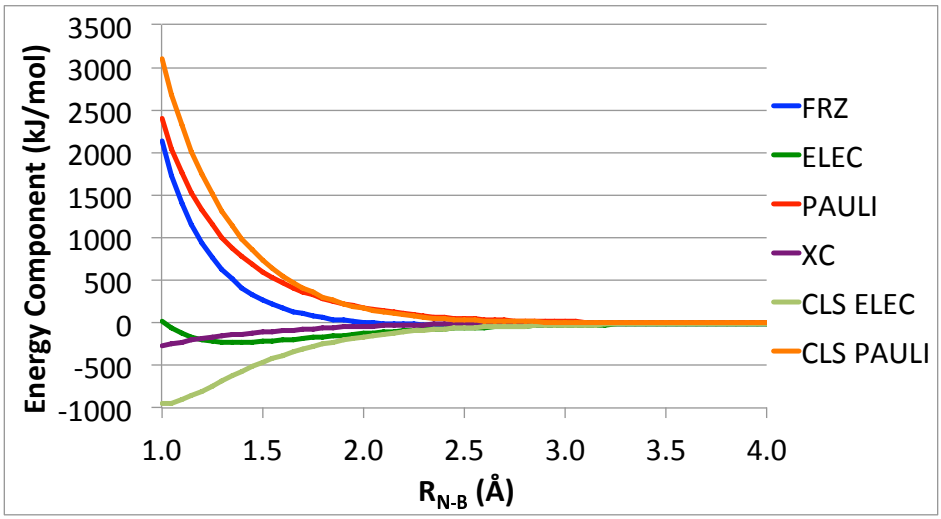

(b) Further decomposition of the frozen energy (FRZ) based on the new scheme presented in this work (ELEC, PAULI, XC) and based on the classical approach (CLS ELEC, CLS Pauli).

Figure B.5: Energy terms computed with HF/aug-cc-pVQZ for the rigid dissociation along the N-B coordinate of the ammonia borane complex relative to the C_{3v} ωB97X-V/aug-cc-pVQZ optimized geometry (equilibrium $R_{N\text{-}B} = 1.65$Å).

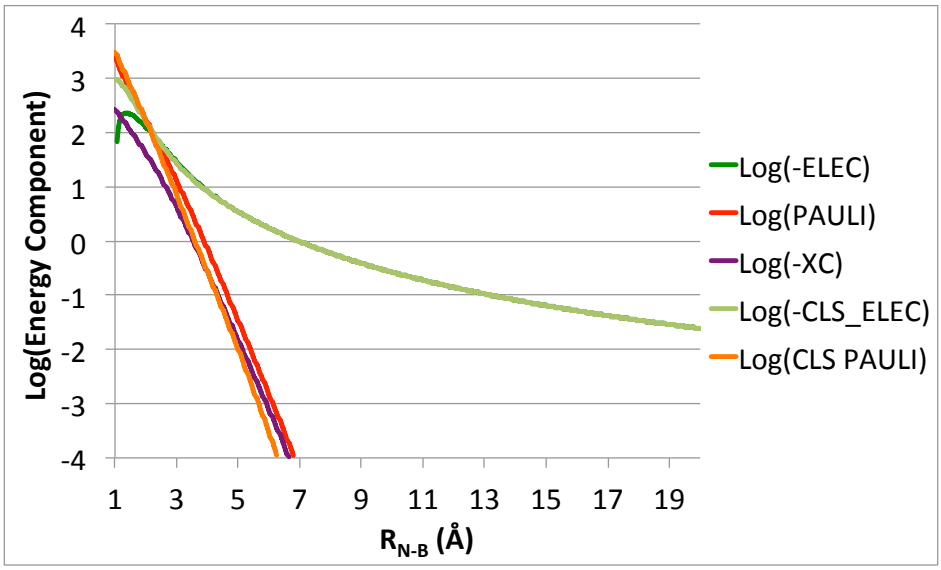

(a) Plot of log(±TERM) vs. $R_{N\text{-}B}$ for terms summing to the frozen energy as computed by the newly introduced and classical approaches. Linear relationships in this plot indicate an exponential decay of the given interaction with distance.

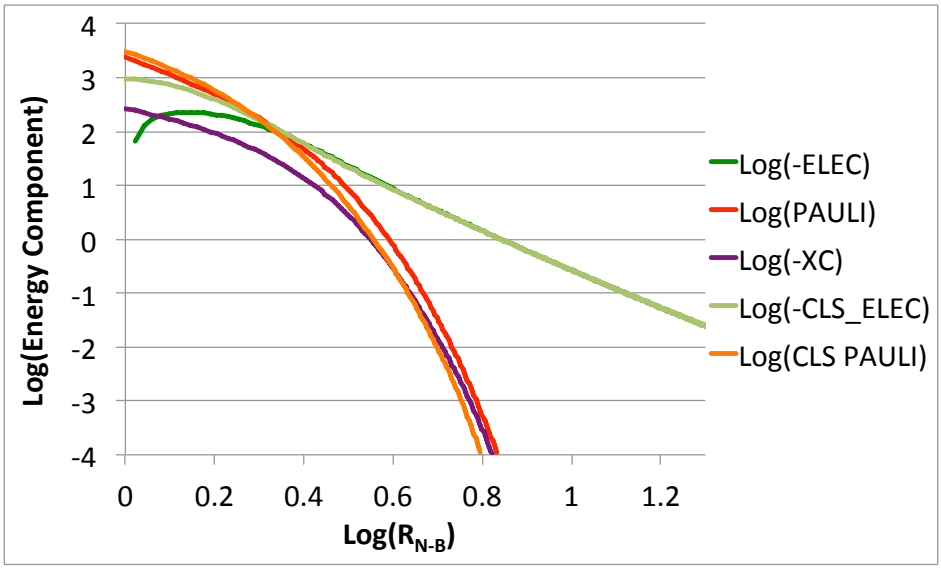

(b) Plot of log(±TERM) vs. log($R_{N\text{-}B}$) for terms summing to the frozen energy as computed by the newly introduced and classical approaches. Linear relationships in this plot indicate a polynomial decay of the given interaction with distance.

Figure B.6: Plots for the assessment of rate of decay of EDA terms computed with HF/aug-cc-pVQZ for the rigid dissociation along the N-B coordinate of the ammonia borane complex relative to the C_{3v} ωB97X-V/aug-cc-pVQZ optimized geometry (equilibrium $R_{N\text{-}B} = 1.65$Å). Terms that are not uniformly signed throughout the coordinate are split into attractive(-) and repulsive(+) portions.

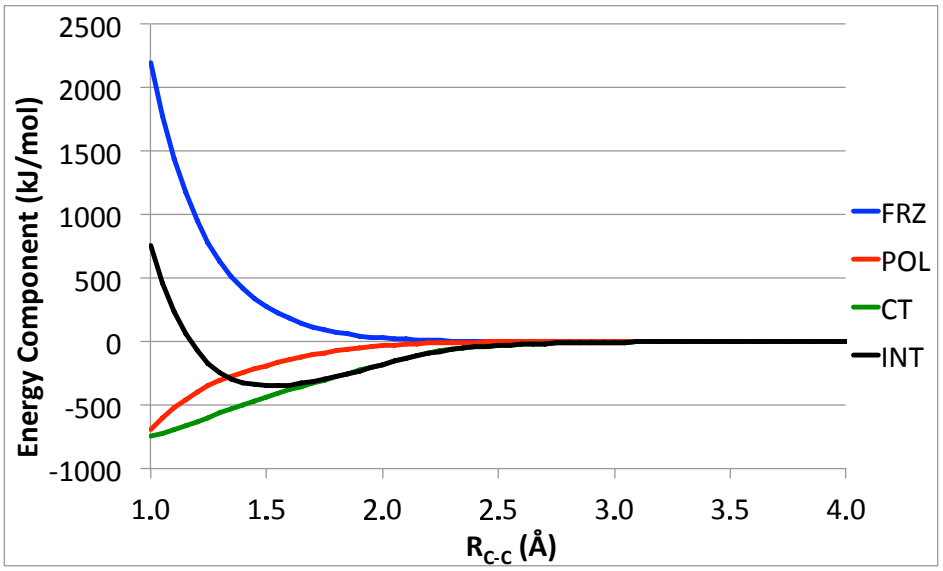

(a) Basic energy decomposition terms (FRZ, POL, CT) as well as the total interaction energy (INT) along the coordinate.

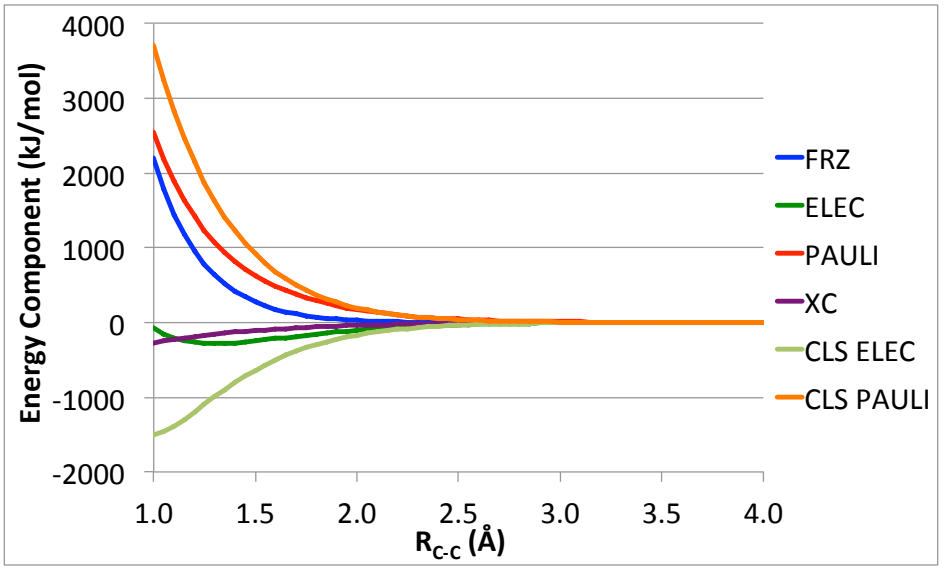

(b) Further decomposition of the frozen energy (FRZ) based on the new scheme presented in this work (ELEC, PAULI, XC) and based on the classical approach (CLS ELEC, CLS Pauli).

Figure B.7: Energy terms computed with HF/aug-cc-pVQZ for the rigid dissociation along the C-C coordinate of ethane relative to the D_{3d} (staggered) ωB97X-V/aug-cc-pVQZ optimized geometry (equilibrium $R_{C\text{-}C} = 1.53$Å) to form two methyl radicals of opposite net spin.

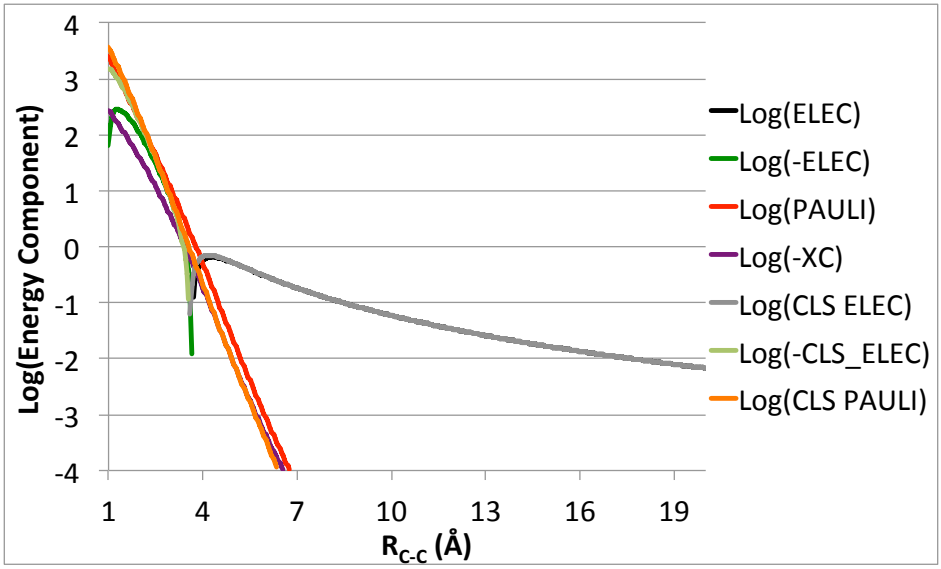

(a) Plot of log(±TERM) vs. $R_{C\text{-}C}$ for terms summing to the frozen energy as computed by the newly introduced and classical approaches. Linear relationships in this plot indicate an exponential decay of the given interaction with distance.

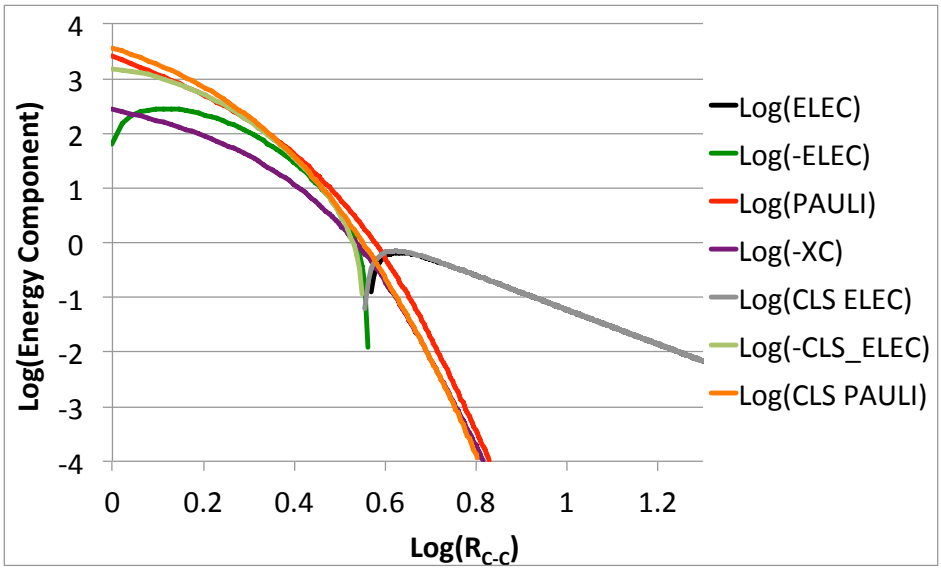

(b) Plot of log(±TERM) vs. log($R_{C\text{-}C}$) for terms summing to the frozen energy as computed by the newly introduced and classical approaches. Linear relationships in this plot indicate a polynomial decay of the given interaction with distance.

Figure B.8: Plots for the assessment of rate of decay of EDA terms computed with HF/aug-cc-pVQZ for the rigid dissociation along the C-C coordinate of ethane relative to the D_{3d} (staggered) ωB97X-V/aug-cc-pVQZ optimized geometry (equilibrium $R_{C\text{-}C} = 1.53$Å) to form two methyl radicals of opposite net spin. Terms that are not uniformly signed throughout the coordinate are split into attractive(-) and repulsive(+) portions.

References

(1) Parr, R. G.; Weitao, Y., *Density-Functional Theory of Atoms and Molecules*; Oxford University Press: New York, 1989.

(2) Perdew, J. P.; Schmidt, K. Jacob's ladder of density functional approximations for the exchange-correlation energy. *AIP Conference Proceedings* **2001**, *577*, 1–20.

(3) Grimme, S. Semiempirical GGA-Type Density Functional Constructed with a Long-Range Dispersion Correction. *Journal of Computational Chemistry* **2006**, *27*, 1787–1799.

(4) Grimme, S.; Antony, J.; Ehrlich, S.; Krieg, H. A consistent and accurate ab initio parametrization of density functional dispersion correction (DFT-D) for the 94 elements H-Pu. *The Journal of Chemical Physics* **2010**, *132*, 154104.

(5) Vydrov, O. A.; Van Voorhis, T. Nonlocal van der Waals density functional: The simpler the better. *The Journal of Chemical Physics* **2010**, *133*, 244103.

(6) Becke, A. D. Density-functional thermochemistry. III. The role of exact exchange. *The Journal of Chemical Physics* **1993**, *98*, 5648–5652.

(7) Lee, C.; Yang, W.; Parr, R. G. Development of the Colle-Salvetti correlation-energy formula into a functional of the electron density. *Physical Review B* **1988**, *37*, 785–789.

(8) Becke, A. D. Density-functional exchange-energy approximation with correct asymptotic behavior. *Physical Review A* **1988**, *38*, 3098–3100.

(9) Chai, J. D.; Head-Gordon, M. Systematic optimization of long-range corrected hybrid density functionals. *The Journal of Chemical Physics* **2008**, *128*, 084106.

(10) Chai, J.-D.; Head-Gordon, M. Long-range corrected hybrid density functionals with damped atom-atom dispersion corrections. *Physical Chemistry Chemical Physics* **2008**, *10*, 6615–6620.

(11) Mardirossian, N.; Head-Gordon, M. xB97X-V: A 10-parameter, range-separated hybrid, generalized gradient approximation density functional with nonlocal correlation, designed by a survival-of-the-fittest strategy. *Physical Chemistry Chemical Physics* **2014**, *16*, 9904–9924.

(12) Zhao, Y.; Truhlar, D. G. The M06 suite of density functionals for main group thermochemistry, thermochemical kinetics, noncovalent interactions, excited states, and transition elements: two new functionals and systematic testing of four M06-class functionals and 12 other function. *Theoretical Chemistry Accounts* **2008**, *120*, 215–241.

(13) Weisskopf, V. F. Of Atoms, Mountains, and Stars: A Study in Qualitative Physics. *Science* **1975**, *187*, 605–612.

(14) Thirman, J.; Head-Gordon, M. Electrostatic Domination of the Effect of Electron Correlation in Intermolecular Interactions. *The Journal of Physical Chemistry Letters* **2014**, *5*, 1380–1385.

(15) Khaliullin, R. Z.; Head-Gordon, M.; Bell, A. T. An efficient self-consistent field method for large systems of weakly interacting components. *The Journal of Chemical Physics* **2006**, *124*, 204105.

(16) Khaliullin, R. Z.; Cobar, E. A.; Lochan, R. C.; Bell, A. T.; Head-Gordon, M. Unravelling the Origin of Intermolecular Interactions Using Absolutely Localized Molecular Orbitals. *The Journal of Physical Chemistry A* **2007**, *111*, 8753–8765.

(17) Khaliullin, R. Z.; Bell, A. T.; Head-Gordon, M. Analysis of charge transfer effects in molecular complexes based on absolutely localized molecular orbitals. *The Journal of Chemical Physics* **2008**, *128*, 184112.

(18) Horn, P. R.; Sundstrom, E. J.; Baker, T. A.; Head-Gordon, M. Unrestricted absolutely localized molecular orbitals for energy decomposition analysis: theory and applications to intermolecular interactions involving radicals. *The Journal of Chemical Physics* **2013**, *138*, 134119.

(19) Rybak, S.; Jeziorski, B.; Szalewicz, K. Many-body symmetry-adapted perturbation theory of intermolecular interactions. H2O and HF dimers. *The Journal of Chemical Physics* **1991**, *95*, 6576–6601.

(20) Jeziorski, B.; Moszynski, R.; Szalewicz, K. Perturbation Theory Approach to Intermolecular Potential Energy Surfaces of van der Waals Complexes. *Chemical Reviews* **1994**, *94*, 1887–1930.

(21) Adams, W. H. Two new symmetry-adapted perturbation theories for the calculation of intermolecular interaction energies. *Theoretical Chemistry Accounts* **2002**, *108*, 225–231.

(22) Misquitta, A. J.; Jeziorski, B.; Szalewicz, K. Dispersion Energy from Density-Functional Theory Description of Monomers. *Physical Review Letters* **2003**, *91*, 033201.

(23) Misquitta, A. J.; Podeszwa, R.; Jeziorski, B.; Szalewicz, K. Intermolecular potentials based on symmetry-adapted perturbation theory with dispersion energies from time-dependent density-functional calculations. *The Journal of Chemical Physics* **2005**, *123*, 214103.

(24) Zuchowski, P. S.; Podeszwa, R.; Moszyinski, R.; Jeziorski, B.; Szalewicz, K. Symmetry-adapted perturbation theory utilizing density functional description of monomers for high-spin open-shell complexes. *The Journal of Chemical Physics* **2008**, *129*, 084101.

(25) Stone, A. J.; Misquitta, A. J. Charge-transfer in Symmetry-Adapted Perturbation Theory. *Chemical Physics Letters* **2009**, *473*, 201–205.

(26) Hapka, M.; Zuchowski, P. S.; Szczesniak, M. M.; Chaasiski, G. Symmetry-adapted perturbation theory based on unrestricted Kohn-Sham orbitals for high-spin open-shell van der Waals complexes. *Journal of Chemical Physics* **2012**, *137*, 164104.

(27) Hohenstein, E. G.; Sherrill, C. D. Wavefunction methods for noncovalent interactions. *WIREs Computational Molecular Science* **2012**, *2*, 304–326.

(28) Lao, K. U.; Herbert, J. M. Accurate Intermolecular Interactions at Dramatically Reduced Cost: XPol+SAPT with Empirical Dispersion. *The Journal of Physical Chemistry Letters* **2012**, *3*, 3241–3248.

(29) Szalewicz, K. Symmetry-adapted perturbation theory of intermolecular forces. *WIREs Computational Molecular Science* **2012**, *2*, 254–272.

(30) Gordon, M. S.; Freitag, M. A.; Bandyopadhyay, P.; Jensen, J. H.; Kairys, V.; Stevens, W. J. The Effective Fragment Potential Method: A QM-Based MM Approach to Modeling Environmental Effects in Chemistry. *The Journal of Physical Chemistry A* **2001**, *105*, 293–307.

(31) Adamovic, I.; Freitag, M. A.; Gordon, M. S. Density functional theory based effective fragment potential method. *The Journal of Chemical Physics* **2003**, *118*, 6725–6732.

(32) Li, H.; Gordon, M. S.; Jensen, J. H. Charge transfer interaction in the effective fragment potential method. *The Journal of Chemical Physics* **2006**, *124*, 214108.

(33) Gordon, M. S.; Mullin, J. M.; Pruitt, S. R.; Roskop, L. B.; Slipchenko, L. V.; Boatz, J. A. Accurate Methods for Large Molecular Systems. *The Journal of Physical Chemistry B* **2009**, *113*, 9646–9663.

(34) Glendening, E. D.; Streitwieser, A. Natural energy decomposition analysis: An energy partitioning procedure for molecular Interactions with application to weak hydrogen bonding, strong ionic, and moderate donor-acceptor interactions. *The Journal of Chemical Physics* **1994**, *100*, 2900–2909.

(35) Schenter, G. K.; Glendening, E. D. Natural Energy Decomposition Analysis: The Linear Response Electrical Self Energy. *The Journal of Physical Chemistry* **1996**, *100*, 17152–17156.

(36) Glendening, E. D. Natural Energy Decomposition Analysis: Extension to Density Functional Methods and Analysis of Cooperative Effects in Water Clusters. *The Journal of Physical Chemistry A* **2005**, *109*, 11936–11940.

(37) Reed, A. E.; Curtiss, L. A.; Weinhold, F. Intermolecular Interactions from a Natural Bond Orbital, Donor-Acceptor Viewpoint. *Chemical Reviews* **1988**, *88*, 899–926.

(38) Kitaura, K.; Morokuma, K. A New Energy Decomposition Scheme for Molecular Interactions within the Hartree-Fock Approximation. *International Journal of Quantum Chemistry* **1976**, *10*, 325–340.

(39) Ziegler, T.; Rauk, A. On the Calculation of Bonding Energies by the Hartree Fock Slater Method. *Theoretical Chemistry Accounts* **1977**, *46*, 1–10.

(40) Ziegler, T.; Rauk, A. A Theoretical Study of the Ethylene-Metal Bond in Complexes between Cu^+, Ag^+, Pt^0, or Pt^{2+} and Ethylene, Based on Hartree-Fock-Slater Transition-State Method. *Inorganic Chemistry* **1979**, *18*, 1558–1565.

(41) Mitoraj, M. P.; Michalak, A.; Ziegler, T. A Combined Charge and Energy Decomposition Scheme for Bond Analysis. *Journal of Chemical Theory and Computation* **2009**, *5*, 962–975.

(42) Bagus, P. . S.; Hermann, K.; Bauschlicher, C. W. J. A new analysis of charge transfer and polarization for ligand-metal bonding: Model studies of Al_4CO and Al_4NH_3. *The Journal of Chemical Physics* **1984**, *80*, 4378–4386.

(43) Stevens, W. J.; Fink, W. H. Frozen Fragment Reduced Variational Space Analysis of Hydrogen Bonding Interactions. Application to the Water Dimer. *Chemical Physics Letters* **1987**, *139*, 15–22.

(44) Bickelhaupt, F. M.; Baerends, E. J. In *Reviews in Computational Chemistry*, Lipkowitz, K. B., Boyd, D. B., Eds.; John Wiley & Sons, Inc.: New York, 2007; Vol. 15; Chapter 1, pp 1–86.

(45) Su, P.; Li, H. Energy decomposition analysis of covalent bonds and intermolecular interactions. *The Journal of Chemical Physics* **2009**, *131*, 014102.

(46) Mo, Y.; Gao, J.; Peyerimhoff, S. D. Energy decomposition analysis of intermolecular interactions using a block-localized wave function approach. *The Journal of Chemical Physics* **2000**, *112*, 5530–5538.

(47) Mo, Y.; Song, L.; Lin, Y. Block-Localized Wavefunction (BLW) Method at the Density Functional Theory (DFT) Level. *The Journal of Physical Chemistry A* **2007**, *111*, 8291–8301.

(48) Mo, Y.; Bao, P.; Gao, J. Energy decomposition analysis based on a block-localized wavefunction and multistate density functional theory. *Physical Chemistry Chemical Physics* **2011**, *13*, 6760–6775.

(49) Steinmann, S. N.; Corminboeuf, C.; Wu, W.; Mo, Y. Dispersion-Corrected Energy Decomposition Analysis for Intermolecular Interactions Based on the BLW and dDXDM Methods. *The Journal of Physical Chemistry A* **2011**, *115*, 5467–5477.

(50) Sadlej, A. J. Long range induction and dispersion interactions between Hartree-Fock subsystems. *Molecular Physics* **1980**, *39*, 1249–1264.

(51) Wu, Q.; Ayers, P. W.; Zhang, Y. Density-based energy decomposition analysis for intermolecular interactions with variationally determined intermediate state energies. *The Journal of Chemical Physics* **2009**, *131*, 164112.

(52) Cohen, M. H.; Wasserman, A.; Car, R.; Burke, K. Charge Transfer in Partition Theory. *The Journal of Physical Chemistry A* **2009**, *113*, 2183–2192.

(53) Elliott, P.; Burke, K.; Cohen, M. H.; Wasserman, A. Partition density-functional theory. *Physical Review A* **2010**, *82*, 024501.

(54) Cobar, E. A.; Horn, P. R.; Bergman, R. G.; Head-Gordon, M. Examination of the hydrogen-bonding networks in small water clusters (n = 2-5, 13, 17) using absolutely localized molecular orbital energy decomposition analysis. *Physical Chemistry Chemical Physics* **2012**, *14*, 15328–15339.

(55) Swanson, J. M. J.; Simons, J. Role of Charge Transfer in the Structure and Dynamics of the Hydrated Proton. *The Journal of Physical Chemistry B* **2009**, *113*, 5149–5161.

(56) Ess, D. H.; Bischof, S. M.; Oxgaard, J.; Periana, R. A.; Goddard, W. A. I. Transition State Energy Decomposition Study of Acetate-Assisted and Internal Electrophilic Substitution C-H Bond Activation by (acac-O , O)$_2$Ir(X) Complexes (X = CH_3COO, OH). *Organometallics* **2008**, *27*, 6440–6445.

(57) Ess, D. H.; Goddard, W. A. I.; Periana, R. A. Electrophilic, Ambiphilic, and Nucleophilic C-H Bond Activation: Understanding the Electronic Continuum of C-H Bond Activation Through Transition-State and Reaction Pathway Interaction Energy Decompositions. *Organometallics* **2010**, *29*, 6459–6472.

(58) Lambrecht, D. S.; Clark, G. N. I.; Head-Gordon, T.; Head-Gordon, M. Exploring the Rich Energy Landscape of Sulfate-Water Clusters SO_4^{2-} (H2O)(n=3-7): an Electronic Structure Approach. *The Journal of Physical Chemistry A* **2011**, *115*, 11438–11454.

(59) Ramos-Cordoba, E.; Lambrecht, D. S.; Head-Gordon, M. Charge-transfer and the hydrogen bond: Spectroscopic and structural implications from electronic structure calculations. *Faraday Discussions* **2011**, *150*, 345–362.

(60) Young, R. M.; Azar, R. J.; Yandell, M. A.; King, S. B.; Head-Gordon, M.; Neumark, D. M. Iodide solvation in tetrahydrofuran clusters : $I^-(THF)_n$ ($1 \leq n \leq 30$). *Molecular Physics* **2012**, *110*, 1787–1799.

(61) Hammerum, S. Alkyl Radicals as Hydrogen Bond Acceptors: Computational Evidence. *Journal of the American Chemical Society* **2009**, *131*, 8627–8635.

(62) Mizuse, K.; Hasegawa, H.; Mikami, N.; Fujii, A. Infrared and Electronic Spectroscopy of Benzene-Ammonia Cluster Radical Cations $[C_6H_6(NH_3)_{1,2}]^+$: Observation of Isolated and Microsolvated σ-Complexes. *The Journal of Physical Chemistry A* **2010**, *114*, 11060–11069.

(63) Head-Gordon, M.; Maslen, P. E.; White, C. A. A tensor formulation of many-electron theory in a nonorthogonal single-particle basis. *The Journal of Chemical Physics* **1998**, *108*, 616–625.

(64) Stoll, H.; Wagenblast, G.; Preuß, H. On the Use of Local Basis Sets for Localized Molecular Orbitals. *Theoretical Chemistry Accounts* **1980**, *57*, 169–178.

(65) Gianinetti, E.; Raimondi, M.; Tornaghi, E. Modification of the Roothaan Equations to Exclude BSSE from Molecular Interaction Calculations. *International Journal of Quantum Chemistry* **1996**, *60*, 157–166.

(66) Gianinetti, E.; Vandoni, A.; Famulari, A.; Raimondi, M. Extenstion of the SCF-MI Method to the Case of K Fragments one of which is an Open-Shell System. *Advances in Quantum Chemistry* **1998**, *31*, 251–266.

(67) Pulay, P. Improved SCF Convergence Acceleration. *Journal of Computational Chemistry* **1982**, *3*, 556–560.

(68) Liang, W.; Head-Gordon, M. Approaching the Basis Set Limit in Density Functional Theory Calculations Using Dual Basis Sets without Diagonalization. *The Journal of Physical Chemistry A* **2004**, *108*, 3206–3210.

(69) Azar, R. J.; Horn, P. R.; Sundstrom, E. J.; Head-Gordon, M. Useful lower limits to polarization contributions to intermolecular interactions using a minimal basis of localized orthogonal orbitals: theory and analysis of the water dimer. *The Journal of Chemical Physics* **2013**, *138*, 084102.

(70) Shao, Y. et al. Advances in methods and algorithms in a modern quantum chemistry program package. *Physical Chemistry Chemical Physics* **2006**, *8*, 3172–3191.

(71) Pettersen, E. F.; Goddard, T. D.; Huang, C. C.; Couch, G. S.; Greenblatt, D. M.; Meng, E. C.; Ferrin, T. E. UCSF Chimera – A Visualization System for Exploratory Research and Analysis. *Journal of Computational Chemistry* **2004**, *25*, 1605–1612.

(72) Hammerum, S.; Nielsen, C. B. Intramolecular Hydrogen Bonding and Hydrogen Atom Abstraction in Gas-Phase Aliphatic Amine Radical Cations. *The Journal of Physical Chemistry A* **2005**, *109*, 12046–12053.

(73) *NIST Chemistry WebBook, NIST Standard Reference Database Number 69*; Linstrom, P. j., Mallard, W. G., Eds.; National Institute of Standards and Technology: Gaithersburg, 2015.

(74) Phipps, M. J. S.; Fox, T.; Tautermann, C. S.; Skylaris, C.-K. Energy decomposition analysis approaches and their evaluation on prototypical protein-drug interaction patterns. *Chemical Society Reviews* **2015**, *44*, 3177–3211.

(75) Wu, Q. Variational nature of the frozen density energy in density-based energy decomposition analysis and its application to torsional potentials. *The Journal of Chemical Physics* **2014**, *140*, 244109.

(76) Krapp, A.; Bickelhaupt, F. M.; Frenking, G. Orbital Overlap and Chemical Bonding. *Chemistry - A European Journal* **2006**, *12*, 9196–9216.

(77) Von Hopffgarten, M.; Frenking, G. Energy decomposition analysis. *Wiley Interdisciplinary Reviews: Computational Molecular Science* **2012**, *2*, 43–62.

(78) Ndambuki, S.; Ziegler, T. An Analysis of Unsupported Triple and Quadruple Metal-Metal Bonds between Two Homonuclear Group 6 Transition Elements Based on the Combined Natural Orbitals for Chemical Valence and Extended Transition State Method. *International Journal of Quantum Chemistry* **2013**, *113*, 753–761.

(79) Reinhardt, P.; Piquemal, J.-P.; Savin, A. Fragment-Localized Kohn-Sham Orbitals via a Singles Configuration-Interaction Procedure and Application to Local Properties and Intermolecular Energy Decomposition. *Journal of Chemical Theory and Computation* **2008**, *4*, 2020–2029.

(80) Su, P.; Liu, H.; Wu, W. Free energy decomposition analysis of bonding and nonbonding interactions in solution. *The Journal of Chemical Physics* **2012**, *137*, 034111.

(81) Su, P.; Jiang, Z.; Chen, Z.; Wu, W. Energy Decomposition Scheme Based on the Generalized Kohn-Sham Scheme. *The Journal of Physical Chemistry A* **2014**, *118*, 2531–2542.

(82) Mandado, M.; Hermida-Ramón, J. M. Electron Density Based Partitioning Scheme of Interaction Energies. *Journal of Chemical Theory and Computation* **2011**, *7*, 633–641.

(83) Hayes, I. C.; Stone, A. J. An intermolecular perturbation theory for the region of moderate overlap. *Molecular Physics* **1984**, *53*, 83–105.

(84) Misquitta, A. J. Charge Transfer from Regularized Symmetry-Adapted Perturbation Theory. *Journal of Chemical Theory and Computation* **2013**, *9*, 5313–5326.

(85) Reed, A.; Weinhold, F. Natural bond orbital analysis of near-Hartree-Fock water dimer. *The Journal of Chemical Physics* **1983**, *78*, 4066–4073.

(86) Morokuma, K. Why Do Molecules Interact? The Origin of Electron Donor-Acceptor Complexes, Hydrogen Bonding and Proton Affinity. *Accounts of Chemical Research* **1977**, *10*, 294–300.

(87) Chen, W.; Gordon, M. S. Energy Decomposition Analyses for Many-Body Interaction and Applications to Water Complexes. *The Journal of Physical Chemistry* **1996**, *100*, 14316–14328.

(88) Fedorov, D. G.; Kitaura, K. Pair Interaction Energy Decomposition Analysis. *Journal of Computational Chemistry* **2007**, *28*, 222–237.

(89) Green, M. C.; Fedorov, D. G.; Kitaura, K.; Francisco, J. S.; Slipchenko, L. V. Open-shell pair interaction energy decomposition analysis (PIEDA): formulation and application to the hydrogen abstraction in tripeptides. *The Journal of Chemical Physics* **2013**, *138*, 074111.

(90) Korchowiec, J.; Uchimaru, T. Mechanism of Addition of Fluoromethyl Radicals to Fluoroethylenes. *The Journal of Physical Chemistry A* **1998**, *102*, 6682–6689.

(91) Korchowiec, J.; Uchimaru, T. New energy partitioning scheme based on the self-consistent charge and configuration method for subsystems: Application to water dimer system. *The Journal of Chemical Physics* **2000**, *112*, 1623–1633.

(92) Kitaura, K.; Sawai, T.; Asada, T.; Nakano, T.; Uebayasi, M. Pair interaction molecular orbital method: an approximate computational method for molecular interactions. *Chemical Physics Letters* **1999**, *312*, 319–324.

(93) Kitaura, K.; Ikeo, E.; Asada, T.; Nakano, T.; Uebayasi, M. Fragment molecular orbital method: an approximate computational method for large molecules. *Chemical Physics Letters* **1999**, *313*, 701–706.

(94) Gordon, M. S.; Fedorov, D. G.; Pruitt, S. R.; Slipchenko, L. V. Fragmentation Methods: A Route to Accurate Calculations on Large Systems. *Chemical Reviews* **2012**, *112*, 632–672.

(95) Mochizuki, Y.; Fukuzawa, K.; Kato, A.; Tanaka, S.; Kitaura, K.; Nakano, T. A configuration analysis for fragment interaction. *Chemical Physics Letters* **2005**, *410*, 247–253.

(96) Řezáč, J.; de la Lande, A. Robust, Basis-Set Independent Method for the Evaluation of Charge-Transfer Energy in Noncovalent Complexes. *Journal of Chemical Theory and Computation* **2015**, *11*, 528–537.

(97) De Silva, P.; Korchowiec, J. Energy Partitioning Scheme Based on Self-Consistent Method for Subsystems: Populational Space Approach. *Journal of Computational Chemistry* **2011**, *32*, 1054–1064.

(98) Yamada, K.; Koga, N. Variationally determined electronic states for the theoretical analysis of intramolecular interaction: I. Resonance energy and rotational barrier of the C-N bond in formamide and its analogs. *Theoretical Chemistry Accounts* **2012**, *131*, 1178.

(99) Nagata, T.; Takahashi, O.; Saito, K.; Iwata, S. Basis set superposition error free self-consistent field method for molecular interaction in multi-component systems: Projection operator formalism. *The Journal of Chemical Physics* **2001**, *115*, 3553–3560.

(100) Stone, A. J. Computation of charge-transfer energies by perturbation theory. *Chemical Physics Letters* **1993**, *211*, 101–109.

(101) Ghanty, T. K.; Staroverov, V. N.; Koren, P. R.; Davidson, E. R. Is the Hydrogen Bond in Water Dimer and Ice Covalent? *Journal of the American Chemical Society* **2000**, *122*, 1210–1214.

(102) Stone, A. J., *The Theory of Intermolecular Forces*, 2nd ed.; Oxford University Press: Oxford, 2013, p 285.

(103) Nocedal, J.; Wright, S. J., *Numerical Optimization*; Glynn, P., Robinson, S. M., Eds.; Springer Series in Operations Research and Financial Engineering; Springer-Verlag: New York, 1999, pp 224–227.

(104) Van Voorhis, T.; Head-Gordon, M. A geometric approach to direct minimization. *Molecular Physics* **2002**, *100*, 1713–1721.

(105) Weinhold, F.; Carpenter, J. E. Some Remarks on Nonorthogonal Orbitals in Quantum Chemistry. *Journal of Molecular Structure: THEOCHEM* **1988**, *165*, 189–202.

(106) Carlson, B. C.; Keller, J. M. Orthogonalization Procedures and the Localization of Wannier Functions. *Physical Review* **1957**, *105*, 102–103.

(107) Liang, W.; Head-Gordon, M. An exact reformulation of the diagonalization step in electronic structure calculations as a set of second order nonlinear equations. *The Journal of Chemical Physics* **2004**, *120*, 10379–10384.

(108) Shao, Y. et al. Advances in molecular quantum chemistry contained in the Q-Chem 4 program package. *Molecular Physics* **2015**, *113*, 184–215.

(109) Dunning, T. H. J. Gaussian basis sets for use in correlated molecular calculations. I. The atoms boron through neon and hydrogen. *The Journal of Chemical Physics* **1989**, *90*, 1007–1023.

(110) Kendall, R. A.; Dunning, T. H. J.; Harrison, R. J. Electron affinities of the first-row atoms revisited. Systematic basis sets and wave functions. *The Journal of Chemical Physics* **1992**, *96*, 6796–6806.

(111) Fornili, A.; Sironi, M.; Raimondi, M. Determination of extremely localized molecular orbitals and their application to quantum mechanics/molecular mechanics methods and to the study of intramolecular hydrogen bonding. *Journal of Molecular Structure: THEOCHEM* **2003**, *632*, 157–172.

(112) Sironi, M.; Genoni, A.; Civera, M.; Pieraccini, S.; Ghitti, M. Extremely localized molecular orbitals: theory and applications. *Theoretical Chemistry Accounts* **2007**, *117*, 685–698.

(113) Harriman, J. E. Geometry of density matrices. IV. The relationship between density matrices and densities. *Physical Review A* **1983**, *27*, 632–645.

(114) McWeeny, R. Some Recent Advances in Density Matrix Theory. *Reviews of Modern Physics* **1960**, *32*, 335–369.

(115) Bowler, D. R.; Gillan, M. J. Density matrices in O(N) electronic structure calculations: theory and applications. *Computer Physics Communications* **1999**, *120*, 95–108.

(116) Smits, G. F.; Altona, C. Calculation and properties of non-orthogonal, strictly local molecular orbitals. *Theoretical Chemistry Accounts* **1985**, *67*, 461–475.

(117) Cullen, J. M. An Examination of the Effects of Basis Set and Charge Transfer in Hydrogen-Bonded Dimers with a Constrained Hartree-Fock Method. *International Journal of Quantum Chemistry* **1991**, *40*, 193–207.

(118) Edelman, A.; Arias, T. A.; Smith, S. T. The Geometry of Algorithms with Orthogonality Constraints. *SIAM Journal on Matrix Analysis and Applications* **1998**, *20*, 303–353.

(119) Moré, J. J.; Thuente, D. J. Line Search Algorithms with Guaranteed Sufficient Decrease. *ACM Transactions on Mathematical Software* **1994**, *20*, 286–307.

(120) Sharada, S. M.; Stück, D.; Sundstrom, E. J.; Bell, A. T.; Head-Gordon, M. Wavefunction stability analysis without analytical electronic Hessians: application to orbital-optimised second-order Mø ller-Plesset theory and VV10-containing density functionals. *Molecular Physics* **2015**, *113*, 1802–1808.

(121) Seeger, R.; Pople, J. A. Self-consistent molecular orbital methods. XVII. Constraints and stability in Hartree-Fock theory. *The Journal of Chemical Physics* **1977**, *66*, 3045–3050.

(122) Becke, A. D.; Johnson, E. R. Exchange-hole dipole moment and the dispersion interaction. *The Journal of Chemical Physics* **2005**, *122*, 154104.

(123) Becke, A. D.; Johnson, E. R. Exchange-hole dipole moment and the dispersion interaction: High-order dispersion coefficients. *Journal of Chemical Physics* **2006**, *124*, 014104.

(124) Becke, A. D.; Johnson, E. R. Exchange-hole dipole moment and the dispersion interaction revisited. *The Journal of Chemical Physics* **2007**, *127*, 154108.

(125) Kong, J.; Gan, Z.; Proynov, E.; Freindorf, M.; Furlani, T. R. Efficient computation of the dispersion interaction with density-functional theory. *Physical Review A* **2009**, *79*, 042510.

(126) Steinmann, S. N.; Corminboeuf, C. A System-Dependent Density-Based Dispersion Correction. *Journal of Chemical Theory and Computation* **2010**, *6*, 1990–2001.

(127) Lu, Z.; Zhou, N.; Wu, Q.; Zhang, Y. Directional Dependence of Hydrogen Bonds: a Density-based Energy Decomposition Analysis and Its Implications on Force Field Development. *Journal of Chemical Theory and Computation* **2011**, *7*, 4038–4049.

(128) Badenhoop, J. K.; Weinhold, F. Natural bond orbital analysis of steric interactions. *The Journal of Chemical Physics* **1997**, *107*, 5406–5421.

(129) Badenhoop, J. K.; Weinhold, F. Natural steric analysis: Ab initio van der Waals radii of atoms and ions. *The Journal of Chemical Physics* **1997**, *107*, 5422–5432.

(130) Badenhoop, J. K.; Weinhold, F. Natural Steric Analysis of Internal Rotation Barriers. *International Journal of Quantum Chemistry* **1998**, *72*, 269.

(131) Liu, S. Steric effect: A quantitative description from density functional theory. *The Journal of Chemical Physics* **2007**, *126*, 244103.

(132) Fang, D.; Piquemal, J.-P.; Liu, S.; Cisneros, G. A. DFT-steric-based energy decomposition analysis of intermolecular interactions. *Theoretical Chemistry Accounts* **2014**, *133*, 1484.

(133) Rappoport, D.; Furche, F. Property-optimized Gaussian basis sets for molecular response calculations. *The Journal of Chemical Physics* **2010**, *133*, 134105.

(134) Janowski, T.; Pulay, P. A Benchmark Comparison of σ/σ and π/π Dispersion: the Dimers of Naphthalene and Decalin, and Coronene and Perhydrocoronene. *Journal of the American Chemical Society* **2012**, *134*, 17520–17525.

(135) Weinhold, F.; Klein, R. A. Anti-Electrostatic Hydrogen Bonds. *Angewandte Chemie International Edition* **2014**, *53*, 11214–11217.

(136) Frenking, G.; Caramori, G. F. No Need for a Re-examination of the Electrostatic Notation of the Hydrogen Bonding: A Comment. *Angewandte Chemie International Edition* **2015**, *54*, 2596–2599.

(137) Weinhold, F.; Klein, R. A. Improved General Understanding of the Hydrogen-Bonding Phenomena: A Reply. *Angewandte Chemie International Edition* **2015**, *54*, 2600–2602.

(138) Jurecka, P.; Sponer, J.; Cerný, J.; Hobza, P. Benchmark database of accurate (MP2 and CCSD(T) complete basis set limit) interaction energies of small model complexes, DNA base pairs, and amino acid pairs. *Physical Chemistry Chemical Physics* **2006**, *8*, 1985–1993.

(139) Whitaker, A.; Jeffery, J. W. The Crystal Structure of Chromium Hexacarbonyl. *Acta Crystallographica* **1967**, *23*, 977–984.

(140) Bell, F.; Ruan, Q. N.; Golan, A.; Horn, P. R.; Ahmed, M.; Leone, S. R.; Head-Gordon, M. Dissociative Photoionization of Glycerol and its Dimer Occurs Predominantly via a Ternary Hydrogen-Bridged Ion-Molecule Complex. *Journal of the American Chemical Society* **2013**, *135*, 14229–14239.